



**ISAS - INTERNATIONAL SCHOOL
FOR ADVANCED STUDIES**

**TIME PROPERTIES OF TWO WIND
FED X-RAY BINARY PULSARS
OBSERVED WITH EXOSAT:
4U 1538-52 AND GX 301-2**

by

Mauro Orlandini

Thesis submitted to the International School for
Advanced Studies, *Astrophysics Sector*,
in partial fulfilment of the requirements for
the degree of

Doctor of Philosophy

Supervisors: Prof. Filippo Frontera
Institute T.E.S.R.E./C.N.R. Bologna

Prof. Massimo Calvani
International School for Advanced Studies, Trieste

Academic Year 1989/90

TRIESTE

**SISSA - SCUOLA
INTERNAZIONALE
SUPERIORE
DI STUDI AVANZATI**

TRIESTE
Strada Costiera 11

**TIME PROPERTIES OF TWO WIND-FED
X-RAY BINARY PULSARS
OBSERVED WITH EXOSAT:
4U 1538-52 AND GX 301-2**

by

Mauro Orlandini

Thesis submitted to the International School for
Advanced Studies, *Astrophysics Sector*,
in partial fulfilment of the requirements
for the degree of

Doctor of Philosophy

Supervisors: Prof. Filippo Frontera
Institute T.E.S.R.E./C.N.R. Bologna

Prof. Massimo Calvani
International School for Advanced Studies, Trieste

December 1990

Ai miei genitori

Acknowledgements

This Thesis is not only the result of much long and hard work so as to understand the subject, but it is also the result of continuous interaction with all the people I have had around, who were not only colleagues but more especially friends. To avoid any injustice I will cite them in *strict* order of appearance in my scientific life:

I would like to thank my professors at the Physics Department of Ferrara, Carlo Gualdi and Pierluigi Fortini, who brought me toward the comprehension of Astrophysics during my undergraduate courses. More than teachers I consider them friends.

Then I had the luck to enter one of the best research centers in Italy, the International School for Advanced Studies of Trieste. There I met Professor Dennis Sciama who, thanks to his wisdom and experience, advised me in making many decisions.

Professor Massimo (Max) Calvani had the ability to understand the most suitable research subject for me, directing me toward the study of X-ray binary pulsars (and introduced me to the art of \TeX .) He also arranged for Professor Filippo Frontera to be my Thesis advisor. Filippo set me on the right path in order to understand the Physics of compact objects, and I am grateful for his precious scientific and personal advice.

I would like to thank the T.E.S.R.E. Institute of the Comitato Nazionale delle Ricerche of Bologna for the warm hospitality, and in particular its Director, Professor Guido Di Cocco, who allowed me to use the facilities where the data analysis has been performed. My gratitude to all the people working there for their friendship. In particular I would like to acknowledge Dr. Daniele Dal Fiume, a true friend for me, for the invaluable help in understanding the data analysis (and it was really an hard job!) and for beautiful discussions, not only on Physics.

Last but not least I would like to express my gratitude to all the people of the Astrophysics group in SISSA. The list should be too long but I will never forget them and their friendship.

The secretaries were very polite to me; in particular I would like to thank Alex, who tried (and failed) to improve my English — or rather my idea of English, and Daniela, who I liked so much that I married her.

Finally, a few words for the people to whom this Thesis is dedicated, my parents, who gave me the possibility to develop my studies but, above all, with their serenity and example, gave me the strength to continue and to enjoy life.

Table of Contents

Acknowledgements	I
Table of Contents	III
Abstract	1
Bibliography	2
1 Introduction	5
Bibliography	12
 I Observations	
2 The EXOSAT Observatory	15
2.1 Experiments on board EXOSAT	17
2.1.1 The Medium Energy Experiment	20
2.1.1.1 ME On Board Computer Programs	21
Bibliography	22
3 The X-ray Pulsar 4U 1538-52	23
3.1 Physical Properties	23
3.2 Timing Analysis	27
3.2.1 Analysis of the Coherent Emission	27
3.2.2 Analysis of the Aperiodic Emission	29
3.3 Spectral Analysis	34
3.3.1 The Pulse-Phase Averaged Spectrum	34
3.3.2 Pulse-Phase Spectroscopy	36
3.4 Discussion	38
3.4.1 Coherent Timing Measurements	38
3.4.2 Aperiodic Timing Measurements	40
3.4.3 Energy Spectrum Measurements	40
Bibliography	42
4 The X-ray Pulsar GX 301-2	45
4.1 Physical Properties	45
4.2 Timing Analysis	49
4.2.1 Analysis of the Coherent Emission	49

4.2.2	Analysis of the Aperiodic Emission	57
4.3	Discussion	63
4.3.1	Coherent Timing Measurements	63
4.3.2	Aperiodic Timing Measurements	69
	Bibliography	72

II Theory

5	Theory of Wind Accretion	75
5.1	Bondi-Hoyle Accretion Theory	75
5.2	Angular Momentum Carried by the Stellar Wind	79
5.2.1	The Case of a Radial Gradient in the Stellar Wind	79
5.2.2	The Case of an Azimuthal Gradient in the Stellar Wind	82
5.3	Plasma Penetration into the Magnetosphere	84
5.3.1	The Region "beyond" the Magnetospheric Radius	84
5.3.2	The Region "onto" the Magnetospheric Radius	85
5.3.3	The Region "inside" the Magnetospheric Radius	89
5.3.4	Numerical Simulations	94
	Bibliography	97
6	Noisy Wind Accretion Model	101
6.1	Statistical Description	102
6.1.1	Power Spectrum of a Shot Noise Process	102
6.1.1.1	Exponential Shot Noise	104
6.1.1.2	Oscillating Exponential Shot Noise	104
6.2	Physical Scenario	108
6.3	Comparison with Observations	111
	Bibliography	113
7	Summary and Conclusions	115
	Bibliography	117

III Appendices

A	Time averaged background Subtracted Pulse Profiles as a Function of Energy of the ME EXOSAT Observations of GX 301-2	119
B	Normalization of Power Spectrum Density Function	131
	Bibliography	134
	List of Tables	135
	List of Figures	137
	Subject Index	141

Abstract

This Thesis deals with a particular class of X-ray binary pulsars, namely the class of pulsars in which accretion takes place directly from the intense stellar wind coming from the optical companion, usually an early type star. Among the wind-fed X-ray binary pulsars observed by the Medium Energy experiment on board the X-ray satellite EXOSAT, we have chosen the pulsars 4U 1538-52 and GX 301-2. We analysed the four EXOSAT observations of 4U 1538-52 and ten GX 301-2 observations, deriving correlations among the observed quantities. We further elaborated a phenomenological model of inhomogeneous wind accretion, developing our theory in two closely related directions: from a statistical point of view our model describes the observed properties of the GX 301-2 power frequency spectra; from the physical point of view we derive the physical properties of the discrete blobs falling onto the neutron star surface, properties which are in agreement with the observations, and we explain the observed correlations between the root mean square variability (rms) associated to the power spectrum and the pulse period derivative, and between the rms and the X-ray luminosity.

The X-ray binary pulsar 4U 1538-52 was observed on four occasions during 1984 March and August. The observed pulsation periods of 529.97 ± 0.16 sec (March 17) and 530.14 ± 0.03 sec (August 10) indicate that the neutron star in the 4U 1538-52 continued to spin down with $\dot{P}_p = +3.9 \cdot 10^{-9}$ sec/sec ($\dot{P}_p/P_p = +2.3 \cdot 10^{-4}$ yr $^{-1}$) in the period 1976-1988. From the observed orbital parameter of the system 4U 1538-52/QV Nor, we were not able to discriminate whether this pulsar is a wind-fed or a disk-fed system, but we assumed the wind accretion hypothesis from the pulse period behaviour, which is in agreement with that expected from the class of wind-fed binaries. In the first observation an absorbing episode has been observed, which may be attributed to an inhomogeneity in the stellar wind of QV Nor; the scale height of this blob is $2 \cdot 10^9 - 2 \cdot 10^{10}$ cm, assuming a blob velocity of 100-1000 Km/sec, of the same kind of inhomogeneities observed in the Vela X-1 system (Nagase *et al.*, 1986). The eclipse transition time of ~ 0.06 days gives a scale height of $\sim 1.5 \cdot 10^{11}$ cm for the atmosphere of the optical counterpart. The frequency spectra for the two observations out of eclipse are well fitted by a power law plus a constant, with slope $\alpha = 1.63 \pm 0.09$ and $\alpha = 1.73 \pm 0.07$ for the March 17 and August 10 observations, respectively. The rms's are in agreement with those observed in other high mass X-ray pulsars (Belloni and Hasinger, 1990): $(26 \pm 5)\%$ for the March observation and $(36 \pm 6)\%$ for the August observation. The phase-average X-ray energy spectrum, consistent with a power-law of photon spectral index ~ 1.5 (March 17) and ~ 1.4 (August 10), shows an Iron line with an E.W. of ~ 100 eV. We performed a fit to the observed pulse profiles in order to extract some information on the emission geometry of the neutron star in 4U 1538-52. We utilized the angular and energy dependence of the X-ray emission given by Meszaros and Nagel (1985) and its analytical fit given by Leahy (1990). We found that the EXOSAT observations are in agreement with the hypothesis that the X-ray emission is emitted mainly in a direction parallel to the magnetic field lines ("pencil" beam emission pattern).

The timing analysis performed on ten ME EXOSAT observations of the wind-fed X-ray binary pulsar GX 301-2 showed that in the 1984 observations the source continued to spin-down while in the 1985 observations GX 301-2 was spinning up, with average pulse period derivatives $\dot{P}_p = +2.2 \cdot 10^{-8}$ sec/sec and $\dot{P}_p = -8.4 \cdot 10^{-8}$ sec/sec, respectively. We found that the pulse period history of GX 301-2 alternates periods of general spin-up to periods of spin-down trend, in a sort of “saw-tooth” behaviour. This same type of recurrence has been observed in another transient X-ray binary pulsar, A0535+25 (Ziolkowski, 1985). The observed “saw-tooth” time scale is of the order of 100-1000 years. The pulse profiles show two peaks of different heights, π separated in phase. The secondary maximum height seems to be correlated with the X-ray intensity, in the sense that lower the X-ray intensity, higher the secondary peak. We interpret this behaviour in terms of change of beaming pattern. As for 4U 1538-52, we repeated the Leahy’s analysis (Leahy, 1990) on the EXOSAT pulse profiles of GX 301-2. We found that the most probable beaming pattern for this source is a pencil beam emission. The power spectra of all the GX 301-2 observations show a change of slope in the frequency range $0.01 < f_o < 0.1$ Hz (it is quite interesting that a “knee” in the same frequency range has been observed in the power spectra of the black hole candidate Cyg X-1 (Nolan *et al.*, 1981)). The rms’s measured in the power spectra, of the order of 20-30%, correlate with the X-ray intensity and the pulse period derivative, showing a different behaviour according to the spinning state of the source.

From a statistical point of view, we were able to describe the presence of an inflexion point in the GX 301-2 power spectra in terms of a shot noise process with a special response function, dependent on two free parameters. We derived a relation between these two parameters in order to obtain the inflexion point in the observed frequency range. Then we linked the statistical description with a physical scenario of inhomogeneous wind accretion onto the neutron star, in which we have assumed that the inhomogeneities are produced by the magnetohydrodynamical instabilities that occur at the magnetospheric limit. It is important to stress that, in our model, the discretization in the accreting mass flux occurs at the level of plasma penetration and not at the level of the incoming stellar wind. By assuming the theory of plasma penetration derived in a series of papers by Arons and Lea (Arons and Lea, 1976b; Arons and Lea, 1976a; Arons and Lea, 1980; Burnard *et al.*, 1983), we derived the physical properties of these instability blobs and verified that they are in agreement with the observations. In the frame of this accretion scenario we explain the observed correlation between pulse period derivative and rms’s. Furthermore we found that the physical properties of the instability blobs at the neutron star surface are the same of those derived in the frame of disk accretion (Morfill *et al.*, 1984). We looked for a correlation between pulse period derivative and rms in the disk-fed X-ray transient binary pulsar EXO 2030+375 (Parmar *et al.*, 1989; Angelini *et al.*, 1989): a correlation seems to be present but with a worse significance than that found in the case of GX 301-2. Finally we gave a physical meaning to the two free parameters of the response function: we relate a time scale to the duration of a shot, while the other to the inverse Compton cooling time scale of the blobs.

Bibliography

- Angelini L., Stella L., and Parmar A.N. 1989. The discovery of 0.2 Hz quasi-periodic oscillation in the X-ray flux of the transient 42 second pulsar EXO 2030+375. *Astrophysical Journal*, **346**, p.911.
- Arons J. and Lea S.M. 1976a. Accretion onto magnetized neutron stars: Normal mode analysis of the interchange instability at the magnetopause. *Astrophysical Journal*, **210**, p.792.
- Arons J. and Lea S.M. 1976b. Accretion onto magnetized neutron stars: Structure and interchange instability of a model magnetosphere. *Astrophysical Journal*, **207**, p.914.
- Arons J. and Lea S.M. 1980. Accretion onto magnetized neutron stars: The fate of sinking filaments. *Astrophysical Journal*, **235**, p.1016.

- Belloni T. and Hasinger G. 1990. An atlas of aperiodic variability in HMXB. *Astronomy & Astrophysics*, **230**, p.103.
- Burnard D.J., Lea S.M., and Arons J. 1983. Accretion onto magnetized neutron stars: X-ray pulsars with intermediate rotation rates. *Astrophysical Journal*, **266**, p.175.
- Leahy D.A. 1990. X-ray pulsar profile analysis. *Monthly Notices of R.a.S.*, **242**, p.188.
- Meszáros P. and Nagel W. 1985. X-ray pulsar models. II. Comptonized spectra and pulse shapes. *Astrophysical Journal*, **299**, p.138.
- Morfill G.E., Trümper J., Bodenheimer P., and Tenorio-Tangle G. 1984. Nonstationary accretion onto neutron stars: some constraints and consequences. *Astronomy & Astrophysics*, **139**, p.7.
- Nagase F., Hayakawa S., Sato N., Masai K., and Inoue H. 1986. Circumstellar matter in the Vela X-1/HD 77581 system. *Publ. Astron. Soc. Japan*, **38**, p.547.
- Nolan P.L., Gruber D.E., Matteson J.L., Peterson L.E., Rothschild R.E., Doty J.P., Levine A.M., Lewin W.H.G., and Primini F.A. 1981. Rapid variability of 10–140 keV X-rays from Cygnus X-1. *Astrophysical Journal*, **246**, p.494.
- Parmar A.N., White N.E., Stella L., Izzo C., and Ferri P. 1989. The transient 42 second X-ray pulsar EXO 2030+375. I. The discovery of the pulse period variations. *Astrophysical Journal*, **338**, p.359.
- Ziolkowski J. 1985. Spin-up and spin-down of X-ray pulsars: Observations vs theory. In *Multifrequency Behaviour of Galactic Accreting Sources*, Giovannelli F., editor, page 138. CNR Frascati.

...Est enim astronomi proprium, historiam motuum caelestium diligenti et artificiosa observatione colligere. Deinde causas eorundem, seu hypotheses, cum veras assequi nulla ratione possit, qualescunque excogitare et confingere, quibus suppositis iidem motus ex geometriae principiis, tam in futurum, quam in praeteritum recte possint calculari... Neque enim necesse est, eas hypotheses esse veras, imo ne verisimiles quidem, sed sufficit hoc unum, si calculum observationibus congruentem exhibeant ...

Andrea Osiander
 Preface to the first edition of
 Mikolaj Kopernik's *De Revolutionibus*
Orbium Caelestium (1543)

1 Introduction

The discovery of X-ray emission from celestial objects further extended the knowledge of our Universe, which resulted very different from the quiet and calm Universe the astronomers of the last century described. Indeed, it was just at the beginning of the 1960's that, by the advent of stratospheric balloons and rockets, it was possible to launch outside our atmosphere some Geiger counters (Giacconi *et al.*, 1962). In this way the first discrete X-ray source in our Galaxy was discovered: Sco X-1. In 1966 the first optical counterpart of a galactic X-ray source, Sco X-1, was identified with an old 12th–13th magnitude star (Sandage *et al.*, 1966). In the following years a theoretical model was developed according to which galactic X-ray sources are close, interacting binary systems composed by a “normal” star and a compact object (Shklovskii, 1967). In those same years it was understood that spherical accretion could become non symmetric, leading to the formation of an accretion disk around the compact object, if the infalling matter has enough angular momentum (Prendergast and Burbidge, 1968). But the decisive step towards the comprehension of this class of objects was performed with the discovery of pulsed emission from some X-ray sources (Tananbaum *et al.*, 1972). Indeed the variability on short time scale — for example the X-ray binary pulsar Her X-1 pulses at 1.24 — implies a little emitting region. Furthermore, because the system is not destroyed by the centrifugal force it is necessary that at the surface of the emitting object the gravitational force is greater than the centrifugal one. This implies that

$$\Omega_p \lesssim \sqrt{G \langle \rho \rangle} \quad (1.1)$$

where Ω_p is the pulse frequency of the emitting object, G is the gravitational constant and $\langle \rho \rangle$ is its mean density. The observed values of Ω_p imply that $\langle \rho \rangle \gtrsim 10^6 \text{ g/cm}^3$ and therefore the compact nature of the object responsible of the pulsed X-ray emission was established. The compact object should be a white dwarf, a neutron star or a black hole but the object which is able to explain all the observed characteristics of X-ray pulsars, as pulse period range and surface magnetic field strength, is a neutron star (Shapiro and Teukolsky, 1983).

The standard model explains the X-ray emission as due to the conversion of the kinetic energy of the infalling matter (coming from the intense stellar wind of an early optical star, in this case we speak about wind-fed binaries, or from an accretion disk due to Roche-lobe overflow, and this is the case of disk-fed binaries) into radiation, because of the interactions with the strong magnetic field of the neutron star. The dipolar magnetic field of the compact object drives the accreted matter onto the magnetic polar caps and if the magnetic field axis is not aligned with the spin axis, the compact object acts as a “lighthouse”, giving rise to a pulsed emission when the beam (or the beams, according to the geometry) crosses our line of sight.

Subsequent observations clearly demonstrated the binary nature of these objects, by observation of X-ray eclipses and Doppler delays in pulse arrival times (Schreier *et al.*, 1972). From these measurements it was possible to “solve” the binary systems, obtaining values of the masses in agreement with that expected for a neutron star.

Let us now enter into more details in the physics of X-ray pulsars. The main problem connected with this class of objects is that we cannot use a linearized theory but we are obliged to use the full magnetohydrodynamical theory. This is due to the fact that the coupling constants of the interactions (in this case the gravitational and the magnetic interactions) are so large that a series expansion is impossible¹. Furthermore, the highly non linear nature of the problem makes its treatment very difficult. In Fig. 1.1 a sort of block diagram of the physical processes of production and emission of the X-ray flux in an X-ray binary pulsar is shown. In the first block the problem of the angular momentum carried by the accreted matter is understood, and it will be discussed in Chapter 5. This topic is very important for what concerns the temporal behaviour of the pulse period.

At a distance of the order of 10^8 cm from the neutron star surface, the magnetic field of the neutron star becomes the main interaction which drives the motion of the captured matter toward the stellar surface. At this distance (called magnetospheric radius r_m) matter is stopped by the very strong magnetic field of the neutron star and accretion can occur only if matter can penetrate the shock layer by means of magnetohydrodynamical instabilities (Elsner and Lamb, 1977). According to fastness of rotation, different types of instability will determine plasma penetration (Arons and Lea, 1980): in the case of slow rotators² plasma penetration will occur mainly by means of gravity-driven interchange (Rayleigh–Taylor) instability. Decreasing the pulse period, the shear between the plasma and the magnetosphere becomes more and more important, leading to the stabilization of the magnetopause with respect to Rayleigh–Taylor instability, and giving rise to the onset of Kelvin–Helmholtz instability.

The two X-ray pulsars we have analysed are both slow rotators, therefore we expect plasma penetration to be dominated by Rayleigh–Taylor instability (see Chapter 5 for a complete discussion on this topic).

Once matter has penetrated the magnetosphere, it will follow the magnetic field lines up to the magnetic polar caps of the neutron star, where it will be decelerated. If the amount of matter falling onto the polar caps is high enough that an X-ray luminosity greater than about 10^{37} erg/sec is reached, then a radiative shock will form (Basko and Sunyaev, 1976). In this case an accretion column just above the polar cap will form; this accretion column will be optically thick to X-rays,

¹ At the surface of a “standard” neutron star, *i.e.* a neutron star of mass $1.4 M_\odot$ and radius 10 Km, the gravitational field has a strength of the order of $10^{11} g$, while the magnetic field strength is of the order of 10^{11} – 10^{13} G.

² A slow rotator have pulse frequency so small that rotation can be neglected in all the equations describing the physics of accretion. A quantitative parameter which measures the importance of rotation is the “fastness parameter”, defined as (Elsner and Lamb, 1977)

$$\omega_s \equiv \frac{\Omega_p}{\Omega_K(r_m)} \quad (1.2)$$

where $\Omega_K(r) = \sqrt{GM_x/r^3}$ is the angular velocity of matter orbiting into Keplerian orbits and r_m is the magnetospheric radius (see Chapter 5). If $\omega_s \ll 1$ then rotation can be neglected.

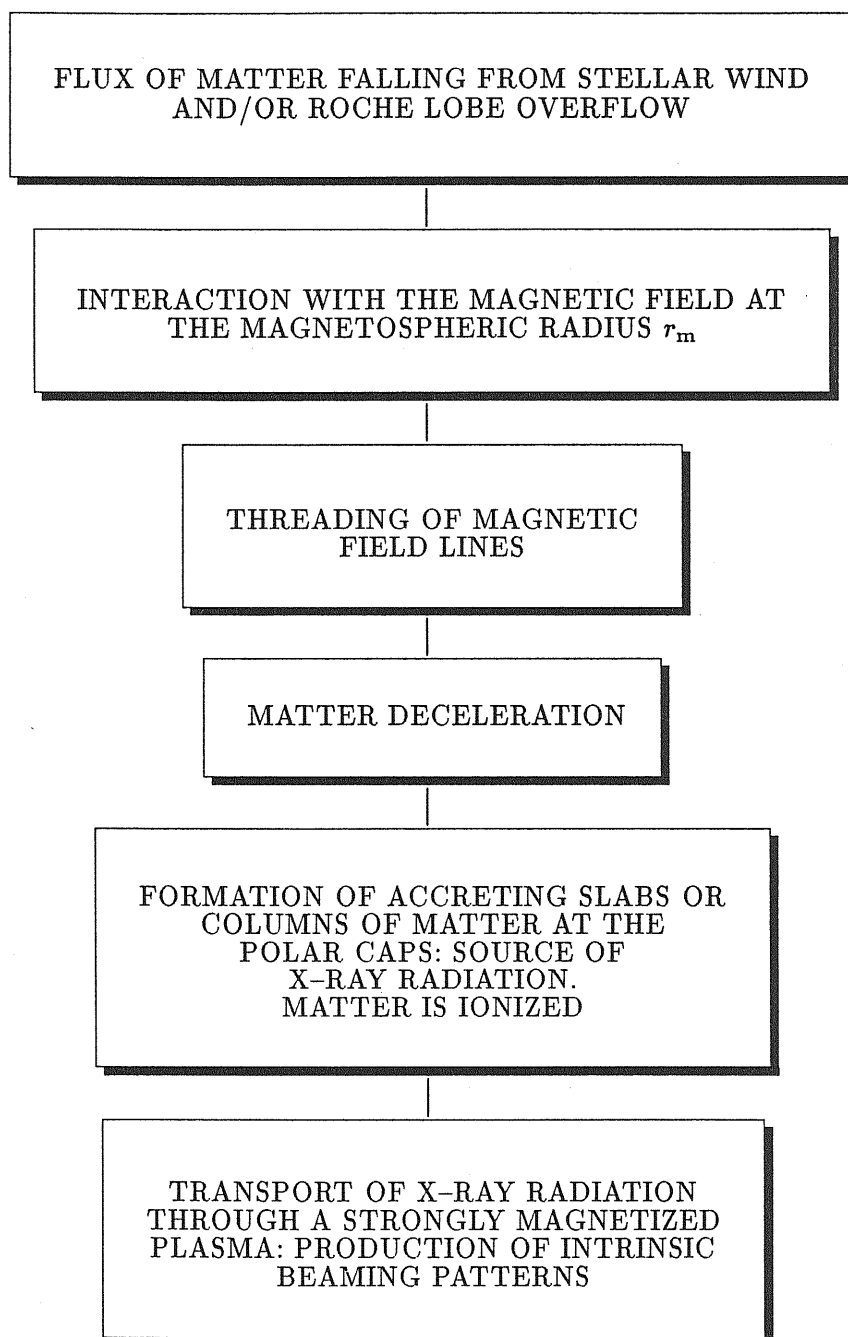


Figure 1.1: Block diagram of the physical processes of production and emission of the X-ray flux in an X-ray binary pulsar.

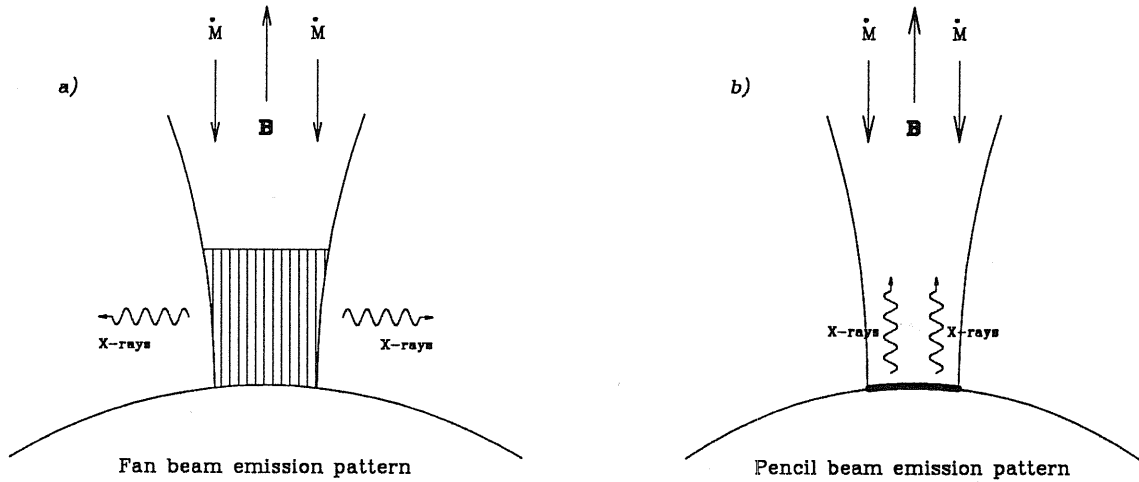


Figure 1.2: The two extreme cases of longitudinal geometries of the emission region above the polar cap of a neutron star. Case *a*) corresponds to the fan beam emission pattern, in which radiation is emitted mainly in a direction perpendicular to the direction of the magnetic field lines. The accretion column is due to the formation of a radiative shock, because of radiation pressure. Case *b*) corresponds to the pencil beam emission pattern, in which an accretion column does not form and therefore radiation can escape mainly in a direction parallel to the magnetic field lines.

therefore radiation will be emitted mainly *sidewise* (see Fig. 1.2, case *a*)). Radiation is emitted mainly in direction perpendicular to the magnetic field lines and we call this pattern “fan beam emission pattern”.

On the other hand, if the X-ray luminosity is lower than about 10^{37} erg/sec, then the radiative shock will not form and matter will be able to reach the neutron star surface. In this case we will have the formation of an emitting “slab” and radiation will be emitted mainly in a direction parallel to the magnetic field lines. We call this pattern “pencil beam emission pattern” (see Fig. 1.2, case *b*)).

Before leaving the neutron star, radiation interacts with the surrounding medium and the very strong magnetic field. As briefly discussed above, this interaction is very difficult to treat because of the impossibility to linearize the theory and because of our substantial ignorance on very strong magnetic fields (surface magnetic field strengths are of the order of 10^{11} – 10^{13} G). One of the most important consequences due to the presence of a very strong magnetic field is the quantization of the electron motion in the direction transverse to B : this leads to the so-called Landau levels. Due to the existence of these levels, an electromagnetic wave which propagates in such a plasma will have well defined polarization normal modes, *i.e.* the medium will be birifringent (Ginzburg, 1970). Furthermore, for magnetic field not far from the critical value of $1.414 \cdot 10^{13}$ G, an important rôle is played by virtual electron-positron pairs (Meszaros and Ventura, 1978; Meszaros and Ventura, 1979). These virtual photons dominate the polarization properties of the medium and therefore the radiative opacity of the plasma (Ventura, 1979). This corresponds to say that the scattering cross sections of X-rays are strongly anisotropic and energy dependent (Herold, 1979).

Further complications arose from the presence of lines in the energy spectra. The line at 6.4 keV is present in the spectra of almost all the X-ray binary pulsars (White *et al.*, 1983; Nagase, 1989). This line is due to K_{α} Iron fluorescence induced by the X-rays emitted by the pulsar (Koyama, 1985). Another interesting feature, due to cyclotron resonances in the electron scattering cross

section, has been observed in the hard X-ray spectra of three X-ray pulsars: Her X-1³ (Trümper *et al.*, 1978), 4U 0115+63 (Wheaton *et al.*, 1979) and 4U 1538-52 (Clark *et al.*, 1990). The importance of these features resides in the possibility of obtaining a measure of the surface magnetic field strength B from the measure of the cyclotron line energy E_{cy}

$$E_{cy} \approx 12 \left(\frac{B}{10^{12} \text{ G}} \right) \text{ keV.} \quad (1.3)$$

From this expression, the mean value of the surface magnetic field strength of the three X-ray pulsars mentioned above is $B \approx (1-5) \cdot 10^{12} \text{ G}$.

Numerous calculations have been performed to compute energy and angular dependence of the scattering cross section of X-rays (Nagel, 1981a; Nagel, 1981b; Meszaros and Nagel, 1985). The goal of these models is to derive information on the physical conditions in the magnetosphere of a neutron star by comparing theoretical and observed spectra. The formidable difficulty that actual theories have is that spectra are not parametrised, *i.e.* theoretical spectra are obtained solving numerically the magnetohydrodynamical equations assigning particular values to the free parameters. To date, a parametric theory of X-ray pulsar spectra does not exist.

Let us now introduce the main topic of this Thesis, *i.e.* the timing analysis of wind-fed X-ray binary pulsars light curves. What we are able to observe from an X-ray source is a series of counts with respect to time. The information contained in each bin is the time at which this event was observed, the intensity (in units of Counts/sec) of the source⁴ and, when possible, the energy of that particular photon. A visual inspection of a light curve of an X-ray pulsar clearly shows the presence of two distinct components in the X-ray flux:

- The *coherent* component of the X-ray flux, *i.e.* the pulsation due to the rotation of the neutron star;
- The *aperiodic* component of the X-ray flux, *i.e.* the “noise” present in the light curve which makes each pulse different from an other.

The information we can obtain from the study of these two components is different. From the study of the coherent variation of X-ray emission we obtain information on how angular momentum is transferred from the wind coming from the optical star to the compact object and on how the neutron star responds to the stresses due to the accreting matter (variations of the pulse period with respect to time).

The study of variations of pulse shapes with respect to energy of observation and intensity of the source gives information on the pattern of emission from the polar caps just above the neutron star magnetic poles, and therefore on the physical mechanisms which occur in these regions. In principle, it should be possible to extract information on the beaming pattern of emission (*i.e.* to discriminate between pencil or fan beam emission) from the analysis of the variation of the pulse shape with respect to energy (this analysis has been performed for the X-ray binary pulsars Vela X-1 (Kanno, 1980) and 4U 1626-67 (Kii *et al.*, 1986)). Furthermore it is possible to correlate the energy dependence of pulse shape with the surface magnetic field strength of the neutron star. With this in mind, Raubenheimer (1990) extracted a magnetic field strength of $(2-5) \cdot 10^{12} \text{ G}$ from EXOSAT observations of Vela X-1.

³Recently the controversy about the absorption or emission nature of the line present in the Her X-1 spectrum seems to have been solved in favour of the absorption hypothesis (Mihara *et al.*, 1990). This leads to a surface magnetic field strength of $(2.9 \pm 0.3) \cdot 10^{12} \text{ G}$.

⁴The problem of conversion of the X-ray intensity from a unit intrinsic to the detector to a standard unit is not simple, because of the non linear response of the detectors. The standard procedure consists in convolving the data with the matrix response of the detector, obtained experimentally, in such a way to obtain the true result. We will assume to know the instrumental effects on the observed counts (see Chapter 2).

The study of the aperiodic variation of X-ray emission by means of their frequency spectra should allow the reconstruction of the statistical processes which determine the non coherent variation and therefore should allow to extract some hints on the physical processes which determine these variations. It is important to stress that the analysis of power spectra allows the reconstruction of *statistical* processes. The last goal of this analysis is to derive the *physical* processes which originate this variation.

From a visual inspection, a general power spectrum of an X-ray pulsar is considered as the sum of three terms:

$$P(f) = \overbrace{C}^{\text{Poissonian}} + \overbrace{k f^{-\alpha}}^{\text{aperiodic}} + \overbrace{\sum_i A_i \delta(f - f_i)}^{\text{coherent}} \quad (1.4)$$

where k and C (Poissonian noise due to the counting) are two constants, f is the frequency and f_i are the frequencies relative to the fundamental and harmonics of pulsation, of amplitudes A_i . The fundamental assumption which is hidden in Eq. 1.4 is the *independence* of the two processes which give rise to the coherent and aperiodic emission. As we discussed above, the photons we observe from X-ray pulsars have suffered two different processes. First, they have been created by the conversion of the kinetic energy of the infalling matter into X-ray photons (the fourth “block” in Fig. 1.1); then these photons interact with the surrounding medium and the strong magnetic field of the neutron star in a quite complicated way, emerging and reaching the observer (the last block in Fig. 1.1). The pulsation mechanism acts in the sense that the emission beams probe different areas of the matter surrounding the neutron star.

Let us now consider two extreme cases: If the “noise” we observe is generated only in the process of accretion of matter (in particular we have in mind the process of plasma penetration) then we expect that the pulsation mechanism should not alter the nature of the “noise”. This corresponds to treat the mechanisms producing pulsation and “noise” as independent and the X-ray flux can be considered as the *sum* of two distinct processes: pulsation and “noise” (see Eq. 1.4). On the other hand, if we consider the “noise” as produced only at the stage of interaction of the radiation with the surrounding medium, then the pulsation and the “noise” are two processes strictly dependent because of the anisotropy of the electron scattering cross section (see above). In this case the X-ray flux can be considered as a non linear operation (for example the product) of the two distinct processes of pulsation and “noise”.

Of course, our lack of knowledge of the true nature of the “noise” associated to the X-ray flux coming from X-ray sources does not allow a discrimination between the two cases; probably the right answer is somewhere in between, *i.e.* we will have a noise generated in the process of accretion and a noise generated in the process of interaction with the medium, which interact non linearly to produce the observed spectra.

Furthermore, from a statistical point of view the Wold theorem states that every stationary (ergodic) process can be decomposed into the sum of a deterministic periodic process and a “noise” (Scargle, 1981), in other words Eq. 1.4 can be applied to every stationary process.

In order to describe the observed power spectra we have treated the problem in two closely related ways: from a statistical point of view and from a physical point of view. Let us first describe the physical scenario which we introduced in order to explain the features observed in the power spectra of GX 301-2.

First of all, we have that the neutron star in GX 301-2 is accreting matter from the intense stellar wind coming from its supergiant companion Wray 977. At the plasmopause (see Chapter 5 for its definition) matter is stopped by the strong neutron star magnetic field and accretion occurs because Rayleigh-Taylor instability sets on. Plasma begins to penetrate the magnetosphere in form of blobs of ionized plasma. At some distance from the neutron star surface plasma is channeled by the magnetic field lines onto the polar caps, where its kinetic energy is transformed in X-ray radiation in the process of deceleration. Therefore the accretion of matter will be “noisy”, in the sense that

matter will not be accreted continuously but in form of discrete blobs. From a statistical point of view we treat this “noise” as a shot noise process (Papoulis, 1965) with a special response function, the parameters of which are related to parameters of the magnetohydrodynamical instability, as the rate of formation of the blobs and their dimensions. Furthermore, this function is able to explain some observed properties of the GX 301–2 power spectra, as the change of slope present in *all* the GX 301–2 observations at the *same* frequency.

In this model, the “noise” is produced at the stage of matter accretion, therefore the assumption of independence of the processes of pulsation and “noise” is valid and Eq. 1.4 holds. Furthermore, we expect that a noise generated in this region should have to show its effects mainly in the pulse period history because a variation in the quantity of accreted matter is transmitted as a variation in the pulse period, according to the relation, valid in the case that matter does not leave the system,

$$I \dot{\Omega}_p = \ell \dot{M}_x \quad (1.5)$$

where I is the moment of inertia of the neutron star, ℓ is the specific angular momentum carried by the accreted matter and \dot{M}_x is the accretion rate of matter onto the neutron star. From Eq. 1.5 we expect a *linear* relation between the variation of the pulse period and the noise observed in the power spectra. Indeed we do observe this correlation between \dot{P}_p/P_p and a quantity which measures the noise (in particular, the rms of the power spectra, defined in Appendix B). This correlation is present for the X-ray pulsar GX 301–2, for which we observe a change of the linear correlation slope according to the fact that the source is spinning-up or spinning-down. We checked for a similar correlation in another X-ray pulsar, EXO 2030+375, and found a similar behaviour, although with less significance. It is quite interesting the fact that EXO 2030+375 is a disk-fed pulsar while GX 301–2 is a wind-fed pulsar. We attribute this similarity to the fact that the instability parameters at the neutron star surface, derived in our model, are the same of those derived in the frame of inhomogeneous disk accretion by Morfill *et al.* (1984).

Finally, a few words for the two X-ray pulsars we choose. EXOSAT observed the X-ray binary pulsar 4U 1538–52 only four times (and in two of them it was in eclipse). As we will discuss in Chapter 3, we are not sure whether this source is accreting from a wind or from a disk (probably both). Anyway, we are inclined to consider this source a wind-fed pulsar from the temporal behaviour of its pulse period, which clearly resembles that of a typical wind-fed pulsar. The main problem connected with this source resides in the secular spin-down trend of its pulse period, behaviour which is not predicted by any theory of wind accretion.

The other X-ray pulsar whose observations we analysed, GX 301–2, is without doubt a wind-fed pulsar. The good quality EXOSAT observations of this source made possible the building of our “noisy” wind accretion theory.

We have divided our Thesis in three parts: Observations, Theory and Appendices. In the first Part, after a very brief description of the EXOSAT observatory in Chapter 2, we present and discuss the results from our timing and spectral (both in the energy and frequency domain) analysis of EXOSAT observations of the two X-ray binary pulsars 4U 1538–52 and GX 301–2. This corresponds to Chapter 3 and Chapter 4. The second Part deals with theory of wind accretion: Chapter 5 treats the “standard” theory of wind accretion, while Chapter 6 presents our theory of “noisy” wind accretion. Conclusions are left in Chapter 7. In the last Part we present the time averaged background subtracted pulse profiles for all the ten EXOSAT observations of GX 301–2 as a function of energy. We made the choice of presenting the pulse shapes in an Appendix for not making heavy the text. Furthermore in the text we present normalized pulse profiles, therefore a sort of atlas of the pulse profiles should be useful. Appendix B deals with our normalization of power spectra, which is different from that adopted, for example, by Leahy *et al.* (1983).

Bibliography

- Arons J. and Lea S.M. 1980. Accretion onto magnetized neutron stars: The fate of sinking filaments. *Astrophysical Journal*, **235**, p.1016.
- Basko M.M. and Sunyaev R.A. 1976. The limiting luminosity of accreting neutron stars with magnetic field. *Monthly Notices of R.a.S.*, **175**, p.395.
- Clark G.W., Woo J.W., Nagase F., Makishima K., and Sakao T. 1990. Discovery of a cyclotron absorption line in the X-ray spectrum of the binary pulsar 4U 1538-52 observed by *Ginga*. *Astrophysical Journal*, **353**, p.274.
- Elsner R.F. and Lamb F.K. 1977. Accretion by magnetic neutron stars. I. Magnetospheric structure and stability. *Astrophysical Journal*, **215**, p.897.
- Giacconi R., Gursky H., Paolini F.R., and Rossi B.B. 1962. Evidence for X-rays from sources outside the solar system. *Physical Review Letters*, **9**, p.439.
- Ginzburg V.L. 1970. *The Propagation of Electromagnetic Waves in Plasmas*. Pergamon Press, Oxford.
- Herold H. 1979. Compton and Thomson scattering in strong magnetic fields. *Physical Review*, **D19**, p.2868.
- Kanno S. 1980. Frequency dependence of pulse profiles of accreting X-ray pulsars. *Publ. Astron. Soc. Japan*, **32**, p.105.
- Kii T., Hayakawa S., Nagase F., Ikegami T., and Kawai N. 1986. Anisotropic X-ray transfer in a strongly magnetized plasma of the X-ray pulsar 4U 1626-67. *Publ. Astron. Soc. Japan*, **38**, p.751.
- Koyama K. 1985. Iron line from compact X-ray sources. In *Japan-USA Seminar on Galactic and Extragalactic Compact X-ray Sources*, Tanaka Y. and Lewin W.H.G., editors, page 153. ISAS, Tokyo.
- Leahy D.A., Darbro W., Elsner R.F., Weisskopf M.C., Sutherland P.G., Kahn S., and Grindlay J.E. 1983. On searches for pulsed emission with application to four globular clusters X-ray sources: NGC 1851, 6441, 6624 and 6712. *Astrophysical Journal*, **266**, p.160.
- Meszaros P. and Nagel W. 1985. X-ray pulsar models. II. Comptonized spectra and pulse shapes. *Astrophysical Journal*, **299**, p.138.
- Meszaros P. and Ventura J. 1978. Vacuum polarization effects on Thomson cross sections in a magnetized plasma. *Physical Review Letters*, **41**, p.1544.
- Meszaros P. and Ventura J. 1979. Vacuum polarization effects on radiative opacities in a strong magnetic field. *Physical Review*, **D19**, p.3565.
- Mihara T., Makishima K., Ohashi T., Sakao T., Tashiro M., Nagase F., Tanaka Y., Kitamoto S., Miyamoto S., Deeter J.E., and Boynton P.E. 1990. New observations of the cyclotron absorption feature in Hercules X-1. *Nature*, **346**, p.250.
- Morfill G.E., Trümper J., Bodenheimer P., and Tenorio-Tangle G. 1984. Nonstationary accretion onto neutron stars: some constraints and consequences. *Astronomy & Astrophysics*, **139**, p.7.
- Nagase F. 1989. Accretion-powered X-ray pulsars. *Publ. Astron. Soc. Japan*, **41**, p.1.
- Nagel W. 1981a. Radiative transfer in a strongly magnetized plasma. I. Effects of anisotropy. *Astrophysical Journal*, **251**, p.278.
- Nagel W. 1981b. Radiative transfer in a strongly magnetized plasma. II. Effects of Comptonization. *Astrophysical Journal*, **251**, p.288.
- Papoulis A. 1965. *Probability, Random Variables, and Stochastic Processes*. McGraw-Hill, New York.
- Prendergast K.H. and Burbidge G.R. 1968. On the nature of some galactic X-ray sources. *Astrophysical Journal*, **151**, p.L83.
- Raubenheimer B.C. 1990. The pulsed light curve of Vela X-1. *Astronomy & Astrophysics*, **234**, p.195.

- Sandage A., Osmer P., Giacconi R., Gorenstein P., Gursky H., Waters J., Bradt H., Garmire G., Sreekantan B.V., Oda M., Osawa K., and Jugaku J. 1966. On the optical identification of Sco X-1. *Astrophysical Journal*, **146**, p.316.
- Scargle J.D. 1981. Studies in astronomical time series analysis. I. *Astrophysical Journal Suppl. Series*, **45**, p.1.
- Schreier E., Levinson R., Gursky H., Kellogg E., Tananbaum H., and Giacconi R. 1972. Evidence for the binary nature of Centaurus X-3 from Uhuru X-ray observations. *Astrophysical Journal*, **172**, p.L79.
- Shapiro S.L. and Teukolsky S.A. 1983. *Black Holes, White Dwarfs and Neutron Stars. The Physics of Compact Objects*. John Wiley & Sons, New York.
- Shklovskii I.S. 1967. On the nature of the source of X-ray emission of Sco XR-1. *Astrophysical Journal*, **148**, p.L1.
- Tananbaum H., Gursky H., Kellogg E.M., Levinson R., Schreier E., and Giacconi R. 1972. Discovery of a periodic pulsating binary X-ray source in Hercules from Uhuru. *Astrophysical Journal*, **174**, p.L143.
- Trümper J., Pietsch W., Reppin C., Voges W., Staubert R., and Kendziorra E. 1978. Evidence for strong cyclotron line emission in the hard X-ray spectrum of Hercules X-1. *Astrophysical Journal*, **219**, p.L105.
- Ventura J. 1979. Scattering of light in a strongly magnetized plasma. *Physical Review*, **D19**, p.1684.
- Wheaton W.A., Doty J.P., Primini F.A., Cooke B.A., Dobson C.A., Goldman A., Hecht M., Hoffman J.A., Howe S.K., Scheepmaker A., Tsiang E.Y., Lewin W.H.G., Matteson J.L., Gruber D.E., Baity W.A., Rothschild R., Knight F.K., Nolan P., and Peterson L.E. 1979. An absorption feature in the spectrum of the pulsed hard X-ray flux from 4U 0115+63. *Nature*, **282**, p.240.
- White N.E., Swank J.H., and Holt S.S. 1983. Accretion powered X-ray pulsars. *Astrophysical Journal*, **270**, p.711.

Part I

Observations

2 The EXOSAT Observatory

The European X-ray Observatory Satellite (EXOSAT) was launched on 26 May 1983 from the flight center in Vandenberg (U.S.A.) by means of a Thor-Delta vector. Due to the natural decay of its orbit, the satellite re-entered in the atmosphere on 6 May 1986. The characteristic of its orbit are shown in Table 2.1 (Taylor *et al.*, 1981) while an exploded view of the entire payload is shown in Fig. 2.1 (Taylor *et al.*, 1981).

The main objectives of the mission were:

- Astrometric measurements of the position of known X-ray sources: $10''$ in the energy band 0.04–2 keV by means of imaging telescopes and $3''$ in the energy band 2–50 keV by means of proportional counters with lunar occultation.
- Imaging of extended sources in the energy band 0.04–2 keV by means of imaging telescopes.
- Broad-band spectroscopy in the energy range 0.04–50 keV.
- Study of temporal variability on time scales from milliseconds to days.
- Discovery of new sources in medium or deep surveys.

It was possible to observe the sky in every direction, apart from about 20% of the celestial sphere (occulted by the Moon) and about 1% occulted by the Earth. Anyway, to avoid damages to the two star trackers for the pointing operations, regions closer than 15° to the Sun, the Earth or the Moon were not observed. Observations with $\beta > 130^\circ$ (where β is the angle between the Sun and the source) were not performed to avoid too large temperature variations, while observations with $\beta < 90^\circ$ were avoided for not introducing too strong variations in the instrumental background.

For slewing and pointing operations a propane cold-gas thruster system was used. The trim was controlled by means of two star trackers, three gyroscopes (one for each axis) and a solar sensor. The star trackers had $3^\circ \times 3^\circ$ field of view and a sensitivity down to the eighth magnitude.

The observatory had two main operational modes: pointing and occultation. When in pointing mode it was possible to follow a single target for up to 80 hours continuously, with an accuracy of $1'$. The time necessary to span from a target to another was of the order of 90 minutes, to allow time for instrument and on board computer reconfiguration, attitude slew and stabilization. It was also possible to perform more rapid pointings but at the expense of the propane gas supply.

The occultation strips are shown in Fig. 2.2 (Taylor *et al.*, 1981); about 100 sources were occulted by the Moon, allowing a precise measurements of the positions of about 50 of them. A typical X-ray source was observed for approximately one hour before the entry and one hour after the exit from the occultation, putting a filter into the star tracker field of view to collect the maximum flux from the X-ray source and to maximize the signal to noise ratio. The uncertainties

Apogee	$2 \cdot 10^5$ Km	Perigee	$5 \cdot 10^2$ Km
Inclination	$72^\circ 30'$	Eccentricity	0.93
Argument of perigee	$286^\circ 30'$	Period	99 Hours

Table 2.1: EXOSAT orbital parameters (Taylor *et al.*, 1981).

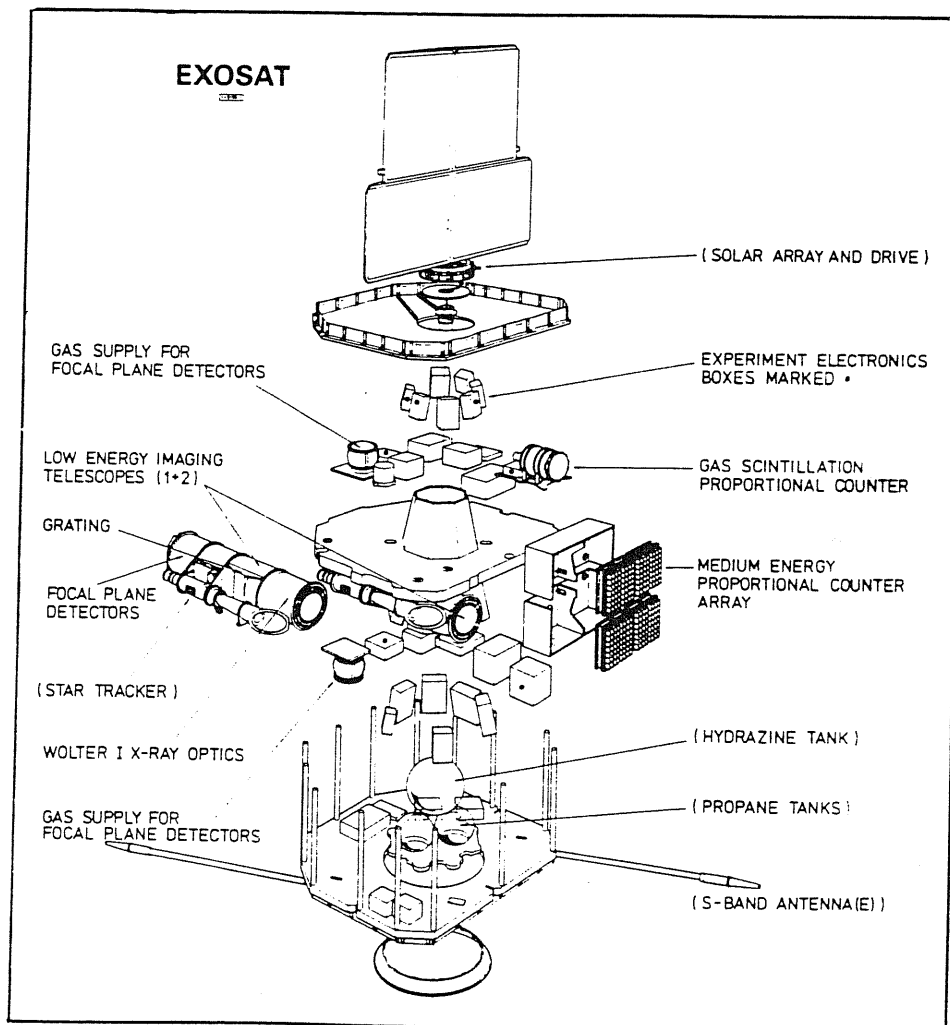


Figure 2.1: Exploded view of the EXOSAT observatory. The three experiments on board EXOSAT are clearly visible: one of the two imaging telescopes (LE), a proportional counter array (ME) and a gas scintillator proportional counter (GSPC). See text for a general description (Taylor *et al.*, 1981).

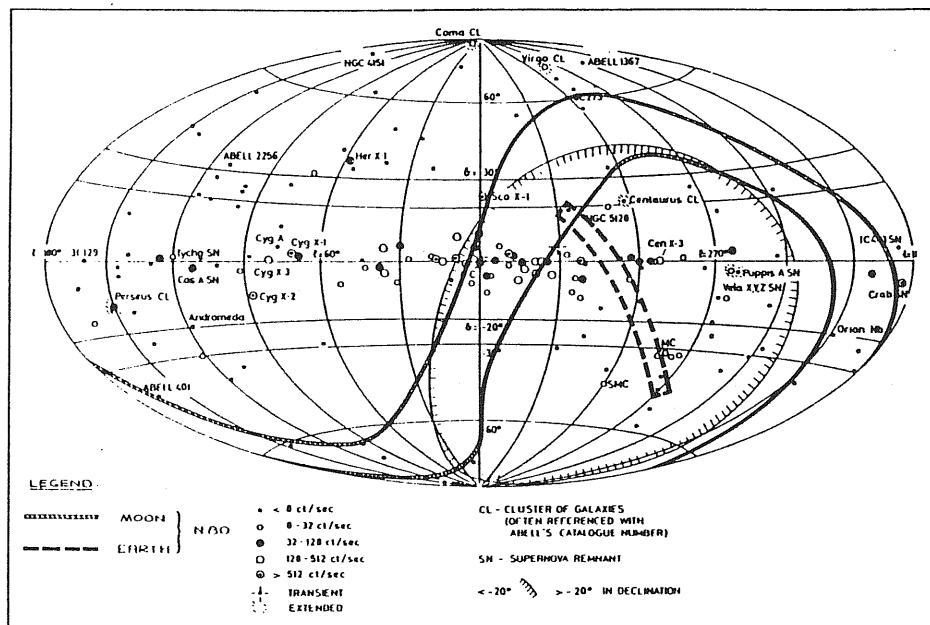


Figure 2.2: Lunar and Earth occultation strips in the EXOSAT orbit (Taylor *et al.*, 1981).

in the position resulted from uncertainties in the spacecraft position, in the lunar limb profile, in the source strength and in the determination of the instant at which the flux disappeared. The best measurements had an accuracy of $3'$ (5σ).

2.1 Experiments on board EXOSAT

On board the observatory there were three different kinds of instruments:

- A large area proportional counter array (Medium Energy experiment) sensitive in the energy range 1–50 keV (Turner *et al.*, 1981), specially designed for occultation observations but which gave very good results also in pointing mode.
- Two imaging telescopes (Low Energy experiment) sensitive in the energy range 0.04–2 keV (Taylor *et al.*, 1981), designed for mapping of extended sources. The main goal of the instrument was to achieve a good energy resolution for allowing multi-color mapping of diffuse sources to a resolution of $1'-2'$ and for determining good spectra.
- A gas scintillator proportional counter (GSPC experiment) sensitive in the energy range 2–40 keV (Peacock *et al.*, 1981). Because of its small effective area and limited background rejection capability it was mainly used for spectroscopy of the stronger X-ray sources, in particular for studies on spectral lines.

The qualified events obtained from the different instruments were sampled by On Board Computer (OBC) programs to reduce the arrival data flux and to allow the transmission to the ground stations. The maximum transmission rate was 7.2 Kbit/sec for every experiment. Of course, this re-processing involved some corrections to both spectroscopic and intensity data (Andrews and Stella, 1985). A typical effect was the presence of dead times in the data transmissions (a sort of “queue”) to allow to all the experiments to send data to the Earth stations. The net effect was the reduction of the counting rates from some instruments, and this effect has to be taken into account when analyzing the data (Andrews and Stella, 1985; Tennant, 1987).

Geometrical area	90 cm ² (52 outer; 37 inner)	
Grazing angles	1.8° outer; 1.5° inner	
Cut-off energy	2 keV	
Angular resolution	5'' FWHM on axis	
Plate scale	5.3 $\mu\text{m}/\text{arcsec}$	
Focal plane detector	PSD	CMA
Energy range	0.1–2 keV	0.04–2 keV
Efficiency 0.05 keV	—	0.28
0.15 keV	0.19	0.24
0.80 keV	0.37	0.12
1.50 keV	0.17	0.05
Energy resolution	$\Delta E/E = 44/\sqrt{E}$	No intrinsic
Field of view	28 mm (\varnothing), 1.5°	42 mm (\varnothing), 2.2°
Angular resolution	45'' at 1.5 keV 180'' at 0.28 keV	10''
Background rate	0.12 cm ⁻² keV ⁻¹ sec ⁻¹	1 cm ⁻² sec ⁻¹

Table 2.2: Technical characteristic of a Low Energy imaging telescope on board the EXOSAT observatory (Taylor *et al.*, 1981). The two detectors were a position sensitive proportional counter (PSD) and a channel multiplier array (CMA), mounted on an exchange mechanism.

Collimator field of view	45' FWHM
Peak collimator transparency	65 %
Nominal energy range	2–40 keV
Available energy range	2–80 keV
Background rejection efficiency (2–10 keV)	97 %
Background rejection efficiency (10–20 keV)	96 %
X-ray acceptance efficiency A_x	80 %
Background after rejection (2–10 keV)	10 Cnt/sec·keV
Background after rejection (10–20 keV)	12 Cnt/sec·keV
Total geometric area for photo-absorption of X-rays (includes the collimator peak transparency and A_x)	160 cm ²
$\Delta E/E$ ($E < 15$ keV at FWHM)	$27/\sqrt{E}$

Table 2.3: Technical characteristics of the Gas Scintillation Proportional Counter on board the EXOSAT observatory (Peacock *et al.*, 1981).

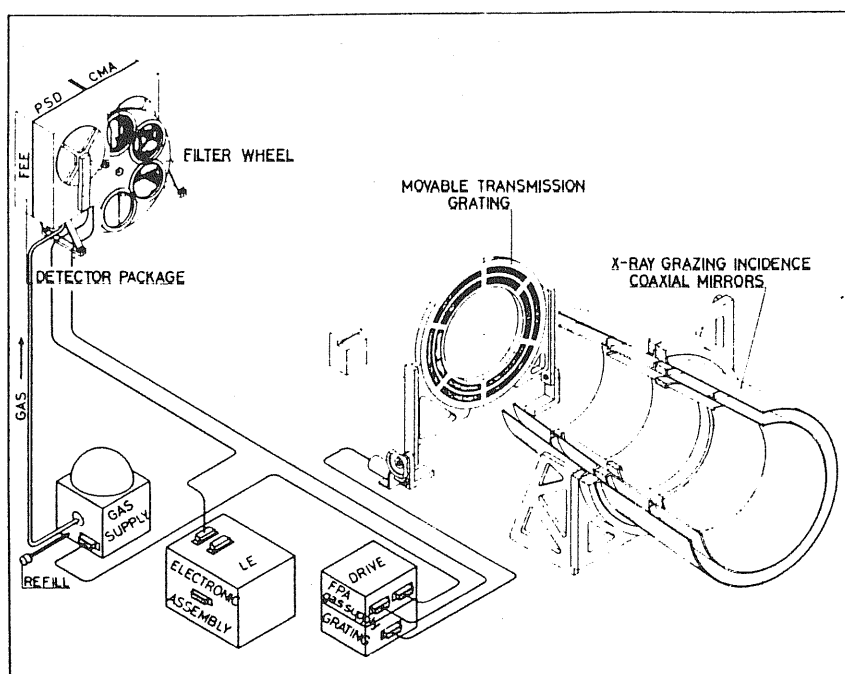


Figure 2.3: A schematic draft of a Low Energy imaging telescope on board the EXOSAT observatory (Taylor *et al.*, 1981).

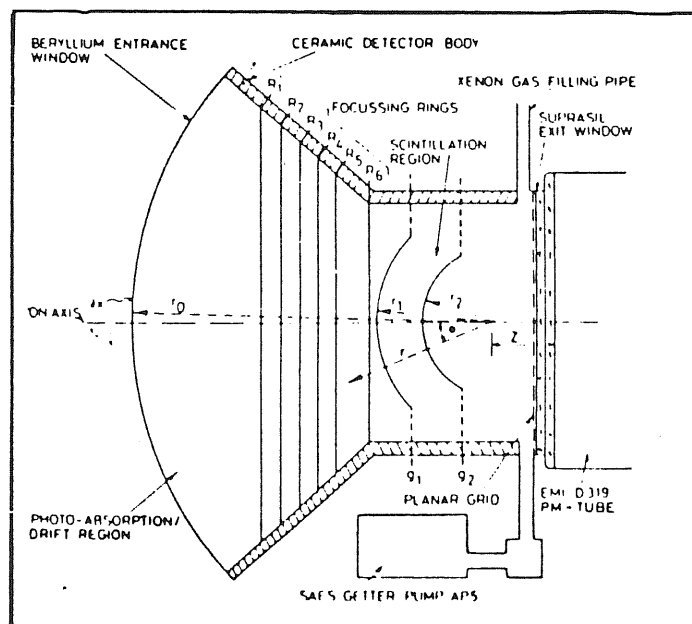


Figure 2.4: A schematic draft of the Gas Scintillator Proportional Counter on board the EXOSAT observatory (Peacock *et al.*, 1981).

Total effective area	1800 cm ² (quadrants co-aligned)
Energy range	1.5–15 keV Argon; 5–50 keV Xenon
Energy resolution (FWHM)	21 % at 6 keV (Argon); 18 % at 22 % (Xenon)
Field of view	45' × 45'
Background rejection	99 % (Argon); 98 % (Xenon)
Background rate	12 Cnt/sec.keV

Table 2.4: Technical characteristics of the Medium Energy experiment on board the EXOSAT observatory (Taylor *et al.*, 1981; Turner *et al.*, 1981).

The technical characteristics of the LE and GSPC experiments are summarised in Table 2.2 (Taylor *et al.*, 1981) and Table 2.3 (Peacock *et al.*, 1981), respectively, while two sketches of the instruments are shown in Fig. 2.3 and Fig. 2.4. We will discuss no more about these two instruments because we did not use observations obtained by them in our data analysis. In the next section a detailed description of the ME experiment, especially for what concerns the characteristics of the OBC programs, will be given.

2.1.1 The Medium Energy Experiment

The large-area proportional counter array, the so called Medium Energy experiment (ME), on board the EXOSAT observatory had an effective area of 1800 cm² (see its technical characteristics in Table 2.4). This area was divided in eight separate detectors, each of them composed by two multi-wire proportional counter chambers. The front chamber was 4 cm deep and filled with an Ar-CO₂ mixture (sensitive to the energy range 1.5–15 keV). Then a 1.5 mm thick beryllium window separated the front chamber from the rear one, filled with a Xe-CO₂ mixture (sensitive to the energy range 5–55 keV). The Argon chamber had a beryllium front window 37 or 62 μm thick, and a 4.5 μm thick, aluminised Kapton foil protected all the instrument, for thermal control purpose (see Fig. 2.5).

The eight detectors were assembled in four “quadrants”; two detectors of each quadrant were bounded together, thus they pointed toward the same direction. Each couple of quadrants, referred as “half experiment”, could be either aligned or offset by the same amount up to 2° from the nominal direction of the source. This feature allowed the simultaneous monitoring of the source and the offset background. During the evolution of the mission it became clear that a systematic error in the determination of the background derived from the fact that the two halves had different count rates, because of the different shielding system of the various detectors. Therefore for the first observations the level to be subtracted was corrected for this effect (Smith, 1984). For the last observations, the problem was solved by applying a sort of “flip-flop” technique to the pointing: the source was observed alternatively by the two halves; then subtracting the background obtained when the same half was offset allowed the exact determination of the background counting of this half. For example, all the 1985 observations of the X-ray pulsar GX 301–2 were obtained by means of this technique (these manoeuvres were called “swaps”).

The data obtained with the ME experiment carry both intensity and energy information. For spectroscopical studies, the ME had a Pulse Height Analyzer (PHA) with 128 channels for each Argon and Xenon cameras. In fact, the large sensitive area of the ME allows the detection of a 1 mCrab¹ source at 5σ significance level in the energy range 1–15 keV in 500 sec with half experiment. The confusion limit is reached at 0.3 mCrab in 5000 sec. For example, a 1 Crab source can be

¹ A Crab unit corresponds to the counting observed by the Crab nebula, in the constellation of Taurus, which has

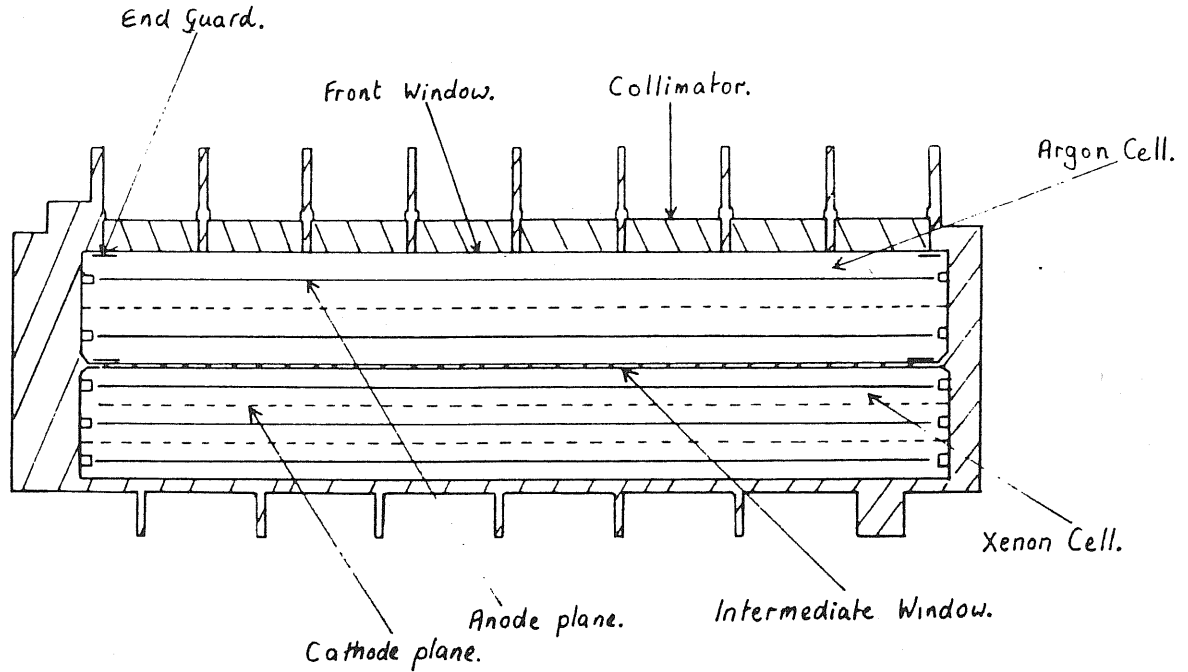


Figure 2.5: A schematic draft of the Medium Energy experiment on board the EXOSAT observatory (Turner *et al.*, 1981).

detected in 1 msec in the 1-15 keV range. In the Argon detectors, the energy range 1-20 keV was covered by the first 68 channels.

2.1.1.1 ME On Board Computer Programs

The OBC programs had the task of sampling in different ways the data obtained by the experiments. Controls on the data formatting were done via software by changing the so called work space parameters (WSP), by means of which it was possible, for example, to select channel compression and/or channel transmission. An effect deriving from the use of the OBC programs was dead time effects (for a discussion on dead time effects see Andrews and Stella (1985); Tennant (1987)).

The main ME OBC programs are:

HER 3 This program produces energy histograms (E3 data type) and intensity samples (I3 data type). The counts are different from Argon and Xenon detectors. It has 4 WSPs.

HER 4 This program, as HER 3, produces both energy histograms (E4 data type) and intensity samples (I4 data type). Again, the counts are different from the two detectors, but in this case we have the options of channel compression and/or channel transmission selection for the half experiment mode. It has 7 WSPs and the collection time for I4 data is fixed to 0.25 sec.

HER 5/1 This program produces energy histograms (E5 data type) from 64 selected Argon channels (4-67, corresponding to 1-20 keV) and 64 selected Xenon channels (132-195, correspond-

a well defined power-law spectrum with $\alpha = 2$ and $N_H = 3 \cdot 10^{21} \text{ H/cm}^2$. It corresponds to

$$1 \text{ Crab} = \begin{cases} 947 & \text{Uhuru counts} & 2-6 \text{ keV} \\ 412 & \text{Ariel V SSI counts} & 2-20 \text{ keV} \\ 1.6 \cdot 10^{-8} & \text{erg/sec}\cdot\text{cm}^2 & 2-6 \text{ keV} \\ 1.06 & \text{mJy} & 2-11 \text{ keV} \end{cases}$$

where $1 \text{ mJy} = 0.242 \cdot 10^{-14} \text{ erg/sec}\cdot\text{cm}^2\cdot\text{keV}$.

ing to 2–30 keV) with the option of compressing the histograms to 32 or 8 channels. It has 8 WSPs. The collection time for I5 data is given by $(\text{WSP \#6} \times 31.25 \text{ msec})$.

HER 5/2 The same as HER 5/1 except that the Argon and Xenon histogram collection times are independently variable. It has 9 WSPs.

HER 6 This program generates intensity profiles separately for each half experiment with one or two selected ranges of energy channels. It has 8 WSPs. The collection time for I6 data is 16 msec in case of one selected range and 32 msec in case of two selected ranges of energy channels.

HTR 3 This program collects data from all the detectors, including the ones coming from the offset detectors. It produces intensity profiles (T3 data type) from the Argon, the Xenon or both detectors. It has 5 WSPs. The collection time for T3 data is given by $(\text{WSP \#2})/(16K)$.

Bibliography

- Andrews D. and Stella L. 1985. ME dead time considerations. *EXOSAT Express*, **10**, p.35.
- Peacock A., Andresen R.D., Manzo G., Taylor B.G., Villa G., Re S., Ives J.C., and Kellock S. 1981. The gas scintillator proportional counter on EXOSAT. *Space Science Review*, **30**, p.525.
- Smith A. 1984. The ME background. *EXOSAT Express*, **5**, p.48.
- Taylor B.G., Andresen R.D., Peacock A., and Zobl R. 1981. The EXOSAT mission. *Space Science Review*, **30**, p.479.
- Tennant A.F. 1987. Power spectra, with application to EXOSAT data. *Monthly Notices of R.a.S.*, **226**, p.963.
- Turner M.J.L., Smith A., and Zimmermann H.U. 1981. The medium energy instrument on EXOSAT. *Space Science Review*, **30**, p.513.

3 The X-ray Pulsar 4U 1538–52

In this Chapter we will give the results from a temporal and spectral (both in the energy and frequency domain) analysis performed on four ME EXOSAT observations of the X-ray binary pulsar 4U 1538–52 (see Chapter 2 for details on the Medium Energy experiment on board EXOSAT), based on data from the Argon cells. In Table 3.1 the journal for the four observations is shown while in Fig. 3.1 they are shown in the orbital plane. In each observation the source was always pointed by the same half detector while the other half detector monitored the background.

After a brief description of the physical properties of the binary system 4U 1538–52, we will present the results from the timing analysis of both the coherent and the aperiodic part of the X-ray emission. Then we will give the result of our spectral analysis, showing that the phase-averaged X-ray energy spectrum of 4U 1538–52 is consistent with the typical power-law plus a fluorescence Iron line at 6.4 keV. In the first observation an interesting absorbing episode was found, which we attribute to a inhomogeneity in the stellar wind of 4U 1538–52 which passed through our line of sight. Finally a discussion on the results follows.

3.1 Physical Properties

The X-ray source located at the position (1950) $\alpha = 15^{\text{h}} 38^{\text{m}} 40.2^{\text{s}}$; $\delta = -52^{\circ} 13' 36''$ (Apparao *et al.*, 1978; Schwartz *et al.*, 1978) was first detected by *Uhuru* in 1970 (Forman *et al.*, 1976). 4U 1538–52 was contemporarily discovered as a 530 seconds X-ray pulsator by the X-ray spectroscopy experiment on board *OSO-8* on August 1976 (Becker *et al.*, 1977) and by Experiment C on board *Ariel 5* (Davison, 1977). Its binary nature was soon evident by the presence of an eclipse which hides the X-ray emission for about half a day and which recurred every 3.7 days (Becker *et al.*, 1977). The optical counterpart of 4U 1538–52 was identified as the 14.5 magnitude

# Obs	Obs ID	Date	Start Time (U.T.)	Duration (sec)	Orbital Phase	Half ME on Source
1	84/077	17 March 1984	09 ^h 36 ^m	35,400	0.40–0.51	H2
2	84/220	7 August 1984	20 ^h 03 ^m	16,400	0.87–0.92	H2
3	84/223	10 August 1984	02 ^h 48 ^m	22,500	0.48–0.54	H1
4	84/224	11 August 1984	12 ^h 53 ^m	25,000	0.86–0.93	H2

Table 3.1: Journal of the four ME EXOSAT observations of 4U 1538–52. The orbital phase is computed by means of the ephemeris given by Makishima *et al.* (1987).

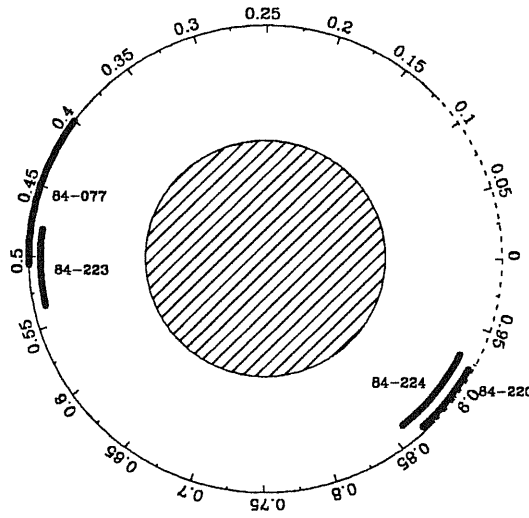


Figure 3.1: Portrait of the 4U 1538-52/QV Nor binary system with the four ME EXOSAT observations. The system is shown in scale, with the orbital parameters given by Makishima *et al.* (1987). The dashed line corresponds to the eclipse found from EXOSAT data.

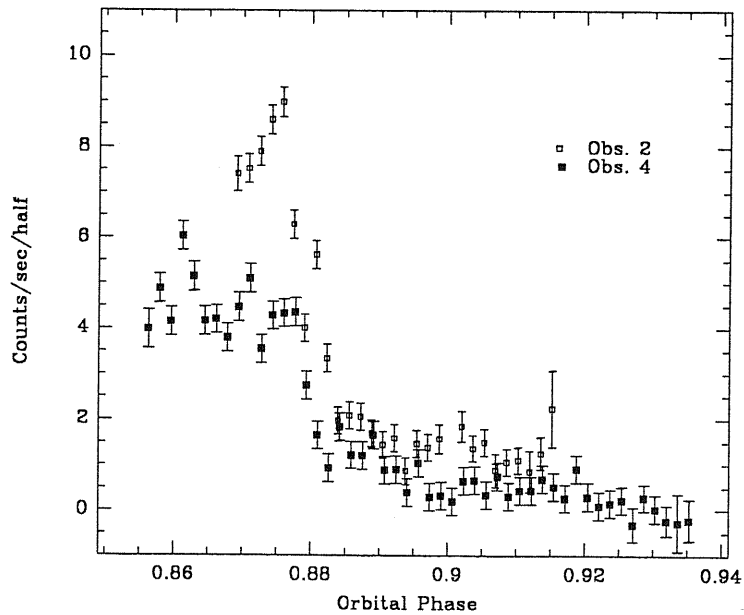


Figure 3.2: Eclipse ingress of 4U 1538-52 in two EXOSAT observations carried out on 7 August 1984 (Observation #2) and 11 August 1984 (Observation #4) (Cusumano *et al.*, 1989). The data are binned at the pulse period and the ephemeris was taken by Makishima *et al.* (1987). It is clearly visible the gradual entrance into eclipse, due to the extended atmosphere of QV Nor, for both the EXOSAT observations. A scale height for the companion atmosphere of $1.5 \cdot 10^{11}$ cm has been extracted (see text).

Parameter	Value	Parameter	Value
$A \equiv a_x \sin i$	52.8 ± 1.8 lt-sec	$f(M_*)$	11.4 ± 1.2 M_\odot
K_x	309 ± 11 Km/sec	K_*	33 ± 7 Km/sec
M_*	20 ± 4 M_\odot	R_*	39 ± 5 lt-sec
Eccentricity	0.14 ± 0.14	$q \equiv M_x/M_*$	0.11 ± 0.02
θ_e	$25^\circ \pm 5^\circ$	P_o	3.72854 ± 0.00002 days
d	5.5 ± 1.5 kpc	\mathcal{L}_x	$2 \cdot 10^{36}$ erg/sec

Table 3.2: Orbital parameters of 4U 1538–52, assuming a $\dot{P}_p = (6.3 \pm 1.5) \cdot 10^{-8}$ sec/sec. All the values are taken from Makishima *et al.* (1987) but the value of K_* and d (Crampton *et al.*, 1978).

B0 supergiant QV Nor (Cowley *et al.*, 1977; Parkes *et al.*, 1978). The studies of the optical light curves (Illovaisky *et al.*, 1979; Pakull *et al.*, 1983) of QV Nor confirmed the identification of the optical counterpart, because of the presence of a 3.7 day modulation.

Observations made by the Japanese X-ray satellite *Tenma* (Makishima *et al.*, 1987), showed that the period between eclipses, assumed to be the orbital period, is $P_o = 3.72854$ days. The eclipse duration is 0.51 ± 0.10 days, which corresponds to 0.14 ± 0.03 in binary phase. This value is consistent with those previously obtained by *Ariel 5*, 0.58 ± 0.06 days (Davison *et al.*, 1977) and *OSO-8*, ~ 0.64 days (Becker *et al.*, 1977). In Fig. 3.2 the eclipse ingress of 4U 1538–52 is shown for two EXOSAT observations, carried out on 7 August and 11 August 1984. From the transition time of about 0.06 days we were able to extract, using the orbital parameters given by Makishima *et al.* (1987) (see below), a scale height for the extended atmosphere of QV Nor of $1.5 \cdot 10^{11}$ cm (Cusumano *et al.*, 1989). This value is in agreement with that obtained by *Tenma* measurements (Makishima *et al.*, 1987).

The orbital parameters of the X-ray binary system 4U 1538–52 are listed in Table 3.2 (Makishima *et al.*, 1987). From these measurements it follows that we are not able to discriminate whether 4U 1538–52 fills or slightly underfills its Roche-lobe, and therefore whether this system is wind-fed or disk-fed, because the radius of QV Nor is very close to its critical Roche-lobe radius. To show this, let us recall that the expressions for the QV Nor radius and critical Roche-lobe radius are, respectively

$$R_* = A(1+q) \sqrt{\sin^2 \theta_e + \cot^2 i} \quad (3.1)$$

$$R_{RL} = A(1+q) \frac{(0.38 - 0.2 \ln q)}{\sin i} \quad (3.2)$$

where the symbols are defined in Table 3.2, i is the inclination angle, θ_e is the semi-eclipse angle (defined as π times the fraction of the orbital period which the star spends in eclipse), and we used the expression for R_{RL} given by Paczynski (1971). By means of the definition of the mass function

$$f(M_*) \equiv \frac{M_* \sin^3 i}{(1+q)^2}$$

we can eliminate $\sin i$ in Eqs. 3.1 and 3.2, obtaining a relation between M_* and R_* , and a relation between M_* and R_{RL} . In Fig. 3.3 with a solid curve the relation between M_* and R_* is indicated, corresponding to the observed range of variability for $f(M_*)$ and θ_e . With a dashed line the relation between M_* and $R_* \equiv \kappa R_{RL}$ is indicated, for the same values of $f(M_*)$ and θ_e and different values of κ . We can see that both the solutions $R_* = R_{RL}$ and $R_* = 0.9 R_{RL}$ are consistent with the observed orbital parameters and hence both a wind accretion or a Roche-lobe overflow are possible.

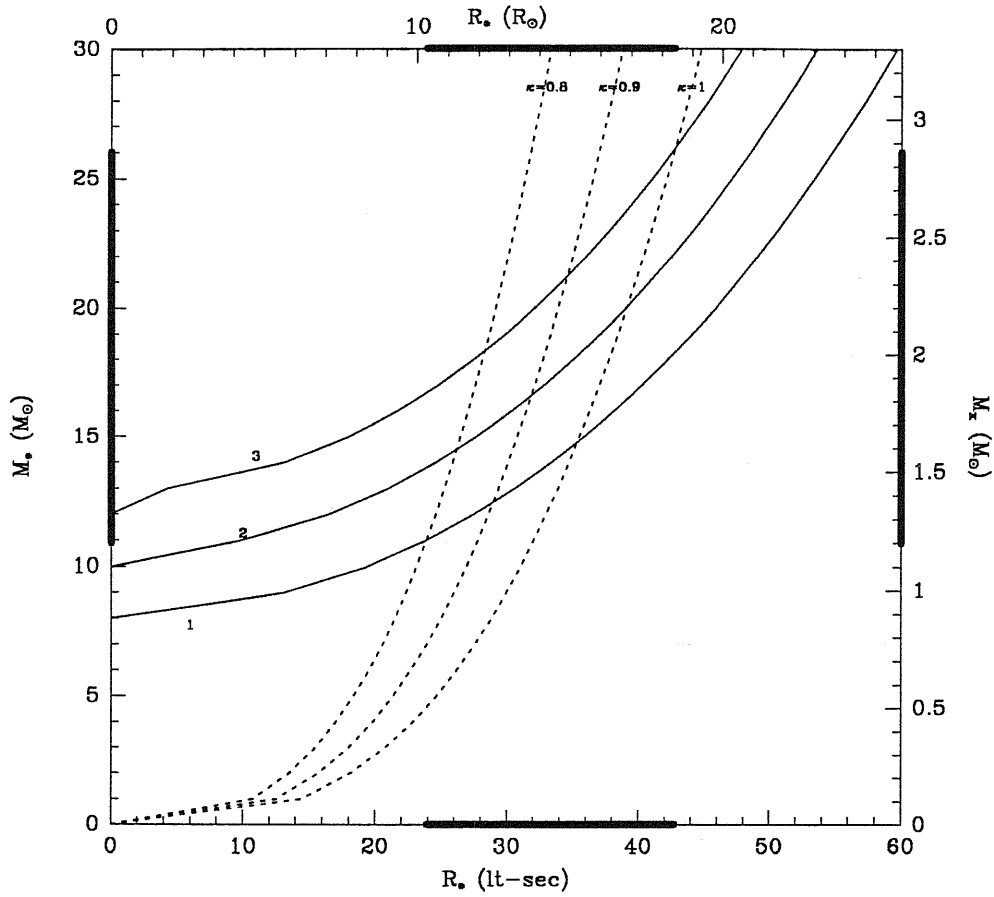


Figure 3.3: M_* – R_* relation for QV Nor, referring to Eqs. 3.1 and 3.2 in the text. The intersection between corresponding curves (solid and dashed lines) gives the solution. We can see that for the observed orbital parameters we obtain $M_* = 16 \pm 3 M_\odot$ and $R_* = 31 \pm 5$ lt-sec in the case of $R_* = 0.9 R_{\text{RI}}$, while the solution for $R_* = R_{\text{RI}}$ is $M_* = 20 \pm 3$ and $R_* = 40 \pm 5$ lt-sec. The three solid curves labelled with numbers correspond to the following cases: 1: $f(M_*) = 10.2$, $\theta_e = 30^\circ$; 2: $f(M_*) = 11.4$, $\theta_e = 25^\circ$; 3: $f(M_*) = 12.6$, $\theta_e = 20^\circ$. Adapted from Makishima *et al.*, 1987.

4U 1538–52 is quite peculiar among the class of X-ray binary pulsars because from its orbital parameters we expect this object is disk-fed (because of its short orbital period, its circular orbit and small binary separation) while we expect it is wind-fed from its long pulse period. Anyway, we will assume that 4U 1538–52 is a wind-fed X-ray binary pulsar, because its pulse period history shows the typical behaviour of this class of objects, *i.e.* random fluctuations of both signs. Makishima *et al.* (1987) have shown that the pulse period history of 4U 1538–52 may be described as the result of small fluctuations in the pulse period that occur randomly¹ on time scale which are comparable to the orbital period. The main problem related to the pulse period behaviour of 4U 1538–52 consists in the fact that no clear episode of spin-up was observed from this source, while we expect that the secular trend of the pulse period should be just spin-up (see Chapter 5).

¹That is, the fluctuations in the pulse period can be described statistically by a random walk (Boynton *et al.*, 1984).

Date of Observation	Mid-Epoch (JD - 2,440,000)	Pulse Period (sec)	Satellite	Reference
25 August 1976	3016.3	528.93 ± 0.10	<i>OSO-8</i>	(Becker <i>et al.</i> , 1977)
6 September 1976	3029.2	528.66 ± 0.36	<i>Ariel 5</i>	(Davison, 1977)
9 September 1976	3032.3	529.20 ± 0.78	<i>Ariel 5</i>	(Davison, 1977)
23 April 1976	3257.7	529.60 ± 0.34	<i>Ariel 5</i>	(Davison <i>et al.</i> , 1977)
2 July 1983	5518.2	529.792 ± 0.009	<i>Tenma</i>	(Makishima <i>et al.</i> , 1987)
17 March 1984	5777.3	529.97 ± 0.16	<i>EXOSAT</i>	
10 August 1984	5923.1	530.14 ± 0.03	<i>EXOSAT</i>	
2 March 1988	7223.0	530.420 ± 0.014	<i>Ginga</i>	(Nagase, 1989)

Table 3.3: Pulse period of 4U 1538–52.

3.2 Timing Analysis

3.2.1 Analysis of the Coherent Emission

The 1–10 keV background subtracted² light curves of the 17 March and the 10 August 1984 observations are shown in Fig. 3.4, with 10 sec time resolution. In the first one we can distinguish an episode of increasing luminosity about 5000 seconds long, while an intensity dip about 1000 seconds long is present at the beginning of the third observation. The intensity was highly variable, ranging from about 50 Counts/sec (the flare) to about 1 Count/sec (the dip), with a mean value of 14 Counts/sec in both the observations.

In the first and third observations the single 530 sec X-ray pulses are well visible (see Fig. 3.4) so the arrival times of each individual pulse could be determined, by measuring the times of pulse minima, after smoothing the data to reduce the effect of random fluctuations, and then using the pulse minima as fiducial points. The pulse arrival times so obtained were corrected to the solar system barycentre and for the orbital motion of the X-ray source. A least squares analysis was used to determine the best fitting constant pulse period.

In the other two observations the single pulses are not well visible so we divided the part of observation in which the source is not in eclipse into intervals of length 2000 to 5000 sec, and we folded the data with the previously obtained period. Using the above procedure we determined the arrival times of these pulses. A least squares analysis was then used again.

The timing residuals were minimized for a period of 529.97 ± 0.16 sec and a rms timing residual of 18 sec for the first observation and for a period of 530.14 ± 0.03 sec for the third, plus the available data from the second and fourth observations, with a rms timing residual of 15 sec.

The EXOSAT pulse period result is shown in Fig. 3.5 together with previous determinations. Our new values, together with values (see Table 3.3) from *OSO-8* (Becker *et al.*, 1977), *Ariel 5* (Davison, 1977; Davison *et al.*, 1977), *Tenma* (Makishima *et al.*, 1987) and *Ginga* (Nagase, 1989), indicate that 4U 1538–52 was spinning-down during 1983–84 with $\dot{P}_p/P_p \sim 2.2 \cdot 10^{-11} \text{ sec}^{-1}$. The general trend in the period 1976–1988 is a spin-down with $\dot{P}_p/P_p \sim 7.3 \cdot 10^{-12} \text{ sec}^{-1}$.

The time averaged background subtracted normalized pulse profiles obtained for the first and third observations by folding the data at the pulse period, are shown in Fig. 3.6 and Fig. 3.7 for six different energy ranges. The counts have been normalized in the interval 0–1, to permit a

²The background subtraction was made as follows: first, a difference between the background in the two halves of the detector was computed using data obtained during the slew manoeuvres; then, the background to be subtracted was evaluated correcting by this difference the background measured by the offset half detector during the observation of the source.

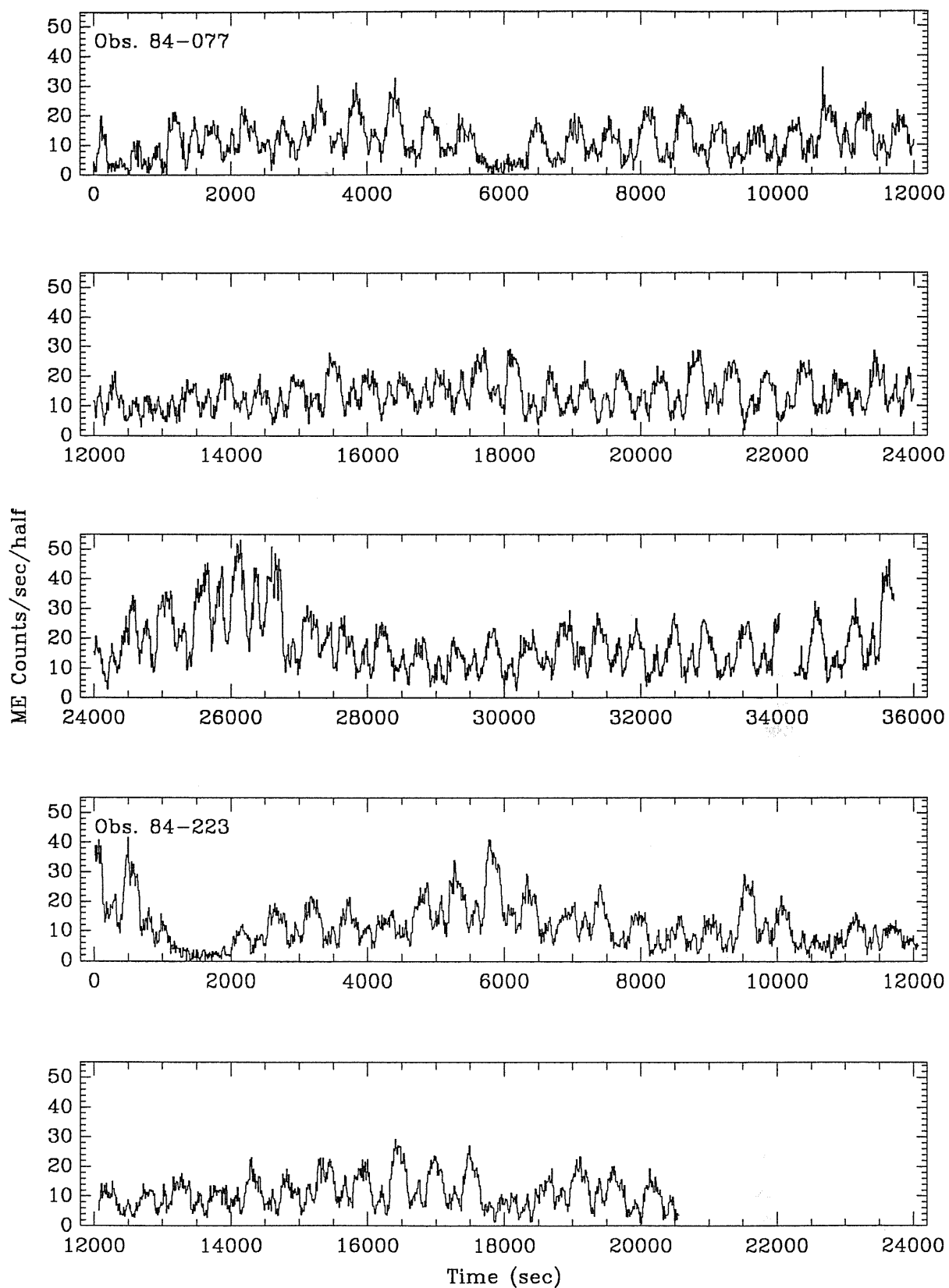


Figure 3.4: The 1-10 keV background subtracted light curves of 17 March and 10 August 1984 ME/HER4 EXOSAT observations of 4U 1538-52. The collection time is 10 sec.

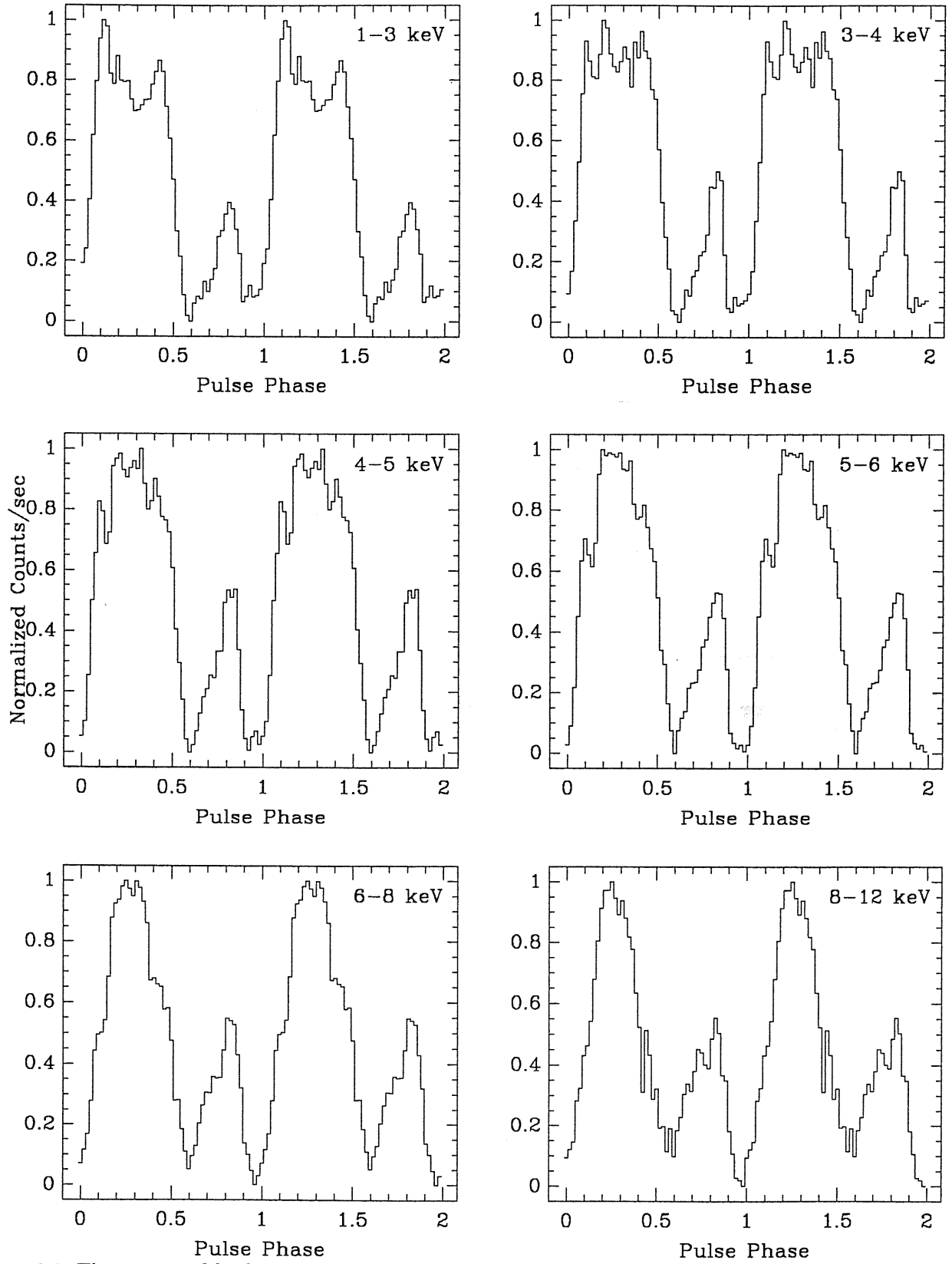


Figure 3.6: Time averaged background subtracted normalized pulse profiles in six different energy bands for the 17 March 1984 EXOSAT observation of 4U 1538-52.

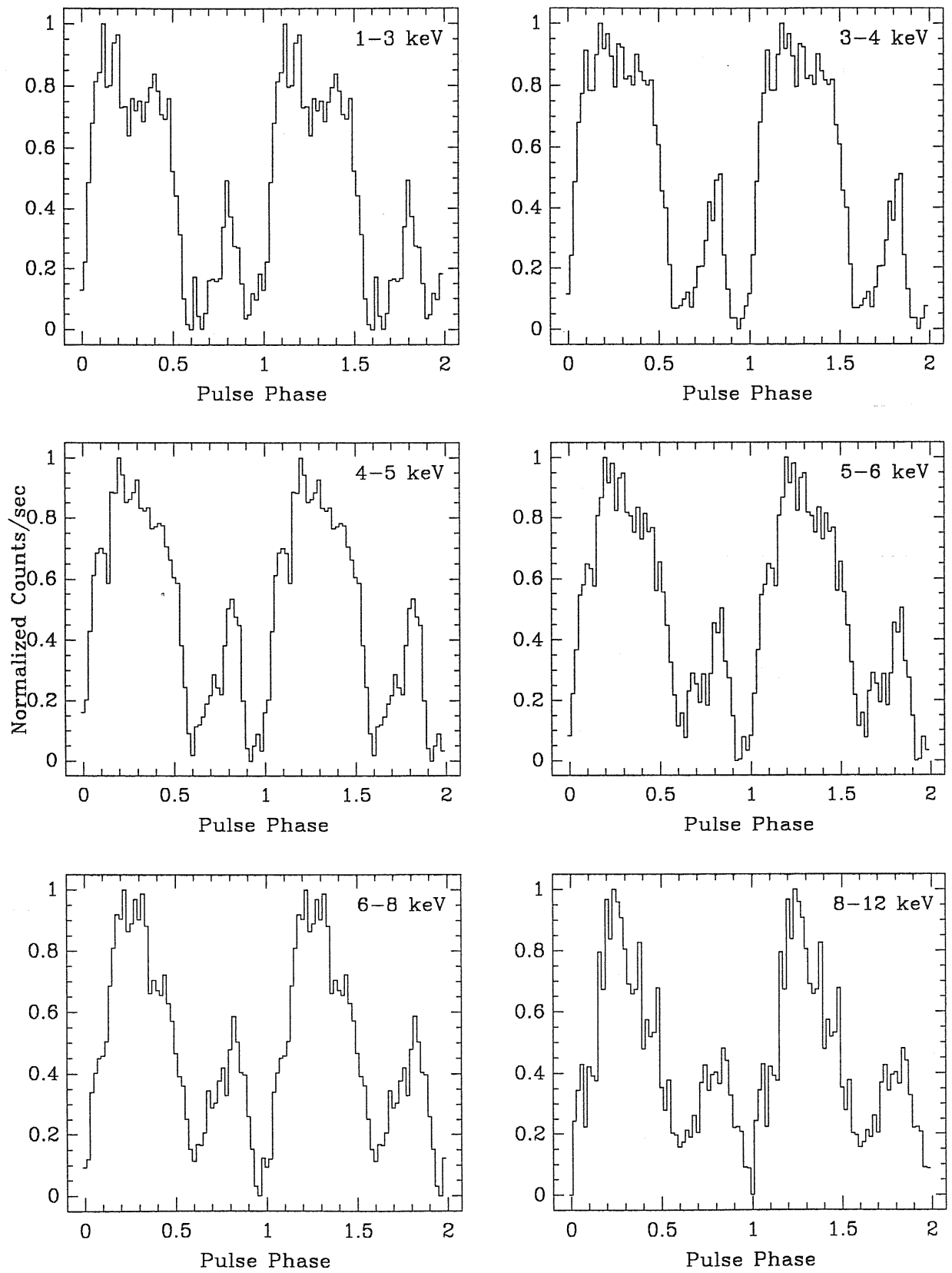


Figure 3.7: Time averaged background subtracted normalized pulse profiles in six different energy bands for the 10 August 1984 EXOSAT observation of 4U 1538-52.

of a typical X-ray pulsar, with almost all the power concentrated in the low frequency part of the spectrum and with a steep fall at higher frequencies.

The PSD function so obtained gives the frequency dependence of the variance of the data due to the aperiodic non-Poissonian flux of the source. The peaks visible in the plots correspond to the fundamental frequency of pulsation and its harmonics and are indicated by arrows in Fig. 3.8. As can be seen from this figure, the source shows aperiodic time variability with time scales down to the Nyquist frequency of 0.05 Hz.

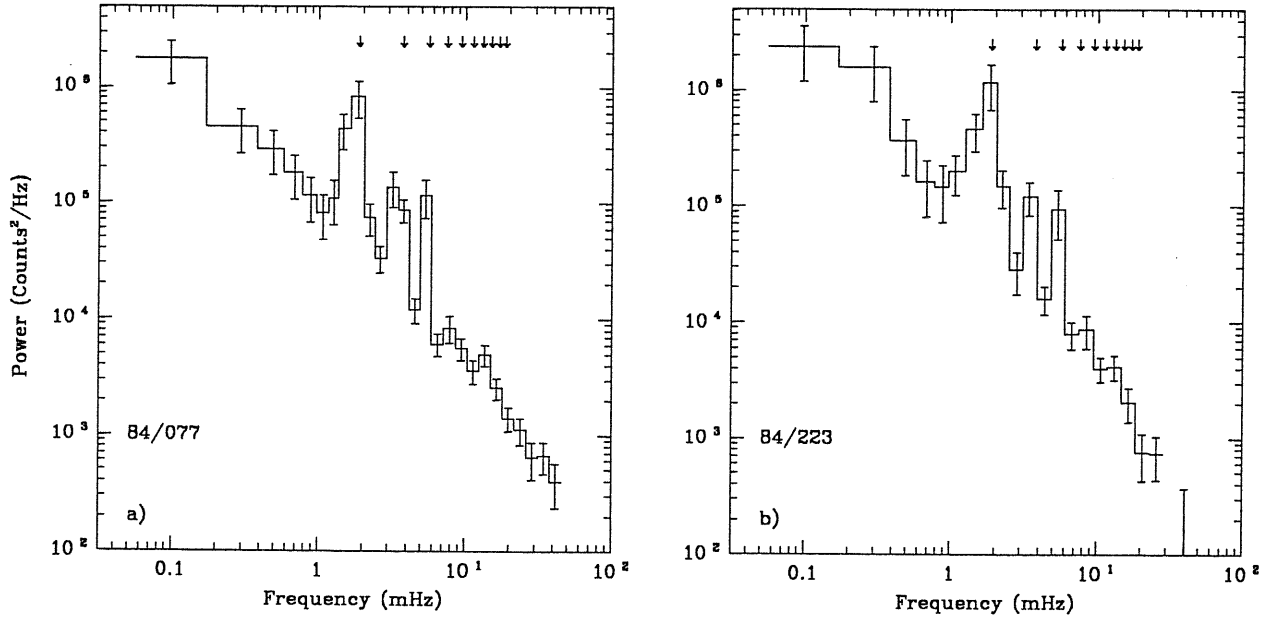


Figure 3.8: PSDs of the 84/077 and 84/220 observations of 4U 1538–52. The peaks visible in the plots corresponds to the contribution of the coherent pulsation. The pulsation frequency and its first nine harmonics are indicated by arrows. In *a*) the PSD spectrum of the 17 March 1984 observation is shown, corresponding to 6 runs of 512 data each. In *b*) the PSD spectrum of the 10 August 1984 observation is shown: it was computed from 4 runs of 512 data each. The collection time for both the two observations was 10 sec.

In order to investigate the continuum component of our spectra the first step was to extract the contribution due to the pulsation, that is the peaks of the fundamental frequency and its harmonics. Recalling our discussion in Chapter 1, we assumed a general power spectrum of a pulsed source as the sum of three terms:

$$P(f) = \underbrace{\widehat{C}}_{\text{Poissonian}} + \underbrace{k f^{-\alpha}}_{\text{aperiodic}} + \underbrace{\sum_n A_n \delta(f - n f_p)}_{\text{coherent}} \quad (3.3)$$

where f is the frequency and $f_p = 1/P_p$. The constants C (the Poissonian counting), k , α (the power law slope) and A_n (the amplitudes of the fundamental frequency and its harmonics) are free parameters. We then fixed A_n by measuring them in the linearly binned power spectrum, and C from the sum of the data counts (as a check we then verified the consistency of the estimated Poissonian variance with the value obtained from the fitting program, assuming C as a free parameter). Finally we estimated the output power spectrum taking into account the effects due to integration and sampling of the data, and the finite time length of the runs.

The result of the fits is shown in Table 3.4. We performed the same analysis on data with 16 ms time resolution taken from the third observation. The result is shown in Fig. 3.9: no power is apparent above 0.05 Hz.

# Obs.	Energy Channels	Energy (keV)	$\langle I \rangle$ (Counts/sec)	α (%)	rms	χ^2_{dof}
1	6-30	1.41-8.02	16.82 ± 0.04	1.63 ± 0.09	26 ± 5	8/12
3	6-30	1.41-8.02	14.09 ± 0.04	1.73 ± 0.07	36 ± 6	9/15

Table 3.4: Fitting results on two ME EXOSAT PSDs of 4U 1538-52. As fitting law we used that defined in Eq. 3.3. The mean intensity of the source was corrected for dead time effects (Tennant, 1987) and it is computed in the 1-12 keV energy band.

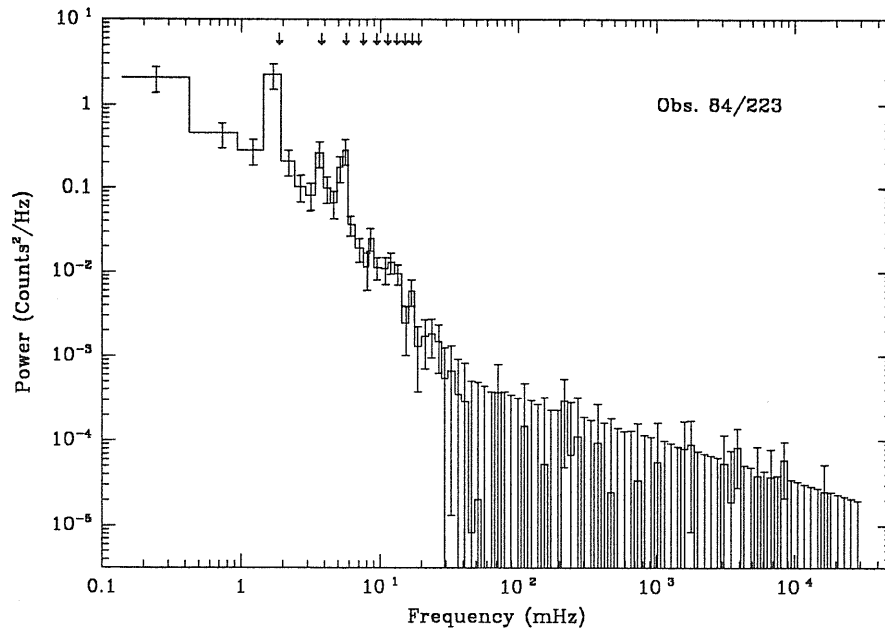


Figure 3.9: Power Spectral Density function of the 84/223 observation of 4U 1538-52, with 16 msec time resolution. Because in this observation the source was very faint, we were not able to extract any characteristic time scale.

We then computed the rms fractional variability (for its definition see Appendix B) of the continuum component (Lewin *et al.*, 1988), which gives an integral measure of the erratic variability associated to the flux from the source. Our values are in agreement with those obtained for other massive X-ray pulsars (Belloni and Hasinger, 1990). The results are given in Table 3.4.

We searched for an energy dependence of the fit parameters, but they remain practically unchanged with respect to energy.

3.3 Spectral Analysis

3.3.1 The Pulse-Phase Averaged Spectrum

The spectral energy analysis has been performed using only the data obtained from Argon ME detectors in the energy range 1.5–12 keV.

In previous observations, the X-ray spectrum of 4U 1538–52 was fitted by a power-law plus a low energy absorption and a high energy cutoff

$$\frac{dN}{dE} = \begin{cases} N_0 A(N_H) E^{-\alpha} & \text{for } E \leq E_c \\ N_0 A(N_H) E^{-\alpha} \exp[(E_c - E)/E_f] & \text{for } E \geq E_c \end{cases} \quad \frac{\text{Photons}}{\text{cm}^2 \text{ sec keV}} \quad (3.4)$$

where E_c and E_f are the cutoff and the folding energy, respectively, and the photoelectric absorption $A(N_H)$ can be written in terms of the column density N_H in two equivalent ways

$$A(N_H) = \exp[-\sigma N_H] \quad (3.5a)$$

$$A(N_H) = \exp \left[\left(\frac{E_a}{E} \right)^{\frac{8}{3}} \right] \quad (3.5b)$$

where σ is the X-ray scattering cross section (Brown and Gould, 1970; Morrison and McCammon, 1983) and E_a is called absorption energy (for a review on the typical spectral fitting laws see Orlandini (1988)). The results obtained from previous observations are summarized in Table 3.5.

Given the limited energy range of our spectral analysis, we used as spectral laws a thermal bremsstrahlung model and a power-law, both of them with low energy photoelectric absorption. Both a power-law and a thin thermal bremsstrahlung law fit well the data. In Table 3.6 we show the results of power-law fits for the first and the third observations. An Iron line with an E.W. ≈ 100 eV is present. This value is in agreement, within the uncertainties, with the *Tenma* measurement (Makishima *et al.*, 1987), but a factor 5 smaller than the *HEAO 1-A2* measurement (White *et al.*, 1983). As pointed out by Makishima *et al.* (1987) this discrepancy is probably due to the contamination by the galactic ridge emission, which is strong in the direction of 4U 1538–52, of galactic coordinates $l^\Pi = 327^\circ$, $b^\Pi = 2^\circ$ (Warwick *et al.*, 1985; Koyama, 1989).

The hardness ratio as a function of time of the first observation, is shown in Fig. 3.10. As can be seen, this quantity does not depend on the intensity of the source: in fact during the flaring episode the hardness ratio does not show any appreciable variation, as we can see from the count rate in the same figure (1–10 keV).

However, an interesting absorbing episode is present, as shown into Fig. 3.10. This may be due to an inhomogeneity in the stellar wind of QV Nor, which passed through our line of sight and caused the observed absorption in the 1–4 keV energy band. From the asymmetry in the raise and fall of the hardness ratio we can infer that the blob might have an asymmetric shape along the direction of motion. The scale height of this inhomogeneity, assuming a blob velocity of the order of

Satellite	Energy (keV)	Photon Index	E_c (keV)	E_f (keV)	N_H	Iron Line E.W. (eV)	References
<i>OSO-8</i>	2-20	1.2 ± 0.2			3.2 ± 1.0		(Becker <i>et al.</i> , 1977)
<i>Ariel 5</i>	2-15	1.1 ± 0.1			2.6 ± 1.0		(Davison, 1977)
<i>HEAO 1-A2</i>	2-30	1.42	17 ± 2	11 ± 3		572 ± 140	(White <i>et al.</i> , 1983)
<i>Tenma</i>	2-12	1.12 ± 0.04	14.8 ± 0.5	5.9 ± 1.2	3.7 ± 0.4	52 ± 30	(Makishima <i>et al.</i> , 1987)

Table 3.5: Previous spectral measurements of 4U 1538-52. The spectral parameters are define in Eq. 3.4. The absorption column density is in units of 10^{22} H/cm² while the Iron line energy measured by *Tenma* is 6.3 ± 0.2 keV.

Nr. Obs.	Photon Index	N_H (10^{22} H/cm ²)	Iron Line Energy (keV)	Iron Line E.W. (eV)	Flux (1-12 keV)	$\langle I \rangle$ (10^{35} erg/sec)	χ^2_{dof}
1	1.49 ± 0.04	2.7 ± 0.2	6.7 ± 0.15	100 ± 30	3.20	11 ± 6	38/34
3	1.40 ± 0.07	2.6 ± 0.3	6.2 ± 0.10	100 ± 40	2.19	8 ± 4	44/34

Table 3.6: EXOSAT spectral measurements of 4U 1538-52. All the measurements have 1σ error, while the 1-12 keV X-ray flux is in units of 10^{-10} erg sec⁻¹ cm⁻².

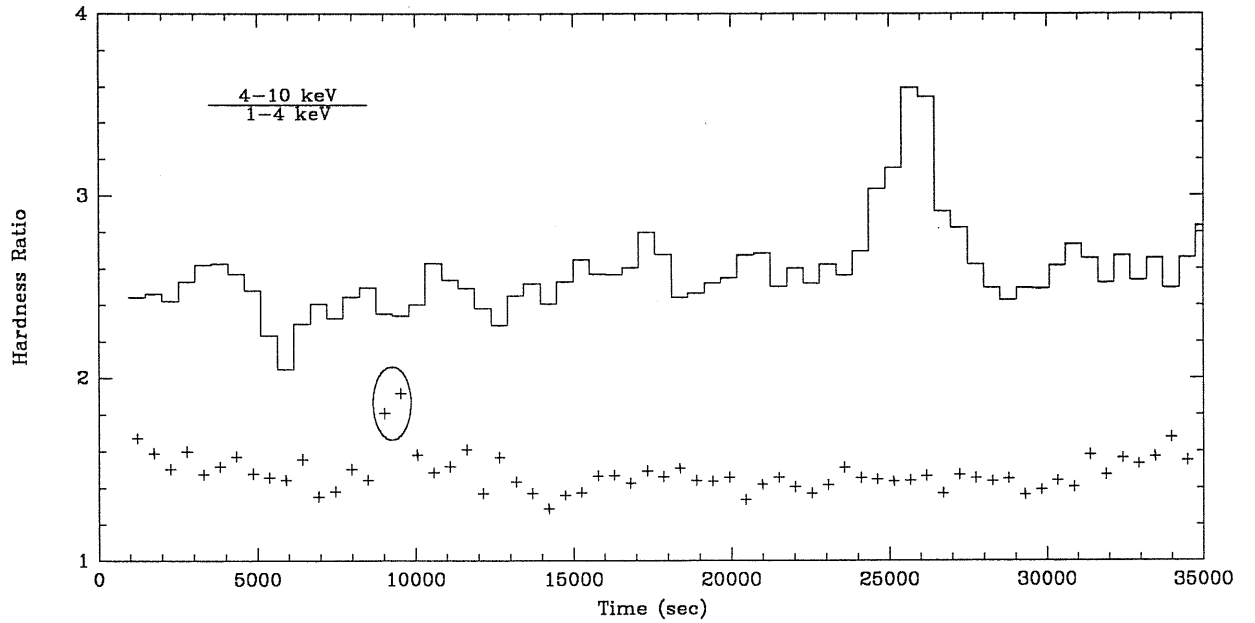


Figure 3.10: Hardness ratio of the 17 March 1984 ME EXOSAT observation of 4U 1538-52. Note that the hardness ratio does not show any correlation with the intensity of the source (energy range 1.5-12 keV, shown as an histogram in the upper part of the Figure, not in scale). An interesting absorbing episode is present at the beginning of the observation (shown in the oval). We interpret this feature as due to a passage of a stellar wind inhomogeneity through our line of sight (see text). The collection time of the data was 10 sec.

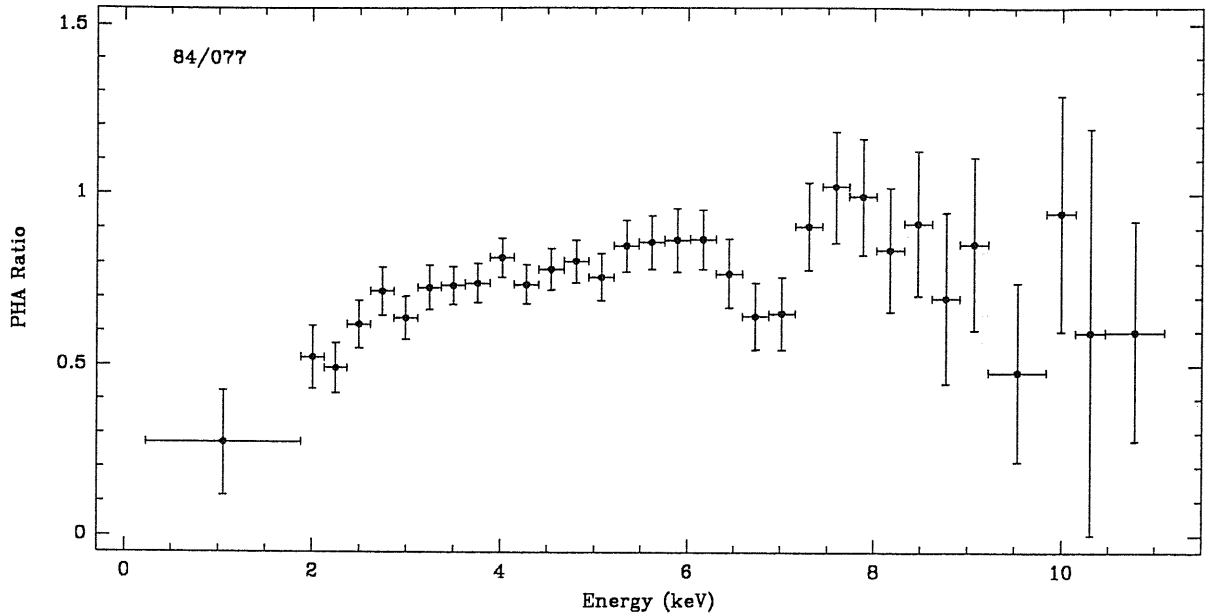


Figure 3.11: Ratio between two energy spectra taken during the absorbing episode and outside it, for the 84/077 ME EXOSAT observation of 4U 1538–52. The two spectra are not normalized, so the ratio is not equal to one. Note the feature present at about 6.3 keV.

100–1000 Km/sec, is $2 \cdot 10^9$ – $2 \cdot 10^{10}$ cm. This is in agreement with observations of inhomogeneities in another wind-fed X-ray pulsar: Vela X–1 (Nagase *et al.*, 1986).

To better analyze this variation with energy we have compared the average energy spectrum recorded during the absorption feature with the ones obtained outside the episode. The spectral ratio is shown in Fig. 3.11, from which we can see that our hypothesis was correct: the hardening was due to absorption because there was a correspondent increase in the column density, which passed from the value of $2.7 \cdot 10^{22}$ H/cm² to the value of $6 \cdot 10^{22}$ H/cm².

3.3.2 Pulse–Phase Spectroscopy

We folded the data from the first observation in the energy intervals 1–4 keV and 4–10 keV and computed the corresponding hardness ratio vs pulse phase. The result is shown in Fig. 3.12 together with the pulse profiles obtained folding the data in the 1–4 and 4–10 keV energy range. The hardness ratio shows a softening of the signal in correspondence of the raise and fall of the main peak of the pulse profile.

In order to study the pulse–phase dependence of the energy spectra of 4U 1538–52 we divided the pulse profile of the first and third observations in four phase intervals as follows (see Fig. 3.12):

Observation	Interval	Pulse Phase	Observation	Interval	Pulse Phase
1	A	0.22 — 0.44	3	A	0.74 — 0.95
	B	0.52 — 0.64		B	0.96 — 0.15
	C	0.66 — 0.96		C	0.16 — 0.45
	D	0.98 — 0.21		D	0.46 — 0.73

We computed the average spectra recorded during the pulse intervals B, C and D and divide them by that obtained during the pulse interval A. These spectral ratios are shown in Fig. 3.13 for the first observation. From them we can see that the hardening is due to a flattening of the spectrum.

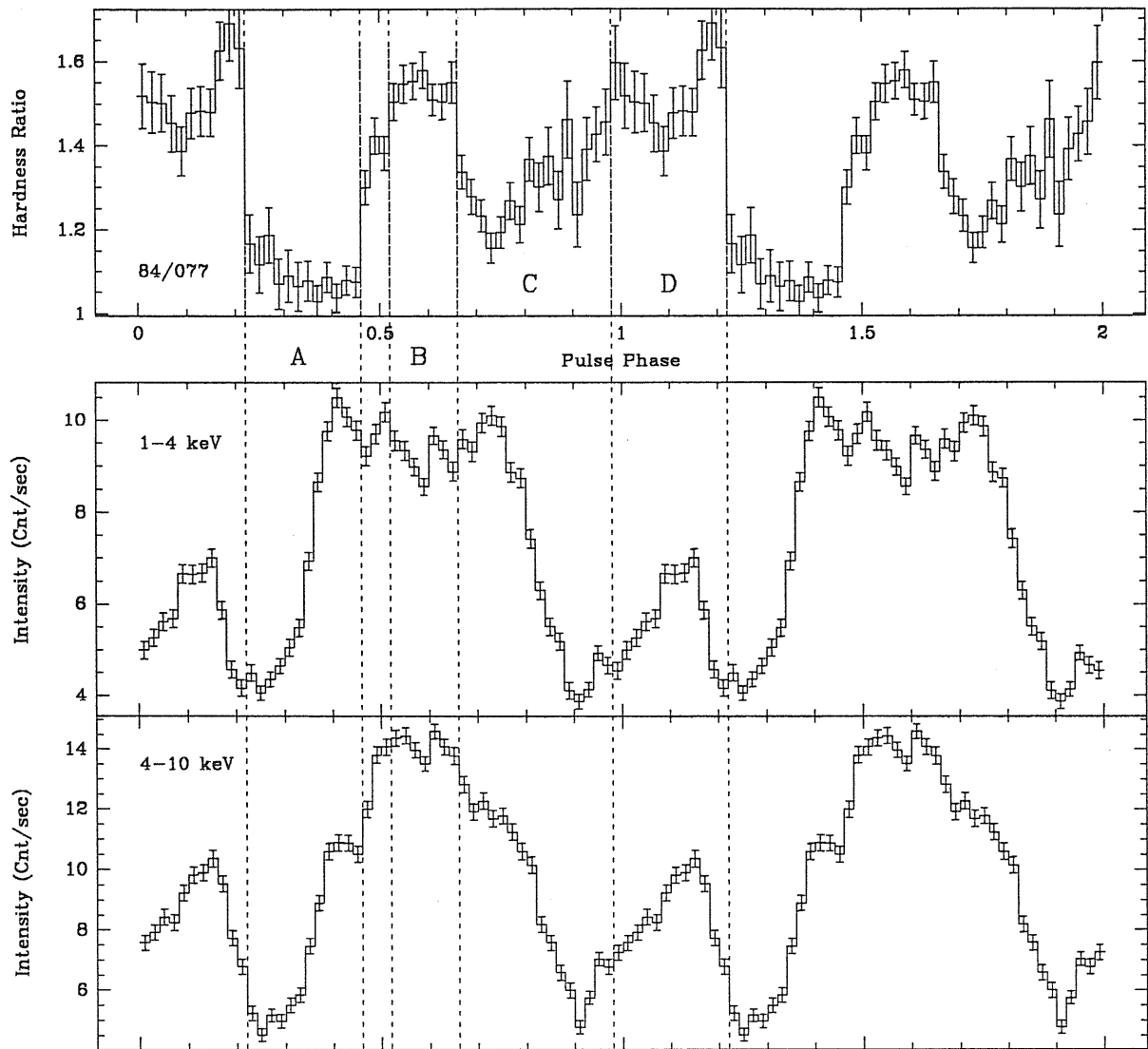


Figure 3.12: Hardness ratio as a function of the pulse phase for the 84/077 ME EXOSAT observation of 4U 1538-52. The two pulse profiles in the 1-4 keV and 4-10 keV energy bands are shown, together with the identification of the pulse phase intervals defined in the text.

We have also computed the modulation index, defined as

$$\Phi(E) = 1 - \frac{I_{\min}(E)}{I_{\max}(E)} \quad (3.6)$$

where I_{\max} is the maximum intensity in the background subtracted pulse profile and I_{\min} is the minimum, at the given energy E . This parameter gives information on the process which gives rise to the pulsed component of the flux, in the sense that if there is not pulsation at all, then $\Phi = 0$; if the emission is totally pulsed then $\Phi = 1$. This approach is slightly different from the pulsed fraction, defined as the ratio of the modulated component of the flux to the total flux. Indeed, the computation of the modulation index does not require the measurement of the continuum level, as the pulsed fraction does.

The modulation index for the first observation is consistent with a constant value of ~ 0.65 , independent of energy, while for the third observation it shows an increase with energy from a value of 0.78 (1–3 keV) to 0.96 (8–13 keV).

3.4 Discussion

3.4.1 Coherent Timing Measurements

The EXOSAT observations of the X-ray binary pulsar 4U 1538–52 confirm the general spin-down trend of the pulse period. Indeed the main theoretical problem about the X-ray binary pulsar 4U 1538–52 consists in the lack of a secular spin-up: theories of both disk and wind accretion predict some occasional spin-down episode but a net spin-up trend over long time scales.

From the conservation of angular momentum in the system QV Nor/4U 1538–52, the time scale due to the accretion torque is computed from the relation (Lamb *et al.*, 1973)

$$\frac{d}{dt}(I\Omega_p) = \dot{M}_x \ell - J_{\text{nm}} \quad (3.7)$$

where I is the moment of inertia of the neutron star, \dot{M}_x is the accretion rate of matter onto the neutron star, ℓ is the specific angular momentum carried by the accreted matter (see Chapter 5 for different expressions) and finally J_{nm} is the (non-material) torque due to magnetic, viscous forces and to matter that leaves the system. Re-arranging the terms in Eq. 3.7, neglecting the term \dot{I} because the time scale due to this variation, \dot{I}/I , is much longer than \dot{P}_p/P_p , assuming that matter does not leave the system and neglecting magnetic and viscous forces (*i.e.* $J_{\text{nm}} \approx 0$) we obtain

$$I \dot{\Omega}_p = \dot{M}_x \ell. \quad (3.8)$$

We will compute the time scale due to accretion from this expression.

From the physical parameters of the 4U 1538–52 system as reported by Joss and Rappaport (1984) (the neutron star mass and radius, the supergiant mass), Parkes *et al.* (1978) (the mass loss rate from the supergiant and the terminal velocity of the wind) and Clark *et al.* (1990) (the magnetic field strength of the neutron star) the characteristic lengths of accretion (see *e.g.* Henrichs, 1983) are:

- Magnetospheric Radius $r_m \simeq 1 \cdot 10^9$ cm;
- Accretion Radius $r_a \simeq 3 \cdot 10^{10}$ cm;
- Corotation Radius $r_c \simeq 1 \cdot 10^{10}$ cm.

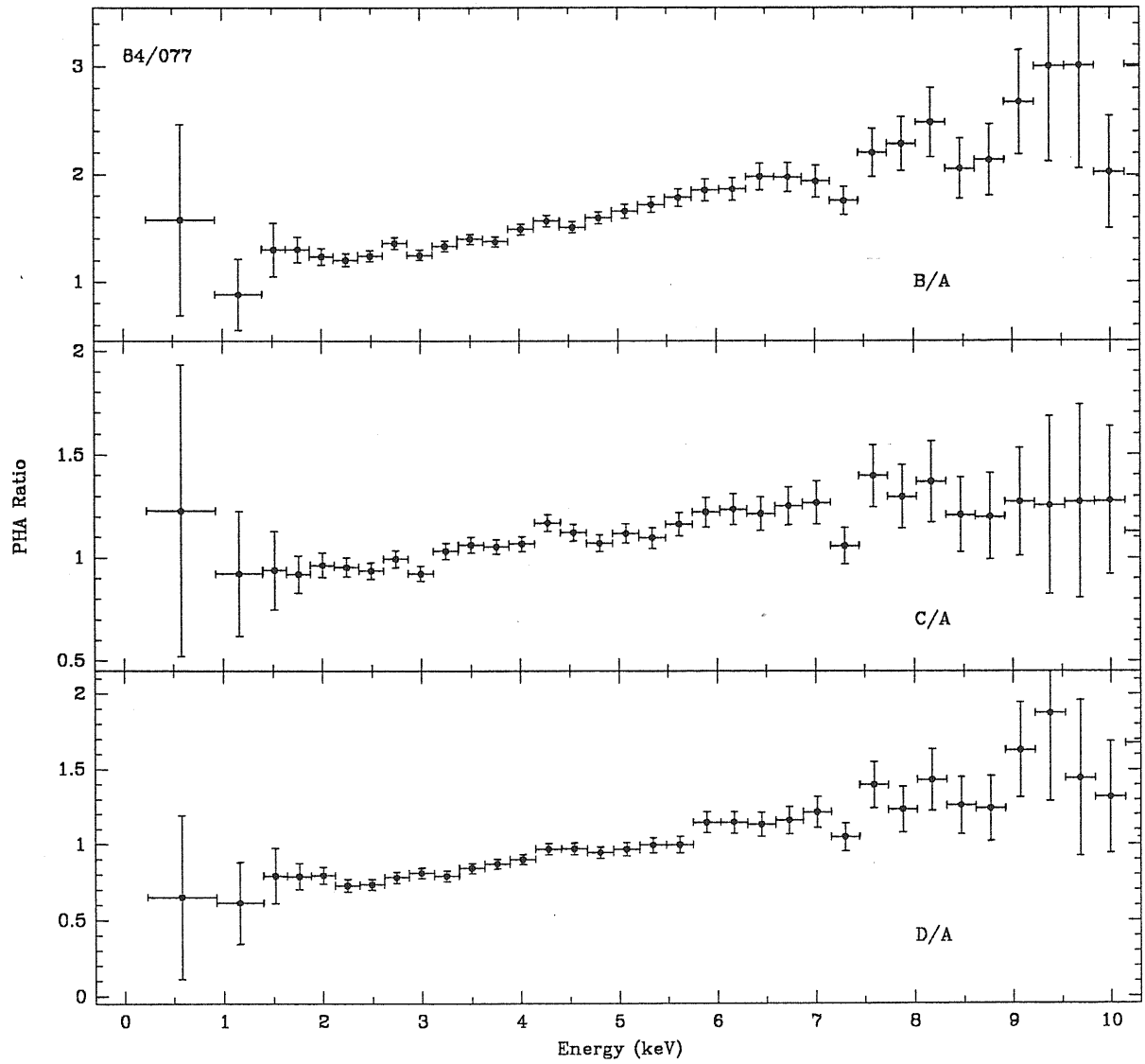


Figure 3.13: Ratio between energy spectra taken at different pulse phases, for the 84/077 ME EXOSAT observation of 4U 1538-52. Note the feature present at about 7.4 keV, the Iron K_{α} edge; this feature was not present in the 84/223 observation.

The fact that $r_a > r_m$ means that this source is accreting matter. Furthermore $r_c > r_m$, so, according to Stella *et al.* (1986), 4U 1538–52 is in the regime of direct wind accretion. The observed X-ray luminosity of $2 \cdot 10^{36}$ erg/sec (Makishima *et al.*, 1987) is in agreement, within the uncertainty in the observed values, with that predicted by Stella *et al.* (1986). By means of Eq.3.8 a value of $\dot{P}_p/P_p \sim -7.0 \cdot 10^{-12} \text{ sec}^{-1}$ is expected in the case of wind accretion with a radial gradient in density and velocity (Wang, 1981) and a value of $\dot{P}_p/P_p \sim -1.3 \cdot 10^{-10} \text{ sec}^{-1}$ is expected in the case of disk accretion with magnetic coupling (Ghosh and Lamb, 1979a; Ghosh and Lamb, 1979b). These values must be compared to the observed value of $\dot{P}_p/P_p = +7.3 \cdot 10^{-12} \text{ sec}^{-1}$.

The modulo of the expected values of \dot{P}_p/P_p in the case of wind accretion agrees well with the observed one, but the general trend of spin-up is not predicted. It has been proposed that the variations in the pulse period of wind-fed X-ray pulsars are the result of small fluctuations of both signs that occur randomly on time scales which are comparable to the orbital period (Boynton *et al.*, 1984). Makishima *et al.* (1987) have shown that the observed period change of 4U 1538–52 in 1976–1983 is really in agreement with this interpretation. The nature of these fluctuations is to date unknown. It can be pointed out that no clear episode of spin-up was observed from this source, therefore a careful monitoring of 4U 1538–52 is necessary in order to clarify its temporal behaviour.

3.4.2 Aperiodic Timing Measurements

From the spectral density analysis performed on the light curve of 4U 1538–52 we were not able to extract any characteristic time scale down to ~ 20 sec; this means that the process (or the processes) which occurs at the magnetospheric limit and might be responsible for the fluctuations in the X-ray intensity does not show a unique time scale for frequencies less than 0.05 Hz. The rms extracted from the power spectrum fits are in agreement with those obtained for other high mass X-ray pulsators (Belloni and Hasinger, 1990) while a remarkable difference with those observed in low mass X-ray binary systems exists (van der Klis, 1989).

We observed a drastic increase of the rms between the first and the third observation, while in correspondence there was a decrease in the luminosity of the source (see Table 3.4). Because of the small number of observations available, it was not possible to search for correlations between rms and physical parameters of the X-ray source, as mean intensity and pulse period derivative. We will see in the next Chapter that in the ten GX 301–2 observations a correlation exists between rms and the accretion time scale \dot{P}_p/P_p .

No evident feature that could be associated to quasi-periodic oscillation is apparent in the 4U 1538–52 PSD spectra.

3.4.3 Energy Spectrum Measurements

The energy spectral analysis has confirmed the form of the spectrum, which is typical of this class of objects, while the presence of a K_α Iron emission line in the case of a power-law spectrum confirms the previous observation by Tenma (Makishima *et al.*, 1987).

The hardness ratio relative to the first observation, computed between the two energy bands 4–10 keV and 1–4 keV, clearly does not show any correlation with the intensity of the source (see Fig. 3.10); indeed during the flaring episode, in which the mean intensity increases by a factor of about 2.2, the hardness ratio remains practically constant. This means that the process (or the processes) responsible for the production of soft photons correlates with that producing hard photons: this should exclude the possibility of the existence of a region which emits intense soft X-rays around 4U 1538–52, as was proposed for the Vela X–1 system by Kallman and White (1982), in order to explain the soft excess in the spectra of this source.

The absorbing episode visible in Fig. 3.10 is interpreted as due to an inhomogeneity in the

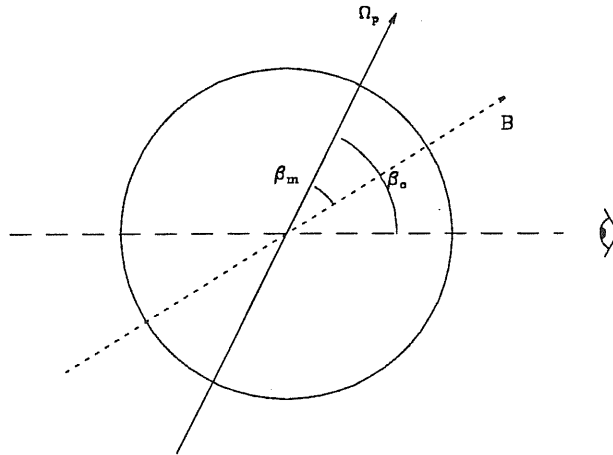


Figure 3.14: Definition of the aspect angles β_m and β_o . According to the fact that $\beta_m + \beta_o > 90^\circ$ or $\beta_m + \beta_o < 90^\circ$, we are able to observe both or only one polar cap, respectively.

stellar wind of QV Nor. To check this hypothesis, we simulated two energy spectra corresponding to the absorption column densities observed outside and inside the episode, and performed their ratio. It was consistent with the ratio observed. The feature in correspondence of the Iron line at 6.4 keV agrees with the interpretation that the blob hid the region responsible of the Iron line emission. Furthermore, the decrease of the line intensity in correspondence of the blob transit is due to a real increase in absorption and not to an independent increase of the line intensity outside the episode. In fact, the ratio between two spectra taken before and after the episode is roughly equal unity. The absorption column density increased from $2.7 \cdot 10^{22} \text{ H/cm}^{-2}$ to $6 \cdot 10^{22} \text{ H/cm}^{-2}$, in correspondence of the transit of the blob, therefore the density inside the blob is about 2.2 times that of the wind.

Another interesting feature consists in the fact that during the blob transit through our line of sight the pulsation does not disappear but remains clearly visible, as can be seen in Fig. 3.4. Passing through the blob the X-ray radiation did not lose the information contained in the pulse shape, therefore the effect of scattering is almost negligible in the matter composing the inhomogeneity, *i.e.* is the blob is optically thin with respect to X-rays.

The fact that the pulse profiles of 4U 1538–52 show a double peak structure is interpreted by assuming that we are able to observe both the emitting polar caps onto the neutron star surface. Indeed, the observed flux from a rotating neutron star as a function of the pulse phase depends on the viewing angle $\theta(\varphi)$, where φ is the pulse phase. The viewing angle depends (see Fig. 3.14) on the angle between the neutron star magnetic field and the spin axis, β_m , and the angle between the spin axis and the line of sight, β_o , according to the following relation

$$\cos \theta = \cos \beta_m \cos \beta_o + \sin \beta_m \sin \beta_o \cos \varphi. \quad (3.9)$$

It is possible to obtain the aspect angles β_m and β_o from the observed pulse profiles, known the angular and energy dependence of the emitted flux. According to the fact that the emission beams have a maximum in a direction perpendicular to the magnetic field lines (“fan beam”) or in a direction parallel to the magnetic field (“pencil beam”), at the same pulse phase we find the minimum or the maximum intensity, respectively. These two cases correspond to two different emission region geometries: in the case of fan beam emission we expect the formation of an accretion

column while in the case of pencil beam emission we expect a slab forms (for a more general review see Orlandini (1988) and reference therein).

The characteristic aspect angles of the neutron star in 4U 1538–52 has been computed by Wang and Welter (1981) utilizing a very simple angular dependence of the emitted flux, by Leahy (1990) and Clark *et al.* (1990) utilizing the angular and energy dependence of the flux given by Meszaros and Nagel (1985). All these authors found that the pulse profiles of 4U 1538–52 are in agreement with a pencil beam emission pattern, with characteristic angles given by

$$\theta_c = \frac{7}{36}\pi \quad \beta_o = \frac{3}{8}\pi \quad \beta_m = \frac{11}{32}\pi$$

where θ_c is the semi-angle subtended by the polar cap, with respect to the center of the neutron star. With these values for some pulse phase the magnetic field direction is pointing toward us, therefore we observe directly the emitting region.

We performed the same Leahy's analysis on our EXOSAT data and achieved the same conclusion, *i.e.* the emission pattern compatible with the EXOSAT pulse profiles of 4U 1538–52 is the pencil beam pattern. Furthermore, other two points agree well with this interpretation: First, the fact that the X-ray luminosity is less than the critical luminosity above which the formation of a radiative shock occurs (Basko and Sunyaev, 1976). For X-ray luminosity above $\sim 10^{37}$ erg/sec, the matter falling onto the polar caps produces a shock just above them. An accretion column forms, which is optically thick, therefore radiation can escape only sideways (fan beam emission pattern). The observed X-ray luminosity of $\mathcal{L}_x \sim 2 \cdot 10^{36}$ erg/sec implies that this shock should not be formed and therefore that X-rays should be emitted mainly in a direction parallel to the magnetic field lines. Another point which agrees with the interpretation that the emission pattern is a pencil beam type is that the rise and fall of the main maximum occur in about the same time. Indeed, if there were an accretion column just above the emitting regions, because of rotation we should observe an asymmetric maximum, with the rise steeper than the fall (Wang and Welter, 1981). This should be due to a deformation of the accretion column because of rotation: this effect is not visible in the light curves of 4U 1538–52.

Assuming that the emission pattern of 4U 1538–52 is a pencil beam, the hardness ratio shown in Fig. 3.12 agrees with this interpretation. Indeed we expect that the hardness ratio is low in the phase intervals A and C, because the emission beams are directed perpendicular to our line of sight and therefore we are observing the most absorbed radiation, because of screening effects due to the magnetospheric layer (Basko and Sunyaev, 1976). On the other hand, in the pulse intervals B and D we expect that the hardness ratio is high because the emission beams are directed toward us, and we are observing deeper in the magnetosphere, where the temperature is higher and radiation less absorbed (for the energy ranges chosen, which are less than the cyclotron energy of ~ 20 keV (Clark *et al.*, 1990), the Thomson scattering cross section is reduced for radiation coming from a pencil beam emission pattern, because the motion of electrons perpendicular to the magnetic field is suppressed (Herold, 1979)).

Bibliography

- Apparao K.M.V., Bradt H.V., Dower R.G., Doxsey R.E., Jernigan J.G., and Li F. 1978. Positions of galactic X-ray sources: $320^\circ < l^{\text{II}} < 340^\circ$. *Nature*, **271**, p.225.
- Basko M.M. and Sunyaev R.A. 1976. The limiting luminosity of accreting neutron stars with magnetic field. *Monthly Notices of R.a.S.*, **175**, p.395.
- Becker R.H., Swank J.H., Boldt E.A., Holt S.S., Pravdo S.H., Saba J.R., and Serlemitsos P.J. 1977. A1540–53, an eclipsing X-ray binary pulsator. *Astrophysical Journal*, **216**, p.L11.
- Belloni T. and Hasinger G. 1990. An atlas of aperiodic variability in HMXB. *Astronomy & Astrophysics*, **230**, p.103.

- Boynton P.E., Deeter J.E., Lamb F.K., Zylstra G., Pravdo S.H., White N.E., Wood K.S., and Yentis D.J. 1984. New evidence on the nature of the neutron star and accretion flow in Vela X-1 from pulse timing observations. *Astrophysical Journal*, **283**, p.L53.
- Brown R.L. and Gould R.J. 1970. Interstellar absorption of cosmic X-rays. *Physical Review*, **D1**, p.2252.
- Clark G.W., Woo J.W., Nagase F., Makishima K., and Sakao T. 1990. Discovery of a cyclotron absorption line in the X-ray spectrum of the binary pulsar 4U 1538-52 observed by *Ginga*. *Astrophysical Journal*, **353**, p.274.
- Cowley A.P., Crampton D., Hutchings J.B., Liller W., and Sanduleak N. 1977. Optical candidates for 3U 1538-52. *Astrophysical Journal*, **218**, p.L3.
- Crampton D., Hutchings J.B., and Cowley A.P. 1978. Optical spectroscopy and system parameters for 4U 1538-52. *Astrophysical Journal*, **255**, p.L63.
- Cusumano G., Robba N.R., Orlandini M., Dal Fiume F., and Frontera F. 1989. X-ray timing and spectral measurements of the X-ray pulsar 4U 1538-52. In *Proc. 23rd ESLAB Symposium on Two Topics in X-ray Astronomy. 1. X-ray Binaries*, page 369. ESA Publications Division, SP-296.
- Davison P.J.N. 1977. A regular pulsation in the X-ray flux from A1540-53. *Monthly Notices of R.a.S.*, **179**, p.35P.
- Davison P.J.N., Watson M.G., and Pye J.P. 1977. The binary X-ray pulsar 3U 1538-52. *Monthly Notices of R.a.S.*, **181**, p.73P.
- Forman W., Jones C., and Tananbaum H. 1976. Uhuru observations of the galactic plane in 1970, 1971 and 1972. *Astrophysical Journal*, **206**, p.L29.
- Frontera F. and Dal Fiume F. 1989. The high-energy properties of X-ray pulsars. In *Proc. 23rd ESLAB Symposium on Two Topics in X-ray Astronomy. 1. X-ray Binaries*, page 57. ESA Publications Division, SP-296.
- Ghosh P. and Lamb F.K. 1979a. Accretion by rotating magnetic neutron stars. II. Radial and vertical structure of the transition zone in disk accretion. *Astrophysical Journal*, **232**, p.259.
- Ghosh P. and Lamb F.K. 1979b. Accretion by rotating magnetic neutron stars. III. Accretion torques and period changes in pulsating X-ray sources. *Astrophysical Journal*, **234**, p.296.
- Henrichs H.F. 1983. Spin-up and spin-down of accreting neutron stars. In *Accretion-Driven Stellar X-ray Sources*, Lewin W.H.G. and van den Heuvel E.P.J., editors. Cambridge University Press, Cambridge.
- Herold H. 1979. Compton and Thomson scattering in strong magnetic fields. *Physical Review*, **D19**, p.2868.
- Ilovaisky S.A., Chevalier C., and Motch C. 1979. Optical light curve of the X-ray binary 4U 1538-52. *Astronomy & Astrophysics*, **71**, p.L17.
- Joss P.C. and Rappaport S.A. 1984. Neutron stars in interacting binary systems. *Annual Review of Astronomy and Astrophysics*, **22**, p.537.
- Kallman T.R. and White N.E. 1982. The anomalous X-ray absorption spectrum of Vela X-1. *Astrophysical Journal*, **261**, p.L35.
- Koyama K. 1989. Tenma observation of diffuse galactic X-ray emission. *Publ. Astron. Soc. Japan*, **41**, p.665.
- Lamb F.K., Pethick C.J., and Pines D. 1973. A model for compact X-ray sources: Accretion by rotating magnetic stars. *Astrophysical Journal*, **184**, p.271.
- Leahy D.A. 1990. X-ray pulsar profile analysis. *Monthly Notices of R.a.S.*, **242**, p.188.
- Lewin W.H.G., van Paradijs J., and van der Klis M. 1988. A review of quasi-periodic oscillations in low-mass X-ray binaries. *Space Science Review*, **46**, p.273.
- Makishima K., Koyama K., Hayakawa S., and Nagase F. 1987. Spectra and pulse period of the binary X-ray pulsar 4U 1538-52. *Astrophysical Journal*, **314**, p.619.

- Meszáros P. and Nagel W. 1985. X-ray pulsar models. II. Comptonized spectra and pulse shapes. *Astrophysical Journal*, **299**, p.138.
- Morrison R. and McCammon D. 1983. Interstellar photoelectric absorption cross sections, 0.03–10 keV. *Astrophysical Journal*, **270**, p.119.
- Nagase F. 1989. Accretion-powered X-ray pulsars. *Publ. Astron. Soc. Japan*, **41**, p.1.
- Nagase F., Hayakawa S., Sato N., Masai K., and Inoue H. 1986. Circumstellar matter in the Vela X-1/HD 77581 system. *Publ. Astron. Soc. Japan*, **38**, p.547.
- Orlandini M. 1988. *Theory and Observations of X-Ray Pulsars in Binary Systems*. Master's thesis, International School for Advanced Studies, Trieste. Unpublished.
- Paczynski B. 1971. Evolutionary processes in close binary systems. *Annual Review of Astronomy and Astrophysics*, **9**, p.183.
- Pakull M., van Amerongen S., Bakker R., and van Paradijs J. 1983. Optical photometry of massive X-ray binaries: 4U 1538-52/QV Nor. *Astronomy & Astrophysics*, **122**, p.79.
- Parkes G.E., Murdin P.G., and Mason K.O. 1978. The optical counterpart of the binary X-ray pulsar 4U 1538-52. *Monthly Notices of R.a.S.*, **184**, p.73P.
- Rappaport S. and Joss P.C. 1977. Accretion torques in X-ray pulsars. *Nature*, **266**, p.683.
- Schwartz D.A., Gursky H., Schwarz J., Bradt H., and Doxsey R. 1978. Location of pulsating binary X-ray source 4U 1538-52 with the HEAO-1 SMC. *Nature*, **275**, p.517.
- Stella L., White N.E., and Rosner R. 1986. Intermittent stellar wind accretion and long-term activity of population I binary systems. *Astrophysical Journal*, **308**, p.669.
- Tennant A.F. 1987. Power spectra, with application to EXOSAT data. *Monthly Notices of R.a.S.*, **226**, p.963.
- van der Klis M. 1989. Quasi-periodic oscillations and noise in low-mass X-ray binaries. *Annual Review of Astronomy and Astrophysics*, **27**, p.517.
- Wang Y.M. 1981. Spin-reversed accretion as the cause of intermittent spin-down in slow X-ray pulsars. *Astronomy & Astrophysics*, **102**, p.36.
- Wang Y.M. and Welter G.L. 1981. An analysis of the pulse profiles of binary X-ray pulsars. *Astronomy & Astrophysics*, **102**, p.97.
- Warwick R.S., Turner M.J.L., Watson M.G., and Willingale R. 1985. The galactic ridge observed by EXOSAT. *Nature*, **317**, p.218.
- White N.E., Swank J.H., and Holt S.S. 1983. Accretion powered X-ray pulsars. *Astrophysical Journal*, **270**, p.711.

4 The X-ray Pulsar GX 301-2

We devote this Chapter to the presentation of results obtained from a temporal analysis of ten ME EXOSAT observations of the X-ray binary pulsar GX 301-2. The journal of all the observations is shown in Table 4.1, while in Fig. 4.1 the binary system GX 301-2 is shown in scale, with depicted the EXOSAT observations. For our analysis we used only the data from the Argon cells of the ME array (see Chapter 2 for a technical description of the Medium Energy experiment on board EXOSAT). As in the previous Chapter on 4U 1538-52, we will start with the presentation of the observed physical properties of the binary system GX 301-2/Wray 977. Then we will enter into the description of the timing analysis performed on both the coherent and aperiodic part of the X-ray emission coming from GX 301-2. We find that the pulse period history we recovered from the EXOSAT data is that of a typical wind-fed pulsar, showing a random behaviour of spin-ups and spin-downs imposed on a secular spin-up trend. The fitting analysis of Power Spectrum Density (PSD) estimates indicates that the rms's are in agreement with those observed in other massive X-ray pulsators, as Vela X-1 (Belloni and Hasinger, 1990). We find a linear correlation between rms and the accretion time scale \dot{P}_p/P_p .

4.1 Physical Properties

The X-ray pulsar GX 301-2 (4U 1223-62) is located at celestial coordinates (1950) $\alpha = 12^h 23^m 49^s$; $\delta = -62^\circ 29' 37''$ (Dower *et al.*, 1978). It was discovered as an X-ray source by a balloon experiment in 1969 (Lewin *et al.*, 1971; McClintock *et al.*, 1971) and it was clearly identified as an X-ray source by *Uhuru* (Forman *et al.*, 1976). Its pulsed emission was discovered by Experiment C on board *Ariel 5* (White *et al.*, 1976). Its binary nature was shown by a Doppler modulation in the X-ray pulse arrival times (White *et al.*, 1978; Swank *et al.*, 1976). The optical counterpart of GX 301-2 was identified with the supergiant Wray 977, of spectral class B2 Iae (Vidal, 1973; Jones *et al.*, 1974; Parkes *et al.*, 1980). The presence of intense P-Cygni profiles in the Hydrogen Balmer line series of Wray 977 (Parkes *et al.*, 1980; Hutchings *et al.*, 1982) clearly indicates the presence of an intense stellar wind, suggesting that the mass loss rate from the supergiant is greater than $3 \cdot 10^{-6} M_\odot/\text{yr}$. From spectroscopic analysis is not easy to extract unique orbital parameters (Hutchings *et al.*, 1982). From the analysis of the X-ray emission the determination was not easy, too. In fact, the orbital period had a different value according to the way in which it was evaluated: from the observation of X-ray pulse arrival times, P_o was found 40.8 days (White *et al.*, 1978) or 35 days (Kelley *et al.*, 1980); from X-ray photometry (*i.e.* recurrence of X-ray flaring episodes) it was found to be 41.5 days (Watson *et al.*, 1982; White and Swank, 1984) and confirmed by Friedhorsky and Teller (1983), and Mitani *et al.* (1984). By joining X-ray observations taken by different satellites, Sato *et al.* (1986) improved the precision of the orbital period, obtaining the value of $P_o = 41.508 \pm 0.007$ days, which is in agreement with that found by the Japanese X-ray satellite

# Obs	Obs ID	Date	Start Time (U.T.)	Duration (sec)	Orbital Phase
1	83/231	19 August 1983	22 ^h 19 ^m	26,400	0.013-0.021
2	84/111	20 April 1984	20 ^h 57 ^m	19,000	0.916-0.922
3	84/113	22 April 1984	17 ^h 20 ^m	7,300	0.962-0.964
4	84/115	24 April 1984	19 ^h 18 ^m	9,500	0.011-0.014
5	84/153	2 June 1984	20 ^h 01 ^m	6,500	0.927-0.929
6	84/159	8 June 1984	18 ^h 59 ^m	4,600	0.071-0.072
7	85/038	7 February 1985	17 ^h 00 ^m	92,100	0.971-0.996
8	85/047	16 February 1985	23 ^h 26 ^m	46,000	0.194-0.207
9	85/050	19 February 1985	16 ^h 18 ^m	86,300	0.259-0.283
10	85/070	11 March 1985	02 ^h 33 ^m	46,800	0.726-0.739

Table 4.1: Journal of the ten ME EXOSAT observations of GX 301-2. The observation durations are referred to the run lengths on which the analysis has been really performed and not to the real duration of the observation, which includes manoeuvres and on flight tests. The orbital phase is referred to the orbital period of $P_o = 45.508$ days given by Sato *et al.* (1986). The first GX 301-2 observation listed here, *i.e.* 83/231, is contaminated by the fact that the angle between the pointed source and the Sun was less than 90° . While this should give problems for what concerns spectral measurements, it should not give for timing measurements (see Fig. 4.3).

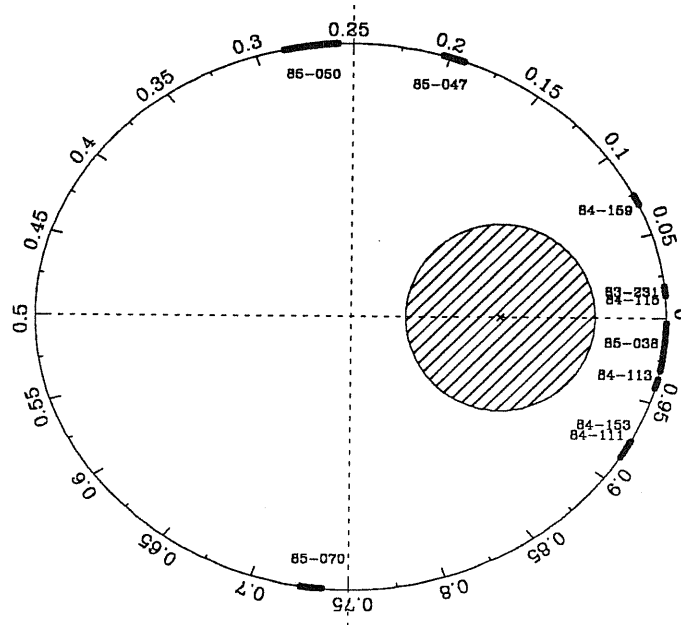


Figure 4.1: Portrait of the GX 301-2/Wray 977 binary system with all the ten ME EXOSAT observations analysed in this Thesis. The system is shown in scale, with the orbital parameters given by Sato *et al.* (1986). The observations are shown with their *real* lengths, comprising manoeuvres and on flight tests.

Parameter	Value	Parameter	Value
$A \equiv a_x \sin i$	$371.2 \pm 3.3 \text{ lt-sec}$	$f(M)$	$31.9 \pm 0.8 \text{ M}_\odot$
M_\star	$30 \pm 5 \text{ M}_\odot$	R_\star	$\approx 40 \text{ R}_\odot$
$q \equiv M_x/M_\star$	$0.03\text{--}0.07$	Eccentricity	0.472 ± 0.011
P_o	$41.508 \pm 0.007 \text{ days}$	d	$1.8 \pm 0.4 \text{ kpc}$

Table 4.2: Orbital parameters of GX 301-2, as obtained by joining the X-ray observations carried out by *Ariel 5*, *SAS 3* and *Hakucho* (Sato *et al.*, 1986). All values are from Sato *et al.* (1986) but M_\star , R_\star , d (Parkes *et al.*, 1980), and q (Hutchings *et al.*, 1982).

Hakucho, $P_o = 41.524 \pm 0.006 \text{ days}$ (Kawai *et al.*, 1985).

The orbital parameters are shown in Table 4.2, as obtained by joining X-ray data from *Ariel 5* (White *et al.*, 1978), *SAS 3* (Kelley *et al.*, 1980) and *Hakucho* (Kawai *et al.*, 1985; Sato *et al.*, 1986).

From spectroscopic measurements the mass of Wray 977 is $M_\star = 30 \pm 5 \text{ M}_\odot$, while from the observed value of the mass function we obtain a lower limit of 30.3 M_\odot . The fact that we do not observe any X-ray eclipse gives a constraint on the inclination angle, which must be $i \lesssim 78^\circ$. Therefore the most plausible value of the Wray 977 mass is $M_\star \approx 38 \text{ M}_\odot$ and $i \approx 75^\circ$ (Sato *et al.*, 1986). Although the orbital parameters of the GX 301-2/Wray 977 system are a bit uncertain, we can surely affirm that GX 301-2 is a wind-fed X-ray binary system, because the typical radius of a supergiant, of the order of 30 R_\odot (Allen, 1973), is always much smaller than R_{R1} (see Eq. 3.2).

GX 301-2 presents the most eccentric orbit among the class of X-ray binary pulsars, and this leads to a variation of the X-ray luminosity with respect to the orbital phase. In particular an X-ray flaring periodicity of about 41 days was discovered (Watson *et al.*, 1982; Friedhorsky and Terrel, 1983), which was the crucial proof for the identification of the true orbital period. As observed by numerous authors (White and Swank, 1984; Sato *et al.*, 1986; Rothschild and Soong, 1987), the maximum of the X-ray intensity does not correspond to the minimum distance of the neutron star to Wray 977 (periastron), but is anticipated a bit more than a day. This behaviour can be explained, at least qualitatively, if we assume the presence of an envelope elongated in the equatorial plane of the Be star Wray 977 (Shibazaki, 1982) (these discs are very common in Be stars, because of the strong rotation of this class of objects, which causes the flattening of the atmosphere (Underhill and Doazan, 1982)). In this case we will have that the maximum of the X-ray emission will occur when the X-ray source passes through the Be disc (see Fig. 4.2), and if this disc is tilted of a small angle with respect to the orbital plane, the pulsar will be able to cross the disk twice (this model was proposed to explain the flaring behaviour of 4U 1907+09 (Makishima *et al.*, 1984) and the anomalous high mass loss rate required for explaining the X-ray emission from 4U 0352+30 (White *et al.*, 1982)). In the case of large eccentricities, as for GX 301-2, the second crossing will lie far beyond the envelope radius and therefore the increase of X-ray luminosity due to the enhancement of the accretion rate will be insignificant with respect to the first one. It is important to stress that these flares may give rise to peak luminosities in excess with respect to that predicted by the standard wind accretion theory, because the accretion occurs from envelope matter.

From the time of anticipation of the maximum intensity we can extract an order of magnitude of the extent of the equatorial envelope of the Be star. In the case in which the disc plane coincides with the orbital plane (if not, this introduces an error of the order of $\cos \theta \approx 1 - \theta^2/2$, where θ is

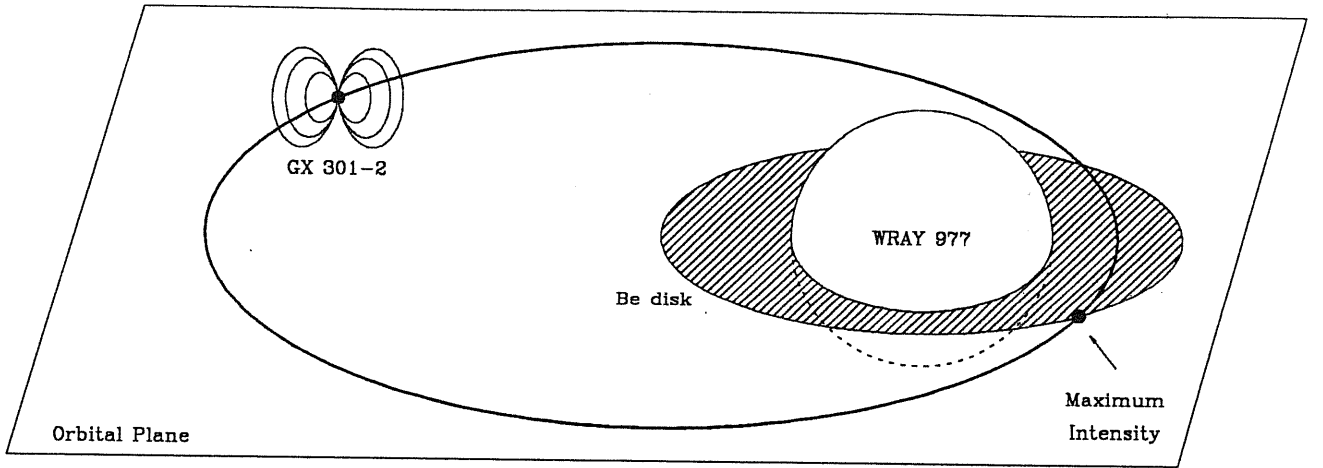


Figure 4.2: Picture of a possible explanation of the observed anticipation of the maximum in the X-ray emission from GX 301-2 with respect to the periastron passage. The Be disc plane in this case coincide with the orbital plane, so the X-ray burst will occur at the crossing of GX 301-2 through the equatorial envelope of WRay 977. In case of tilted disc and great eccentric orbit, the second crossing will not give rise to an enhancement of the X-ray luminosity.

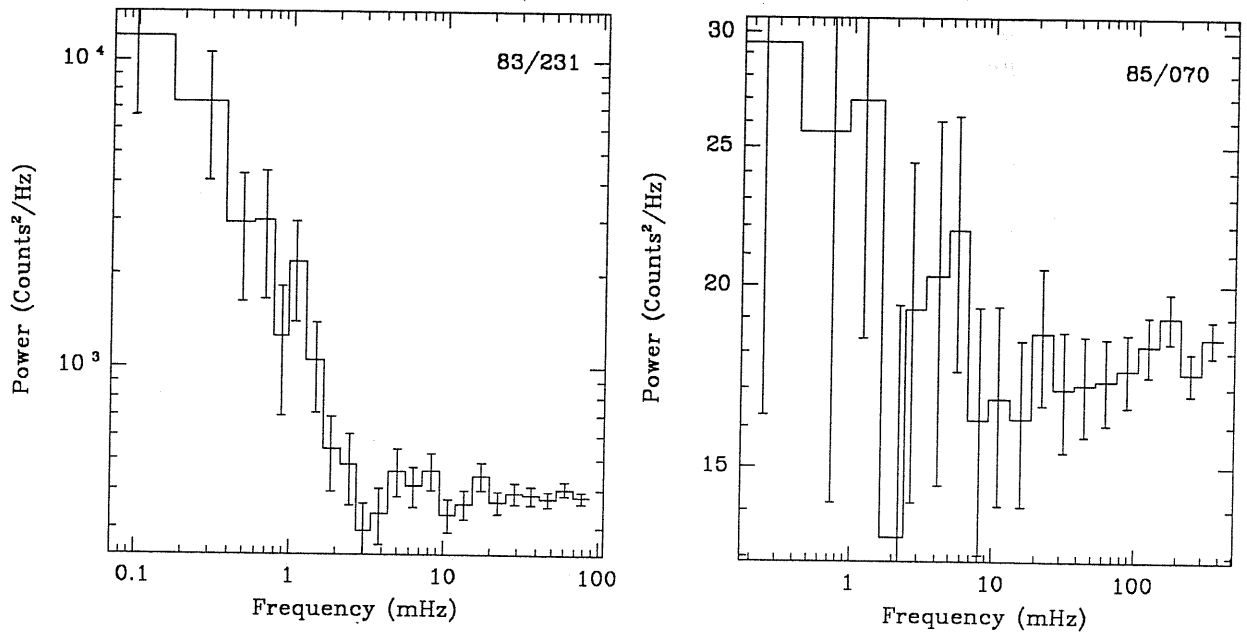


Figure 4.3: PSDs performed on the background of the 83/231 (left) and 85/070 (right) observations of GX 301-2. As we can see, in the former a time scale is present, probably due to the presence of some spurious flux from the Sun (the angle between the source and the Sun was less than 90°). On the other hand, in the 85/070 observation the spectrum was consistently flat, not showing any characteristic time scale.

the angle between the disk plane and the orbital plane), we have that R_{disk} will be

$$R_{\text{disk}} \approx \frac{a(1 - e^2)}{1 - e \cos \varphi_{\text{fla}}}$$

where e is the eccentricity of the orbit, φ_{fla} is the orbital phase (in units of 2π !!!) of the maximum of the X-ray luminosity, measured anticlockwise from the periastron passage and a is the semi amplitude of the orbital ellipse (of the order of half the binary separation). Inserting the observed values of a , e (see Table 4.2) and $\varphi_{\text{fla}} \approx 33\pi/17$ (Rothschild and Soong, 1987) we obtain

$$R_{\text{disk}} \approx 0.69a \approx 55 \sin i R_{\odot}$$

where i is the inclination angle. This value has to be compared with the radius of the Be star, which is of the order of $40 R_{\odot}$ (Parkes *et al.*, 1980).

4.2 Timing Analysis

Due to the very high number of observations, in this Chapter we will not show all the light curves and the pulse profiles for each observation (they are shown in Appendix A); instead we will show only the most characteristic ones. With respect to the observations performed on 4U 1538–52, in which the source was pointed always by the same ME half detector (see Chapter 2 for details on the ME array on board EXOSAT), in some observations GX 301–2 was observed alternatively by the two ME halves, allowing a better determination of the background level (as discussed in Chapter 2, the two ME halves had different responses and therefore different background levels). This technique was called “swapping” and we will refer to the manoeuvre which inverts the half pointing the source as “swap”.

The background level for each observation was carefully checked for the presence of spurious noise. In Fig. 4.3 two PSDs performed on background counting rate taken during 83/231 and 85/070 GX 301–2 observations are shown. As it is easy to note, the first observation shows some characteristic time scale in the X-ray background while the second does not. This is due to the fact that the 83/231 observation was performed with the angle between GX 301–2 and the Sun less than 90° . This has probably inserted some spurious emission from the Sun in the ME array, leading to the not flat spectrum. In discussing results obtained for this observation, attention must be paid.

4.2.1 Analysis of the Coherent Emission

As we can see from Table 4.1 and better from Fig. 4.1, the orbit of the X-ray binary pulsar GX 301–2 was sampled by EXOSAT four times. The first time the GX 301–2 orbit was observed in 1983 and it was covered just at the periastron passage; the second time it was observed in 1984 just before the periastron passage (observations 84/111 and 84/113); the third time it was observed in 1984 before and after the periastron passage (observations 84/153 and 84/159) finally, the fourth time the orbit was explored in 1985 by means of four very long continuous observations¹. As it was discussed by Rothschild and Soong (1987), the X-ray intensity of GX 301–2 shows modulation with the orbital phase. In particular, also for the EXOSAT observations we can divide the binary orbit of GX 301–2 in three roughly portions, according to the X-ray intensity (see Table 4.3 and Fig. 4.4):

¹There is another observation (ID 85/058), that was not analysed here, lasting about 160,000 sec, from orbital phase $\varphi_{\text{orb}} = 0.428$ to $\varphi_{\text{orb}} = 0.464$. This same observation was analysed by Belloni and Hasinger (1990) to extract information on the aperiodic component of the X-ray emission.

Obs ID	$\langle\varphi_{\text{orb}}\rangle$	Mid-Epoch (MJD80)	1-10 keV $\langle I \rangle$ (Counts/sec)
83/231	0.017	1527.1	70.4 ± 0.8
84/111	0.919	1572.1	50.9 ± 0.6
84/113	0.963	1573.9	46.3 ± 0.9
84/115	0.013	1576.0	21.6 ± 0.6
84/153	0.928	1613.9	56.1 ± 1.1
84/159	0.071	1619.9	8.0 ± 0.5
85/038	0.983	1865.3	126.3 ± 1.2
85/047	0.200	1873.3	3.8 ± 0.1
85/050	0.271	1877.3	8.2 ± 0.1
85/070	0.732	1896.4	18.2 ± 0.2

Table 4.3: Orbital phases (computed by means of the ephemeris given by Sato *et al.* (1986)) and mean intensities (computed in the energy interval 1–10 keV, corresponding to ME PHA channels 4–37) for the ten EXOSAT observations of GX 301-2. The averaged intensities are in agreement with the orbital modulation found by *HEAO 1* (Rothschild and Soong, 1987).

- A region “just before” the periastron passage, in which the X-ray intensity is very high (in observation 85/038 the 1–10 keV (corresponding to ME PHA channels 4–37) mean intensity was about 126 Counts/sec, with a peak intensity of about 171 Counts/sec).
- A region “soon after” the periastron passage, in which the X-ray intensity is very low (in observation 85/047 the mean intensity of GX 301-2 was 3.8 Counts/sec).
- The “rest” of the orbit, in which the X-ray intensity is about 20 Counts/sec.

Because we have not a complete sample of the GX 301-2 orbit, as it was the case for *HEAO 1* observations (Rothschild and Soong, 1987), we are not able to give precise orbital positions of these regions. Anyway, our measurements are in agreement with those given by Rothschild and Soong (1987) (see Fig. 4.4), *i.e.* the luminous region seems to be centered at orbital phase $\varphi_{\text{orb}} \approx 0.98$ (observation 85/038), while the low luminosity region lasts at least up to orbital phase $\varphi_{\text{orb}} = 0.28$ (observation 85/050).

In Fig. 4.5 we show the 1–10 keV background subtracted light curve relative to the most intense ME EXOSAT observation of GX 301-2. The single pulses are well visible, with their characteristic double peak structure. The source was highly variable, with a violent flaring episode in the center of the observation (see Fig. 4.6 in which data were rebinned at the pulse period). Note the ingress and egress of the source in the field of view of the ME detectors at the begin and at the end of the observation, respectively.

To obtain the pulse periods for each of the ME EXOSAT observations we do the following (see, *e.g.* (Marshall and Ricketts, 1980)):

- We computed a Fourier transform on the intensity vs time data set to obtain a first estimate of the pulse period.
- The data set was then folded modulo a series of trial periods around the period estimated from Fourier analysis, with step δP_p . For each trial period a χ^2 test was applied against the hypothesis of constant intensity (*i.e.* stationary flux). The period which gave the maximum

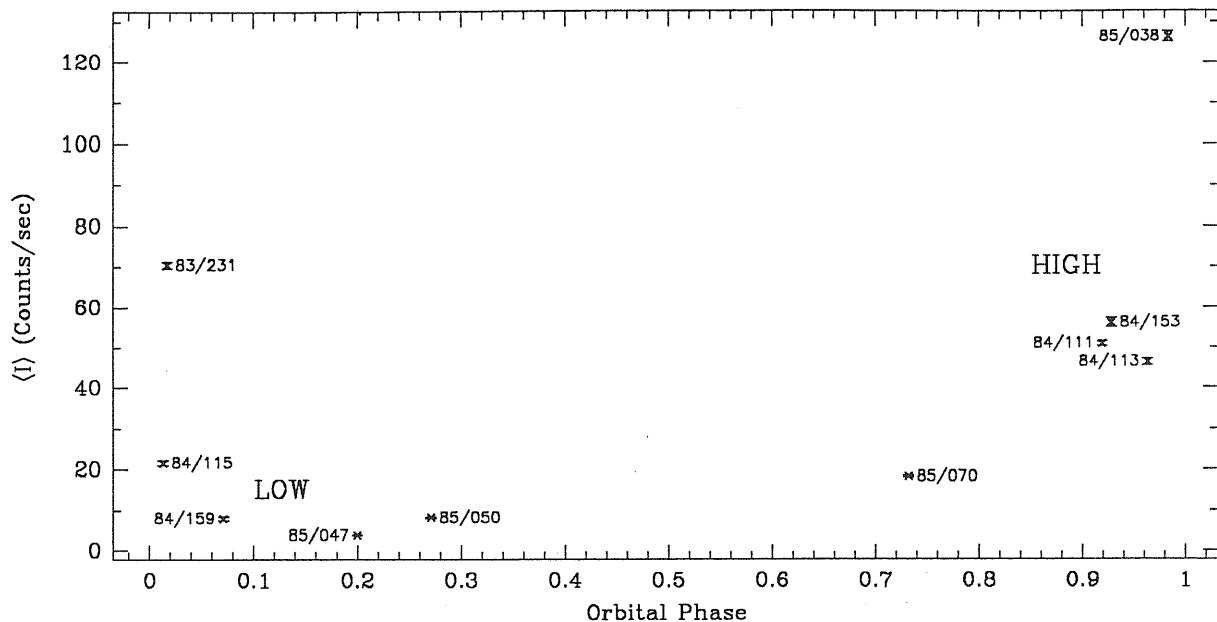


Figure 4.4: The 1–10 keV mean intensity vs orbital phase for the ten ME EXOSAT observations of GX 301–2. As we can see, our data are in agreement with the orbital modulation found by *HEAO 1* (Rothschild and Soong, 1987). The observation 83/231 does not fit with this model and it might be due to an enhancement in the X-ray flux because of the vicinity of the Sun (see text).

value for the χ^2 was then considered as the best value of the periodicity (see Lampton *et al.* (1976) for a discussion on the use of the χ^2 test for testing parametric models).

In Fig. 4.7 we show the χ^2 vs pulse period for the 85/038 observation of GX 301–2. To obtain the centroid of the curve, we fitted a gaussian to the curve shown in Fig. 4.7. The main problem connected with this method of computing pulse periods is that the error associated with the measure is not easily computable (Leahy *et al.*, 1983). We propagated the error in the χ^2 relation, taking into account the fact that the bins are correlated among them. Applying the standard formalism we have that

$$\begin{aligned} \sigma^2 &= \frac{1}{(N_b - 1)^2} \sum_{i=1}^{N_b} \left[\frac{\partial}{\partial x_i} \frac{(x_i - \mu)^2}{x_i} \right]^2 \sigma_{x_i}^2 \\ &= \frac{1}{N_b - 1} \sum_{i=1}^{N_b} \left[1 - \left(\frac{\mu}{x_i} \right)^2 \right]^2 \sigma_{x_i}^2 \end{aligned} \quad (4.1)$$

where x_i is the χ^2 value obtained for each trial period P_i , μ is the mean of the data, N_b is the number of trials and σ_{x_i} is the error associated to each bin.

A method which allows us to determine the error associated to the measurement consists in “marking” some characteristic point of the pulse profile and to record the pulse arrival time associated to these points (normally well identifiable points, as the maximum or the minimum of pulse profiles. As was discussed in Chapter 3, the pulse period of 4U 1538–52 was determined in this way). A least square analysis is then used to determine the best fitting constant pulse period, after having removed trends due to orbital period and corrected the arrival times to the solar system barycentre. The pulse periods obtained from EXOSAT observations by means of the χ^2 method are listed in Table 4.4, while in Table 4.5 are listed the measurements of the GX 301–2 pulse period obtained by other satellites. By “marking” points, we obtained a pulse period relative to the

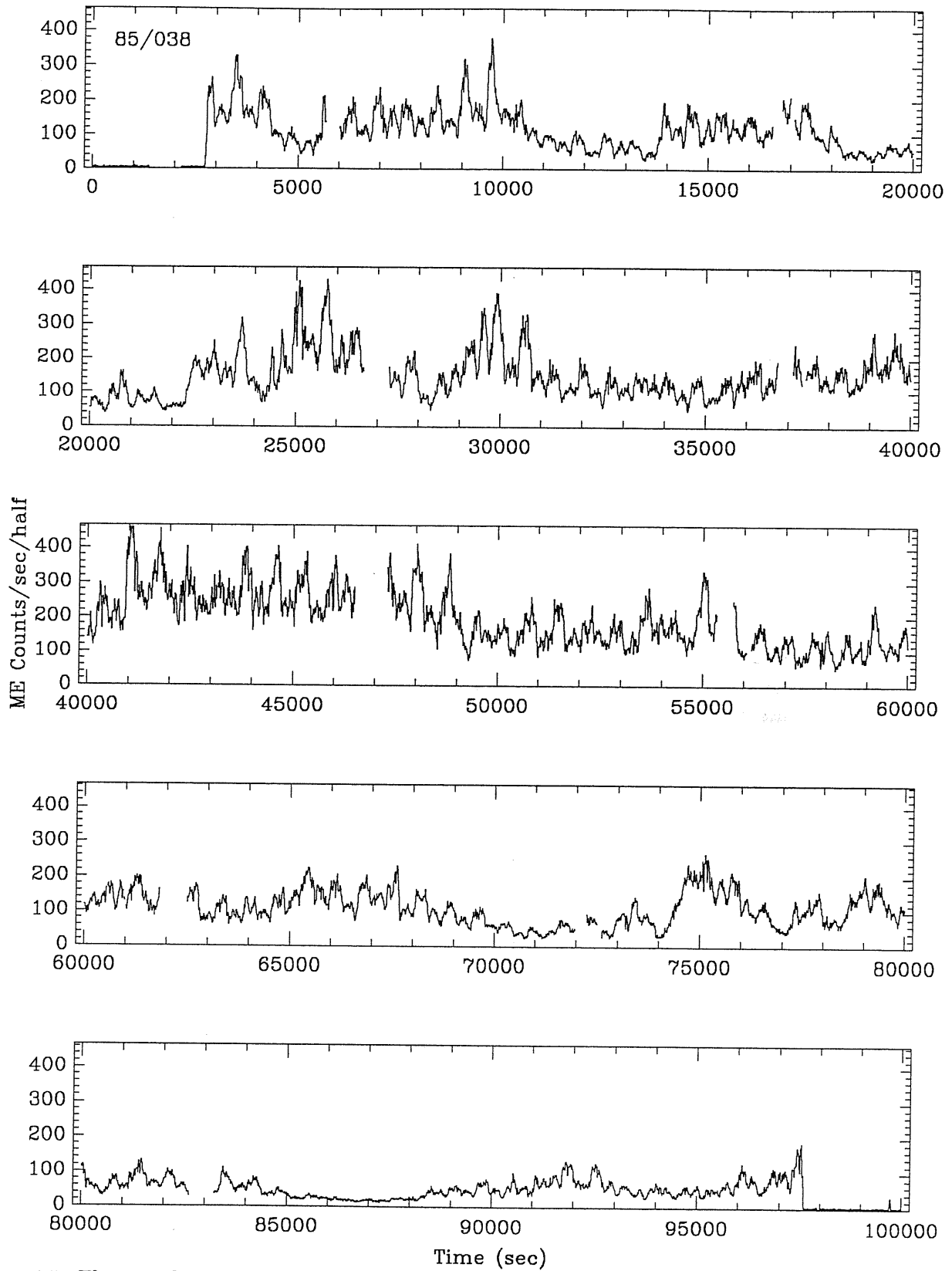


Figure 4.5: The 1-10 keV time averaged background subtracted light curve of the 85/038 observation of GX 301-2. The resolution time is 10 sec.

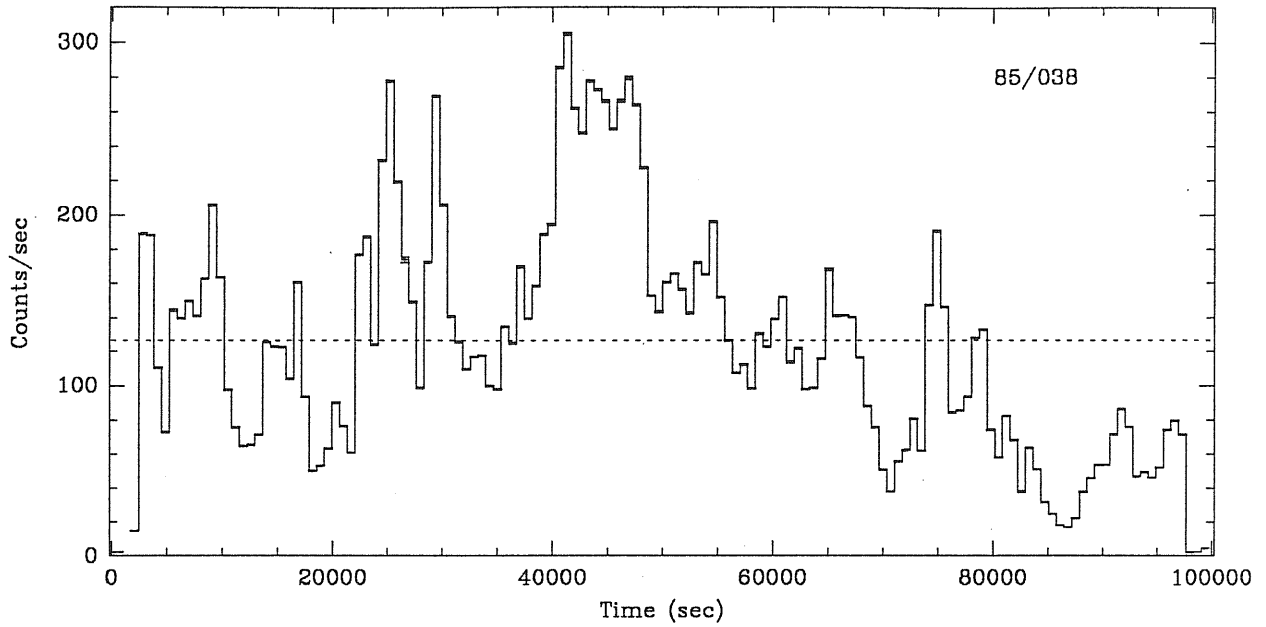


Figure 4.6: The 1–10 keV time averaged background subtracted 700 sec rebinned light curve of the 85/038 GX 301–2 observation. The dashed line corresponds to the mean intensity. Error bars are plotted, too.

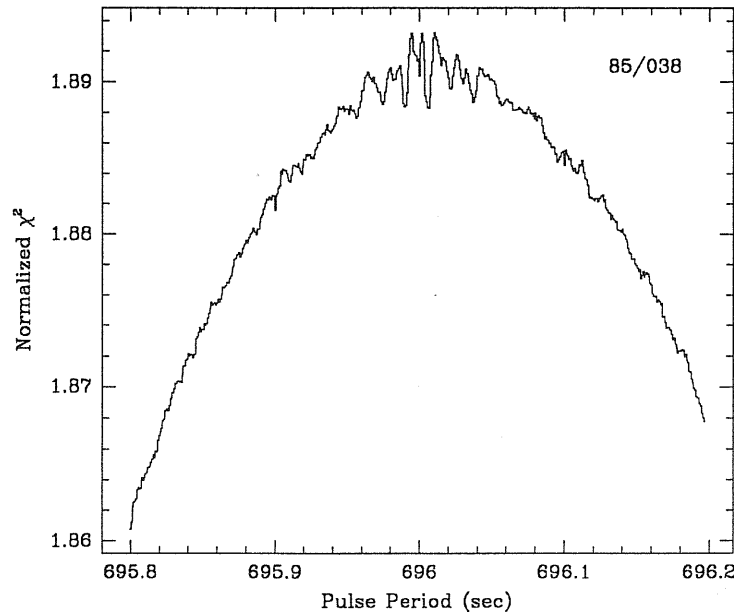


Figure 4.7: χ^2 vs pulse period for the 85/038 EXOSAT observation of GX 301–2. This curve was fitted by a gaussian to obtain the centroid of the curve which, in this case, is $P_p = 696.01$ sec. The χ^2 is normalized to 500 degrees of freedom.

Obs ID	Mid-Epoch (JD - 2,440,000)	P_p (sec)
83/231	5766.6	700.65 ± 0.05
84/111	5811.6	701.53 ± 0.05
84/113	5813.4	701.92 ± 0.06
84/153	5853.4	701.69 ± 0.08
84/159	5859.4	700.98 ± 0.11
85/038	6104.8	696.01 ± 0.02
85/047	6112.8	695.83 ± 0.18
85/050	6116.8	695.93 ± 0.09
85/070	6135.9	695.52 ± 0.05

Table 4.4: ME EXOSAT pulse period measurements of GX 301-2, corrected to the solar system barycentre and for the orbital motion of the source. For observation 84/115 the statistics was too low to allow the determination by means of the χ^2 method.

Date	Mid-Epoch (JD - 2,440,000)	P_p (sec)	Satellite	Reference
Jan 1975	2417.5	700.0 ± 1.3	<i>Ariel 5</i>	(White <i>et al.</i> , 1976)
Jul 1975	2612.7	699.89 ± 0.13	<i>OSO-8</i>	(Swank <i>et al.</i> , 1976)
Jul 1975	2614.9	700.03 ± 0.12	<i>OSO-8</i>	(Swank <i>et al.</i> , 1976)
Jul 1975	2617.5	700.49 ± 0.20	<i>OSO-8</i>	(Swank <i>et al.</i> , 1976)
Dec 1975	2754.5	696.8 ± 1.5	<i>Ariel 5</i>	(White <i>et al.</i> , 1976)
Dec 1975	2762.0	696.45 ± 0.25	<i>SAS 3</i>	(Kelley <i>et al.</i> , 1980)
Jan 1976	2805.3	696.1 ± 0.2	<i>OSO-8</i>	(Swank <i>et al.</i> , 1976)
Jan 1976	2807.5	695.7 ± 0.15	<i>OSO-8</i>	(Swank <i>et al.</i> , 1976)
Jan 1976	2809.5	695.7 ± 0.2	<i>OSO-8</i>	(Swank <i>et al.</i> , 1976)
Feb 1977	3186.0	696.10 ± 0.10	<i>SAS 3</i>	(Kelley <i>et al.</i> , 1980)
Jun 1977	3297.0	696.62 ± 0.15	<i>Ariel 5</i>	(White <i>et al.</i> , 1978)
				(White and Swank, 1984)
Oct 1977	3451.0	696.290 ± 0.017	<i>Ariel 5</i>	(White <i>et al.</i> , 1978)
				(Sato <i>et al.</i> , 1986)
Jan 1978	3535.0	696.35 ± 0.15	<i>SAS 3</i>	(Kelley <i>et al.</i> , 1980)
Jul 1978	3718.0	697.68 ± 0.24	<i>OSO-8</i>	(White and Swank, 1984)
Feb 1979	3906.5	698.220 ± 0.015	<i>SAS 3</i>	(White and Swank, 1984)
				(Sato <i>et al.</i> , 1986)
Apr 1982	5072.5	697.820 ± 0.041	<i>Hakucho</i>	(Kawai <i>et al.</i> , 1985)
				(Sato <i>et al.</i> , 1986)
May 1982	5108.0	698.246 ± 0.043	<i>Hakucho</i>	(Kawai <i>et al.</i> , 1985)
				(Sato <i>et al.</i> , 1986)
Apr 1984	5806.0	701.14 ± 0.03	<i>Tenma</i>	(Sato <i>et al.</i> , 1986)
Dec 1987	7146.0	689.80 ± 0.07	<i>Ginga</i>	(Nagase, 1989)

Table 4.5: Pulse period measurements of GX 301-2 obtained by other satellites than EXOSAT.

Obs	Mid-Epoch (MJD80)	P_p (sec)	$\dot{P}_p _{\text{inst}}$ (sec/sec)	$\dot{P}_p _{\text{inst}}/P_p$ (yr ⁻¹)
83/231	1527.1	700.65	$+4.22 \cdot 10^{-8}$	$+1.90 \cdot 10^{-3}$
84/111	1572.1	701.53	$+2.26 \cdot 10^{-7}$	$+1.02 \cdot 10^{-2}$
84/113	1573.9	701.92	$+2.51 \cdot 10^{-6}$	$+1.13 \cdot 10^{-1}$
84/153	1613.9	701.69	$-6.65 \cdot 10^{-8}$	$-2.99 \cdot 10^{-3}$
85/038	1865.3	696.01	$-2.61 \cdot 10^{-7}$	$-1.18 \cdot 10^{-2}$
85/050	1877.3	695.83	$-7.72 \cdot 10^{-8}$	$-3.50 \cdot 10^{-3}$
85/070	1896.4	695.52	$-2.48 \cdot 10^{-7}$	$-1.13 \cdot 10^{-2}$

Table 4.6: Instantaneous pulse period change rates for the EXOSAT observations of GX 301-2. In computing the values of $\dot{P}_p|_{\text{inst}}$ we averaged between two successive measurements. For the first observation we used the value given by Kawai *et al.* (1985) (see Table 4.5).

84/111–84/113 joined observations of $P_p = 701.25 \pm 0.08$ sec, and a value of $P_p = 700.98 \pm 0.06$ sec for the 84/153–84-159 joined observations.

In Fig. 4.8 the pulse period history of GX 301-2 is shown. The 1983–1984 EXOSAT observations are in agreement with the general trend of spin-up which started at the beginning of 1984 and interrupted a spin-down trend present from 1977. This time behaviour of the pulse period is typical of a wind-fed X-ray binary pulsar (Joss and Rappaport, 1984; Nagase, 1989). The instantaneous rate of pulse period change $\dot{P}_p|_{\text{inst}}$ in the wind-fed X-ray pulsar Vela X-1 has been found to change its sign randomly with time scale of the order of the orbital period (Nagase *et al.*, 1984b; Boynton *et al.*, 1984), while the secular trend of the pulse period may be well described as the superposition of these small random fluctuations. As we have seen in the previous Chapter, the same pulse period behaviour was shown by the X-ray pulsar 4U 1538-52 (Makishima *et al.*, 1987; Cusumano *et al.*, 1989). In Table 4.6 the instantaneous rates of pulse period change are shown for seven EXOSAT observations. These values were evaluated averaging between the available previous pulse period measurements. For the first EXOSAT observation we choose for reference the pulse period reported by Kawai *et al.* (1985) (see Table 4.5). We have used the term “instantaneous” although we performed an average because the observations are very close in time. As we can see, the modulo of $\dot{P}_p|_{\text{inst}}$ change of two orders of magnitude in our sample, ranging from $\approx 7.7 \cdot 10^{-8}$ to $\approx 2.5 \cdot 10^{-6}$ sec/sec.

The most important feature we can notice in the pulse period history of GX 301-2 is the fact that the source seems to alternate periods of general spin-up to periods of spin-down trend, in a sort of “saw-tooth” behaviour (this same behaviour has been observed in another recurrent X-ray pulsar, A0535+26 (Ziolkowski, 1985). See Fig. 4.9). We want to stress that this oscillating behaviour is connected with the *secular* trend of the pulse period, not with the random oscillations which are still present in each “tooth”. The pulse period derivatives for the two spin-up “teeth” are $-1.6 \cdot 10^{-7}$ sec/sec, $-8.4 \cdot 10^{-8}$ sec/sec respectively, while for the spin-down “tooth” is $+2.2 \cdot 10^{-8}$ sec/sec.

From Fig. 4.9 we can see that three characteristic time scales are present:

- a *secular* time scale relative to the secular spin-down trend of the pulse period. This time scale is greater than 10^4 years (Nagase, 1989).
- a *saw-tooth* time scale, of the order of 100–1000 years.

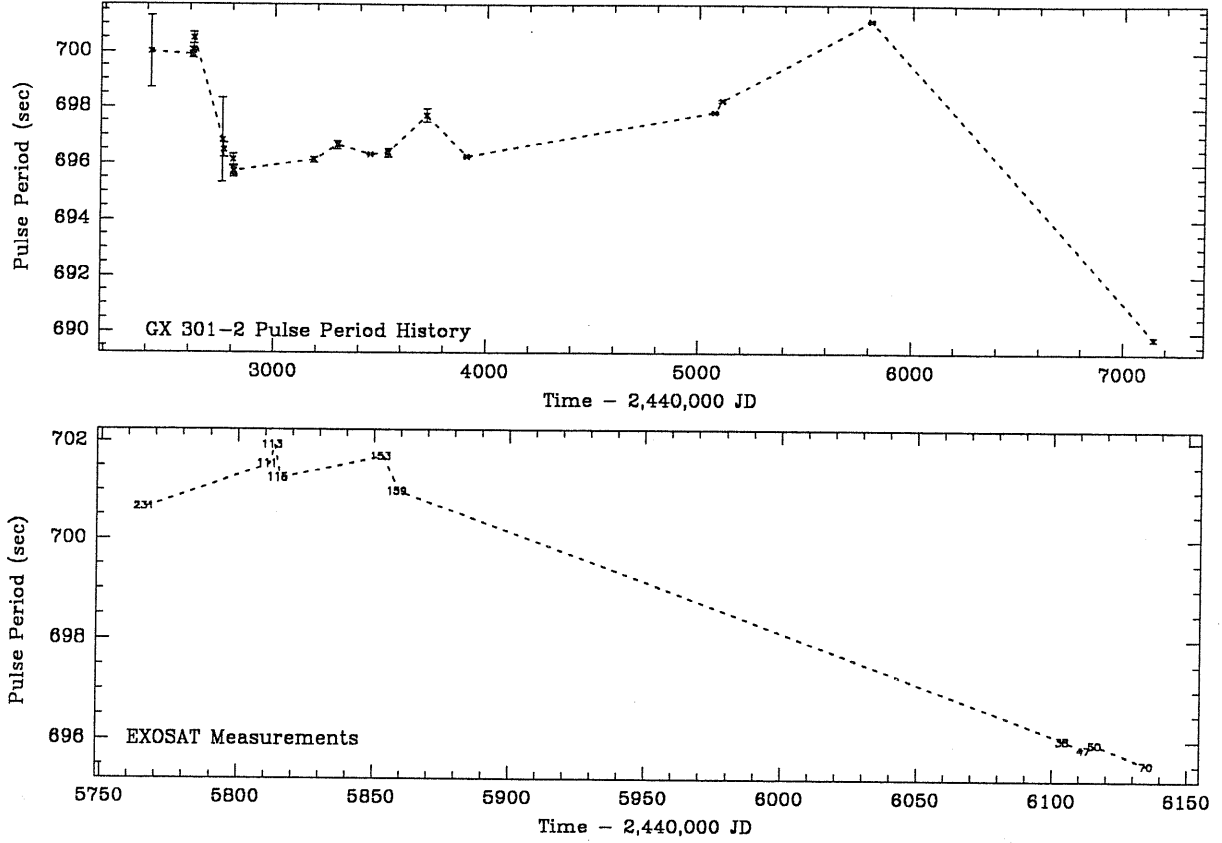


Figure 4.8: Pulse period history of GX 301-2. In the lower plot only the EXOSAT measurements are shown (see Table 4.4), while in the upper plot the measurements taken by other satellites are listed (see Table 4.5).

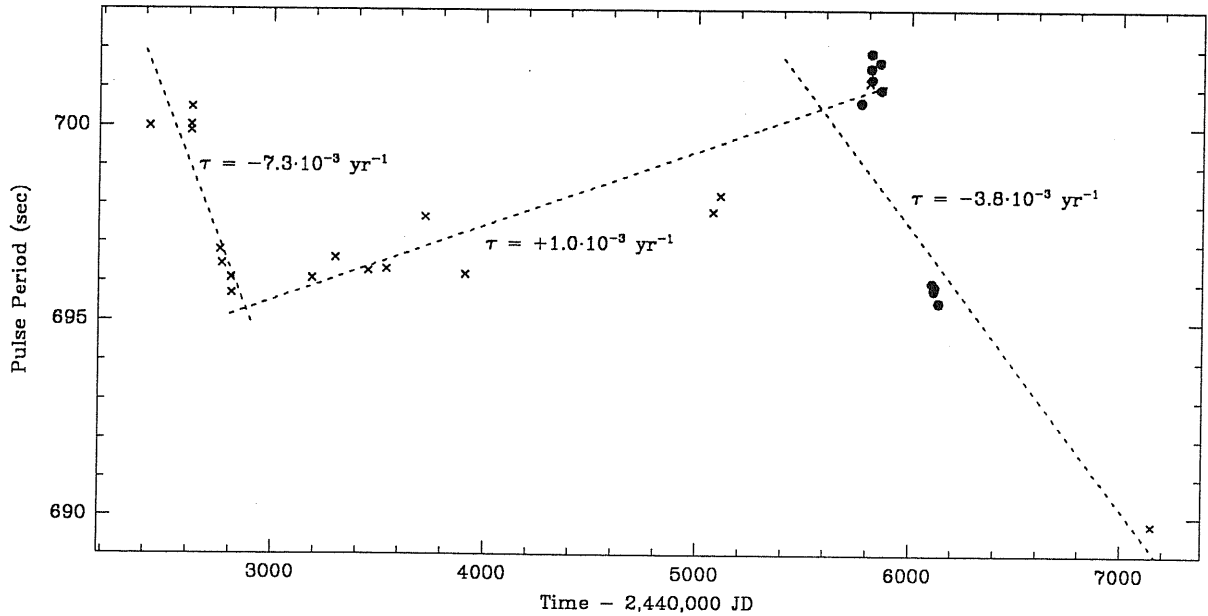


Figure 4.9: "Saw-tooth" behaviour of the pulse period history of GX 301-2. We put together all the data available; with dots EXOSAT data are indicated. The three straight lines are least square fits to the corresponding subset of data. τ is defined as $\dot{P}_p / \langle P_p \rangle$, where $\langle P_p \rangle$ is the mean period in each subset.

- a *random* time scale of the fluctuations². This time scale is of the order of the orbital period (Boynton *et al.*, 1984; Nagase *et al.*, 1984b).

The time averaged background subtracted normalized pulse profiles as a function of energy for two ME EXOSAT observations of GX 301–2 are shown in Fig. 4.10 (observation 85/038) and Fig. 4.11 (observation 85/070). The normalization was performed to allow a better comparison among different profiles (see Chapter 3 for the definition of the normalization). In each energy channel the typical error bar is shown.

The pulse profiles show the characteristic double peak structure, with one peak brighter than the other. The two peaks are π separated. As for the case of 4U 1538–52 (see Section 3.2.1), also for GX 301–2 we notice an energy dependence of the pulse profiles, in the sense that at higher energies the main pulse becomes sharper. A characteristic feature is that at lower energy the maximum of the secondary peak is smaller than at higher energy. Note in Fig. 4.11 the presence at all energies of a sharp peak at the minimum between the main peak and the secondary one.

The shape of the main peak changes from observation to observation. The key changing feature is the number of “horns” present at the top of the main peak, ranging from a minimum of two in observation 85/038 to a maximum of four in observation 85/050 (see Appendix A). The relative strengths and heights of these “horns” change with energy.

For each of the ten ME EXOSAT observations of GX 301–2 we computed the modulation index (see Eq. 3.6 for the definition) and it is shown in Fig. 4.12. As we can see the behaviour of $\Phi(E)$ is different from observation to observation, showing a general increase with energy (observations 84/153, 85/047 and 85/050), a practically independence of energy (observations 84/111, 84/153, 84/159 and 85/038) and a decrease with energy (observations 83/231, 84/113, 84/115 and 85/070). It is worthy of note the presence of a feature in the 5–8 keV band in almost all the observations.

4.2.2 Analysis of the Aperiodic Emission

For each of the ten ME EXOSAT observations listed in Table 4.1 we estimated the Power Spectral Density (PSD) functions of the X-ray intensity data runs to study the aperiodic intensity variability, *i.e.* the variability not associated to the pulsation. As described in the Chapter on 4U 1538–52, to increase the significance of the PSDs we divided our observations in N equal segments³, we computed a PSD function for each of them and we summed the resulting N power spectra (Bendat and Piersol, 1971). Finally, we subtracted the contribution due to the counting statistics (in this respect our procedure differs from that of Leahy *et al.* (1983) (see the discussion made by Lewin *et al.*, 1988) because our PSD normalization is different. See Appendix B). In Fig. 4.13 two PSD functions are shown. In the case of 84/111 (left), we divided the observation in 5 runs 5120 sec each long. The resolution time of these data was 10 sec (with a Nyquist frequency of 0.05 Hz). For 85/038 (right), we divided the observation in 36 runs 2048 sec long. The resolution time of the data was 1 sec (corresponding to a Nyquist frequency of 0.5 Hz). The shape of the power spectrum is that typical of a binary pulsar, showing a steep fall at higher frequency, with almost all the power concentrated in the low frequency part (Boynton *et al.*, 1986; Belloni and Hasinger, 1990). In both the PSDs the peaks due to pulsation are clearly visible.

To investigate the continuum component of the power spectra, the first step is to decouple this part from the part due to the coherent emission. Recalling the discussion made in the Introduction,

²As recently discussed by Livio (1990), a possible explanation of the *random* fluctuations in the pulse period might be connected to the “flip-flop” behaviour found in numerical simulations of accretion flows (see Chapter 5 and reference therein for a review on this subject).

³Particular attention was paid in order that swaps were not present in the segment.

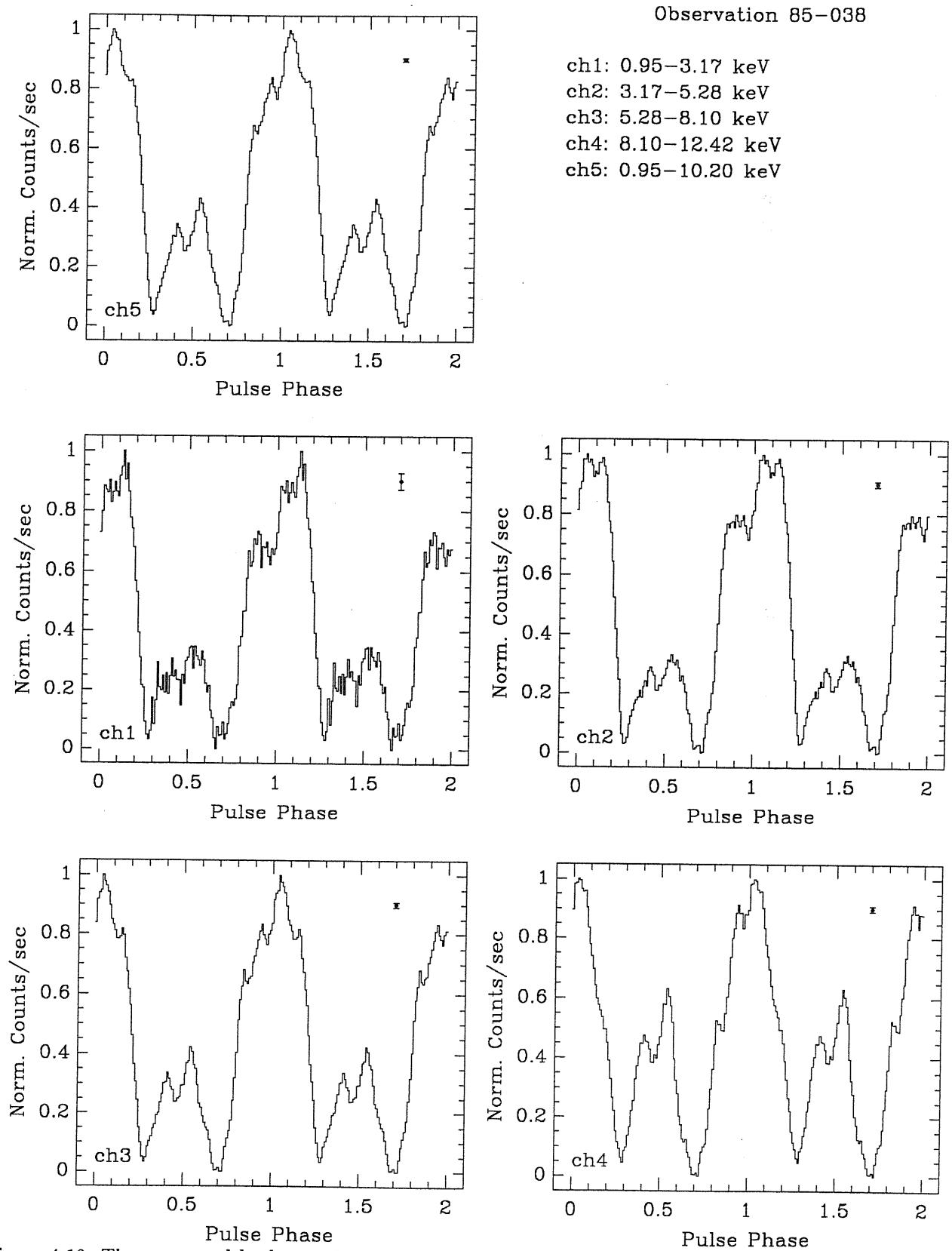


Figure 4.10: Time averaged background subtracted normalized pulse profiles as a function of energy of the 85/038 ME EXOSAT observation of GX 301-2. In each energy channel the typical error bar is shown.

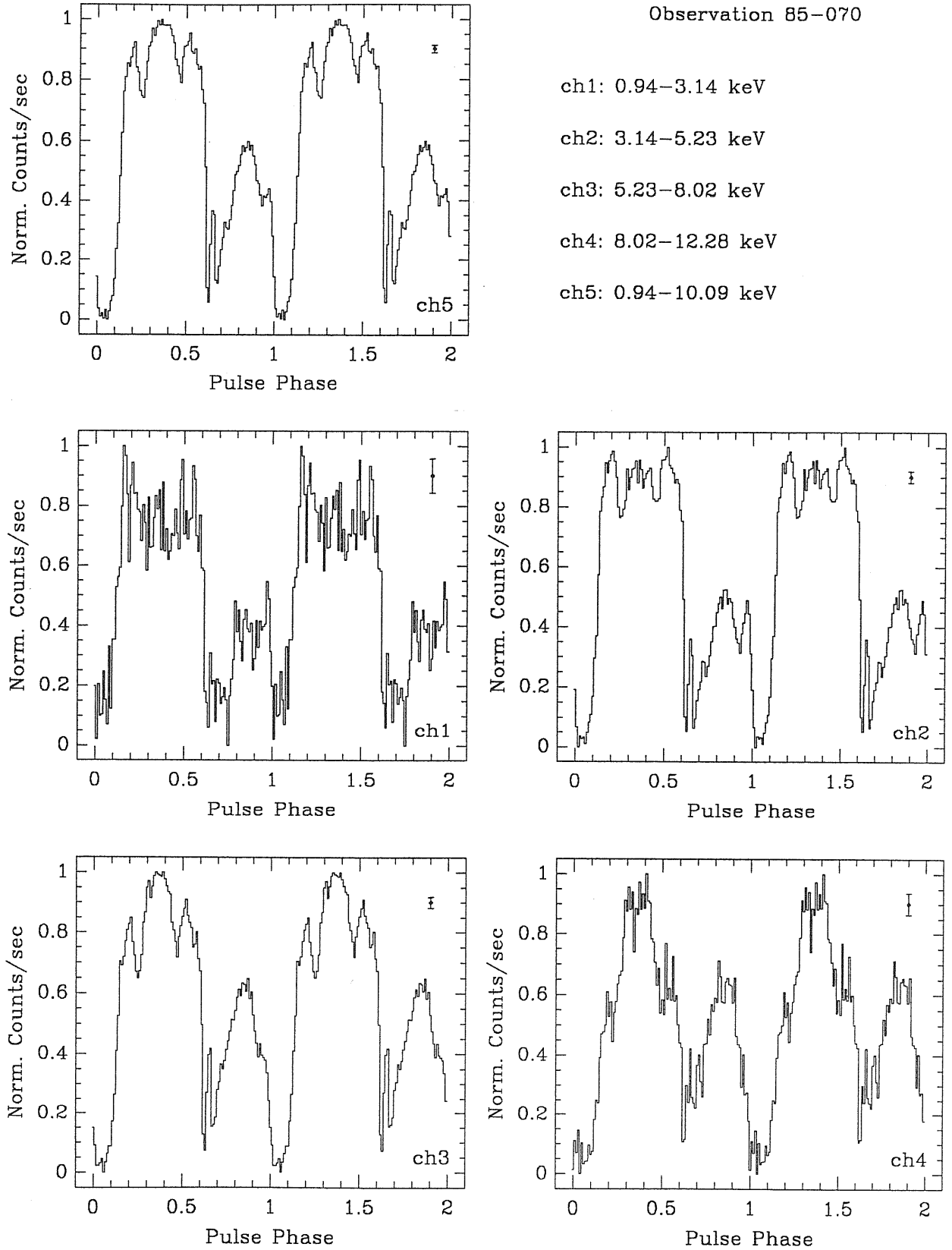


Figure 4.11: Time averaged background subtracted normalized pulse profiles as a function of energy of the 85/070 ME EXOSAT observation of GX 301-2. In each energy channel the typical error bar is shown. Note the feature that appears at all energies in the minimum between the main and the secondary peak.

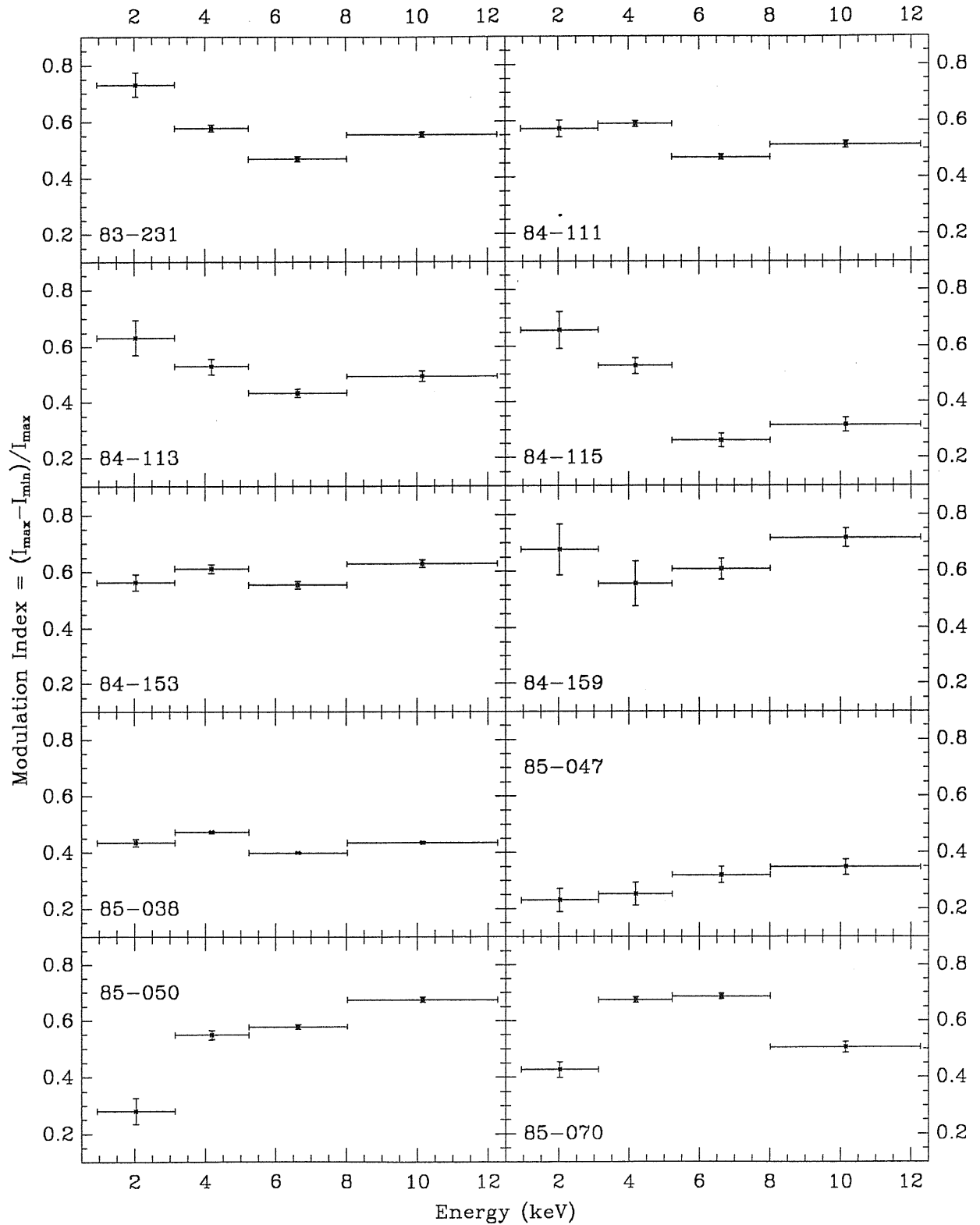


Figure 4.12: Modulation index vs energy for the ten ME EXOSAT observations of GX 301-2. The behaviour is different from observation to observation, showing an increase, a decrease or a independence of energy. Note the feature corresponding to the Iron line.

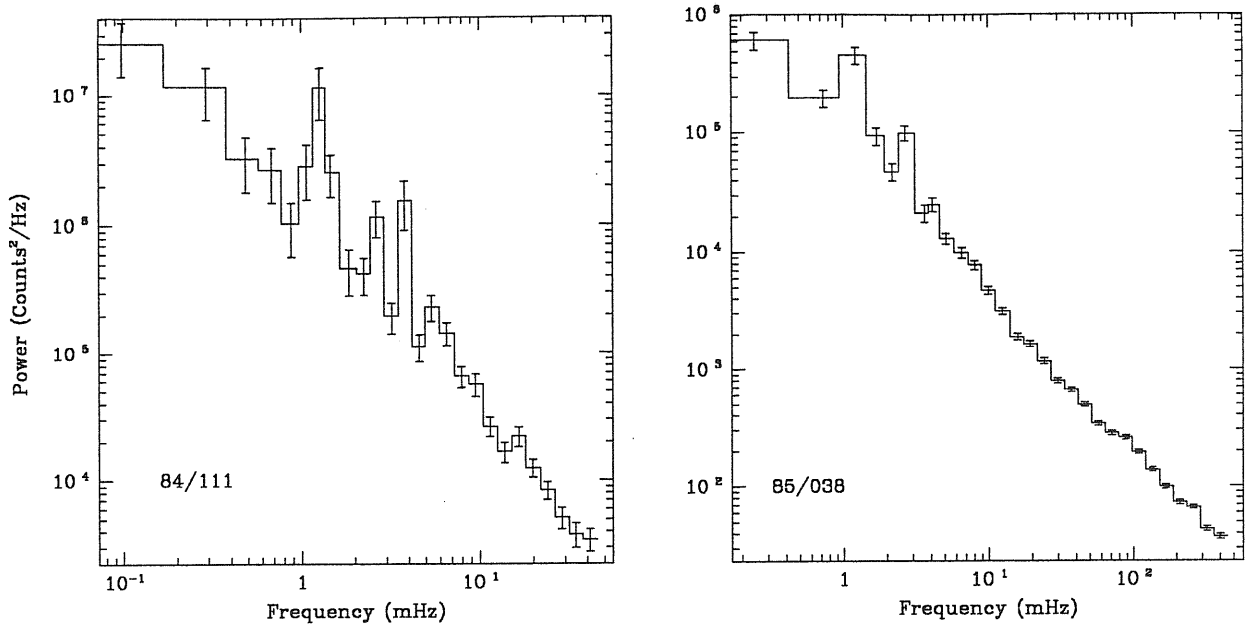


Figure 4.13: PSDs of two ME EXOSAT observations of GX 301-2: 84/111 (left) and 85/038 (right). The resolution time for the two observations was 10 sec for the former and 1 sec for the latter. In both the observations the peaks due to the coherent emission are clearly visible.

we describe a general power spectrum of a pulsar as the sum of three terms:

$$P(f) = \underbrace{C}_{\text{Poissonian}} + \underbrace{kf^{-\alpha}}_{\text{aperiodic}} + \underbrace{\sum_n A_n \delta(f - nf_p)}_{\text{coherent}} \quad (4.2)$$

where k and C (the Poissonian counting) are two constants, f is the frequency, $f_p = 1/P_p$ and A_n are the amplitudes of the fundamental frequency and its harmonics.

We performed a fit to our spectra by means of a fitting program which computed the effect due to the leakage of power in the peaks, integration and sampling of the data, and the finite length of the runs (Bendat and Piersol, 1971). We considered as fixed parameters in the fit the amplitudes A_n and the Poissonian counting C (as in the 4U 1538-52 case, we checked that the value obtained by the fitting program, by assuming C as a free parameter, is in agreement with that computed from the sum of the data counts), while the other parameters were free (see also section 3.2.2). The results of the fits are shown in Table 4.7. An important feature common to the fits to the PSDs of *all* the observations, *independently of the resolution of the data*, was that a change of slope of the power law was present in the frequency range 0.01–0.1 Hz, causing a good fit to all the data difficult (see Fig. 4.14). In fact, the fitting program gave good results with the first part of the spectrum or with the last part of the spectrum, but when the fit was performed on all the data the goodness decreased. The flattening at high frequencies in the spectra, visible in Fig. 4.14 but not in Fig. 4.13 is due to the subtraction of the Poissonian counting in the latter, which was not performed in the former.

We then computed the rms variability (for its definition see Appendix B) associated to the continuum component (Lewin *et al.*, 1988). The results are listed in Table 4.7. As we can see, these measurements are in agreement with those obtained for other high-mass X-ray pulsators (Belloni and Hasinger, 1990).

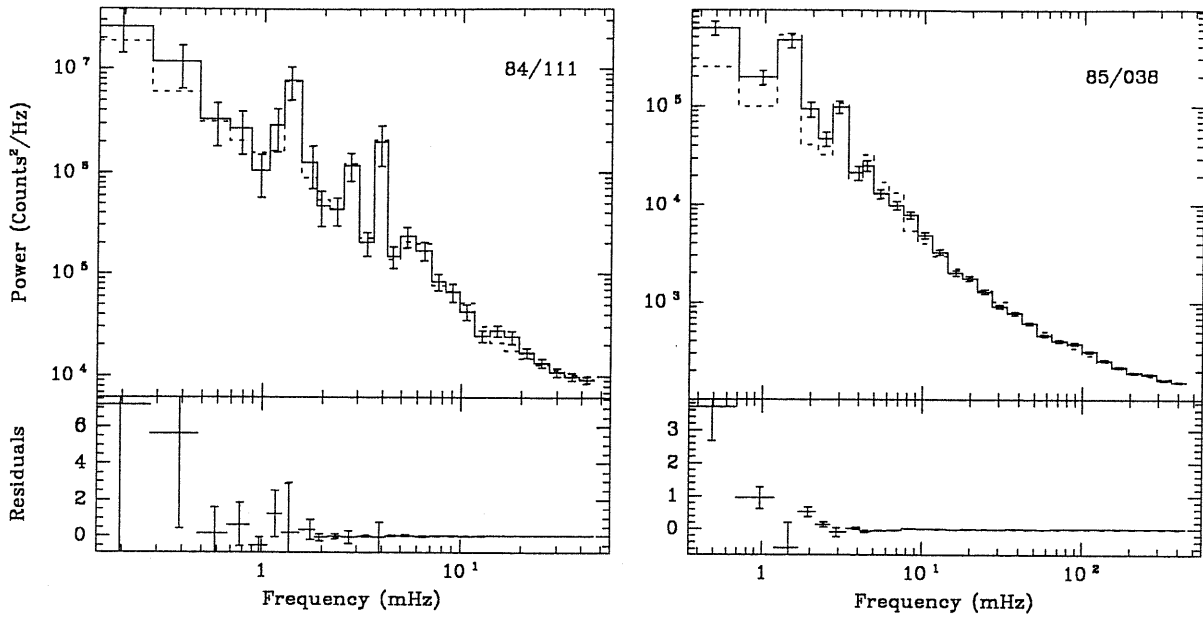


Figure 4.14: Fits to the two power spectra shown in Fig. 4.13. On the bottom the residuals (defined as the difference between the observed (full line) and the fit (dashed line) value in each bin) are shown, in units of 10^6 and 10^5 Counts²/Hz, respectively. In performing the fits the Poissonian component was not subtracted to the power spectra, but it was left as a free parameter (see text).

Obs ID	$\langle\varphi_{\text{orb}}\rangle$	P_p (sec)	$\langle I \rangle$ (Cnt/sec)	Pow.Ind. α	rms (%)	χ^2_{dof}	dof
83/231	0.017	700.65	70.4 ± 0.8	1.56 ± 0.06	30 ± 4	1.11	16
84/111	0.919	701.53	50.9 ± 0.6	1.62 ± 0.08	25 ± 5	0.81	15
84/113	0.963	701.92	46.3 ± 0.9	1.57 ± 0.26	13 ± 6	0.60	19
84/153	0.928	701.69	56.1 ± 1.1	1.23 ± 0.21	13 ± 3	0.89	10
				1.40 ± 0.37	10 ± 6	1.21	15
85/038	0.983	696.01	126.3 ± 1.2	1.33 ± 0.02	22.4 ± 0.6	5.59	21
				1.50 ± 0.04	26 ± 2	4.57	46
85/050	0.271	695.93	8.2 ± 0.1	1.45 ± 0.14	18 ± 5	1.35	14
				1.50 ± 0.12	18 ± 4	1.81	3
85/070	0.732	695.52	18.2 ± 0.2	1.59 ± 0.06	19 ± 2	0.98	5
				1.53 ± 0.06	19 ± 2	1.10	7

Table 4.7: Summary of power spectra fits on the GX 301-2 EXOSAT observations, together with other physical measurements. The fits on the power spectra of observations 84/115, 84/159 and 85/047 do not give good results because the source is faint and the statistics is low.

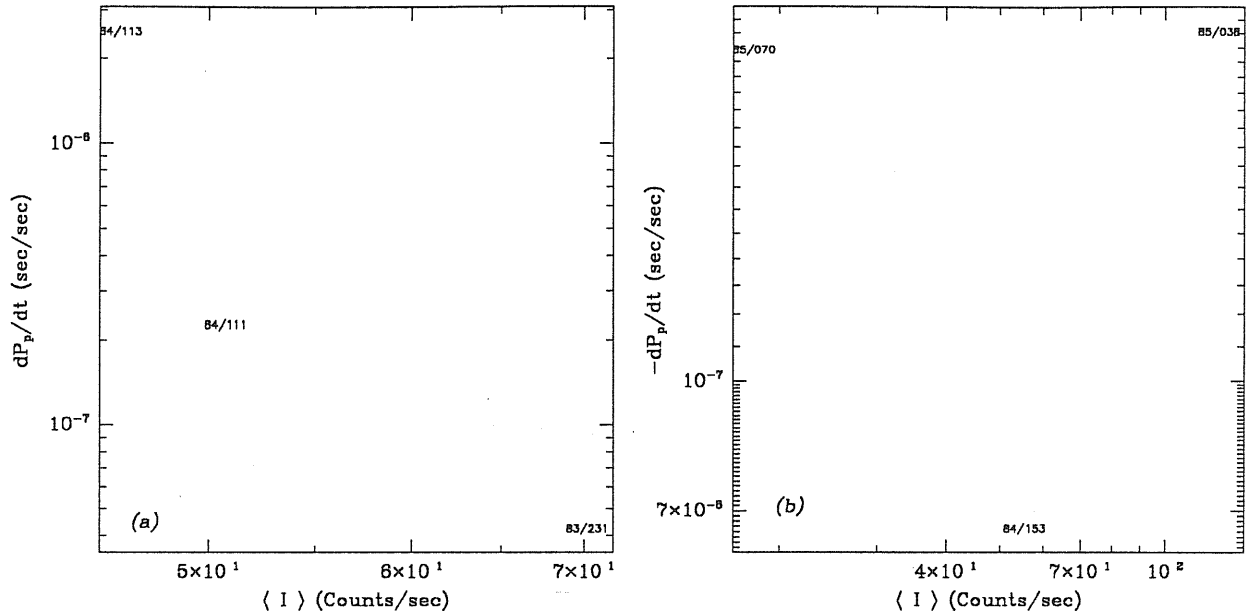


Figure 4.15: Pulse period derivative as a function of the X-ray intensity for the X-ray pulsar GX 301-2. Data are taken from Table 4.6, excluding observation 85/047 because of its low luminosity. On the left panel (a) we plot the pulse period derivative vs $\langle I \rangle$ for the observations for which \dot{P}_p is positive (*i.e.* the source is spinning-down). In the right panel (b) we plot the observations in which GX 301-2 is spinning-up. While in the former case a correlation seem to exist (of the same type of that observed in EXO 2030+375 (Parmar *et al.*, 1989b)), in the latter case this does not occur.

4.3 Discussion

4.3.1 Coherent Timing Measurements

From the physical properties of the binary system GX 301-2/Wray 977 we have argued that the neutron star accretes from the intense stellar wind coming from its supergiant companion. Its pulse period history is in agreement with this hypothesis, showing an alternation of spin-up and spin-down episodes imposed onto a secular spin-up trend (see Fig. 4.8). Furthermore we found a “saw-tooth” behaviour (see Section 4.2.2), with a “saw-tooth” time scale of the order of 10^{-3} – 10^{-2} yr $^{-1}$. We checked whether the pulse period history of GX 301-2 can be modeled by a random walk behaviour in its pulse frequency, with a time scale of the order of the orbital period, as the theory predicts (Boynton *et al.*, 1984; Nagase *et al.*, 1984a). We proceeded as follows: we found the magnitude of a typical pulse period change per step, c (in this case a step is an orbital period, $P_o = 41.508$ days (Sato *et al.*, 1986)); then after N steps we will have a mean rms period change of the order of $c\sqrt{N}$ (Papoulis, 1965). To compute c we assume that the instantaneous rate of pulse period change is given by the observed values $\dot{P}_p|_{\text{inst}}$ (see Table 4.6). Taking the two extreme values for the modulo of $\dot{P}_p|_{\text{inst}}$ we obtain $0.3 < c < 9$ sec. While in the spin-down “tooth” of the pulse period history (see Fig. 4.9) the observations are in agreement with this model (indeed rms $\approx 0.3\sqrt{64} \approx 2.4$ sec) the same does not occur in the two spin-up teeth.

Because of the flaring nature of GX 301-2, we have the possibility to study the variations of the pulse period with respect to a wide intensity range (two order of magnitude). This analysis was performed for another Be/X-ray binary pulsar: EXO 2030+375 (Parmar *et al.*, 1989b; Parmar *et al.*, 1989a). These authors found a relation between the pulse period derivative and the high and intermediate X-ray luminosity of the source, of the form $-\dot{P}_p \propto \mathcal{L}_x^{1.08-1.35}$. We checked the existence of a similar correlation in our GX 301-2 data. In Fig. 4.15 we plotted the pulse period derivative as a function of the mean intensity of the source, dividing the observations according to

the spin-down (Case (a)) or spin-up (Case (b)) state of GX 301-2. Of course, our sample is too small to obtain quantitative information on the correlation, anyway we can see that when the source is spinning-down a correlation between \dot{P}_p and $\dot{\mathcal{L}}_x$ is present. On the other hand, when GX 301-2 is spinning-up this correlation is not present. This is the same behaviour we have found above about the possibility to describe the pulse period history as a random walk in its pulse frequency. In the spin-down “tooth” the variation in the pulse period is in agreement with that predicted by the model of Boynton *et al.* (1984) and Nagase *et al.* (1984a); during the two spin-up “teeth” this does not occur. At this point of the discussion it is necessary to stress that a direct comparison between the pulse period behaviour of GX 301-2 and EXO 2030+375 has to be made with care. Indeed GX 301-2 accretes matter directly from the intense stellar wind coming from Wray 977; on the other hand, EXO 2030+375 is a disk-fed binary system, therefore the specific angular momentum carried by the accreted matter is different (Ghosh and Lamb, 1979a; Ghosh and Lamb, 1979b) and consequently the response of the neutron star to external stresses is different, too (see Eq. 4.3 below).

As we made in the previous Chapter for the X-ray binary 4U 1538-52, also for GX 301-2 we computed the characteristic lengths of accretion (see *e.g.* Henrichs, 1983) :

- Magnetospheric Radius $r_m \simeq 3.6 \cdot 10^8$ cm;
- Accretion Radius $5 \cdot 10^{10} \lesssim r_a \lesssim 5 \cdot 10^{12}$ cm;
- Corotation Radius $r_c \simeq 1.3 \cdot 10^{10}$ cm;

where we have utilized the physical parameters given by Parkes *et al.* (1980) (the supergiant mass and radius, the mass loss rate from Wray 977), the orbital parameters given by Sato *et al.* (1986) (the orbital separation) and we assumed a “standard” neutron star. The main uncertainties are in the measurement of the terminal velocity of the wind (Hutchings *et al.*, 1982), which we take in the range 100–1000 Km/sec (we assume the Castor *et al.* (1973) radial velocity law).

According to Stella *et al.* (1986), the fact that $r_a > r_m$ and $r_c > r_m$ implies that the source is in the regime of *direct wind accretion*. The X-ray luminosity predicted in this regime for GX 301-2 is in the range $4 \cdot 10^{35}$ – $4 \cdot 10^{39}$ erg/sec. This wide range is due to the large uncertainty in the terminal velocity of the wind.

As we have just discussed for 4U 1538-52 (see Section 3.4.1), the accretion time scale is computed from the relation

$$I \dot{\Omega}_p = \dot{M}_x \ell. \quad (4.3)$$

where I is the moment of inertia of the neutron star, Ω_p is the pulse frequency, \dot{M}_x is the accretion rate of matter onto the neutron star and ℓ is the specific angular momentum carried by the accreted matter (see Chapter 5 for a discussion on different expressions). It is important to stress that this relation is valid in the case in which matter does not leave the system GX 301-2/Wray 977 and we neglect viscous forces in the accreting matter. From Eq. 4.3 it follows

$$\tau \equiv \frac{\dot{P}_p}{P_p} = - \frac{\dot{M}_x \ell}{I \Omega_p}. \quad (4.4)$$

Substituting the value of the specific angular momentum carried by the stellar wind (Shapiro and Lighthman, 1976; Wang, 1981)

$$\ell = \frac{1}{2} \eta \Omega_{\text{orb}} r_a^2 \quad (4.5)$$

where η is a parameter, $\eta \lesssim 1$, whose expressions are given in Chapter 5, we obtain

$$\tau = - \left(\frac{\eta}{8} \right) \frac{1}{I} \left(\frac{r_a^4}{D^2} \right) \left(\frac{P_p}{P_{\text{orb}}} \right) \dot{M}_* \quad (4.6)$$

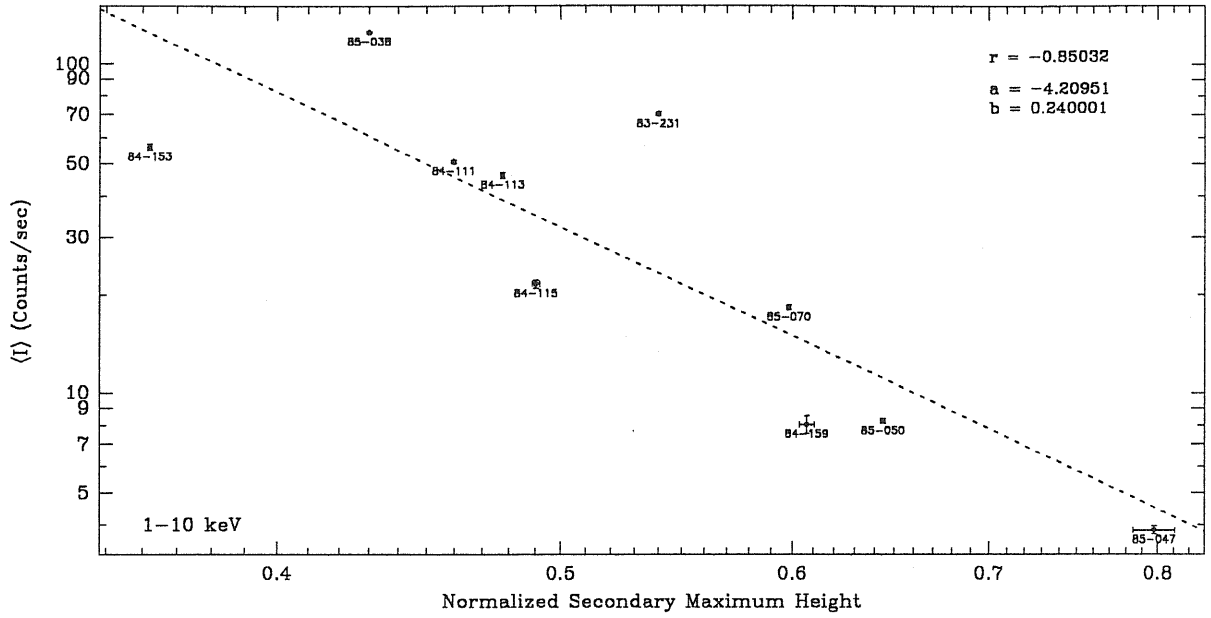


Figure 4.16: Normalized secondary maximum heights as a function of the average X-ray intensity for the ten EXOSAT observations of GX 301-2. When not visible, the error bars are smaller than the dimension of the point. The coefficients shown in the upper right refer to the fitting law $y = bx^a$. The coefficient r is the correlation coefficient.

where D is the orbital separation between the neutron star and Wray 977, while \dot{M}_* is the mass loss rate from the supergiant. Substituting the observed values in Eq. 4.6 we obtain

$$-7 \cdot 10^{-6} \lesssim \eta\tau \lesssim -7 \cdot 10^2 \text{ yr}^{-1}. \quad (4.7)$$

Again, the wide range is due to the large uncertain in the accretion radius, which is amplified by the strong dependence on it. We can see that the observed accretion time scales (see Fig. 4.9) are in the range expected from Eq. 4.7. This agreement does not occur for A0535+26, the other X-ray pulsar which shows this “saw-tooth” pulse period behaviour. In this latter case, Giovannelli and Ziolkowski (1990) claimed that a temporary disk might form at the periastron passage. The fact that we observe a minimum in the intensity of GX 301-2 just after the periastron passage is probably due to the presence of matter which has been accumulated around the neutron star (Rotschild and Soong (1987) arrived to this same conclusion). According to Sato *et al.* (1986) this matter might be an accretion wake due to the motion of the neutron star in the wind of Wray 977. This hypothesis was confirmed by the observation of a 5^h long X-ray intensity dip, during which the pulsation disappeared (Leahy *et al.*, 1988). This vanishing gives a constraint on the density of the matter, which must have $N_H > 10^{24} \text{ H/cm}^2$ (Leahy *et al.*, 1988). At the light of Eq. 4.7, we are inclined to favorite the hypothesis of the accretion wake, instead of a temporary disk, as the cause of the intensity decrease just after the periastron passage.

The time averaged background subtracted pulse profiles for all the ten EXOSAT observations of GX 301-2 are shown in Appendix A, while in Fig. 4.10 and Fig. 4.11 the pulse profiles normalized in the interval 0-1 were shown for the 85/038 and 85/070 observations (see Section 3.2.1 for the definition of the normalization). In all the observations, the pulse profile shows a double peak structure, with the first peak brighter than the second, π separated in phase. The relative height of the secondary peak with respect to the first drastically changed with time. In Fig. 4.16 we plotted the normalized secondary maximum height as a function of the intensity of the source in the 1-10 keV energy range. A correlation between these two quantities is present; in particular, higher the height of the secondary maximum, lower the intensity of the source. This behaviour was

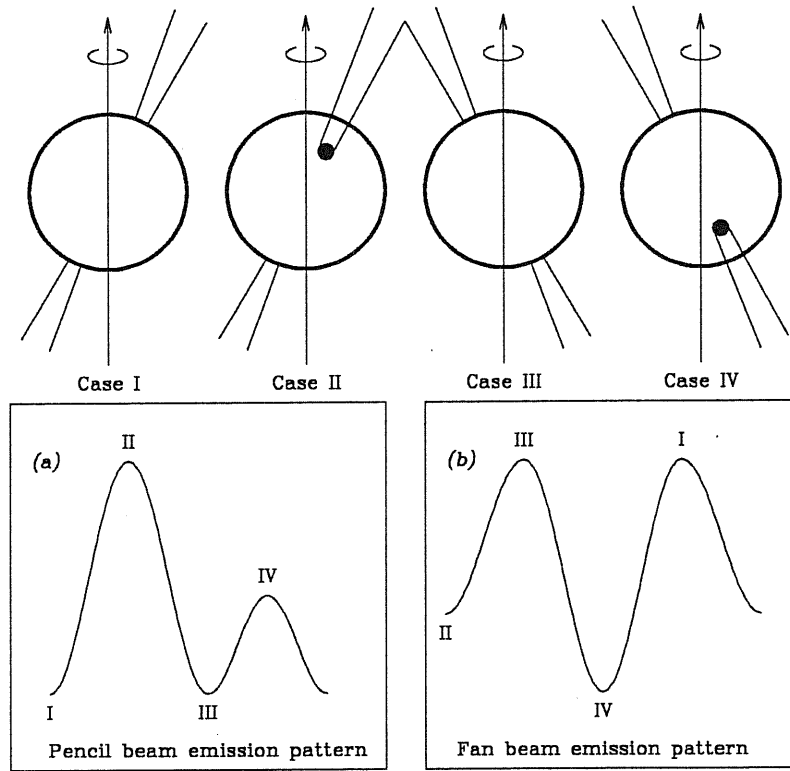


Figure 4.17: Sketch of the emission geometry as a function of the pulse phase. On the top four panels, the pulse phases corresponding to the points marked in the low panels are shown (the observer is assumed to be perpendicular to the plane of the figure and the picture is not in scale). Case (a) corresponds to a theoretical pulse profile obtained with a pencil beam emission pattern; Case (b) corresponds to a theoretical fan beam pulse profile.

not present in the GX 301-2 data from *Hakucho* (Mitani *et al.*, 1984), in which the ratio between the amplitude of the main peak to the secondary one changed drastically with time, but with any correlation with the X-ray intensity.

To interpret this behaviour, let us assume that in GX 301-2 we observe radiation which has been emitted in both the directions perpendicular and parallel to the magnetic field lines. This hypothesis is plausible because our pulse profiles present features expected for both the beaming patterns, *i.e.* we have maxima of different heights (pencil beam) and minima of different depths (fan beam). Furthermore, Mitani *et al.* (1984) concluded that a possible explanation of the pulse amplitude variations observed in GX 301-2 with *Hakucho* is a “disturbed” beaming pattern, *i.e.* a variable pattern of emission. With this in mind, let us describe the X-ray emission E_x as a mixture of two components

$$F = a E_x \quad P = b E_x \quad (4.8)$$

where F and P are the X-ray emission emitted in fan and pencil beam pattern, respectively, and a and b are the percentage of X-rays emitted with that particular pattern (of course $a + b = 1$). The standard theory (see Chapter 1 and *e.g.* Meszaros, 1984) predicts a fan beam emission pattern (*i.e.* $a = 1$) for luminosity higher than 10^{37} erg/sec, because of the formation of a radiative shock (Basko and Sunyaev, 1976), and a pencil beam emission pattern (*i.e.* $b = 1$) for lower luminosity. We will

not consider these extreme cases, but we will assume that both the components are always present, therefore for $\mathcal{L}_x \gtrsim 10^{37}$ erg/sec we will have $a \gg b$, and the opposite for $\mathcal{L}_x \lesssim 10^{37}$ erg/sec, but a and b will never vanish. In GX 301-2 we observe a decrease in the secondary maximum with respect to the main peak as the X-ray intensity increases. This is in agreement with an enhancement of one coefficient with respect to the other (see Fig 4.17). In the case $a \gg b$ (fan emission), the secondary maximum corresponds to Case I in Fig. 4.17. An increase of b (or a decrease of a) will remove radiation from that emitted toward the observer (because $a + b = 1$), producing a decrease in the X-ray intensity. In the case $a \ll b$ (pencil emission), the secondary maximum corresponds to Case IV in Fig. 4.17. Again, an increase of a (or a decrease of b) will remove radiation from the secondary maximum, causing the decrease of it. As an observational evidence of this behaviour, we have the formation of a secondary maximum in correspondence of the minimum of the pulse profile in the observation 85/070 (see Fig. 4.11). This can be explained as an enhancement in the X-ray emission emitted in the direction perpendicular to that along which X-ray are produced in the main peak. The fact that we have only one extra peak and not two, as we might expect in a symmetric case, should be due to the geometry of the system (see below): the emission from the second polar cap does not point directly toward the observer in the case of change of beaming pattern.

Theory favorites pencil beam emission in GX 301-2 (Meszaros, 1984), essentially because the pulse profile shows maxima of different heights with minima of almost equal depths (but we have a different behaviour in the 84/113 observation. See Appendix A). As discussed below, our analysis seems to favorite a pencil beaming pattern, but anyway the variation of the secondary peak height with respect to the intensity of the source (and consequently with respect to the accretion rate) is in agreement with the hypothesis of a variation of the emission pattern at the polar caps, independently of the emission pattern⁴.

In Fig. 4.18 the normalized secondary maximum heights for the GX 301-2 observations are shown as a function of energy of observation. As we can see, the pulse height increases with energy (observation 85/047 was too faint to permit this analysis. See Appendix A for its pulse profiles). This behaviour might be explained qualitatively as due to absorption effects. Because the secondary maximum is due to the emission of the polar cap which does not point directly to the observer, this means that we are observing the emitting region through a higher layer of plasma. At higher energy absorption is less efficient, leading to an increase of the radiation emitted in the secondary cap.

As we have discussed for 4U 1538-52 (see Section 3.4.3), from the analysis of the pulse profiles is possible to obtain the geometrical aspect angles β_m and β_o , known the angular and energy dependence of the X-ray emission in the strongly magnetized plasma surrounding the neutron star⁵. All the authors who computed the GX 301-2 aspect angles assumed an emission from a “slab”, giving rise a pencil beaming pattern (Wang and Welter, 1981; Leahy, 1990). While Wang and Welter (1981) used a very simple angular dependence of the X-ray flux in the magnetized plasma, Leahy (1990) utilized an analytical fit to the angular and energy dependence X-ray emission given by Meszaros and Nagel (1985). The result is (Leahy, 1990)

$$\theta_c = \frac{9}{41}\pi \quad \beta_o = \frac{3}{23}\pi \quad \beta_m = \frac{15}{31}\pi$$

where θ_c is the semi-angle subtended by the polar cap, with respect to the center of the neutron star. We want to remind that the two angles β_m and β_o are not univocally determined, but are interchangeable, due to the symmetry in Eq. 3.9 with respect to these angles. We repeated the same

⁴The parameter which might have given information on the beaming pattern, *i.e.* the modulation index $\Phi(E)$ (see Section 3.3.2 for its definition), does not show any correlation with the intensity of the source.

⁵We repeat here the definition of the two aspect angles: β_m is the angle between the neutron star magnetic field and the spin axis; β_o is the angle between the spin axis and the line of sight.

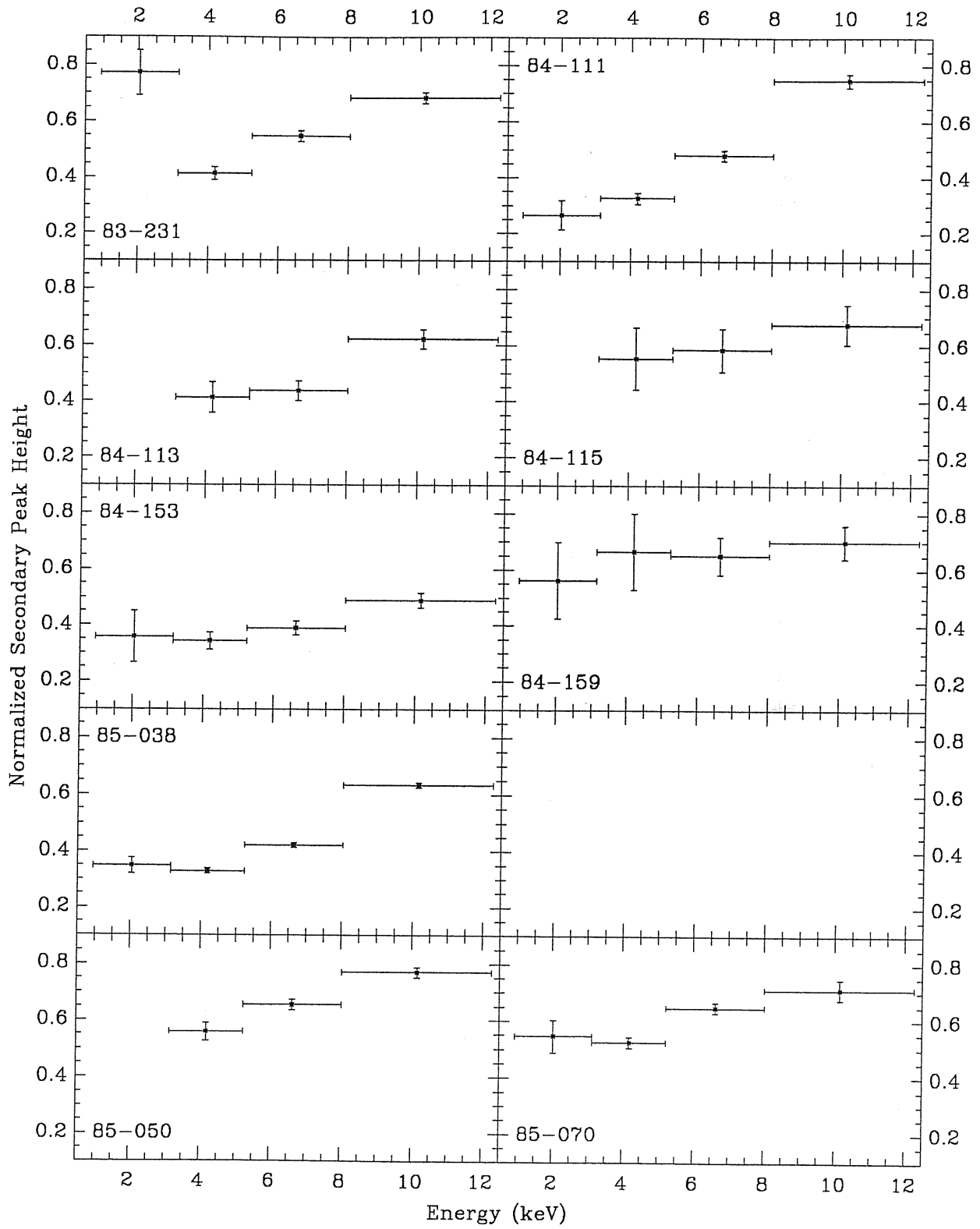


Figure 4.18: Normalized secondary peak height as a function of energy of observation. Observation 85/047 is not shown because the source was too faint.

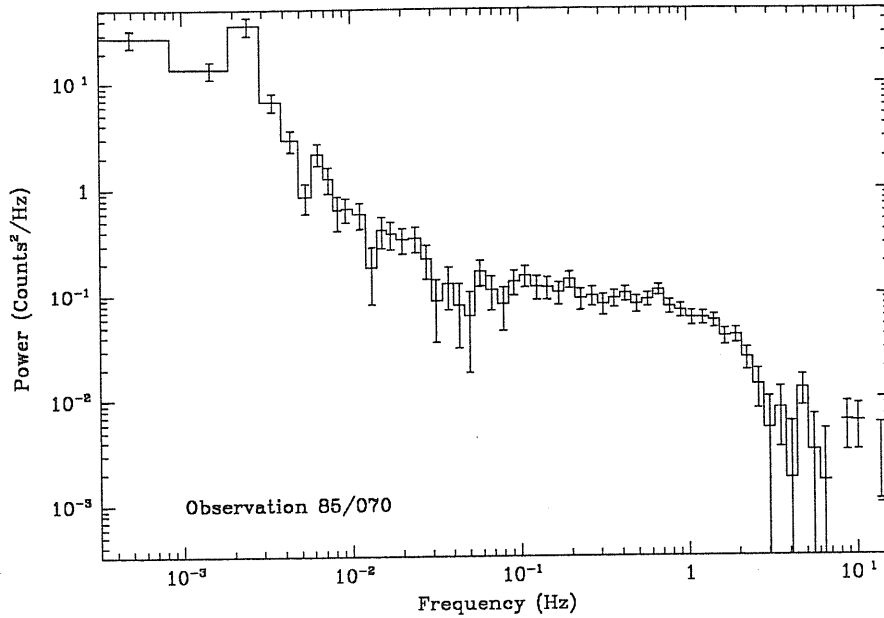


Figure 4.19: Power spectrum of the 85/070 observation obtained by the HTR3 ME OBC program. The collection time is 13.25 msec. Note the bump centered at about 0.1 Hz, of the same type as that observed by Belloni and Hasinger (1990). Because this feature was present only in HTR3 data, we prefer not discuss in our analysis the results obtained from this OBC program.

Leahy's analysis on our EXOSAT data, obtaining the same results: the likely beaming pattern in GX 301-2 is of pencil type. Unlikely from 4U 1538-52, in the case of GX 301-2 the magnetic field never points toward the observer. Furthermore, in the case of change of the beaming pattern, the two polar caps will be observed under different angles, allowing the observation of only one extra maximum in correspondence of a minimum in the pulse profile (see the discussion above).

4.3.2 Aperiodic Timing Measurements

The main feature common to all the fits to GX 301-2 PSD functions, independent of the data time resolution, is the presence of a change of slope in the power law used in fitting the continuum component. Furthermore, this change of slope occurs in the same frequency range for all the observations: 10–100 mHz, which corresponds to a time scale of 10–100 sec. The bump like feature at 0.1 Hz observed by Belloni and Hasinger (1990) was present only in the spectra obtained by HTR3 (see Chapter 2 for the properties of the ME OBC program HTR3) but not in the spectra obtained from other OBC programs, even if this same frequency was covered (see Fig. 4.19). We carefully checked the data and the background to search for spurious effects, but we find nothing strange. Because of this behaviour, we prefer to not discuss in our analysis the results obtained from this OBC program.

We computed for all the PSDs the rms (see Appendix B for its definition) and searched for correlations between this quantity and other observational properties of the source, as the mean intensity $\langle I \rangle$ and the modulation index $\Phi(E)$. In Fig. 4.20 the result of a linear fit⁶ to the data is shown. It is important to stress that we have to treat differently the observations relative to spin-up and spin-down episodes because, as we have shown above, the different “teeth” of the “saw-tooth” pulse period history have different behaviour. The fact that $\langle I \rangle$ and $\Phi(E)$ seem to correlate with rms's, *i.e.* with the “noise” responsible of the aperiodic variation in the X-ray flux, is interesting in itself, because can give some hints on the physics of the processes which determine

⁶A power law did not improve the fit.

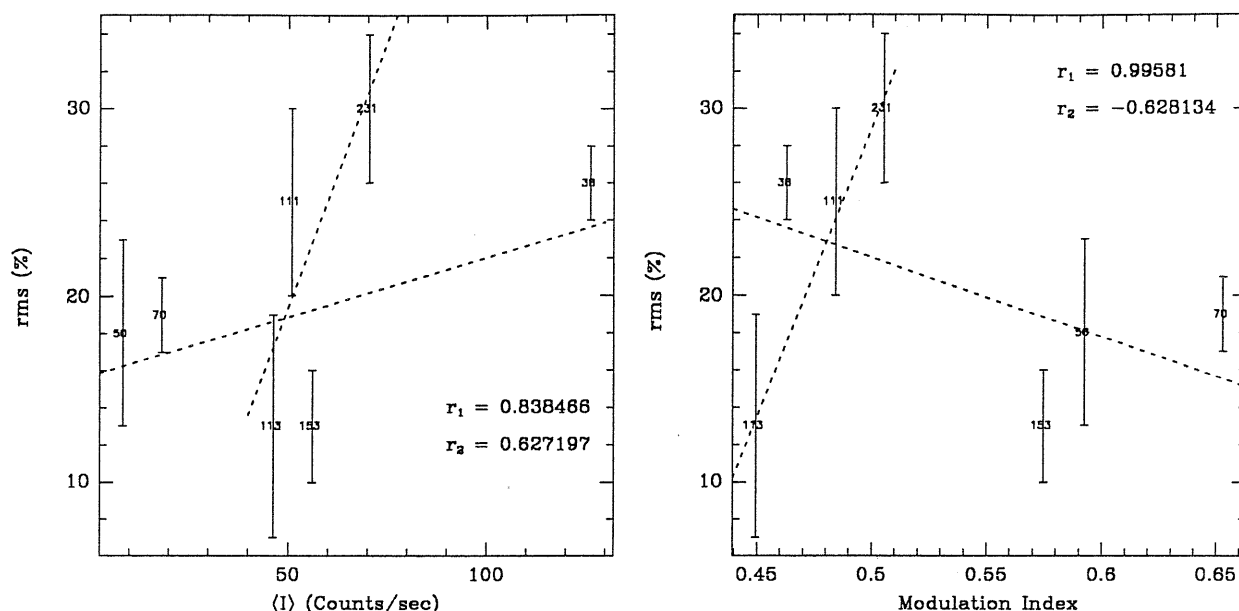


Figure 4.20: Root-mean-square variability of power spectra as a function of mean intensity and modulation index of the EXOSAT observations of GX 301-2. The two lines fit data with the same spinning behaviour, *i.e.* all the observations spinning-up and all those spinning-down. A power law fit gave a correlation coefficient r_2 slightly worse. Note the variation of slope occurring between the two spin states.

the pulse to pulse variability. But the most important result, shown in Fig. 4.21, is the correlation between the rms and the accretion time scale $\tau \equiv \dot{P}_p / P_p$ (90% significance level).

With the data available in literature, we checked whether EXO 2030+375 shows a similar behaviour. We utilized the pulse period and pulse period derivative given by Parmar *et al.* (1989b), and the rms measurements on the same data given by Angelini *et al.* (1990). The result is shown in Fig. 4.22; as we can see a correlation seems to be present, although with a worse significance than that found for GX 301-2. Because this source is a disk-fed pulsar, unlikely of GX 301-2 which is wind-fed, this correlation seems to be independent of the modality of accretion (or it is connected with a process common to both the pulsars). We individuate this process in the plasma penetration of the magnetosphere.

As it was discussed in the Introduction, the fact that the “noise” is correlated to the accretion time scale (and, as we have shown, with the intensity of the source) means that the process which yields the aperiodic variability in the observed X-ray flux is connected with the accretion process itself. We identify this process with the magnetohydrodynamical instabilities which occur at the magnetospheric limit; in other words we consider a discrete accretion onto the neutron star, the discretization due to the fragmentation of the accreted matter during the penetration of the plasmopause (Arons and Lea, 1980; Hameury *et al.*, 1980; Morfill *et al.*, 1984; Demmel *et al.*, 1990) (the whole theory will be developed in Chapter 6. Here we will give only a brief description of the physical scenario). As it was suggested by Rothschild and Soong (1987), we consider the X-ray emission in GX 301-2 as a superposition of flaring episodes which occur randomly. This flaring behaviour should be due to the discretization of the matter falling onto the neutron star, *i.e.* a discretization of the accretion rate \dot{M}_x . In this physical scenario, we developed a statistical model to describe the change of slope of the PSDs (see Chapter 6 for details). The random flaring behaviour is described as a shot noise process (Papoulis, 1965) with a particular response function, the parameters of which are related to the magnetohydrodynamical instability parameters, as the rate of formation of the blobs of plasma and their dimensions. Furthermore, the position of the knee at which the PSDs change slope is a function of these parameters; therefore some constraints

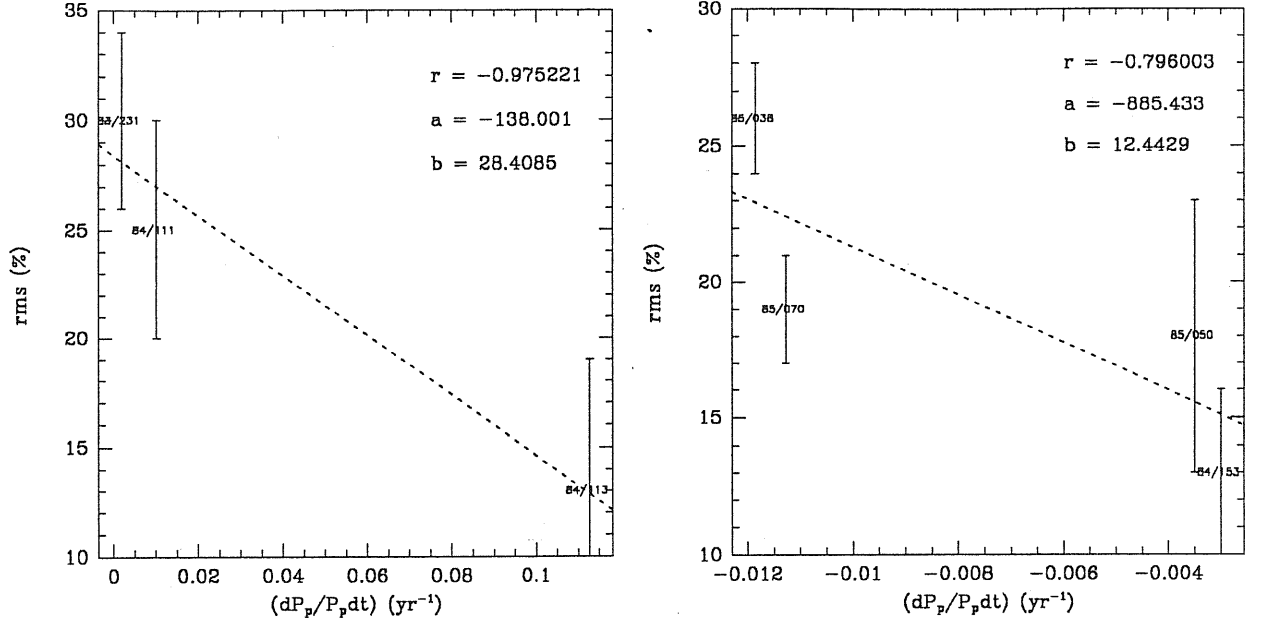


Figure 4.21: Root-mean-square variability of power spectra as a function of the accretion time scale, defined as $\tau \equiv \dot{P}_p/P_p$. On the left panel the spinning-down observations are shown, while on the right panel the spinning-up observations are plotted. Note the variation of slope occurring between the two spin states.

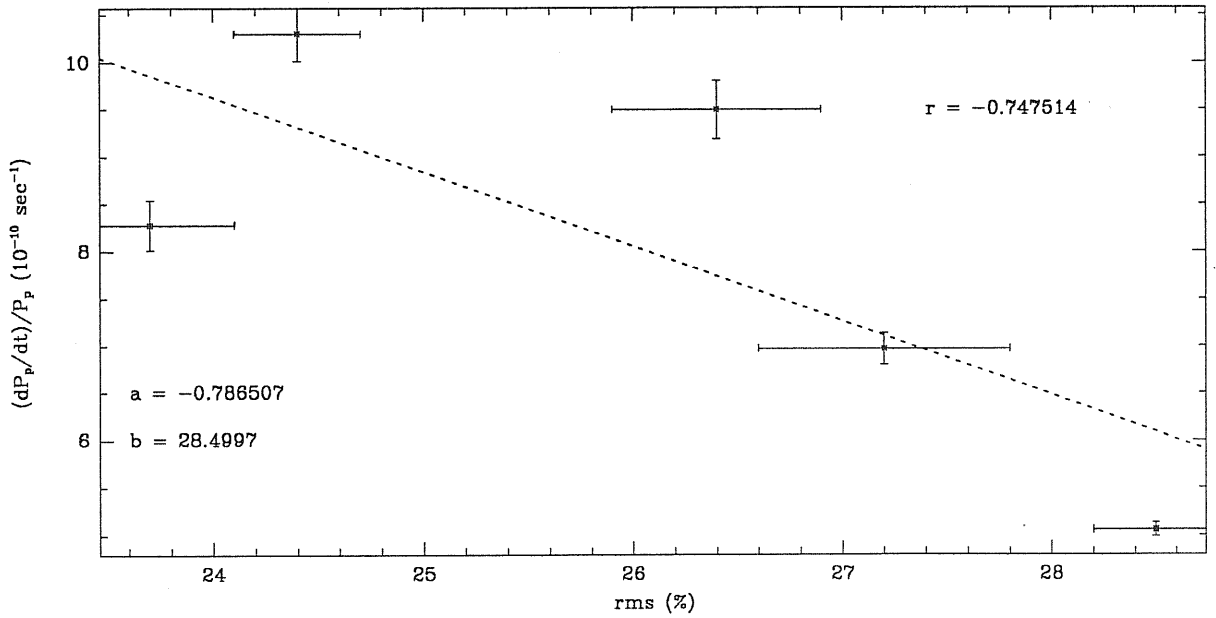


Figure 4.22: Root-mean-square variability of power spectra as a function of the accretion time scale, defined as $\tau \equiv \dot{P}_p/P_p$, for the X-ray pulsar EXO 2030+375. In this case all the observations are in the same spin state. Pulse period and pulse period derivative are obtained from Parmar *et al.* (1989b), while rms power spectrum measurements are taken from Angelini *et al.* (1990). The significance of the relation is worse than that obtained in the case of GX 301-2.

on the parameters can be done.

Bibliography

- Allen C.W. 1973. *Astrophysical Quantities*. Athlone Press, London.
- Angelini L., Stella L., and Parmar A.N. 1989. The discovery of 0.2 Hz quasi-periodic oscillation in the X-ray flux of the transient 42 second pulsar EXO 2030+375. *Astrophysical Journal*, **346**, p.911.
- Arons J. and Lea S.M. 1980. Accretion onto magnetized neutron stars: The fate of sinking filaments. *Astrophysical Journal*, **235**, p.1016.
- Basko M.M. and Sunyaev R.A. 1976. The limiting luminosity of accreting neutron stars with magnetic field. *Monthly Notices of R.a.S.*, **175**, p.395.
- Belloni T. and Hasinger G. 1990. An atlas of aperiodic variability in HMXB. *Astronomy & Astrophysics*, **230**, p.103.
- Bendat J.S. and Piersol A.G. 1971. *Random Data: Analysis and Measurement Procedures*. Wiley Interscience, New York.
- Boynton P.E., Deeter J.E., Lamb F.K., and Zylstra G. 1986. Vela X-1 pulse timing. I. Determination of the neutron star orbit. *Astrophysical Journal*, **307**, p.545.
- Boynton P.E., Deeter J.E., Lamb F.K., Zylstra G., Pravdo S.H., White N.E., Wood K.S., and Yentis D.J. 1984. New evidence on the nature of the neutron star and accretion flow in Vela X-1 from pulse timing observations. *Astrophysical Journal*, **283**, p.L53.
- Castor J.I., Abbott D.C., and Klein R.I. 1975. Radiation-driven winds of Of stars. *Astrophysical Journal*, **195**, p.157.
- Cusumano G., Robba N.R., Orlandini M., Dal Fiume F., and Frontera F. 1989. X-ray timing and spectral measurements of the X-ray pulsar 4U 1538-52. In *Proc. 23rd ESLAB Symposium on Two Topics in X-ray Astronomy. 1. X-ray Binaries*, page 369. ESA Publications Division, SP-296.
- Demmel V., Morfill G., and Atmanspacher H. 1990. A discrete-time model for inhomogeneous spherical accretion onto neutron stars. *Astrophysical Journal*, **354**, p.616.
- Dower R.G., Apparao K.M.V., Bradt H.V., Doxsey R.E., Jernigan J.G., and Kulik J. 1978. Positions of galactic X-ray sources: $55^\circ < l^{II} < 320^\circ$. *Nature*, **273**, p.364.
- Forman W., Jones C., and Tananbaum H. 1976. Uhuru observations of the galactic plane in 1970, 1971 and 1972. *Astrophysical Journal*, **206**, p.L29.
- Ghosh P. and Lamb F.K. 1979a. Accretion by rotating magnetic neutron stars. II. Radial and vertical structure of the transition zone in disk accretion. *Astrophysical Journal*, **232**, p.259.
- Ghosh P. and Lamb F.K. 1979b. Accretion by rotating magnetic neutron stars. III. Accretion torques and period changes in pulsating X-ray sources. *Astrophysical Journal*, **234**, p.296.
- Giovannelli F. and Ziolkowski J. 1990. On the presence of two discs in the X-ray/Be binary A0535+26/HDE 245770. *Acta Astronomica*, **40**, p.95.
- Hameury J.M., Bonazzola S., and Heyvaerts J. 1980. Stability of accretion column flows. *Astronomy & Astrophysics*, **90**, p.359.
- Henrichs H.F. 1983. Spin-up and spin-down of accreting neutron stars. In *Accretion-Driven Stellar X-ray Sources*, Lewin W.H.G. and van den Heuvel E.P.J., editors. Cambridge University Press, Cambridge.
- Hutchings J.B., Crampton D., Cowley A.P., and Bord D.J. 1982. The spectroscopic orbit of Wra 977 (= X-ray source 4U 1223-62). *Publ. Astron. Soc. Pacific*, **94**, p.541.
- Jones C.A., Chetin T., and Liller W. 1974. Optical studies of Uhuru sources. VIII. Observations of 92 possible counterparts of X-ray sources. *Astrophysical Journal*, **190**, p.L1.

- Joss P.C. and Rappaport S.A. 1984. Neutron stars in interacting binary systems. *Annual Review of Astronomy and Astrophysics*, **22**, p.537.
- Kawai N., Makishima K., Matsuoka M., Mitani K., Murakami T., and Nagase F. 1985. Hakucho observation of the pulse period of GX 301-2 and confirmation of the orbital period. *Publ. Astron. Soc. Japan*, **37**, p.647.
- Kelley R., Rappaport S., and Petre R. 1980. A determination of the orbit of GX 301-2. *Astrophysical Journal*, **238**, p.699.
- Lampton M., Margon B., and Bowyer S. 1976. Parameter estimation in X-ray astronomy. *Astrophysical Journal*, **208**, p.177.
- Leahy D.A. 1990. X-ray pulsar profile analysis. *Monthly Notices of R.a.S.*, **242**, p.188.
- Leahy D.A., Darbro W., Elsner R.F., Weisskopf M.C., Sutherland P.G., Kahn S., and Grindlay J.E. 1983. On searches for pulsed emission with application to four globular clusters X-ray sources: NGC 1851, 6441, 6624 and 6712. *Astrophysical Journal*, **266**, p.160.
- Leahy D.A., Nakajo M., Matsuoka M., Kawai N., Koyama K., and Makino F. 1988. Detection of an X-ray intensity dip from GX 301-2. *Publ. Astron. Soc. Japan*, **40**, p.197.
- Lewin W.H.G., McClintock J.E., Ryckman S.G., and Smith W.B. 1971. Detection of a high-energy X-ray flare from a source in Crux. *Astrophysical Journal*, **166**, p.L69.
- Lewin W.H.G., van Paradijs J., and van der Klis M. 1988. A review of quasi-periodic oscillations in low-mass X-ray binaries. *Space Science Review*, **46**, p.273.
- Livio M. 1990. On accretion by compact objects from stellar wind. In *Vulcano Workshop on Frontier Objects in Astrophysics and Particle Physics*, Giovannelli F., editor. in press.
- Makishima K., Kawai N., Koyama K., Shibazaki N., Nagase F., and Nakagawa M. 1984. Discovery of a 437.5 second X-ray pulsation from 4U 1907+09. *Publ. Astron. Soc. Japan*, **36**, p.679.
- Makishima K., Koyama K., Hayakawa S., and Nagase F. 1987. Spectra and pulse period of the binary X-ray pulsar 4U 1538-52. *Astrophysical Journal*, **314**, p.619.
- Marshall N. and Ricketts M.J. 1980. Determination of a binary period for the variable X-ray source A1907+09. *Monthly Notices of R.a.S.*, **193**, p.7P.
- McClintock J.E., Ricker G.R., and Lewin W.H.G. 1971. Rapid fluctuations in the high-energy flux from a source in Crux. *Astrophysical Journal*, **166**, p.L73.
- Meszáros P. 1984. Radiation from accreting magnetized neutron stars. *Space Science Review*, **38**, p.325.
- Meszáros P. and Nagel W. 1985. X-ray pulsar models. II. Comptonized spectra and pulse shapes. *Astrophysical Journal*, **299**, p.138.
- Mitani K., Matsuoka M., Makishima K., and Inoue H. 1984. Variations of the pulse profile and the X-ray intensity of GX 301-2 (4U 1223-62). *Astrophysics and Space Science*, **103**, p.345.
- Morfill G.E., Trümper J., Bodenheimer P., and Tenorio-Tangle G. 1984. Nonstationary accretion onto neutron stars: some constraints and consequences. *Astronomy & Astrophysics*, **139**, p.7.
- Nagase F. 1989. Accretion-powered X-ray pulsars. *Publ. Astron. Soc. Japan*, **41**, p.1.
- Nagase F., Hayakawa S., Kii T., Sato N., Ikegami T., Kawai N., Makishima K., Matsuoka M., Mitani K., Murakami T., Oda M., Ohashi T., Tanaka Y., and Kitamoto S. 1984a. Pulse-period changes of X-ray pulsars measured with Hakucho and Temna. *Publ. Astron. Soc. Japan*, **36**, p.667.
- Nagase F., Hayakawa S., Kunieda H., Masai K., Sato N., Tawara Y., Inoue H., Koyama K., Makino F., Makishima K., Matsuoka M., Murakami T., Oda M., Ogawara Y., Ohashi T., Shibazaki N., Tanaka Y., Miyamoto S., Tsunemi H., Yamashita K., and Kondo I. 1984b. Secular variation and short-term fluctuations of the pulse period of Vela X-1. *Astrophysical Journal*, **280**, p.259.
- Papoulis A. 1965. *Probability, Random Variables, and Stochastic Processes*. McGraw-Hill, New York.

- Parkes G.E., Mason K.O., Murdin P.G., and Culhane J.L. 1980. A spectral study of Wray 977, the optical counterpart of the binary X-ray pulsar 4U 1223-62. *Monthly Notices of R.a.S.*, **191**, p.547.
- Parmar A.N., White N.E., and Stella L. 1989a. The transient 42 second X-ray pulsar EXO 2030+375. II. The luminosity dependence of the pulse profile. *Astrophysical Journal*, **338**, p.373.
- Parmar A.N., White N.E., Stella L., Izzo C., and Ferri P. 1989b. The transient 42 second X-ray pulsar EXO 2030+375. I. The discovery of the pulse period variations. *Astrophysical Journal*, **338**, p.359.
- Priedhorsky W.C. and Terrel J. 1983. Long-term X-ray observations of Cen X-3, GX 301-2, GX 304-1 and 4U 1145-61. *Astrophysical Journal*, **273**, p.709.
- Rothschild R.E. and Soong Y. 1987. Two binary cycles of GX 301-2. *Astrophysical Journal*, **315**, p.154.
- Sato N., Nagase F., Kawai N., Kelley R.L., Rappaport S., and White N.E. 1986. Orbital elements of the binary X-ray pulsar GX 301-2. *Astrophysical Journal*, **304**, p.241.
- Shapiro S.L. and Lighthman A.P. 1976. Black holes in X-ray binaries: Marginal existence and rotation reversal of accretion disks. *Astrophysical Journal*, **204**, p.555.
- Shibazaki N. 1982. Hard X-ray recurrent transients. In *Accreting Neutron Stars, MPE Report 177*, page 57. Max-Planck Institut für Physik und Astrophysik, Garching bei München.
- Stella L., White N.E., and Rosner R. 1986. Intermittent stellar wind accretion and long-term activity of population I binary systems. *Astrophysical Journal*, **308**, p.669.
- Swank J.H., Becker R.H., Boldt E.A., Holt S.S., Pravdo S.H., Rothschild R.E., and Serlemitsos P.J. 1976. Variations in the spectra and pulse period of GX 301-2. *Astrophysical Journal*, **209**, p.L57.
- Underhill A. and Doazan V. 1982. *B Stars with and without Emission Lines*. NASA SP-456.
- Vidal N.V. 1973. The association of a high-luminosity B star with 3U 1223-62. *Astrophysical Journal*, **186**, p.L81.
- Wang Y.M. 1981. Spin-reversed accretion as the cause of intermittent spin-down in slow X-ray pulsars. *Astronomy & Astrophysics*, **102**, p.36.
- Wang Y.M. and Welter G.L. 1981. An analysis of the pulse profiles of binary X-ray pulsars. *Astronomy & Astrophysics*, **102**, p.97.
- Watson M.G., Warwick R.S., and Corbet R.H.D. 1982. The orbital period of 2S 1223-624 (GX 301-2). *Monthly Notices of R.a.S.*, **199**, p.915.
- White N.E., Mason K.O., Huckle H.E., Charles P.A., and Sanford P.W. 1976. Periodic modulation of three galactic X-ray sources. *Astrophysical Journal*, **209**, p.L119.
- White N.E., Mason K.O., and Sanford P.W. 1978. The binary X-ray pulsar 3U 1223-62. *Monthly Notices of R.a.S.*, **184**, p.67P.
- White N.E. and Swank J.H. 1984. The 41.5 day binary X-ray pulsar 4U 1223-62 (GX 301-2). *Astrophysical Journal*, **287**, p.856.
- White N.E., Swank J.H., Holt S.S., and Parmar A.N. 1982. A comparison of the X-ray properties of X Persei and γ Cassiopeiae. *Astrophysical Journal*, **263**, p.277.
- Ziolkowski J. 1985. Spin-up and spin-down of X-ray pulsars: Observations vs theory. In *Multifrequency Behaviour of Galactic Accreting Sources*, Giovannelli F., editor. CNR Frascati.

Part II

Theory

5 Theory of Wind Accretion

Let us consider a close, interacting binary system formed by a compact object (thereafter we will always consider as compact object a neutron star) and an early type star emitting a stellar wind. If this companion star has evolved enough to fill its critical Roche-lobe, then matter will be accreted mainly through the inner Lagrangian point (Frank *et al.*, 1985). In this case an accretion disk will form, because of the high angular momentum carried by the accreted matter (and because of the low velocity of the fluid that allows a simpler capture). On the other hand, when the companion star does not fill its critical Roche-lobe, then matter can be accreted directly from the stellar wind. To obtain the intense X-ray luminosities as those observed in this class of objects ($\mathcal{L}_x \approx 10^{36}-10^{38}$ erg/sec), very intense mass loss rates from the optical star are required ($\dot{M}_* \approx 10^{-7}-10^{-6} M_\odot/\text{yr}$ (White, 1985)).

In this chapter we will review and discuss the theory of wind accretion in binary system, starting from the “classical” Bondi and Hoyle (1944) theory, and introducing all the problems connected with this field of research; in particular, it will be stressed the importance of the evaluation of the angular momentum carried by a stellar wind. Then an analysis of the processes which the accreting plasma exerts in the three regions “beyond”, “onto” and “inside” the magnetospheric radius is given, to obtain some clues on the way in which matter penetrates the magnetosphere and is accreted. Particular attention is posed to the magnetohydrodynamical instabilities which allow the plasma penetration, but a brief description of other processes is given. In particular, the state of the art about numerical simulations of stellar wind around compact objects is discussed. It is important to stress here that in this class of binary systems the gravitational and the magnetic interactions are very strong: indeed, at the surface of a standard neutron star¹, the gravitational field has a strength of the order of $2 \cdot 10^{11} g$, while the magnetic field has a surface magnetic field strength of the order of $10^{11}-10^{13} \text{ G}$.

About notation: in all this chapter we will indicate with r a distance measured from the center of the neutron star, while we will indicate with R the radial coordinate measured from the center of the companion star.

5.1 Bondi–Hoyle Accretion Theory

First of all, let us consider the question which first arises in the study of wind accretion around a compact object, *i.e.*

1. *How much stellar wind will the gravitational field of the neutron star be able to capture ?*

To answer this question let us consider a neutron star of mass M_x and radius r_x moving with velocity v_{rel} through a medium of sound velocity c_s at a distance a from a companion of mass

¹From here on we will consider a “standard” neutron star that of mass $M_x = 1.4 M_\odot$ and radius $r_x = 10 \text{ Km}$.

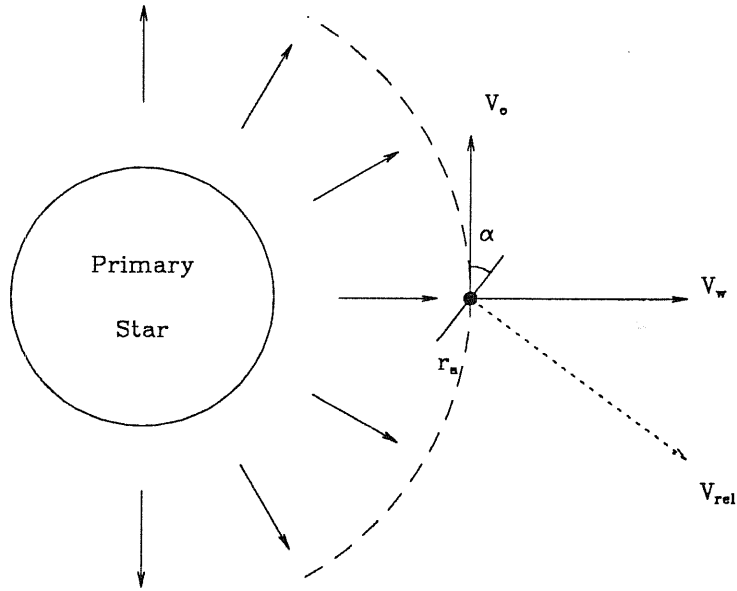


Figure 5.1: A neutron star that accretes from a stellar wind may capture angular momentum, depending on existing gradients across the target face r_a .

M_* and radius R_* (see Fig. 5.1). It will gravitationally capture matter from a roughly cylindrical volume of radius r_a given by (Bondi and Hoyle, 1944)

$$r_a = \frac{2GM_x}{v_{rel}^2 + c_s^2} \quad (5.1)$$

which is called *accretion radius*.

In most of all applications we can neglect the term c_s^2 , i.e. we can consider the stellar wind supersonic (Elsner and Lamb, 1977). In fact, since the radiation heating and cooling time scales are short with respect to the flow time scale (Buff and McCray, 1974), the plasma is approximately in thermal equilibrium and the electron and ion temperature are comparable. Because the radiation temperature of the X-rays is typically of the order of 10^7 – 10^8 °K (Hayakawa, 1985), it follows that the free-fall velocity at distances of the order of the accretion radius is much greater than the ion thermal velocity and therefore the flow is supersonic (of course it is possible that X-ray heating may cause the departure from the local thermal equilibrium and therefore the formation of a subsonic flow. See page 85 for another demonstration).

The relative velocity v_{rel} is given by

$$v_{rel}^2 = v_o^2 + v_w^2 \quad (5.2)$$

where $v_o \equiv v_x$ is the orbital velocity of the compact object and v_w is the wind velocity at the orbital radius (see Fig. 5.1).

The orbital velocity is given by

$$v_o^2 = \frac{G(M_* + M_x)}{a}.$$

From this expression we can see that, generally, a is much greater than the accretion radius because

$$\frac{r_a}{a} = \frac{2GM_x}{v_o^2 + v_w^2} \frac{v_o^2}{G(M_* + M_x)} = \frac{2}{1 + (v_w/v_o)^2} \frac{1}{1 + M_*/M_x} \ll 1. \quad (5.3)$$

The accretion rate onto the compact object will be

$$\dot{M}_x = \pi \rho v_{rel} r_a^2 \quad (5.4)$$

where ρ is the mass density of the stellar wind near the accretion radius. This density may be estimated, assuming *symmetric* and *spherical accretion* and *steady mass loss*, using the continuity equation

$$\dot{M}_* = 4\pi\rho v_w a^2. \quad (5.5)$$

Combining Eqs. 5.4 and 5.5 we obtain

$$\frac{\dot{M}_x}{\dot{M}_*} = \frac{1}{(1 + M_*/M_x)^2} \left(\frac{v_o}{v_w} \right)^4 \frac{1}{[1 + (v_o/v_w)^2]^{3/2}}. \quad (5.6)$$

In case of a rotating primary and steady stellar wind which conserves its angular momentum, the orbital velocity of the compact object will be reduced because of the rotation of its companion, in the equatorial plane, by the quantity (Petterson, 1978)

$$v_o \rightarrow v'_o = v_x - v_* \quad (5.7)$$

where v_* is the velocity due to the rotation of the companion star, the value of which is given by

$$\begin{aligned} v_* &= \Omega_* R_* \\ &= \left(\frac{\Omega_*}{\Omega_o} \right) \Omega_o a \left(\frac{R_*}{a} \right) \\ &= \lambda v_x \left(\frac{R_*}{a} \right) \end{aligned} \quad (5.8)$$

where λ is the ratio between the angular velocity of the rotating primary and of the orbital angular velocity of compact object. Substituting Eq. 5.8 in Eq. 5.7 we have that

$$v'_o = v_x \left[1 - \lambda \left(\frac{R_*}{a} \right) \right].$$

Therefore Eq. 5.6 will contain a correction factor α

$$\frac{\dot{M}_x}{\dot{M}_*} = \frac{1}{(1 + M_*/M_x)^2} \left(\frac{v_o}{v_w} \right)^4 \frac{1}{[1 + \alpha (v_o/v_w)^2]^{3/2}}$$

with α given by

$$\alpha = \left[1 - \lambda \left(\frac{R_*}{a} \right) \right]^2.$$

The second question to solve concerns the interaction between the gravitational field and the magnetic field of the neutron star, *i.e.*

2. *At what distance from the neutron star surface will the magnetic field begin to influence the motion of the stellar wind ?*

Far from the neutron star we expect that the magnetic field will be screened by the currents induced in the infalling matter (see Section 5.3 for details), while very close to the neutron star surface we expect that the gravitational field will dominate, enforcing corotation. We define magnetospheric radius r_m , the length scale at which the dynamics of a stellar wind fluid element becomes to be driven by the magnetic field of the compact object. In the idealized case of a diamagnetic plasma which falls freely and spherical symmetrically onto the compact object, r_m is determined imposing the balance between its magnetic pressure and the ram pressure

$$\frac{B^2(r)}{8\pi} = \rho(r) v_{ff}^2(r) \quad (5.9)$$

where $B(r)$ is the magnetic field strength of the neutron star as a function of the distance r from it, v_{ff} is the free-fall velocity of the accreting matter and $\rho(r)$ is the stellar wind density. For a dipolar magnetic field configuration we have $B(r) = \mu/r^3$, with the dipolar magnetic moment defined as $\mu = B_0 r_x^3$, with B_0 the surface magnetic field strength. The density is correlated to the accretion rate (assumed stationary) by the expression

$$\dot{M}_x = 4\pi r^2 \rho(r) v_{\text{in}}(r)$$

where we are obliged to use \dot{M}_x and not \dot{M}_* because we are inside the accretion radius (otherwise accretion should not occur!).

We can consider the infall velocity as a fraction ξ ($\lesssim 1$) of the free-fall velocity

$$v_{\text{in}}(r) \equiv \xi v_{\text{ff}}(r) = \xi \sqrt{\frac{2GM_x}{r}}$$

therefore solving for $r = r_m$ we obtain

$$r_m = \left(\frac{1}{2}\xi\right)^{2/7} \mu^{4/7} (2GM_x)^{-1/7} \dot{M}_x^{-2/7}. \quad (5.10)$$

We can re-express Eq. 5.10 in terms of the X-ray luminosity \mathcal{L}_x starting from the expression

$$\mathcal{L}_x = G \frac{M_x \dot{M}_x}{r_x} = \left(\frac{GM_x}{c^2 r_x}\right) \dot{M}_x c^2 = \varepsilon \dot{M}_x c^2$$

where c is the light velocity and ε is the efficiency of the accretion process. Therefore an estimate of r_m is given by (Henrichs, 1983; Hayakawa, 1985)

$$r_m = \begin{cases} (2.7 \cdot 10^8 \text{ cm}) \xi^{2/7} \mu_{30}^{4/7} m^{-1/7} \dot{M}_{17}^{-2/7} \\ (3.8 \cdot 10^8 \text{ cm}) \xi^{2/7} \mu_{30}^{4/7} m^{-1/7} \varepsilon_{0.1}^{2/7} L_{37}^{-2/7} \\ (2.9 \cdot 10^8 \text{ cm}) \xi^{2/7} \mu_{30}^{4/7} m^{-1/7} r_6^{-2/7} L_{37}^{-2/7} \end{cases} \quad (5.11)$$

where we have define $\mu_{30} \equiv \mu/10^{30} \text{ G} \cdot \text{cm}^3$; $r_6 \equiv r_x/10^6 \text{ cm}$; $L_{37} \equiv \mathcal{L}_x/10^{37} \text{ erg/sec}$; $m \equiv M_x/M_\odot$ and $\varepsilon_{0.1} \equiv \varepsilon/0.1$.

The last expression in Eq. 5.11 is valid only assuming that *all* the accreted matter is converted into X-ray radiation. Note that $r_m \simeq 100 r_x$ for a standard neutron star.

It is important to stress that the assumptions which are implicit in Eq. 5.11 are:

1. spherical infall;
2. neglecting of the outgoing velocity;
3. neglecting of the thermal pressure of the infalling matter;
4. neglecting of the plasma pressure within the magnetosphere with respect to the magnetic pressure.

Before going on, let us introduce the key question about accretion, *i.e.*

3. What are the assumptions we need for accretion to occur ?

Because we assume that the neutron star rotates, otherwise we should not see pulsed emission, an obvious condition is that the neutron star rotates not so fast that plasma is expelled because of the centrifugal force.

The distance at which there is balance between the centrifugal force of the neutron star and the gravitational force is called *corotation radius* r_c , defined by the expression

$$r_c = \sqrt[3]{\frac{GM_x}{\Omega_p^2}} = \sqrt[3]{\frac{GM_x P_p^2}{4\pi^2}} \quad (5.12)$$

where $P_p \equiv 2\pi/\Omega_p$ is the pulse period. Eq. 5.12 may be written as

$$r_c = (1.5 \cdot 10^8 \text{ cm}) m^{1/3} P_p^{2/3}.$$

5.2 Angular Momentum Carried by the Stellar Wind

After having defined the three fundamental length scales we meet studying accretion in X-ray binary systems, let us introduce one of the main problem connected with this theory, *i.e.* the evaluation of the angular momentum carried by the accreted matter emitted by the optical companion with respect to the neutron star. This problem is of fundamental importance because it is observationally connected with the variations of pulsation periods with respect to time in X-ray pulsars. In fact, known the specific angular momentum carried by the stellar wind, l_w , and assuming the conservation of the total angular momentum of the binary system², then it is possible to predict the pulse period history of pulsars from the conservation of angular momentum

$$\frac{d}{dt}(I\Omega_p) = l_w \dot{M}_x \quad (5.13)$$

where I is the moment of inertia of the neutron star and $\Omega_p \equiv 2\pi/P_p$, with P_p the pulse period of the pulsar³.

From an observational point of view, wind-fed X-ray pulsars generally show a typical random behaviour of spin-ups and spin-downs with time scale of the order of the orbital period (*e.g.* Vela X-1 (Boynton *et al.*, 1984) and 4U 1538-52 (Makishima *et al.*, 1987)) imposed to a secular spin-up trend, which has a much longer time scale, of the order of 10^4 – 10^5 years (Nagase, 1989; Cusumano *et al.*, 1989). From Eq. 5.13 it follows that, on average, the neutron star will tend to spin-up, in the sense that the accretion torque will act to align the spin axis of the neutron star with that of the orbit. Therefore it is difficult to explain the “change of sign” of the accretion torque in the context of spherical symmetric wind emission. In what follows we will review some consequences of density and velocity gradients in the stellar wind and how they can “change the sign” to the accretion torque.

5.2.1 The Case of a Radial Gradient in the Stellar Wind

In the following analysis we will follow that of Wang (Wang, 1981) and Shapiro and Lightman (Shapiro and Lightman, 1976), *i.e.* we will restrict to the case of spherical symmetric wind. The neutron star is assumed to orbit at a velocity $v_o = \Omega_o a$ (see Fig. 5.1) and we will assume that it captures *all* the material which falls inside the accretion “tube”. Because the tube is not aligned with respect to v_w but is tilted of an angle $\sin \alpha = v_x/v_{rel}$ with respect to v_{rel} , the two faces of the tube will capture a different amount of matter, due to density and velocity gradients⁴. So a

²In the case in which the total angular momentum of the binary system is not conserved, because *e.g.* magnetic and/or viscous stresses and matter that leaves the system (Henrichs, 1983), then we have to add a term to the right hand side of Eq. 5.13 to take into account these effects.

³Normally in Eq. 5.13 we neglect the term \dot{I}/I with respect to \dot{P}_p/P_p because the former is much longer than the latter. Anyway, the study of the temporal behavior of \dot{I}/I is very important because it can give useful information on the internal structure of the neutron star (Ögelman, 1987).

⁴Of course, in this case the accretion flow will be non-axisymmetric.

To obtain the expression for v'_{rel} we put $v_x \simeq 2\pi R/P_o$ in Eq. 5.2 and differentiate with respect to R

$$v'_{rel}(a) = \frac{v_w(a)}{v_{rel}(a)} \left\{ v'_w(a) + \frac{\Omega_o^2 a}{v_w(a)} \right\}. \quad (5.18)$$

Substituting Eqs. 5.17 and 5.18 into Eqs. 5.16a and 5.16b we obtain

$$\rho(R) \simeq \rho(a) \left\{ 1 + \left[\frac{2}{a} + \frac{v'_w(a)}{v_w(a)} \right] y \sin \alpha \right\} \quad (5.19a)$$

$$v_{rel}(R) \simeq v_{rel}(a) \left\{ 1 - \frac{v_w(a)}{v_o^2(a)} \left[v'_w + \frac{\Omega_o^2 a}{v_w(a)} \right] y \sin \alpha \right\}. \quad (5.19b)$$

Following Wang (1981) let us introduce the parameter α_o such that $\sin \alpha_o = v_x/v_{rel}(a)$. Then we will substitute Eqs. 5.19a and 5.19b into Eq. 5.15, considering only terms in the first order in $\sin \alpha_o$. The angular momentum per unit mass becomes

$$dN \simeq \rho(a) v_{rel}^2(a) \left\{ 1 + \left[\frac{2}{a} - \frac{v'_w(a)}{v_w(a)} \right] y \sin \alpha_o \right\} y dy dz. \quad (5.20)$$

Clearly, the two terms in square brackets correspond to the contributions of the density and velocity gradients, respectively, to the angular momentum flux. The next step is to integrate Eq. 5.20 on the target area, which is defined by the equation

$$y^2 + z^2 = r_a^2 \simeq r_{a,o}^2 \left(1 + 4 \frac{v'_w(a)}{v_w(a)} y \sin \alpha_o \right)$$

where we have defined

$$r_{a,o} = \zeta \frac{GM_x}{v_{rel}^2(a)}. \quad (5.21)$$

Performing the integration (for details see Wang, 1981) the wind torque becomes

$$N \simeq \frac{1}{2} \pi \rho(a) v_{rel}^2(a) \left(\frac{r_{a,o}^4}{a} + \frac{7}{2} r_{a,o}^4 \frac{v'_w(a)}{v_w(a)} \right) \sin \alpha_o. \quad (5.22)$$

To obtain the specific angular momentum of the accreting matter we have to divide Eq. 5.22 by the accretion rate $\dot{M}_x \simeq \pi \rho(a) v_{rel}(a) r_{a,o}^2$, obtaining

$$l_w^r \simeq \frac{1}{2} \Omega_o r_{a,o}^2 \eta \quad (5.23)$$

where the term η takes into account the velocity gradient in the stellar wind

$$\eta = 1 + \frac{7}{2} a \frac{v'_w(a)}{v_w(a)}. \quad (5.24)$$

In the case in which a velocity gradient in the stellar wind is not present, *i.e.* $\eta = 1$, we obtain the result given by Shapiro and Lightman (Shapiro and Lightman, 1976). Because $r_a \propto v_w^{-2}$, the presence of a velocity gradient in the wind will have the effect of distorting the target face of the accretion tube: the face in which the wind velocity is higher will have a smaller radius than that in which the wind is slower. This corresponds to a smaller net angular momentum passing through the high-velocity part of the target area than that passing through the low-velocity part (because $l_w^r \propto r_a^2$). Of course, the opposite will occur for what concerns the angular momentum flux (see Eq. 5.15).

From Eq. 5.23 it follows that the “sign” of the specific angular momentum carried by the accreting matter, *i.e.* if the stellar wind will give angular momentum to the neutron star or if the neutron star gives angular momentum to the wind, will depend on the sign of the parameter η : the condition if $\eta \leq 0$ will be fulfilled if

$$\frac{\partial v_w}{\partial R}(a) \leq -\frac{2}{7} \frac{v_w(a)}{a}. \quad (5.25)$$

5.2.2 The Case of an Azimuthal Gradient in the Stellar Wind

Again we will follow the discussion given by Wang (Wang, 1981). The azimuthal dependence is introduced by means of the angle φ , which is measured on the orbital plane of the neutron star, increasing in the direction of the orbital motion (see Fig. 5.2). We will neglect any dependence on the latitude θ . Expanding ρ and v_{rel} about the position ($R = a, \varphi = 0$) we obtain

$$\rho(R, \varphi) \simeq \rho(a, 0) - \frac{\partial \rho}{\partial R}(a, 0) y \sin \alpha - \frac{1}{a} \frac{\partial \rho}{\partial \varphi}(a, 0) y \cos \alpha \quad (5.26a)$$

$$v_{rel}(R, \varphi) \simeq v_{rel}(a, 0) - \frac{\partial v_{rel}}{\partial R}(a, 0) y \sin \alpha - \frac{1}{a} \frac{\partial v_{rel}}{\partial \varphi}(a, 0) y \cos \alpha. \quad (5.26b)$$

From Fig. 5.2 we can see that

$$\begin{aligned} R - a &= -y \sin \alpha \\ \varphi a &= -y \cos \alpha \\ \sin \alpha &= v_x / v_{rel} \simeq \sin \alpha_o \\ \cos \alpha &= v_w / v_{rel} \simeq 1 \end{aligned} \quad (5.27)$$

therefore, repeating what was done in the case of a radial gradient the expression for the angular momentum crossing a surface element $dydz$ of the accretion target is

$$\begin{aligned} dN \simeq \rho(a, 0) v_{rel}^2(a, 0) \left\{ 1 + \left[\frac{2}{a} \sin \alpha_o - \frac{1}{v_w(a, 0)} \frac{\partial v_w}{\partial R}(a, 0) \sin \alpha_o \right. \right. \\ \left. \left. - \frac{1}{a \rho(a, 0)} \frac{\partial \rho}{\partial \varphi}(a, 0) - \frac{2}{a v_w(a, 0)} \frac{\partial v_w}{\partial \varphi}(a, 0) \right] y \right\} y dydz \end{aligned} \quad (5.28)$$

The equation defining the target area is

$$y^2 + z^2 = r_{a,o}^2 \left\{ 1 + \frac{4}{v_w(a, 0)} \left[\frac{\partial v_w}{\partial R}(a, 0) \sin \alpha_o + \frac{1}{a} \frac{\partial v_w}{\partial \varphi}(a, 0) \right] y \right\}.$$

Integrating Eq. 5.28 on the target area and dividing by \dot{M}_x will give the expression of the specific angular momentum in presence of a stellar wind with azimuthal and radial gradients

$$l_w^\varphi \simeq \frac{1}{2} \Omega_o r_{a,o}^2 \tilde{\eta} \quad (5.29)$$

where the coefficient $\tilde{\eta}$ is given by

$$\tilde{\eta} = 1 + \frac{7}{2} \frac{a}{v_w(a, 0)} \frac{\partial v_w}{\partial R}(a, 0) + \frac{3}{v_x} \frac{\partial v_w}{\partial \varphi}(a, 0) - \frac{1}{2} \frac{v_w(a, 0)}{v_x} \frac{1}{\rho(a, 0)} \frac{\partial \rho}{\partial \varphi}(a, 0) \quad (5.30)$$

(Of course, setting derivatives with respect to φ to zero this equation reduces to Eq. 5.23).

This time the “sign” of the angular momentum carried by the accreting matter will depend on both radial and azimuthal gradients in density and velocity of the stellar wind; in particular we will have $l_w^\varphi \gtrless 0$ if one of this two inequalities holds

$$\frac{1}{a} \frac{\partial v_w}{\partial \varphi}(a, 0) \gtrless -\frac{1}{3} \frac{v_x}{a} \quad (5.31a)$$

$$\frac{1}{a} \frac{\partial \rho}{\partial \varphi}(a, 0) \gtrless 2 \left[\frac{v_x}{v_w(a, 0)} \right] \frac{\rho(a, 0)}{a}. \quad (5.31b)$$

From these expressions we can see that the variations in density and velocity across the target area required to change the sign to the angular momentum l_w^φ are very small

$$\left| \frac{\Delta v_w}{v_w} \right| \approx \left(\frac{v_x}{v_w} \right) \left(\frac{r_{a,o}}{a} \right) \approx \left| \frac{\Delta \rho}{\rho} \right| \ll 1.$$

At this point we are able to give conditions for the formation of a Keplerian accretion disk around a compact object which is accreting matter from a stellar wind. Indeed, the distance r_d from the neutron star at which matter will begin to orbit in a Keplerian orbit will be reached when $|l_w^\varphi| \approx |l_d| \approx \sqrt{GM_x r_d}$, i.e.

$$r_d \approx \left(\frac{\tilde{\eta}}{2} \right)^2 \Omega_o^2 \frac{r_{a,o}^4}{GM_x} \approx (2\Omega_o \eta \zeta^2)^2 \frac{(GM_x)^3}{v_{rel}^8(a)} \quad (5.32)$$

Imposing $r_d > r_m$ (see Eq. 5.10) we obtain an upper limit on the relative wind velocity for the formation of a Keplerian disk around a compact object accreting from a stellar wind, i.e. (Wang, 1981)

$$v_{rel}(a) \lesssim 2^{17/56} (\tilde{\eta} \Omega_o \zeta^2)^{1/4} \xi^{-1/28} \dot{M}_x^{-1/28} \mu^{-1/14} (GM_x)^{11/28}. \quad (5.33)$$

Putting the physical parameters of a typical wind-fed X-ray pulsar into Eq. 5.33 we obtain a velocity of the order of 300–400 Km/sec. From this follows that we do not expect the formation of a Keplerian accretion disk from matter captured gravitationally from a moderately fast stellar wind.

Before concluding this section let us stress some open problems; as we have seen, we introduced inhomogeneities directly in the expressions of ρ and v_{rel} (Eqs. 5.16a and 5.16b) assuming that $r_a \ll a$. While this argument is correct for what concerns the computation of \dot{M}_x , it cannot be applied for the evaluation of the angular momentum transfer (Eq. 5.15). In fact, the introduction of inhomogeneity effects only in the expressions for ρ and v_{rel} has the physical meaning of neglecting the interactions among different fluid elements during the accretion process (Davies and Pringle, 1980).

Davies and Pringle (1980) arrived to the opposite conclusion that there is no angular momentum transfer from the stellar wind to the compact object. Their method consists in following the fluid particles in their motion around the gravitational object onto ballistic trajectories. Wang (1981) argued that if we follow the particle along a finite size accretion column instead of along infinitesimal lines, then angular momentum can be yet transferred.

Numerical simulations of accretion flows around neutron stars have shown that stellar winds are focused into an accretion cone situated to the rear of the compact object (Shima *et al.*, 1985; Taam and Fryxell, 1988). While it was found that the accretion rate (see Eq. 5.4) is in reasonable agreement with that predicted by the theory (within a factor 2), the same is not true for what concerns the angular momentum accreted. For example, it was found that the accreted angular momentum is about a factor 5–10 smaller than that estimated by the theory (Anzer *et al.*, 1987). Another interesting feature that many researchers found is that in the presence of a density gradient two-dimensional simulations do not show a steady state behaviour but present random change

of sign of the accreted angular momentum (Anzer *et al.*, 1987; Matsuda *et al.*, 1987; Taam and Fryxell, 1989). Recently, it was stressed that three-dimensional simulations do not show this flip-flop behaviour but they always show quasi-steady solutions (Sawada *et al.*, 1989). To date, we are not able to decide whether this difference is due to different numerical methods or is intrinsic in the 2D and 3D flows.

5.3 Plasma Penetration into the Magnetosphere

In the previous section we have defined the magnetospheric radius as the distance at which the motion of the infalling plasma begins to be influenced by the neutron star magnetic field. In our treatment we completely neglected the thermal structure of the plasma in the region in which it is stopped and assumed that r_m is obtained by equalling the kinetic energy density of the infalling matter to the magnetic energy density of the stellar magnetic field. In this section we will enter into the details of the processes which occur at the magnetospheric limit, studying the way in which matter is stopped and how matter can penetrate the magnetosphere. We will divide our treatment into three parts, describing the regions beyond, onto and inside the magnetospheric radius.

5.3.1 The Region “beyond” the Magnetospheric Radius

First of all, let us define the accreting matter coming from the optical companion as a neutral electron-ion plasma. Then, because we are interested in the way in which the plasma interacts with the magnetic field of the neutron star, let us consider what are the effects due to the presence of a significant magnetic field in the infalling matter. Because we are considering binary systems in which the stellar wind is emitted by an early type star (typically of spectral type O–B), the typical mean magnetic field (*i.e.* averaged over the whole disk) of this class of objects is of the order of 100 G (Borra *et al.*, 1982). Elsner and Lamb (1984) discussed about the physical properties of the magnetic field embedded in the stellar wind and arrived at the conclusion that *the magnetic field embedded in the stellar wind has to be small in scale at the companion surface* (their argument essentially takes into account the turbulent nature of the wind close to the optical star). These small-scale structures in the wind will be present also at the neutron star orbit (because a is not much greater than the companion radius and therefore the properties of the wind at the photosphere are essentially the same at the neutron star orbit) and therefore at the accretion radius r_a (because $r_a \ll a$). The presence of the X-ray radiation from the neutron star will tend to further complicate the structure of the wind magnetic field near r_a , and therefore to form a smaller scale structure in the wind magnetic field.

Let us consider the motion of the plasma, with embedded a magnetic field \mathbf{B}_w , from r_a to r_m . If these small-scale magnetic fields are completely frozen into the plasma, falling spherically symmetric and radially without dissipation or turbulence, then the radial component of the wind magnetic field, \mathbf{B}_w^r , will depend on the distance from the neutron star as r^{-2} while the azimuthal component \mathbf{B}_w^\perp will depend as $r^{-1/2}$ (Zeldovich and Novikov, 1971). Therefore \mathbf{B}_w^\perp will not affect the motion of the infalling plasma, since it will not be sufficiently amplified, while \mathbf{B}_w^r can be amplified in such a way to stop the inflow matter. In practice this will not occur because the plasma has a high electrical conductivity and therefore ordinary ohmic losses are ineffective in reducing the field (Lamb *et al.*, 1973), *i.e.* dissipative processes will cause the decaying of the wind magnetic field.

A much more efficient process able to amplify the wind magnetic field is “topological dissipation” (Parker, 1972). This process reduces both the strength of any embedded magnetic field and the scale of the dominant field component (creating a cellular structure). To obtain an order of magnitude estimate of the dominant field component strength (in this case \mathbf{B}_w^r), let us define the dissipation

time (Parker, 1972)

$$\tau_{dis} \approx \alpha \frac{\lambda_B(r)}{v_A} \quad (5.34)$$

where α is a number of the order of unity for a turbulent plasma and larger than unity in the case of a quiescent plasma, $\lambda_B(r)$ is the scale length of the magnetic field \mathbf{B}_w^r and v_A is the Alfvén velocity of the plasma, defined as

$$v_A = \sqrt{\frac{\mathbf{B}_w^r{}^2}{4\pi\rho}}. \quad (5.35)$$

This time scale gives an estimate on the time in which the field varies. Equalling τ_{dis} to the characteristic time for amplification of the field, which is of the order of r/v_{ff} we obtain (Lamb *et al.*, 1973)

$$\frac{\mathbf{B}_w^r}{8\pi} \lesssim \frac{1}{2} \alpha^2 \rho_{ff} v_{ff}^2 \left(\frac{\lambda_B(r_a)}{r_a} \right)^2 \quad (5.36)$$

where we used the fact that $r \sim \lambda_B(r)$ (Lamb *et al.*, 1973). Therefore in case of topological dissipation, the kinetic energy density will be comparable to the magnetic energy density, and the motion will be free-falling. For comparison, the magnetic field at the magnetopause satisfies Eq. 5.9. In case of turbulent motion a similar result occurs (Elsner and Lamb, 1984).

Therefore we can conclude that \mathbf{B}_w will be comparable in strength to the magnetospheric field at r_m in the case of laminar, radial flow⁵, only if $\lambda_B(r_a) \gtrsim \alpha r_a$. In the following we therefore will neglect the magnetic field embedded in the infalling plasma.

The first consequence of Eq. 5.36 in the case of neglecting \mathbf{B}_w is that

$$\frac{\mathbf{B}_w^r}{8\pi} \ll \frac{1}{2} \rho_{ff} v_{ff}^2 \quad (5.37)$$

from which follows that the flow from the companion star to the magnetosphere will be supersonic. In fact, the acoustic Mach number \mathcal{M}_s ,

$$\mathcal{M}_s \equiv \frac{v}{c_s} = \sqrt{\left(\frac{2GM_x}{r} \right) \left(\frac{m_i}{\gamma k_B T} \right)} \gg 1$$

where we have considered the case of free-fall motion and a perfect law for the ion gas, with ratio of the specific heats γ , is much greater than unity if Eq. 5.37 holds. Indeed the increase in c_s due to the topological dissipation is much smaller than the increase in v_{ff} , also if X-ray heating is taken into account (Lamb *et al.*, 1973). From Eq. 5.37 it immediately follows that the Alfvén Mach number \mathcal{M}_A is much greater than unity

$$\mathcal{M}_A \equiv \frac{v}{v_A} = \sqrt{\left(\frac{2GM_x}{r} \right) \left(\frac{4\pi\rho_{ff}}{\mathbf{B}_w^r} \right)} \gg 1$$

Because the motion is supersonic, we expect that a stand-off shock will form at the plasmopause. The next section will be devoted to the description of the physical processes which occur at the magnetospheric limit.

5.3.2 The Region “onto” the Magnetospheric Radius

As we have shown in the previous section, we expect that the stellar wind coming from the optical companion will be stopped by the magnetic field of the neutron star by a stand-off shock. We expect that this shock is collisionless because the mean free path for electron-ion collision is much

⁵In the case of turbulent flow we have $\lambda_B(r_a) \gtrsim \alpha^2 r_a$ (Elsner and Lamb, 1984).

greater than all the microscopic length scales of interest (Lamb *et al.*, 1973). Furthermore, because $\mathcal{M}_A \gg 1$, this shock will be turbulent. The directed kinetic energy of the infalling matter is then transformed, during the shock, into random thermal motion; therefore the ion temperature behind the shock T_i^1 will be of the order of the free-fall temperature

$$T_i^1(r) = \frac{GM_x m_i}{k_B r} \quad (5.38)$$

where we have to put $r = r_s$, with r_s the distance of the shock above the neutron star surface. Assuming a spherically symmetric, radial free accretion of plasma, the radial velocity v_r , the density ρ and the dynamical time scale τ_d as a function of r in the preshock plasma will be

$$v_r(r) = v_{\text{ff}} = \sqrt{\frac{2GM_x}{r}} \quad (5.39a)$$

$$\rho(r) = \rho_{\text{ff}} = \frac{\dot{M}_x}{4\pi r^2 v_{\text{ff}}} \quad (5.39b)$$

$$\tau_d = \frac{2}{3} \frac{r}{v_{\text{ff}}} \quad (5.39c)$$

In Eq. 5.39b we have assumed a steady rate of accretion \dot{M}_x .

Because the flow is highly supersonic we can apply the Rankine-Hugoniot condition at the jump (Frank *et al.*, 1985) obtaining the respective quantities behind the shock (Arons and Lea, 1976b). At this point a strong condition is posed, *i.e.* we assume that the neutron star rotates sufficiently slow that the effect of rotation can be neglected. We have previously defined corotation radius r_c the distance from the neutron star at which matter corotates with the compact object (see Eq. 5.12) therefore a first approximation for neglecting rotation is that, at r_m , the centrifugal force be much smaller than the gravitational force. This corresponds to put $r_m \ll r_c$, or equivalently (Elsner and Lamb, 1977)

$$\Omega_p \ll \Omega_K(r_m) = \sqrt{\frac{GM_x}{r_m^3}} \quad (5.40)$$

where $\Omega_K(r) \equiv \sqrt{GM_x/r^3}$ is the angular velocity of matter orbiting into Keplerian orbits. This constraint is usually well satisfied in the wind-fed X-ray binaries we are interested in, and therefore from here on we will consider only wind accretion onto slow rotators.

Now, let us consider what occur at magnetopause. We are in presence of two fluids: a neutral plasma and a magnetic field parallel to the interface separating the two fluids. Because collisions in the plasma are neglected (the shock is collisionless), a charged particle at the interface will suffer the magnetic field and will perform a circular orbit, half in its own fluid and half in the other. Since the electron and ion have opposite velocities parallel to the interface, the net effect will be an electrical current. If ρ , v and \mathbf{B} are related by Eq. 5.9 then at the boundary surface there will be a jump in the magnetic field of the order \mathbf{B} (Lamb *et al.*, 1973). This means that the currents induced at the boundary surface will screen the magnetic field for points outside it. With the same terminology used in geophysics, we call the region containing these currents *magnetopause*.

Summing up, we are in presence of two regions: the first is determined by the distance at which the plasma produces the collisionless shock, the second is determined by the screening of the stellar magnetic field because of the currents induced by the infalling matter (see Fig. 5.4). To compute the height of the shock above the magnetopause, $\Delta_s \equiv r_s - r_m$, it is necessary to compute explicitly the thermal history of the plasma during the shock, *i.e.* to take into account the heating and cooling processes which occur there. Arons and Lea (1976) showed that under the condition of high X-ray luminosity ($\mathcal{L}_x \approx 10^{37}$ erg/sec), the Compton scattering is the dominant heating and cooling

process at the magnetopause. On the other hands, Elsner and Lamb (1977) showed that in the absence of cooling the magnetosphere is stable, therefore not allowing accretion. Because, of course, the accretion does occur, a cooling mechanism is necessary. To show it, let us consider a dipolar configuration of the magnetosphere (*i.e.* $B^2 \propto r^{-6}$). The magnetic pressure gradient then provides a buoyancy force $\propto r^{-7}$, which opposes the gravitational pull on the incoming matter. Let us compute the gravitational force per unit mass on the plasma. If the plasma density obeys a polytropic law under compression, then the inward force increase as $\rho g \propto p^{1/\gamma} r^{-2} \propto B^{2/\gamma} r^{-2} \propto r^{-(6/\gamma)-2}$. Thus the system will be unstable and accretion will proceed only if the inward force will be greater than the buoyancy force $\rho g \propto r^{-(6/\gamma)-2} \geq r^{-7}$ which is valid if $\gamma \leq 6/5$. In practice, this means that some radiative cooling of the heavy material is required. Therefore

For accretion to occur Compton cooling is needed.

Let us compute the characteristic time scales for heating and cooling (Elsner and Lamb, 1977). If the electron temperature T_e is much greater than the radiation temperature T_x (Buff and McCray, 1974) then non relativistic electrons cool via inverse Compton scattering on a time scale (Weymann, 1965)

$$\tau_c = \frac{3m_e c}{8\sigma_T u_r} \quad (5.41)$$

where σ_T is the Thomson scattering cross section and $u_r = \mathcal{L}_x/4\pi r^2 c$ is the radiation energy density (for an optically thin plasma). At $r = r_m$ we have that $\tau_c \ll \tau_d$ (Eq. 5.39c) if the X-ray luminosity exceeds $\mathcal{L}_x \gg 3 \cdot 10^{36}$ erg/sec.

The bremsstrahlung time scale τ_{br} in the case in which $T_e/T_i > m_e/m_i$ is given by (Allen, 1973)

$$\tau_{br} \approx 1.4 \left(\frac{10^{15} \text{ cm}^{-3}}{Z\bar{g}n_e} \right) \left(\frac{T_e}{10^8 \text{ }^\circ\text{K}} \right) \quad (5.42)$$

where \bar{g} is the Gaunt factor, of order unity, and Z is the atomic number.

Finally, the exchange time scale τ_{e-i} on which the ions exchange their energy with the electrons is given by (Elsner and Lamb, 1977)

$$\tau_{e-i} = \frac{3m_e m_i}{8\sqrt{2\pi} Z^2 e^4 n_e \ln \Lambda} \left(\frac{k_B T_e}{m_e} + \frac{k_B T_i}{m_i} \right)^{3/2} \quad (5.43)$$

where $\ln \Lambda$ is the Coulomb logarithm⁶. The shock height is determined by the duration of the plasma cooling (Arons and Lea, 1976b; Elsner and Lamb, 1977) and it decreases with increasing accretion rate. In the magnetospheric field it is of the order of the ion Larmor radius (Arons and Lea, 1976b). This corresponds to few centimeters and therefore the magnetopause can be treated as a mathematical discontinuity.

The next step consists in the calculation of the equilibrium surface between the stellar magnetic field and the plasma pressure. This task is very complicated because the problem is non linear (Arons and Lea, 1976b; Elsner and Lamb, 1977). Using a spherical coordinate system r, θ, φ

⁶Let us recall that the Coulomb logarithm is defined by the expression of the collision right angle cross section of electron with ions: Cross section $= \pi p_0^2 \ln \Lambda$ where p_0 is the collision right angle radius, and

$$\ln \Lambda = \int_a^b \frac{dp}{p}.$$

The limits of integration are tabulated numbers according to the target ion, while the most general approximation for $\ln \Lambda$ is (Allen, 1973)

$$\ln \Lambda \approx 9.00 + 3.45 \log T - 1.15 \log N_e.$$

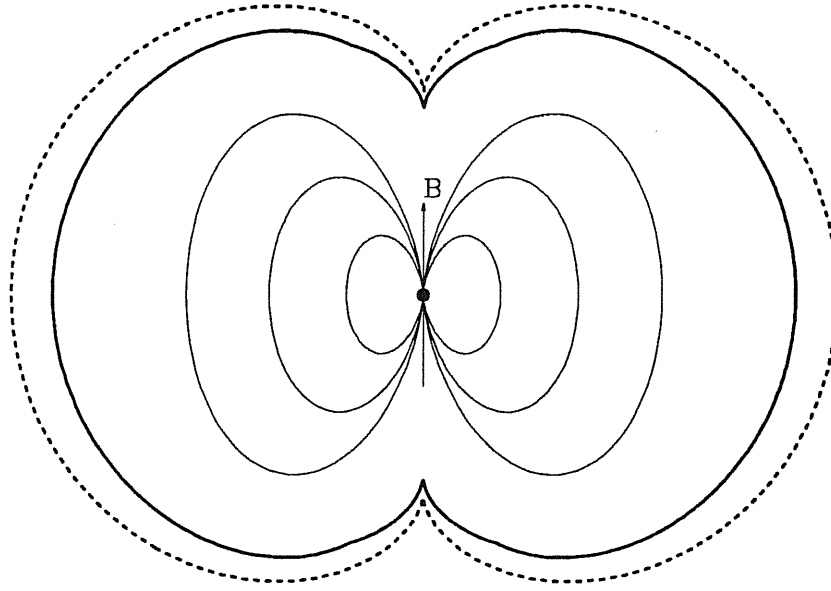


Figure 5.3: The equilibrium shape of the magnetosphere as computed by Arons and Lea (1976) (continuum line) and Elsner and Lamb (1977) (dashed line). In both the solutions polar cusps are present.

centered on the neutron star, with the polar axis coincident with the magnetic axis, we have to solve

$$\begin{cases} \nabla \times \mathbf{B} = \frac{4\pi}{c} \mathbf{J}(\mathcal{R}(\theta), \theta) \delta(\mathbf{r} - \mathcal{R}(\theta)\mathbf{e}_r) \\ \nabla \cdot \mathbf{B} = 0 \end{cases} \quad (5.44)$$

where the surface $\mathcal{R}(\theta)$ satisfies the condition

$$p(\mathcal{R}(\theta), \theta) = \frac{\mathbf{B}^2}{8\pi}(\mathcal{R}(\theta), \theta) \quad (5.45)$$

In Eq. 5.44 \mathbf{J} is the total surface current onto the magnetosphere and p is the total pressure of the accreting plasma. Arons and Lea (1977) resolved this problem by means of a multipole expansion of the vector potential \mathbf{A} in the Coulomb gauge. An important property of the solution is the presence of “cusps” just above the magnetic poles. In fact, a singularity at $|\theta| \rightarrow \pi/2$ must exist for any axisymmetric⁷ magnetic field derived from a nonsingular vector potential (Arons and Lea, 1976b). These cusps are present also above the magnetic poles of the Earth and they allow the penetration of matter from the solar wind forming the dawns.

The equilibrium shape of the magnetosphere, in units of r_m , is shown in Fig. 5.3 as computed by Arons and Lea (1976), and Elsner and Lamb (1977). In the former case the magnetosphere has equation

$$\mathcal{R}(\theta) = X_0 \begin{cases} (\cos \theta)^{0.27} & |\theta| \lesssim \theta_c \\ H_c + S(1 - 2|\theta|/\pi)^{2/3} & |\theta| \gtrsim \theta_c \end{cases} \quad (5.46)$$

where the parameters of the cusp solution are (Arons and Lea, 1976b)

$$X_0 = 1.19896 \quad H_c = 0.50984 \quad S = 0.62987 \quad \theta_c = 73^\circ 19'$$

⁷The solution will be axisymmetric because we neglect the effects of rotation.

On the other hands, Elsner and Lamb (1977) obtain the equilibrium configuration of the magnetospheric limit by means of a conformal mapping technique, imposing a power law dependence⁸ of the plasma pressure of the form $p \propto r^{-n}$. They found the following solution

$$x = \sin\left(\frac{\psi}{2}\right) - \frac{1}{3} \sin\left(\frac{3\psi}{2}\right) \quad y = \cos\left(\frac{\psi}{2}\right) - \frac{1}{3} \cos\left(\frac{3\psi}{2}\right) \quad (5.47)$$

where $0 \leq \psi \leq 4\pi$ and the cusp is located at $\psi = 0$. Both the solutions are symmetric with respect to the two axis.

The position at which the polar cusp closes, $\mathcal{R}(\pi/2)$, and the radius of the magnetic equator, *i.e.* $\mathcal{R}(0)$, for the two solutions are quite similar. For the polar cusp we have $\mathcal{R}_{\text{AL}}(\pi/2) = 0.65$ and $\mathcal{R}_{\text{EL}}(\pi/2) = 0.67$ while for the magnetic equator $\mathcal{R}_{\text{AL}}(0) = 1.20$ and $\mathcal{R}_{\text{EL}}(0) = 1.30$.

5.3.3 The Region “inside” the Magnetospheric Radius

Let us enter into the main topic of this section, *i.e.* the description of the way in which plasma can enter into the magnetosphere. Of course, for accretion to occur, plasma must win the magnetic force exerted by the stellar magnetic field and if the boundary is stable the only way in which matter can enter is through the polar cusps (which is the way in which matter enters the atmosphere on the Earth), diffusion across the magnetosphere and/or magnetic field reconnection. Elsner and Lamb (1984) have analyzed all these processes and concluded that diffusion is never an important process under the conditions which normally exist in wind-fed X-ray binary systems. The plasma entry through polar cusps might be an important process only if the X-ray luminosity were less than a critical value of the order of 10^{36} erg/sec and the emission were strongly anisotropic. Finally, plasma entry via magnetic field reconnection might be an important process only if the magnetic field embedded in the accreting matter were of the same order of the stellar magnetic field. As we have shown this is unlikely, therefore the most important mechanism of plasma penetration into the magnetosphere is via interchange (Rayleigh–Taylor) instabilities.

The magnetohydrodynamical stability of the magnetosphere can be studied by means of the energy principle (Bernstein *et al.*, 1958), according to which the magnetospheric boundary is stable with respect to an infinitesimal perturbation ξ if

$$\delta W_p = -\frac{1}{2} \int_{S_m} dS (\mathbf{n} \cdot \xi)^2 \mathbf{n} \cdot \nabla(p - \mathbf{B}^2/8\pi) > 0 \quad (5.48)$$

where \mathbf{n} is a versor perpendicular to the bounding surface S_m , pointing toward the vacuum region. Eq. 5.48 neglects viscous effects, but Elsner and Lamb (1984) demonstrated that this does not alter significantly the analysis. The condition of Eq. 5.48 is equivalent to

$$\mathbf{n} \cdot \nabla p - \mathbf{n} \cdot \nabla(\mathbf{B}^2/8\pi) > 0 \quad (5.49)$$

which we refer as the stability condition. Substituting the expressions for p and \mathbf{B} at the magnetospheric boundary, we obtain

$$\cos \chi \frac{GM_x}{r_m^2} - \kappa \frac{\mathbf{B}_{in}^2}{4\pi\rho_{out}} > 0 \quad (5.50)$$

where χ is the angle between r and the *outward* normal to the boundary, κ is the curvature⁹ of the magnetic field lines at the boundary and the pedices in and out refer to the plasma inside and outside the boundary, respectively (Elsner and Lamb, 1977).

⁸The case discussed in Arons and Lea (1977) corresponds to $n = 5/2$.

⁹The curvature of the magnetic field lines is defined by the relation

$$\mathbf{n} \cdot (\mathbf{B} \cdot \nabla) \mathbf{B} = \kappa \mathbf{B}^2.$$

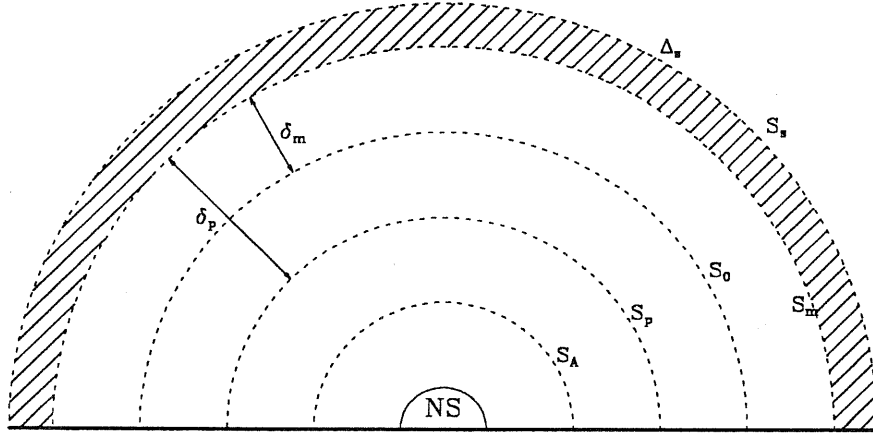


Figure 5.4: Schematic sketch of the regions around an accreting neutron star. From outside we have: S_s : the region defined by the stand-off shock; S_m : the region beyond which we can neglect the stellar magnetic field; S_0 : the region in which the stellar magnetic field does not exert the influence of the infalling plasma; S_p : the region inside which matter is disrupted by Kelvin–Helmholtz instability; S_A : the region inside which matter is channeled by the magnetic field lines. The scale in the figure is not exact and has been enlarged for clarity.

In the case of *static* equilibrium we have that (see Eq. 5.9)

$$\frac{\mathbf{B}_{in}^2}{8\pi} = (n_i k_B (T_i + Z T_e))_{out}$$

where n_i is the ion number density and k_B is the Boltzmann constant. Substituting this expression in Eq. 5.50 we obtain a condition for the onset of Rayleigh–Taylor instability at the magnetospheric boundary in terms of the electron and ion temperature in the postshock plasma, *i.e.*

$$(T_i + Z T_e)_{out} < T_{crit}(\theta) = \alpha(\theta) T_{ff}(\mathcal{R}(\theta)) \quad (5.51)$$

where we have defined (Elsner and Lamb, 1977)

$$\alpha(\theta) = \frac{\cos \chi}{2\kappa r_m} \quad (5.52)$$

Because normally in the postshock plasma we have thermal equilibrium we can put $T_i = T_e$ (Buff and McCray, 1974) and therefore the condition for the onset of instability becomes

$$(1 + Z) T_{out} < T_{crit}(\theta). \quad (5.53)$$

In the more realistic case of plasma flow into the magnetosphere we have that Eq. 5.9 is no more valid; instead we have to use

$$\left[\frac{\mathbf{B}^2}{8\pi} + p + \rho v^2 \right]_{out} = \left[\frac{\mathbf{B}^2}{8\pi} + p + \rho v^2 \right]_{in} \quad (5.54)$$

where we have to intend for \mathbf{B} the tangential component of the stellar magnetic field to the boundary surface S_m , and with v the normal component of the velocity. The pedices in and out as usual refer to the condition of the accreted plasma inside and outside the boundary surface.

As we have previously shown, we can neglect the magnetic field embedded in the stellar wind, therefore we will put $\mathbf{B}_{out} \approx 0$. As before, the surface S_m , of radius r_m , is such that the plasma flow

is not influenced by the stellar magnetic field; this corresponds to have $B^2/8\pi \ll p + \rho v^2$. On the other hand there will be another surface, which we will call S_0 (of radius r_0) such that the stellar magnetic field will not be affected by the presence of the infalling plasma: in this region the screening currents will be negligible. From these definitions we have that the magnetopause, *i.e.* the region containing the screening currents, will have height $\delta_m = r_m - r_0$ (see Fig. 5.4). Of course, once matter has entered the magnetosphere it will be not immediately channeled by the magnetic field lines, but will penetrate for some distance until it will be threaded. We will call the surface which bounds this region Alfvén surface S_A , of radius r_A and height $\delta_p = r_m - r_A$.

If $\delta_m \ll r_m$ then we can neglect the gravitational force acting on the matter within the magnetopause, therefore the terms “out” in Eq. 5.54 have to be evaluated at $r = r_m$, while the terms “in” have to be evaluated at $r = r_0$. Having an accumulation of matter outside, with $p_{out} \approx \rho_{ff} v_{ff}^2$ we obtain again Eq. 5.9. Anyway, matter cannot accumulate indefinitely outside the magnetopause because when the temperature drops below T_{crit} (because of Compton cooling) the boundary becomes Rayleigh–Taylor instable and matter becomes to enter¹⁰.

In the way we have defined S_A , the flow inside this region will be channeled by the magnetic field lines, therefore it is necessary that

$$\frac{1}{2} \rho v_{\parallel}^2 < B^2/8\pi \quad (5.55)$$

where v_{\parallel} is the plasma velocity parallel to the magnetic field. Therefore the Alfvén radius r_A is just the distance at which Eq. 5.55 holds.

To study the instability, the magnetopause is linearly perturbed in the azimuthal direction (Arons and Lea, 1976a), *i.e.* the linear perturbation $\xi(r, t)$ is such that

$$\xi(r, t) \rightarrow \xi' = \hat{\xi} e^{im\phi}.$$

The wave number of the perturbation is given by

$$k_m \simeq \frac{m}{\mathcal{R}(\theta) |\cos \theta|}$$

where $\mathcal{R}(\theta)$ is the magnetopause as a function of the magnetic latitude θ (see Eqs. 5.46 and 5.47). The growth rate of the modes is given by (Arons and Lea, 1976a)

$$\omega_{RT}^2 = g_{eff} k_m \tanh(k_m \Delta_s(\theta)) \quad (5.56)$$

where g_{eff} is the component of the effective gravitational field normal to the boundary ($g_{eff} = \alpha_g g_n$, with α_g a quantity less than unity which takes into account the effects due to magnetic tension and field curvature). This result has been obtained neglecting the effect of viscosity in the plasma, and this assumption is satisfied if the magnetic field embedded in the accreting matter is negligible (Arons and Lea, 1976b; Arons and Lea, 1980).

Once Rayleigh–Taylor instability sets on, plasma is absorbed and enters the magnetosphere in form of filaments. The velocity of a plasma blob inside the magnetosphere is

$$v_b(z) \simeq v_{ff} \sqrt{\frac{\alpha_g |\cos \theta|}{m}} - v(z) \quad (5.57)$$

¹⁰Strictly speaking, at the very beginning, when there is no X-ray radiation at all, matter can accumulate much more than in the case when it is radiated by the X-rays. In fact, the plasma will accumulate on a time scale of the order of τ_d while the cooling will occur on a time scale of the order of τ_{br} , which is much greater than τ_d . Therefore the cooling time scale will be very long and a consistent quantity of matter will accumulate outside the magnetopause, up to the onset of the Rayleigh–Taylor instability.

where z is the height measured from the boundary surface and $v(z)$ is the flow velocity at z . From Eq. 5.57 we can see that $v_b > 0$, i.e. matter can penetrate, only if the buoyancy force is less than the ram pressure of the plasma, and that the instability does not occur if the fall is supersonic. At the equilibrium we will have a dominant scale height, described by the mode number $m_0 \equiv b \mathcal{R}(\theta)/\Delta_s$, where $b \simeq 2$ (Arons and Lea, 1980; Arons and Lea, 1976b). This scale height corresponds to the longest wavelength mode which can grow (Hayakawa, 1985). With this in mind, the absorption velocity of the plasma at the magnetopause is given by

$$v_{\text{abs}} \simeq f v_{\text{ff}} \sqrt{\frac{\alpha_g |\cos \theta|}{m_0}} \quad (5.58)$$

where f is the fraction of the magnetopause surface covered by the absorbed plasma (of the order of 30–50%). The infalling matter consists of blobs of mean length $r_b \simeq \pi r_m/m_0$ and length $l_b \simeq \pi r_m/\sqrt{m_0}$. In their fall, the blobs will reduce their size due to the increase of the magnetic pressure. At the very beginning of the blob history we will have that $T_b \approx T_x$, where T_b is the blob temperature, and because the absorption optical depth for primary X-ray radiation is very small, the blobs behave isothermally. This cannot continue indefinitely, because $\rho_b \propto r^{-6}$ while $\mathcal{L}_x \approx r^{-2}$. Therefore there will be transition between a region in which Compton scattering is important and a region in which it is not. We will call this region *plasmopause*.

The radius and density of a blob as a function of the distance from the neutron star surface are given by (Arons and Lea, 1980; Hayakawa, 1985)

$$r_b(r) = \pi \left(\frac{r_m}{m_0} \right) \left(\frac{r}{r_m} \right)^2 \quad (5.59a)$$

$$\rho_b(r) = \rho_{\text{ff}}(r_m) \frac{v_{\text{ff}}(r_m)}{v_{\text{abs}}(r_m)} \left(\frac{r_m}{r} \right)^6 \quad (5.59b)$$

As the blob goes deeper in the magnetopause, at a distance of the order of $r_m/10$ the blob matter will pass from being optically thin to being optically thick. In this situation, the blob temperature is determined by the X-rays

$$T_b(r) = \sqrt[4]{\frac{\mathcal{L}_x}{4\pi r^2 \sigma}} = T_x \sqrt{r_x r} \quad (5.60)$$

where σ is the Stefan–Boltzmann constant, and Eqs. 5.59 are modified to

$$r'_b(r) = r_b(r) \left(\frac{r_x}{r} \right)^{1/6} \quad (5.61a)$$

$$\rho'_b(r) = \rho_b(r) \sqrt{\frac{r}{r_x}}. \quad (5.61b)$$

Once the blob arrives to the plasmopause, the interaction with the surrounding medium gives rise the onset of Kelvin–Helmholtz instability (Arons and Lea, 1980), which completely destroy the blobs. In this sense, the Alfvén surface defined by Elsner and Lamb (1977) will coincide with the plasmopause surface, but the way in which matter begins to be threaded by the magnetic field lines is quite different. In the case of the plasmopause a second type of instability sets on, Kelvin–Helmholtz instability. The expression of the plasmopause radius will have to take into account the thermal history of the blobs and the turbulent nature of the flow. Following Arons and Lea (1980), the turbulent velocity of the blob is written in the form

$$\delta v = \frac{\eta_{\text{KH}} \omega_{\text{KH}}}{k_m}$$

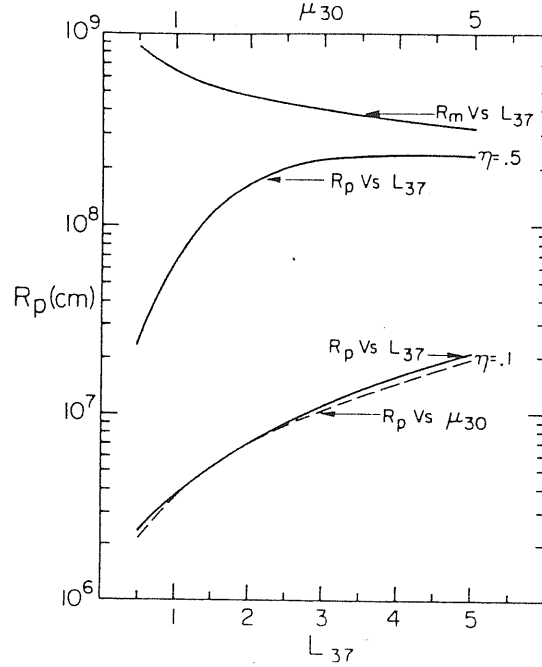


Figure 5.5: Expression of the plasmopause radius of Eq. 5.62 as a function of the X-ray luminosity for two values of the parameter η_{KH} , which defines the turbulent velocity of the infalling blobs in terms of the growth rate of the Kelvin-Helmholtz instability and the wave number of the perturbation (Arons and Lea, 1980).

where η_{KH} is a parameter of the order of 0.1, ω_{KH} is the growth rate of Kelvin-Helmholtz instability while the blob mass decreases accordingly the expression $\dot{M}_b = -4\pi r_b^2 \rho_b \delta v$. This expelled matter will contribute to disrupt more blobs. Because the number of blobs depends on the X-ray luminosity, an increase of the luminosity will disintegrate more blobs. On the other hand, the magnetopause radius depends inversely on the X-ray luminosity but its dependence is not so strong as the former, therefore the plasmopause will form farther from the neutron star surface the stronger the luminosity is. The plasmopause radius is given by (Arons and Lea, 1980)

$$r_p \approx 8 \cdot 10^6 \left(\frac{T_x}{7 \text{ keV}} \right)^{6/13} \left(\frac{T_b}{T_x} \right)^{2/13} \left(\frac{\eta_{KH}}{0.1} \right)^{12/13} L_{37}^{0.56} \varepsilon_{0.1}^{-0.004} \mu_{30}^{1.52} m^{-1.38} (1 + \alpha_m)^{12/13} \text{ cm} \quad (5.62)$$

where all the symbols are defined at page 78 but

$$\alpha_m = 0.34 L_{37}^{54/35} \left(\frac{\varepsilon}{0.1} \right)^{-12/35} \left(\frac{\eta_{KH}}{0.1} \right)^2 \left(\frac{T_x}{7 \text{ keV}} \right)^{32/35} m^{-134/35}.$$

In Fig. 5.5 (Arons and Lea, 1980) numerical solutions of Eq. 5.62 as a function of the X-ray luminosity are shown for two different values of the parameter η_{KH} . For comparison the value of the magnetopause radius is plotted.

The value of the plasmopause radius will define also the area of the polar caps A_{cap} onto the neutron star, which will be (Arons and Lea, 1980)

$$\frac{2A_{cap}}{A_x} = 1 - \sqrt{1 - \frac{r_x}{r_p}} \quad (5.63)$$

where A_x is the neutron star surface area. Substituting Eq. 5.62 into Eq. 5.63 we obtain the expression for the area of a polar cap onto a neutron star which, in the case $2A_{cap}/A_x \ll 1$ becomes

$$A_{cap} \approx 3.9 \cdot 10^{11} \left(\frac{T_x}{7 \text{ keV}} \right)^{0.462} \left(\frac{T_b}{T_x} \right)^{0.154} r_6^3 L_{37}^{-0.56} \mu_{30}^{-1.52} \varepsilon_{0.1}^{0.004} m^{1.38} (1 + \alpha_m)^2 \text{ cm}^2. \quad (5.64)$$

From this expression we can see that A_{cap} decreases with the X-ray luminosity: when L_{37} is low the blobs are larger and can penetrate deeply into the magnetopause, leading to smaller polar caps. On the other hands, when L_{37} is high, the dissipation process of disruption of infalling blobs is very efficient and quite rapid so the blobs are small and will be threaded by magnetic field lines which cross the stellar surface near the magnetic axis leading to small polar caps.

This result is exactly the opposite of that of Lamb *et al.* (1973), in which the polar cap area is computed by means of r_m and not by means of r_p . Substituting Eq. 5.10 into Eq. 5.63 we obtain the result (Lamb *et al.*, 1973)

$$A'_{cap} \approx 5 \cdot 10^9 r_6^3 \varepsilon_{0.1}^{-0.285} \mu_{30}^{-0.57} m^{0.142} L_{37}^{0.285} \text{ cm}^2. \quad (5.65)$$

The reason of this discrepancy resides in the fact that in Eq. 5.65 we have assumed that matter is immediately threaded by the magnetic field lines as soon as it passes the magnetospheric surface S_m . If the X-ray luminosity is high, then the dipolar configuration is very distorted and some field lines will pass outside r_m , giving a larger polar cap. The opposite will occur in case of low luminosity.

5.3.4 Numerical Simulations

Let us summarize the way in which matter can penetrate the magnetosphere and give rise to X-ray emission. In slow rotators, the main way of plasma penetration is interchange (Rayleigh–Taylor) instability in the magnetopause. Matter enters in form of filaments which are disrupted by the onset of Kelvin–Helmholtz instability. For $L_{37} \gtrsim 0.1$ the blobs are not coupled with the magnetic field (because of Compton cooling), therefore they will not corotate with the star but they will fall radially toward the neutron star surface (Arons and Lea, 1980). In this treatment we completely neglected the effect of viscosity (which is essentially the same that considering slow rotators), but what happens in the case in which we are in presence of a shear at the magnetospheric limit? Arons and Lea (1980) have shown that if the plasma has a shear velocity parallel to the magnetospheric boundary, then it might occur that the blobs cannot penetrate because the buoyant magnetic field cannot rise into the plasma. Therefore, if the bubble buoyancy is greater than the ram pressure we obtain the criterion

$$\Omega_p \ll \frac{\Omega_K(r_m)}{\sqrt{m_0}} \quad (5.66)$$

which corresponds to a constrain to the pulse period

$$P_p \gg 17 L_{37}^{1/5} \mu_{30}^{33/35} \varepsilon_{0.1}^{3/7} m^{-97/70} \text{ sec}. \quad (5.67)$$

Therefore, according to the fastness of the rotation, we expect that a different type of instability will occur at the magnetospheric limit: in the case of slow rotators plasma penetration will occur mainly by means of the gravity-driven interchange (Rayleigh–Taylor) instability. Decreasing the pulse period, the shear between the plasma and the magnetosphere begins to be very important, leading to the stabilization of the magnetopause with respect to Rayleigh–Taylor instability, and giving rise to Kelvin–Helmholtz instability. The linear growth times for the two types of instabilities, considering the two fluids incompressible and unmagnetized, are (Chandrasekhar, 1961)

$$\omega_{\text{RT}}^2(k) = g_{\text{eff}} k \left(\frac{\rho_{\text{out}} - \rho_{\text{in}}}{\rho_{\text{out}} + \rho_{\text{in}}} \right) \quad (5.68a)$$

$$\omega_{\text{KH}}(k) = k u \left(\frac{\sqrt{\rho_{\text{out}} \rho_{\text{in}}}}{\rho_{\text{out}} + \rho_{\text{in}}} \right). \quad (5.68b)$$

where g_{eff} is the effective gravitational field, $k = 2\pi/\lambda$ is the wave number relative to a perturbation of wavelength λ , u is the relative velocity of the outer fluid with respect to the inside fluid, considered

at rest. After a bit of algebra we have that the characteristic linear time scales for growing of instabilities are

$$\tau_{\text{RT}} \equiv \frac{1}{\omega_{\text{RT}}} = \sqrt{\frac{\lambda}{2\pi g} \left(\frac{\rho_{\text{out}} + \rho_{\text{in}}}{\rho_{\text{out}} - \rho_{\text{in}}} \right)} \quad (5.69a)$$

$$\tau_{\text{KH}} \equiv \frac{1}{\omega_{\text{KH}}} = \frac{\lambda}{2\pi u} \left(\frac{\rho_{\text{in}} + \rho_{\text{out}}}{\sqrt{\rho_{\text{in}}\rho_{\text{out}}}} \right) = \frac{\lambda}{2\pi u} \left(\sqrt{\frac{\rho_{\text{in}}}{\rho_{\text{out}}}} + \sqrt{\frac{\rho_{\text{out}}}{\rho_{\text{in}}}} \right) \quad (5.69b)$$

Equalling this two quantities and putting $h_{\text{out}} = c_s^2|_{\text{out}}/g_{\text{eff}}$, where $c_s|_{\text{out}}$ is the sound velocity relative to the outer medium, the critical Mach number at which the two time scales are equal is (Wang and Robertson, 1985)

$$\mathcal{M}_{\text{crit}} \sim \sqrt{\frac{(\rho_{\text{out}}/\rho_{\text{in}})^2 - 1}{\rho_{\text{out}}/\rho_{\text{in}}} \left(\frac{\lambda}{2\pi h_{\text{out}}} \right)} \quad (5.70)$$

In the Kelvin–Helmholtz regime, Burnard *et al.* (1983) have shown that the density and the temperature of the plasma at the magnetopause is higher than that obtained in the Rayleigh–Taylor regime; however this matter accumulated at the magnetospheric limit has an optical depth which is not able to alter the emerging X-ray radiation. This is due to the fact that the region where the plasma becomes to be threaded by the magnetic field lines is thinner than in the Rayleigh–Taylor regime and this gives rise to smaller polar caps. Therefore *outside* the magnetopause the matter will form optically thin shells for both the two types of instabilities.

These two regimes have been studied numerically by numerous authors (Anzer and Börner, 1980; Wang and Welter, 1980; Wang *et al.*, 1984; Wang and Robertson, 1984; Wang and Robertson, 1985) and a general result is that in both the instabilities short-wavelength modes are the first to develop but, for Kelvin–Helmholtz instability, vortex structures clump, becoming larger and wider. On the other hands, in the Rayleigh–Taylor regime this merging does not occur (see Fig. 5.6). Therefore we have that

Kelvin–Helmholtz Instability Long wavelength modes dominate

Rayleigh–Taylor Instability Short wavelength modes dominate

These results are obtained by means of 2D simulations. The main problem connected in this approach consists in the fact that we are able to follow the diffusion processes between the two fluids only for a relatively short period because the interface becomes very stretched and distorted due to vortex motions. Therefore the fact that Rayleigh–Taylor instability does not show the mixing of the vortexes might be due to the fact that the mode–mode interactions occur on time scale longer than that we are using¹¹.

Other problems exist: First, the maximum wavelength of a perturbation is given by the dimension of the grid on which we perform the calculation; second, the 2D nature of simulations. The latter problem is very serious because the independence (by definition) of the velocity field on the third coordinate suppresses the expansion, stretching and shrinking of the turbulence features in that direction, suppressing the amplification of small-scale vorticities.

Finally, we want to stress here that the influence of the strong magnetic field of the neutron star on the onset of instability is an open problem, too. Wang and Robertson (1984) have shown that in the situation in which the magnetic field is aligned with the direction of the flow, *i.e.* $\mathbf{k} \cdot \mathbf{B} = 0$, the linear growth time for Kelvin–Helmholtz instability (Eq. 5.69b) is increased by the effect due to

¹¹Wang and Robertson (1985) have analysed the development of Rayleigh–Taylor instability for several τ_{RT} and found two opposite trends: a first phase in which short wavelengths dominate and a subsequent phase in which the clumping of the “mushrooms” favorites longer wavelengths.

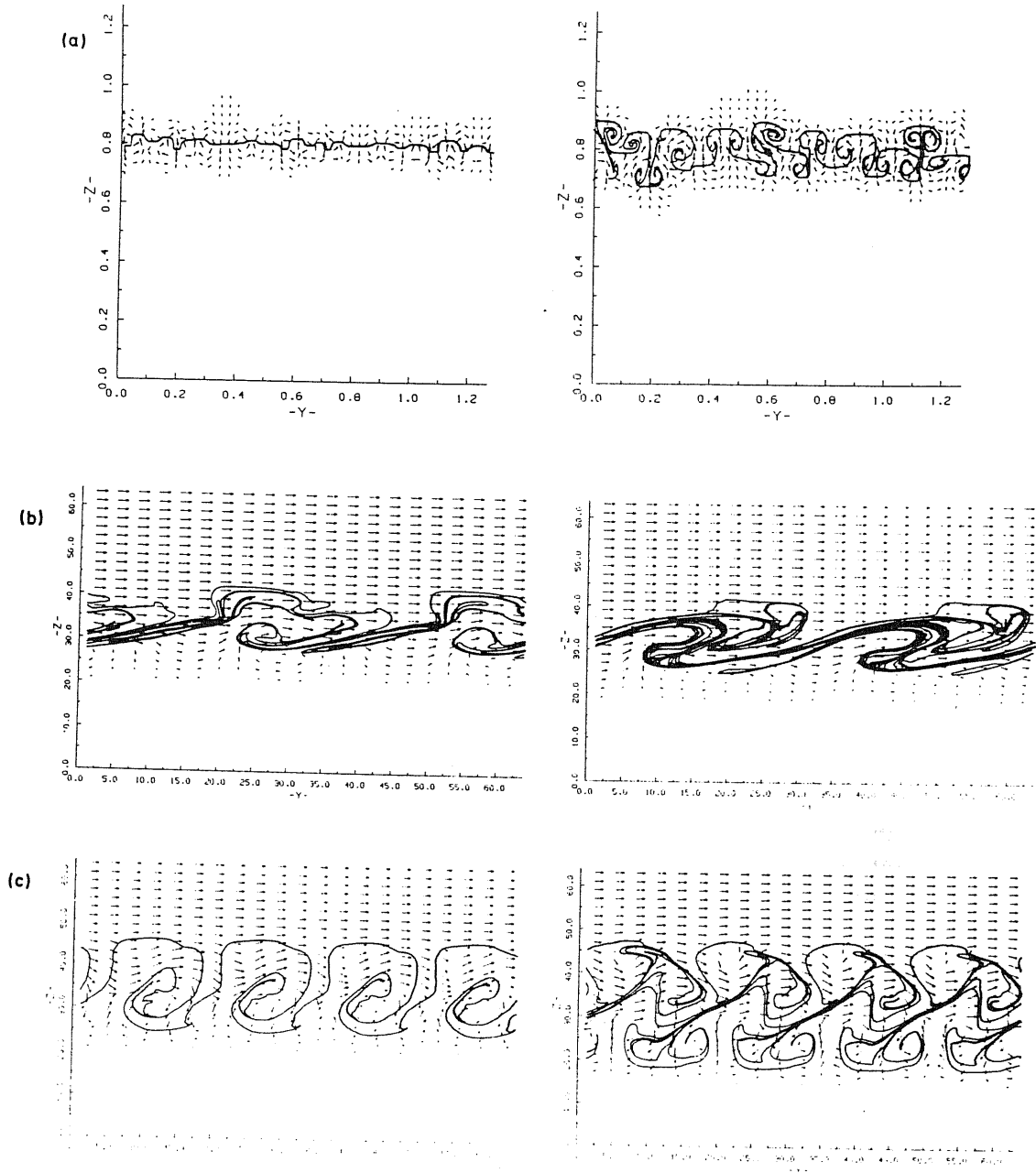


Figure 5.6: Numerical simulations of magnetohydrodynamical instabilities which occur at the magnetopause. For slow rotators gravity driven Rayleigh–Taylor instability gives rise to “mushroom” structures (Wang *et al.*, 1984). In a) this instability is generated from a random noise with a strong shock condition applied to the interface. For fast rotators the main way of plasma penetration is through Kelvin–Helmholtz instability. In b) a strong magnetic field is present, perpendicular to the plane of the grid, with $\varepsilon_y = 96$, $\mathcal{M}_{out} = 3$ and $\rho_{out}/\rho_{in} = 49$ (Wang and Robertson, 1984). Case c) corresponds to the intermediate case in which both the two instabilities are present and the media are unmagnetized. The case shown corresponds to $\mathcal{M}_{out} = 0.4$ and $\rho_{out}/\rho_{in} = 9$ (Wang and Robertson, 1984).

the magnetic tension, $\tau_{KH} \rightarrow \tau'_{KH} = \alpha_{KH} \tau_{KH}$. The coefficient α_{KH} is given by (Wang and Robertson, 1984)

$$\alpha_{KH} = \left[1 - \frac{\varepsilon_y}{\gamma \mathcal{M}_{out}^2} \left(\frac{T_{in}}{T_{out}} + \frac{2}{2 + \varepsilon_y} \right) \right]^{-1/2} \quad (5.71)$$

where $\varepsilon_y \equiv B_y^2/4\pi p_{in}$, B_y is component of the stellar magnetic field in the y direction and γ is, as usual, the ratio of the specific heats. From this expression we can see that the magnetic tension will suppress the instability in the case of equal temperature between the two media if

$$\varepsilon_y \gtrsim \frac{1}{2} (\gamma \mathcal{M}_{out}^2 + \sqrt{\gamma^2 \mathcal{M}_{out}^4 + 16} - 4). \quad (5.72)$$

In the case of Rayleigh–Taylor instability the inclusion of magnetic tension will have the effect of increasing the Rayleigh–Taylor growth time by a factor of the order of (Wang and Robertson, 1985)

$$\alpha_{RT} = \left[1 - \frac{B_r^2}{4\pi \rho_{out} g r_m} \right]^{-1/2} \quad (5.73)$$

where B_r is the radial component of the magnetic field.

Bibliography

- Allen C.W. 1973. *Astrophysical Quantities*. Athlone Press, London.
- Anzer U. and Börner G. 1980. Accretion by neutron stars: Accretion disk and rotating magnetic field. *Astronomy & Astrophysics*, **83**, p.133.
- Anzer U., Börner G., and Monaghan J.J. 1987. Numerical studies of wind accretion. *Astronomy & Astrophysics*, **176**, p.235.
- Arons J. and Lea S.M. 1976a. Accretion onto magnetized neutron stars: Normal mode analysis of the interchange instability at the magnetopause. *Astrophysical Journal*, **210**, p.792.
- Arons J. and Lea S.M. 1976b. Accretion onto magnetized neutron stars: Structure and interchange instability of a model magnetosphere. *Astrophysical Journal*, **207**, p.914.
- Arons J. and Lea S.M. 1980. Accretion onto magnetized neutron stars: The fate of sinking filaments. *Astrophysical Journal*, **235**, p.1016.
- Bernstein I.G., Frieman E.A., Kruskal M.D., and Kulsrud R.M. 1958. An energy principle for hydromagnetic stability problems. *Proc. Royal Society of London*, **A224**, p.17.
- Bondi H. and Hoyle F. 1944. On the mechanism of accretion by stars. *Monthly Notices of R.a.S.*, **104**, p.273.
- Borra E.F., Landstreet J.D., and Mestel L. 1982. Magnetic stars. *Annual Review of Astronomy and Astrophysics*, **20**, p.191.
- Boynton P.E., Deeter J.E., Lamb F.K., Zylstra G., Pravdo S.H., White N.E., Wood K.S., and Yentis D.J. 1984. New evidence on the nature of the neutron star and accretion flow in Vela X-1 from pulse timing observations. *Astrophysical Journal*, **283**, p.L53.
- Buff J. and McCray R. 1974. Accretion flows in galactic X-ray sources. I. Optically thin spherically symmetric model. *Astrophysical Journal*, **189**, p.147.
- Burnard D.J., Lea S.M., and Arons J. 1983. Accretion onto magnetized neutron stars: X-ray pulsars with intermediate rotation rates. *Astrophysical Journal*, **266**, p.175.
- Chandrasekhar S. 1961. *Hydrodynamic and Hydromagnetic Stability*. Oxford University Press, Oxford.

- Cusumano G., Robba N.R., Orlandini M., Dal Fiume F., and Frontera F. 1989. X-ray timing and spectral measurements of the X-ray pulsar 4U 1538-52. In *Proc. 23rd ESLAB Symposium on Two Topics in X-ray Astronomy. 1. X-ray Binaries*, page 369. ESA Publications Division, SP-296.
- Davies R.E. and Pringle J.E. 1980. On accretion from an inhomogeneous medium. *Monthly Notices of R.a.S.*, **191**, p.599.
- Elsner R.F. and Lamb F.K. 1977. Accretion by magnetic neutron stars. I. Magnetospheric structure and stability. *Astrophysical Journal*, **215**, p.897.
- Elsner R.F. and Lamb F.K. 1984. Accretion by magnetic neutron stars. II. Plasma entry into the magnetosphere via diffusion, polar cups, and magnetic field reconnection. *Astrophysical Journal*, **278**, p.326.
- Frank J., King A.R., and Raine D.J. 1985. *Accretion Processes in Astrophysics*. Cambridge University Press, Cambridge.
- Hayakawa S. 1985. X-rays from accreting neutron stars. *Physics Reports*, **121**, p.318.
- Henrichs H.F. 1983. Spin-up and spin-down of accreting neutron stars. In *Accretion-Driven Stellar X-ray Sources*, Lewin W.H.G. and van den Heuvel E.P.J., editors. Cambridge University Press, Cambridge.
- Lamb F.K., Pethick C.J., and Pines D. 1973. A model for compact X-ray sources: Accretion by rotating magnetic stars. *Astrophysical Journal*, **184**, p.271.
- Makishima K., Koyama K., Hayakawa S., and Nagase F. 1987. Spectra and pulse period of the binary X-ray pulsar 4U 1538-52. *Astrophysical Journal*, **314**, p.619.
- Matsuda T., Inoue M., and Sawada K. 1987. Spin-up and spin-down of an accreting compact object. *Monthly Notices of R.a.S.*, **226**, p.785.
- Nagase F. 1989. Accretion-powered X-ray pulsars. *Publ. Astron. Soc. Japan*, **41**, p.1.
- Ögelman H. 1987. The 35 day cycle of Her X-1: Quality of the clock mechanism. *Astronomy & Astrophysics*, **172**, p.79.
- Parker A.N. 1972. Topological dissipation and the small-scale fields in turbulent gases. *Astrophysical Journal*, **174**, p.499.
- Petterson J.A. 1978. On occurrence of streams and disks in massive X-ray binary systems. *Astrophysical Journal*, **224**, p.625.
- Sawada K., Matsuda T., Anzer U., Börner G., and Livio M. 1989. Inhomogeneous wind accretion: Comparison between 3D and 2D computations. *Astronomy & Astrophysics*, **221**, p.263.
- Shapiro S.L. and Lighthman A.P. 1976. Black holes in X-ray binaries: Marginal existence and rotation reversal of accretion disks. *Astrophysical Journal*, **204**, p.555.
- Shima E., Matsuda T., Takeda H., and Sawada K. 1985. Hydrodynamic calculations of axisymmetric accretion flow. *Monthly Notices of R.a.S.*, **217**, p.367.
- Taam R.A. and Fryxell B.A. 1989. Numerical studies of asymmetric adiabatic flow: The effect of velocity gradients. *Astrophysical Journal*, **339**, p.297.
- Taam R.E. and Fryxell B.A. 1988. On nonsteady accretion in stellar wind-fed X-ray sources. *Astrophysical Journal*, **327**, p.L73.
- Wang Y.M. 1981. Spin-reversed accretion as the cause of intermittent spin-down in slow X-ray pulsars. *Astronomy & Astrophysics*, **102**, p.36.
- Wang Y.M., Nepveu M., and Robertson J.A. 1984. Further numerical studies of the Rayleigh-Taylor instability in the context of accreting X-ray sources. *Astronomy & Astrophysics*, **135**, p.66.
- Wang Y.M. and Robertson J.A. 1984. A numerical investigation of the Kelvin-Helmholtz instability in the context of accreting neutron stars. *Astronomy & Astrophysics*, **139**, p.93.

- Wang Y.M. and Robertson J.A. 1985. Late stages of the Rayleigh–Taylor instability: A numerical study in the context of accreting neutron stars. *Astrophysical Journal*, **299**, p.85.
- Wang Y.M. and Welter G.L. 1980. Plasma–magnetospheric interaction in X-ray sources: An analysis of the linear K–H instability. *Astronomy & Astrophysics*, **113**, p.113.
- Weymann R. 1965. Diffusion approximation for a photon gas interacting with a plasma via the Compton effect. *Phys. Fluids*, **8**, p.2112.
- White N.E. 1985. Massive X-ray binaries. In *Interacting Binaries, NATO ASI Series, Vol.150*, Eggleton P.P. and Pringle J.E., editors, page 249. Reidel Pub. Co.
- Zeldovich Y.B. and Novikov I.D. 1971. *Relativistic Astrophysics*, volume I. University of Chicago Press, Chicago.

6 Noisy Wind Accretion Model

In this Chapter we will develop a phenomenological model in which the accretion onto a neutron star does not occur from a continuous flux of plasma, but from blobs of matter which are threaded by the magnetic field lines onto the magnetic polar caps of the neutron star. These “lumps” are not the inhomogeneities present in the stellar wind coming from the optical companion, as those observed in the two wind-fed pulsars 4U 1538–52 (see Chapter 3) and Vela X–1 (Nagase *et al.*, 1986), but are produced at the magnetospheric radius r_m (see Chapter 5 for its definition) by magnetohydrodynamical instability (Arons and Lea, 1976b; Arons and Lea, 1976a). Once formed, these blobs of plasma fall toward the neutron star surface since they are channeled by the magnetic field lines onto the magnetic polar caps, where their kinetic energy is converted into X-ray radiation in the process of deceleration. In this frame, it is easy to understand that a sort of “noise” is introduced in the accretion process, due to the discontinuity in the flux of matter onto the neutron star.

It is possible to find in literature numerous models for non homogeneous accretion onto neutron stars (Arons and Lea, 1980; Hameury *et al.*, 1980; Morfill *et al.*, 1984; Demmel *et al.*, 1990), essentially developed for explaining the super Eddington luminosity observed in some X-ray pulsars (*e.g.* the X-ray transient A0538–66 shows a peak X-ray luminosity of 10^{39} erg/sec (White and Carpenter, 1978)), but here we will link a physical description of accretion to a statistical description of the “noise” generated in the X-ray emission by the accretion process. This type of analysis has been performed for isolated pulsars (Lamb *et al.*, 1978a; Lamb *et al.*, 1978b), in order to obtain information of the internal structure of the neutron star, but it is the first time that a statistical description of the “noise” present in the X-ray flux of an X-ray pulsar has been linked to the physics of the magnetohydrodynamical instabilities at the magnetospheric limit.

This Chapter will be divided into two main parts: in the first part of the Chapter we will develop a statistical model able to describe the presence of an inflexion point in the power spectra of GX 301–2: we will describe the non coherent component of the X-ray flux as a shot noise process with a special response function (depending on two free parameters α and β). We will further derive some relations between the two free parameters of the model in order to obtain the inflexion point in the frequency range observed. In the second part the physical scenario of noisy accretion will be described, by assuming the theory of plasma penetration developed in a series of papers by Arons and Lea (Arons and Lea, 1976b; Arons and Lea, 1976a; Arons and Lea, 1980) (this theory is described into details in Chapter 5; for a review see Hayakawa, 1985). In the frame of this theory we will derive the physical properties of the “lumps” of matter falling onto the neutron star. Then we will link the two descriptions, by describing a general time series observed from an X-ray pulsar as the sum of the effects due to the discrete blobs falling onto the neutron star (*i.e.* a shot noise process). Finally, we will compare the theoretical with the observed power spectra, in order to extract information on the physical parameters of the magnetohydrodynamical instability.

6.1 Statistical Description

In this Section we will treat the statistical description of power spectra, in particular we will compute the power spectrum of a shot noise process with a special response function (see *e.g.* Papoulis (1965) for definitions and theorems on the shot noise process), which is able to describe in a simple form and with only two free parameters the change of slope observed in the power spectra of GX 301-2. It is important to stress here that our theoretical power spectra do not take into account the effects due counting statistics, time resolution and finite observing time (these effects have been evaluated by Sutherland *et al.*, 1978), but they are computed only to extract a quantitative information on the behaviour of the shape of the spectra. In other words we will not perform any fit to the observed spectra in order to derive the values of the free parameters.

Let us first begin with some definitions.

6.1.1 Power Spectrum of a Shot Noise Process

First of all, let us define a shot noise process. Consider a series of t_i points distributed according to a Poisson distribution¹. Let us consider a stochastic function $x(t)$ defined as follows (Papoulis, 1965):

1. $x(0) = 0$
2. $x(t_2) - x(t_1) = \text{number of points in the interval } t_2 - t_1.$

Then the family of functions $x(t)$ is called a *Poisson process*.

With t_i distributed according to a Poisson distribution, let us form the following stochastic process:

$$z(t) = \sum_i \delta(t - t_i). \quad (6.1)$$

with $\delta(x)$ the Dirac delta-function. This process consists of a succession of pulses in the points t_i .

If $x(t)$ is a Poisson process and

$$y(t) = \frac{x(t + \varepsilon) - x(t)}{\varepsilon} \quad (6.2)$$

we have that

$$z(t) = \frac{d x(t)}{dt} = \lim_{\varepsilon \rightarrow 0} y(t). \quad (6.3)$$

From this relation follows that

$$E\{z(t)\} = \lim_{\varepsilon \rightarrow 0} \frac{E\{x(t + \varepsilon)\} - E\{x(t)\}}{\varepsilon} = \lambda \quad (6.4)$$

in which we assume that λ does not depend on time.

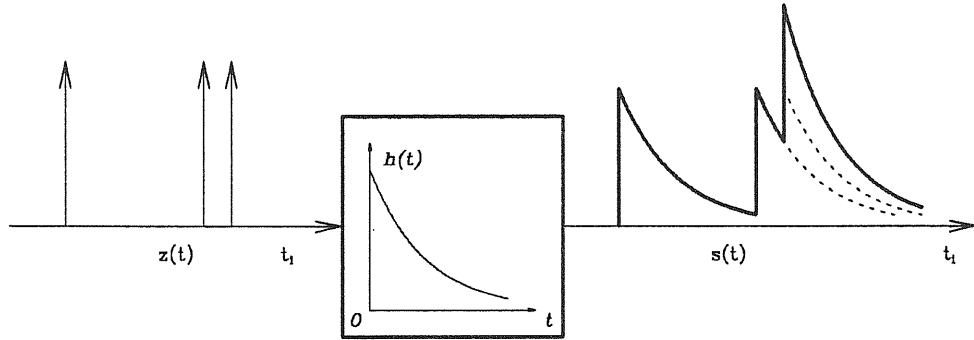
We define a shot noise process $s(t)$ as

$$s(t) = \sum_i h(t - t_i) \quad (6.5)$$

¹From a physical point of view, a Poisson distribution is generated by processes in which a large number of cells, squares, leaves, petals, or interval of time are hit by a relatively small number of events (births, deaths, blood cells, particles of nuclear decay, balls, etc) such that the occurrence or non occurrence of an event in any interval has no effect on the further occurrence or non occurrence in that interval and that the probability of two or more occurrences in a short interval of time is almost zero; *i.e.* a cell (or interval) with lots of counts is as likely to get another count as a cell with fewer counts or no counts at all (Consul, 1989).

obtained shifting of t_i ; the function $h(t)$, which is called response function. We can consider the shot noise as the output signal of a linear system, with input signal $z(t)$ and response $h(t)$

$$s(t) = z(t) * h(t) \quad (6.6)$$



The frequency spectrum of a shot noise process, by means of Eq. 6.6, is

$$S_s(f) = S_z(f) |H(f)|^2 \quad (6.7a)$$

where $H(f)$ is the Fourier transform of $h(t)$.

Because, by definition, t_i are Poissonian distributed, we will have from Eq. 6.4

$$E\{z(t)\} = \lambda \quad \sigma^2 = \lambda \quad (6.7b)$$

$$R_z(\tau) = \lambda^2 + \lambda \delta(\tau). \quad (6.7c)$$

So we can write

$$S_z(f) = \int_{-\infty}^{+\infty} \exp[-if\tau] R_z(\tau) d\tau = 2\pi\lambda^2\delta(f) + \lambda. \quad (6.8)$$

The power spectrum of a shot noise process, according to Eq. 6.7a, is given by

$$\begin{aligned} S_s(f) &= [2\pi\lambda^2\delta(f) + \lambda] |H(f)|^2 \\ &= 2\pi\lambda^2 H^2(0) \delta(f) + \lambda |H(f)|^2. \end{aligned} \quad (6.9a)$$

Furthermore we have (Campbell theorem)

$$E\{s(t)\} = \lambda \int_{-\infty}^{+\infty} h(t) dt \quad \sigma^2 = \lambda \int_{-\infty}^{+\infty} h^2(t) dt \quad (6.9b)$$

$$R_s(\tau) = \lambda^2 H^2(0) + \lambda \int_{-\infty}^{+\infty} h(\tau + \beta) h(\beta) d\beta. \quad (6.9c)$$

6.1.1.1 Exponential Shot Noise

As an example, let us consider the response function defined as

$$h(t) = A \exp[-\alpha t] u(t) \quad u(t) = \begin{cases} 0 & t < 0 \\ 1 & t \geq 0. \end{cases} \quad (6.10)$$

($u(t)$ is also called step function). The Fourier transform of $h(t)$ is

$$H(f) = A \int_{-\infty}^{+\infty} \exp[-\alpha t] u(t) \exp[-ift] dt = \frac{A}{\alpha + if} \quad (6.11)$$

$$|H(f)|^2 = \frac{A^2}{\alpha^2 + f^2} \quad (6.12)$$

and, from Eqs. 6.9, it follows

$$S_s(f) = A^2 \left(\frac{2\pi\lambda^2}{\alpha^2} \delta(f) + \frac{\lambda}{\alpha^2 + f^2} \right) \quad (6.13a)$$

$$E\{s(t)\} = A \frac{\lambda}{\alpha} \quad \sigma_s^2 = A^2 \frac{\lambda}{2\alpha} \quad (6.13b)$$

$$R_s(\tau) = A^2 \left(\frac{\lambda^2}{\alpha^2} + \frac{\lambda}{2\alpha} \exp[-\alpha|\tau|] \right). \quad (6.13c)$$

6.1.1.2 Oscillating Exponential Shot Noise

Let us suppose that the response function $h(t)$ has the form

$$h(t) = (A \sin \beta t + B \cos \beta t) \exp[-\alpha t] u(t). \quad (6.14)$$

To compute its power spectrum, let us call

$$h^{(1)}(t) = A \sin \beta t \exp[-\alpha t] u(t)$$

$$h^{(2)}(t) = B \cos \beta t \exp[-\alpha t] u(t)$$

Their Fourier transforms are

$$H^{(1)}(f) = \frac{A\beta}{(\alpha + if)^2 + \beta^2} \quad H^{(2)}(f) = \frac{B(\alpha + if)}{(\alpha + if)^2 + \beta^2} \quad (6.15)$$

The Fourier transform of $h(t)$ is

$$H(f) = \frac{A\beta + B(\alpha + if)}{(\alpha + if)^2 + \beta^2} \quad (6.16)$$

and so

$$|H(f)|^2 = \frac{(A\beta + \alpha B)^2 + B^2 f^2}{(\alpha^2 + \beta^2 - f^2)^2 + 4\alpha^2 f^2} \quad (6.17)$$

The power spectrum of an oscillating exponential shot noise is

$$S_s(f) = 2\pi\lambda^2 \left(\frac{A\beta + \alpha B}{\alpha^2 + \beta^2} \right)^2 \delta(f) + \lambda \frac{(A\beta + \alpha B)^2 + B^2 f^2}{(\alpha^2 + \beta^2 - f^2)^2 + 4\alpha^2 f^2} \quad (6.18a)$$

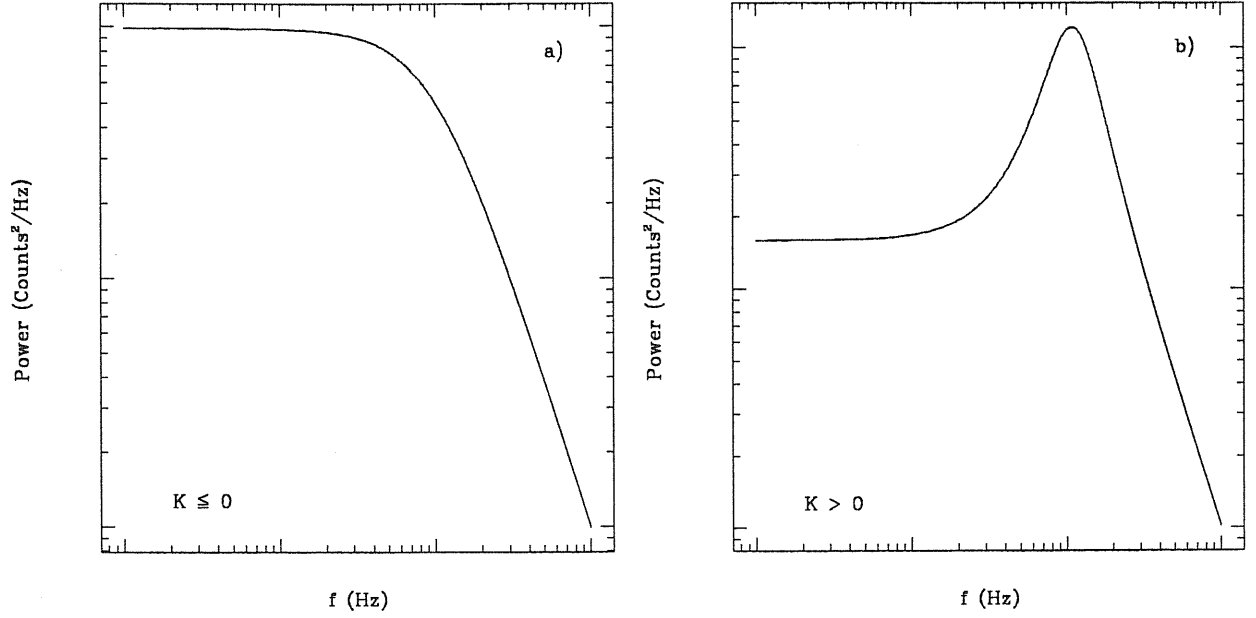


Figure 6.1: Form of the power spectrum of an oscillating exponential shot noise, according to the K parameter (for simplicity we show here the case $A = 0$). Case a) corresponds to $K \leq 0$; Case b) to the case $K \geq 0$.

and

$$E\{s(t)\} = \lambda \left(\frac{A\beta + \alpha B}{\alpha^2 + \beta^2} \right) \quad \sigma^2 = \frac{\lambda}{4\alpha} \left(\frac{(A\beta + \alpha B)^2}{\alpha^2 + \beta^2} + B^2 \right) \quad (6.18b)$$

Note that in the case $A = 0$, $B = 1$ and $\beta = 0$ we obtain the results of the previous Section.

By studying Eq. 6.18a we can easily see that the power spectrum shape changes according to the parameter K , defined as

$$K \equiv B^2(\alpha^2 + \beta^2)^2 + 2(A\beta + \alpha B)^2(\alpha^2 + \beta^2) - 4\alpha^2(A\beta + \alpha B)^2. \quad (6.19)$$

If $K \leq 0$ then the power spectrum has the typical shape of a shot noise process (see Fig. 6.1a); when $K \geq 0$ the shape is completely different, showing a maximum at a given frequency f_{\max} and an inflexion point (see Fig. 6.1b). In the latter case, the abscissa of the maximum is given by

$$f_{\max} = \sqrt{\frac{-(A\beta + \alpha B)^2 + \sqrt{(A\beta + \alpha B)^4 + KB^2}}{B^2}}. \quad (6.20)$$

In the particular case $A = 0$ (Cosinusoidal Exponential Shot Noise), we have that Case a) is achieved if

$$\alpha^4 - 4\alpha^2\beta^2 - \beta^4 \geq 0. \quad (6.21)$$

independent of the amplitude B . The two regions defined in the above expression in the α^2 - β^2 plane are shown in Fig. 6.2.

In the case $A = 0$ Eq. 6.20 becomes

$$f_{\max}^{A=0} = \sqrt{\beta^2 \sqrt{1 + \left(\frac{2\alpha}{\beta}\right)^2} - \alpha^2}. \quad (6.22)$$

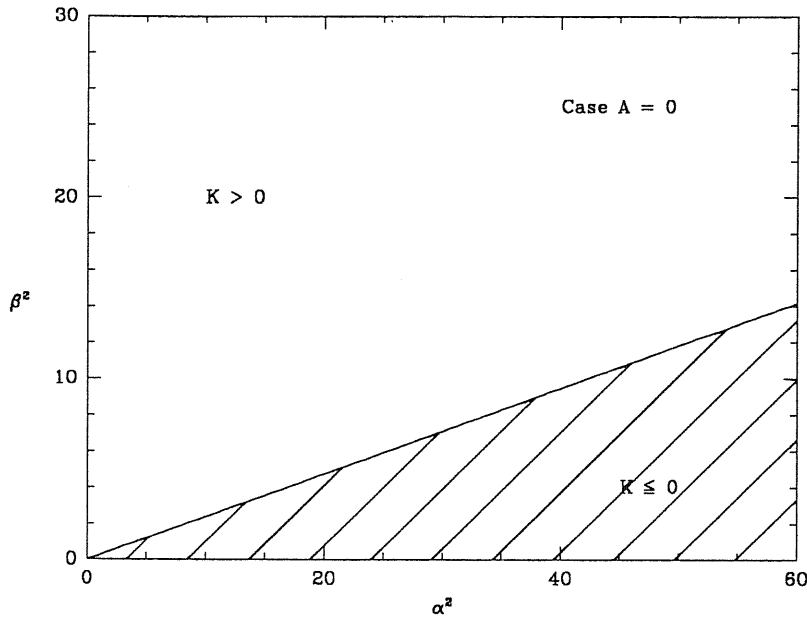


Figure 6.2: The α^2 - β^2 plane and the two different solutions for the power spectrum shape of an oscillating exponential shot noise with $A = 0$. The shadowed region corresponds to the case $K \leq 0$.

The position of the inflexion point in the power spectrum, *i.e.* the point at which the change of slope occurs, is obtained by imposing

$$\frac{d^2 S_s(f)}{d f^2} = 0. \quad (6.23)$$

Substituting Eq. 6.18a in Eq. 6.23 we obtain a eighth order polynomial in f , the coefficients of which are² (the odd coefficients are all null)

$$\begin{aligned} C_8 &= 3B^2 \\ C_6 &= 2\beta^2 B^2 + 8\alpha^2 B^2 + 10\beta^2 A^2 + 20\alpha\beta AB \\ C_4 &= 6\alpha^4 B^2 - 12\beta^4 B^2 - 18\beta^4 A^2 - 42\alpha^2 \beta^2 B^2 + 18\alpha^2 \beta^2 A^2 + 36\alpha^3 \beta AB - 36\alpha \beta^3 AB \\ C_2 &= 6\beta(\beta^5 B^2 + \beta^5 A^2 - 7\alpha^4 \beta B^2 + 2\alpha^2 \beta^3 B^2 + \alpha^4 \beta A^2 - 6\alpha^2 \beta^3 A^2 + 2\alpha^5 AB - 12\alpha^3 \beta^2 AB + 2\alpha \beta^4 AB) \\ C_0 &= (\alpha^2 + \beta^2)^2 (2\beta^4 A^2 - 2\alpha^2 \beta^2 A^2 + 4\alpha \beta^3 AB - 4\alpha^3 \beta AB + \beta^4 B^2 + 4\alpha^2 \beta^2 B^2 - \alpha^4 B^2) \end{aligned}$$

Thereafter we will treat the case $A = 0$ (and the corresponding quantites will be denoted with an hat above); the five coefficients above become

$$\begin{aligned} \hat{C}_8 &= 3B^2 \\ \hat{C}_6 &= 2B^2(4\alpha^2 + \beta^2) \\ \hat{C}_4 &= 6B^2(\alpha^4 - 7\alpha^2 \beta^2 - 2\beta^4) \\ \hat{C}_2 &= -6\beta^2 B^2(7\alpha^4 - 2\alpha^2 \beta^2 - \beta^4) \\ \hat{C}_0 &= -B^2(\alpha^2 + \beta^2)^2(\alpha^4 - 4\alpha^2 \beta^2 - \beta^4). \end{aligned}$$

To check quantitatively this model we need some physical interpretation of the parameters α , β

²All the analytical computations have been checked with MAPLE (version 4.1, May 1987), an interactive algebraic manipulator developed by the University of Waterloo, Canada.

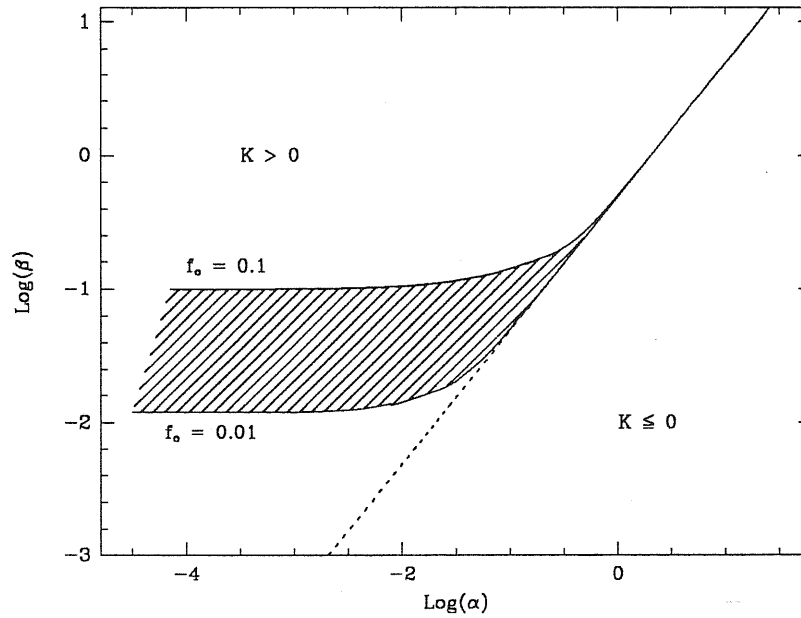


Figure 6.3: Allowed values of α and β for being in agreement with the observed inflexion point in the GX 301-2 power spectra. The dotted line corresponds to Eq. 6.26, *i.e.* the relation determining the shape of a power spectrum in our model. The values of α and β compatible with the observed inflexion point in the GX 301-2 power spectra are shown as a shadowed region. Note that, for $\alpha \gtrsim 1$, α and β converge to the relation of Eq. 6.26.

and B , some numerical value for them, to solve the equation

$$\sum_{n=0}^4 \hat{C}_{2n} f^{2n} = 0 \quad (6.24)$$

with the coefficients \hat{C}_{2n} given above (therefore the dependence on B disappears), and to compare the numerical solution with the observed position of the inflexion point $0.01 < f_o < 0.1$, obtained from the GX 301-2 power spectra.

On the other hand, we can obtain a relation between α and β by imposing $0.01 < f_o < 0.1$ in Eq. 6.24 which can be rewritten as a polynomial in β^2 of the form

$$\sum_{n=0}^4 \hat{B}_n (\beta^2)^n = 0 \quad (6.25)$$

with the four coefficients \hat{B}_n , function of the solution f_o and α^2 , given by

$$\begin{aligned} \hat{B}_4 &= 1 \\ \hat{B}_3 &= 6(\alpha^2 + f_o^2) \\ \hat{B}_2 &= 4(2\alpha^4 + 3\alpha^2 f_o^2 - 3f_o^4) \\ \hat{B}_1 &= 2(\alpha^2 + f_o^2)(\alpha^2 - 22\alpha^2 f_o^2 + f_o^4) \\ \hat{B}_0 &= -(\alpha^2 - 3f_o^2)(\alpha^2 + f_o^2)^3. \end{aligned}$$

In Fig. 6.3 we show the numerical solutions of Eq. 6.25 in the α - β plane for α ranging over seven orders of magnitude, together with the relation of Eq. 6.21, corresponding to the two cases $K \leq 0$. We can see that for $\alpha \gtrsim 1$ the allowed values of α and β compatible with the inflexion point at $f = f_o$ belong to the curve

$$\beta = (\sqrt{5} - 2)^{1/2} \alpha \approx \frac{1}{2} \alpha. \quad (6.26)$$

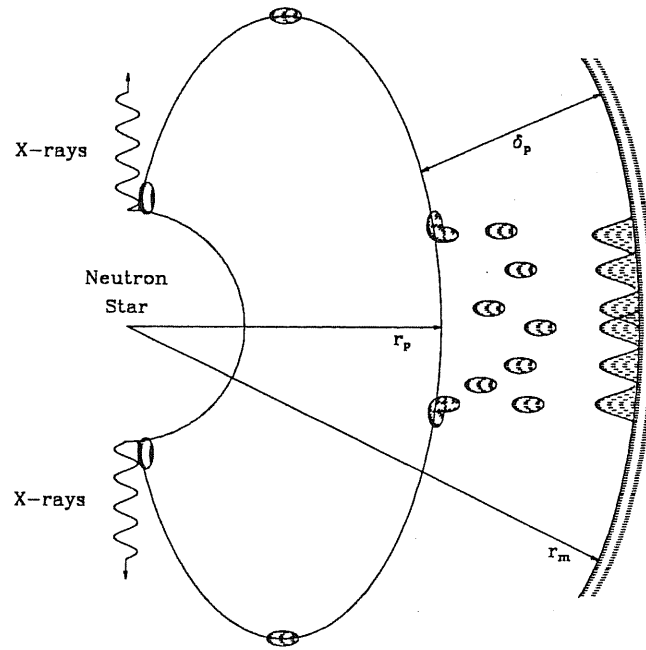


Figure 6.4: Picture of the physical scenario of noisy wind accretion. The picture is not in scale; it has been enlarged for clarity.

For $\alpha \lesssim 1$ we have a region of allowed solutions (shadowed in Fig. 6.3) but, in both cases, the solutions belong to the $K > 0$ plane (see Fig. 6.2).

6.2 Physical Scenario

Let us first describe our physical scenario of discrete accretion onto a neutron star from a stellar wind (see Fig. 6.4). As discussed in the Introduction, the stellar wind coming from the optical companion of the neutron star is captured by its intense gravitational field and accreted. The strong magnetic field halts the incoming matter at a distance of the order of $r_m \approx 10^8$ cm from the neutron star surface. At a distance of Δ_s above r_m a standoff shock forms; because the magnetosphere is magnetohydrodynamically unstable, plasma can enter in form of long filaments of mean width $\approx \pi r_m / m_0$ and mean length³ $\approx \pi r_m / \sqrt{m_0}$, where m_0 is the mode number which describe the dominant scale height at the equilibrium, defined as (Arons and Lea, 1976b)

$$m_0 \equiv b \frac{\mathcal{R}(\theta)}{\Delta_s} \approx 15 \left(\frac{\mathcal{L}_x}{10^{37} \text{ erg/sec}} \right)^{32/35} \left(\frac{\mu}{10^{30} \text{ G cm}^3} \right)^{6/35} \left(\frac{M_x}{M_\odot} \right)^{-47/35} \quad (6.27)$$

where $b \simeq 2$, $\mathcal{R}(\theta)$ is the equilibrium shape of the magnetosphere as a function of the magnetic latitude θ , in units of r_m , and μ is the magnetic moment of the dipolar magnetic field. We have assumed an efficiency of the accretion process, defined as $\mathcal{L}_x = \epsilon \dot{M}_x c^2$, equal to 0.1. As previously discussed in Chapter 5, the blob dimension strongly depends on the Compton cooling of the plasma

³For simplicity we will assume spherical blobs since the time scale necessary to change their length is longer with respect to the flight time necessary to cover a distance r (Arons and Lea, 1980).

behind the shock. Because Eq. 6.27 is valid it is necessary that the X-ray luminosity of the neutron star is (Arons and Lea, 1980)

$$L_{37} > 0.01 \mu_{30} m^{-47/32} \quad (6.28)$$

where L_{37} is the X-ray luminosity in units of 10^{37} erg/sec, μ_{30} is the magnetic moment in unit of 10^{30} G cm³ and m is the neutron star mass in solar mass units.

Furthermore, for allowing penetration, the buoyancy force acting on a blob must be smaller than the ram pressure, therefore a constraint results, *i.e.* (see Eq. 5.66)

$$\Omega_p \ll \frac{\Omega_K(r_m)}{\sqrt{m_0}} \quad (6.29)$$

which corresponds to a constraint in the pulse period

$$P_p \gg 17 L_{37}^{1/5} \mu_{30}^{33/35} m^{-97/70} \text{ sec.} \quad (6.30)$$

As the last request, we impose that the specific angular momentum carried by the accreting matter is much less than the Keplerian angular momentum, in order for plasma to not corotate but radially fall toward the neutron star surface. This is equivalent to impose that the total relative velocity of matter at the accretion radius (*i.e.* including thermal motion) satisfies

$$v > 700 \left(\frac{M_\star}{20 M_\odot} \right)^{1/8} \left(\frac{D}{10^{12} \text{ cm}} \right)^{-3/8} m^{157/280} L_{37}^{3/20} \mu_{30}^{1/20} \text{ Km/sec} \quad (6.31)$$

where M_\star is the mass of the optical star and D is the orbital separation (Arons and Lea, 1980). These requirements are satisfied by GX 301-2 (Burnard *et al.*, 1983), therefore this theory of plasma penetration is applicable to this source. Once formed, the blobs fall toward the neutron star surface. At the beginning Compton cooling is very efficient and therefore the blob temperature is constant, equal to the X-ray temperature. This corresponds to a increase of the blob density ρ_b as r^{-6} (we assume a dipolar magnetic field) and a consequent decrease of the blob radius r_b as r^2 . Assuming a constant mass blob, we have (Arons and Lea, 1980; Hayakawa, 1985)

$$r_b(r) = \pi \left(\frac{r_m}{m_0} \right) \left(\frac{r}{r_m} \right)^2 \approx 2.5 \cdot 10^7 \mu_{30}^{2/5} L_{37}^{-6/5} m^{6/5} \left(\frac{r}{r_m} \right)^2 \left(\frac{\mathcal{R}(\theta)}{(1 + 3 \sin^2 \theta)^{1/3}} \right) \text{ cm} \quad (6.32a)$$

$$\rho_b(r) = \rho_{ff}(r_m) \frac{v_{ff}(r_m)}{v_{abs}(r_m)} \left(\frac{r_m}{r} \right)^6 \approx 7.6 \cdot 10^{-10} \mu_{30}^{-27/35} L_{37}^{66/35} m^{-67/70} \left(\frac{r_m}{r} \right)^6 \text{ g/cm}^3 \quad (6.32b)$$

where the absorption velocity v_{abs} is defined in Eq. 5.58. For $r \lesssim 0.1 r_m$, Eqs. 6.32 are substituted by (Hayakawa, 1985)

$$r'_b(r) = r_b(r) \left(\frac{r_x}{r} \right)^{1/6} \quad \rho'_b(r) = \rho_b(r) \left(\frac{r}{r_x} \right)^{1/2}. \quad (6.32c)$$

We furthermore assume a free fall velocity of the blobs through the magnetic field at a given magnetic latitude θ , given by (Arons and Lea, 1980)

$$v_b(r, \theta) = \sqrt{\frac{2GM_x}{r} \left(1 - \frac{r}{r_m} + a^2 \frac{r}{r_m} \right)} \approx \sqrt{\frac{2GM_x}{r} \left(1 - \frac{r}{r_m} \right)} \quad (6.32d)$$

where the parameter a is of the order of 0.1.

At the magnetospheric interface we will have two fluids: the outer plasma, of density ρ_{out} , and the inner plasma, of density ρ_{in} . The outer fluid is denser than the inner but cooler.

At the plasmopause the infalling blobs are channeled by the magnetic field lines toward the neutron star polar caps. At this distance particles will exchange angular momentum with the surrounding radiation field by the emission of Alfvén waves (Arons and Lea, 1980), leading to the confinement of the motion in a thin skin around the force line.

The last quantities we need are some characteristic time scales. One will be related to the rate of formation of the blobs, the other to the dynamical time scale of falling of the blobs. To compute the former, let us remind that, as we have seen in the previous Chapter, the linear growth time for Rayleigh–Taylor instability is (Chandrasekhar, 1961)

$$\omega_{\text{RT}}^2(k) = g_{\text{eff}} k \left(\frac{\rho_{\text{out}} - \rho_{\text{in}}}{\rho_{\text{out}} + \rho_{\text{in}}} \right) \quad (6.33)$$

where g_{eff} is the effective gravitational field and $k = 2\pi/\lambda$ is the wave number relative to a perturbation of wavelength λ . With this definition, the characteristic time scale for growing of instabilities becomes

$$\tau_{\text{RT}} \equiv \frac{1}{\omega_{\text{RT}}} = \sqrt{\frac{\lambda}{2\pi g} \left(\frac{\rho_{\text{out}} + \rho_{\text{in}}}{\rho_{\text{out}} - \rho_{\text{in}}} \right)}. \quad (6.34)$$

Including the effect of magnetic tension, this time scale will be increased by a factor of the order of (Wang and Robertson, 1985)

$$\alpha_{\text{RT}} = \left[1 - \frac{B_r^2}{4\pi\rho_{\text{out}}g_{\text{eff}}r_{\text{m}}} \right]^{-1/2} \quad (6.35)$$

where B_r is the component of the magnetic field in the radial direction.

We will assume that the outer density ρ_{out} be a factor Γ higher than the free fall density at r_{m} ; furthermore we apply the Rankine–Hugoniot condition at the jump (Frank *et al.*, 1985) (the flow is highly supersonic. See Chapter 5) and we put $\lambda \approx r_b(r_{\text{m}})$, obtaining

$$\tau_{\text{RT}} \approx \alpha_{\text{RT}} \sqrt{\frac{5}{6\pi} \frac{r_{\text{m}}^2}{GM_x}} r_b(r_{\text{m}}) \approx \sqrt{\frac{5}{6\pi} \frac{r_{\text{m}}^2}{GM_x}} r_b(r_{\text{m}}) \left(1 - \frac{\mu^2}{\Gamma} \sqrt{\frac{2}{GM_x} \frac{1}{M_x} r_{\text{m}}^{-7/2}} \right)^{-1} \quad (6.36)$$

The dynamical time scale of free falling of the blobs from $r = r_{\text{m}}$ to $r = r_x$ is given by

$$\tau_{\text{dy}} = \frac{1}{\sqrt{2GM_x}} (r_{\text{m}}^{3/2} - r_x^{3/2}) \approx \frac{r_{\text{m}}^{3/2}}{\sqrt{2GM_x}} \quad (6.37)$$

obtained by Eq. 6.32d neglecting the a^2 term.

The last quantity we computed is the free fall time of a blob onto a polar cap, defined as (Morfill *et al.*, 1984)

$$\tau_{\text{ff}} \equiv \frac{2}{3} \frac{r_x}{v_b(r_x)} \left[\left(\frac{r_x + r_b(r_x)}{r_x} \right)^{3/2} - 1 \right]. \quad (6.38)$$

Now we have all the elements to compute the physical parameters of the infalling blobs for the X-ray binary pulsar GX 301–2. The magnetospheric radius for this source is $r_{\text{m}} = 6 \cdot 10^8$ cm. We will further assume a plasmopause radius (see Chapter 5 for its definition) of the order of $r_p \approx 10^7$ cm. In Table 6.1 the results are summarized for two different X-ray luminosity states.

Low State	High State	Reference
$\mathcal{L}_x \approx 10^{36}$ erg/sec	$\mathcal{L}_x \approx 10^{37}$ erg/sec	
$\dot{M}_x \approx 10^{16}$ g/sec	$\dot{M}_x \approx 10^{17}$ g/sec	
$r_b(r_m) = 6 \cdot 10^8$ cm	$r_b(r_m) = 3.7 \cdot 10^8$ cm	Eq. 6.32a
$\rho_b(r_m) = 7.2 \cdot 10^{-12}$ g/cm ³	$\rho_b(r_m) = 5.5 \cdot 10^{-10}$ g/cm ³	Eq. 6.32b
$M_b = 6.5 \cdot 10^{15}$ g	$M_b = 1.2 \cdot 10^{14}$ g	
$r_b(r_p) = 1.1 \cdot 10^5$ cm	$r_b(r_p) = 7.0 \cdot 10^3$ cm	Eq. 6.32a
$\rho_b(r_p) = 1.1 \cdot 10^{-1}$ g/cm ³	$\rho_b(r_p) = 8.2 \cdot 10^{-1}$ g/cm ³	Eq. 6.32b
$r_b(r_x) = r_b(r_p)$	$r_b(r_x) = r_b(r_p)$	
$\rho_b(r_x) = \rho_b(r_p)$	$\rho_b(r_x) = \rho_b(r_p)$	
$\alpha_{RT} = (1 - 2/\Gamma)^{-1/2}$	$\alpha_{RT} = (1 - 0.2/\Gamma)^{-1/2}$	Eq. 6.35
$\tau_{RT} = 0.55\alpha_{RT}$ sec	$\tau_{RT} = 0.14\alpha_{RT}$ sec	Eq. 6.36
$\tau_{dy} = 0.76$ sec	$\tau_{dy} = 0.76$ sec	Eq. 6.37
$\tau_{ff} = 5.6 \cdot 10^{-6}$ sec	$\tau_{ff} = 3.5 \cdot 10^{-7}$ sec	Eq. 6.38

Table 6.1: Blob physical properties computed for the X-ray binary pulsar GX 301-2. We have assumed a magnetospheric radius $r_m = 6 \cdot 10^8$ cm and a plasmopause radius $r_p = 10^7$ cm. The blob mass is assumed constant, and equal to $4\pi\rho_b r_b^3/3$.

6.3 Comparison with Observations

At this point we have all the information we need to make a quantitative analysis of our phenomenological model. The first step consists in checking whether our results are in agreement with the observed properties of X-ray pulsars, and in particular with the observed properties of GX 301-2. The first constraint on the physical parameters of the instability blobs derives from the observed pulse to pulse variations. The formation rate of the blobs has to be in agreement with the observed luminosity fluctuations. In our model the X-ray luminosity is due to a sum of events that occur randomly (shot noise process)

$$\mathcal{L}_x(t) = \sum_k \mathcal{S}(t - t_k) \quad (6.39)$$

where t_k is the time at which the event (shot) occur. The events occur at an average rate λ (in units of events/sec), and the probability that there is an event between t and $t + dt$ is given by

$$P(t) dt = \lambda e^{-\lambda t} dt. \quad (6.40)$$

With this in mind, the accretion rate \dot{M}_x onto the neutron star will be given by

$$\dot{M}_x = \lambda M_b \quad (6.41)$$

We will set λ equal to τ_{RT}^{-1} , and substituting in Eq. 6.41 the values of \dot{M}_x and M_b from Table 6.1 we have

$$\lambda^{-1} \equiv \tau_{RT} = \frac{M_b}{\dot{M}_x} = \begin{cases} 0.65 & \text{Low State} \\ 0.001 & \text{High State} \end{cases} \quad (6.42)$$

These values are to be compared with the observed value of $\lambda \approx 10^{-2} \text{ sec}^{-1}$ (Morfill *et al.*, 1984). Because of the uncertainty in α_{RT} the agreement is acceptable.

As a cross referenced check, from the observed λ the blob mass is constrained to be of the order of 10^{14} – 10^{15} g. Again the agreement with the blob mass predicted in Table 6.1 is good, and the

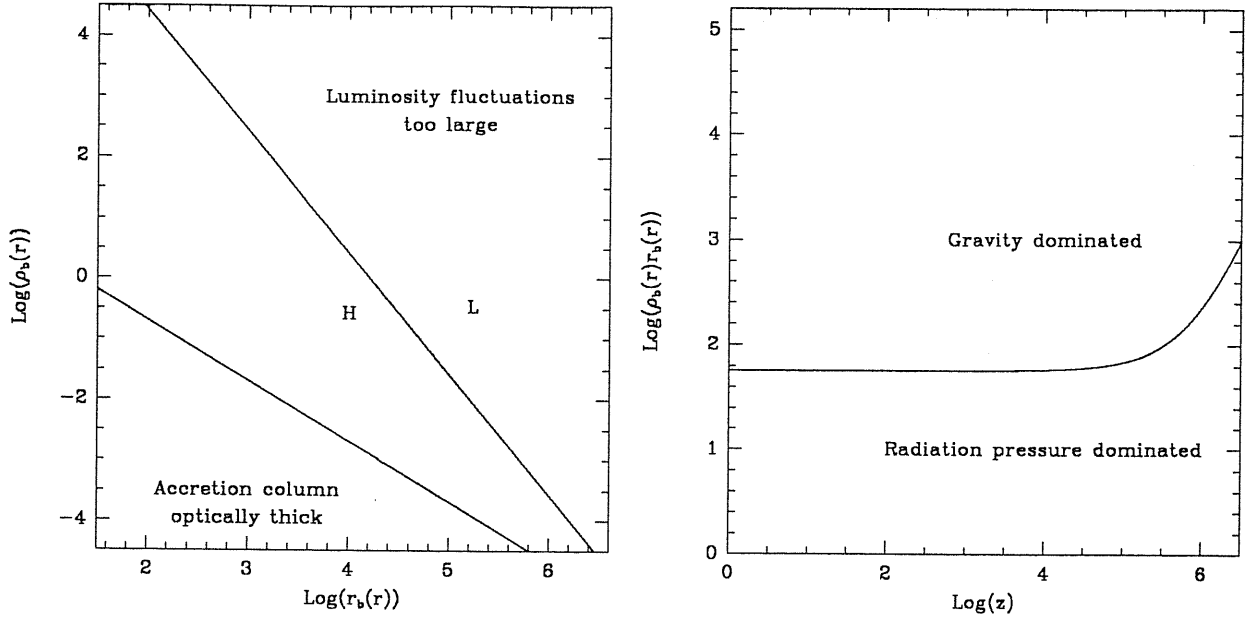


Figure 6.5: Constraints on the physical characteristics of instability blobs derived by imposing (a): accretion column is optically thin and pulse-to-pulse variation are not too large (H and L indicate the blob parameters derived in our model for the High and Low luminosity state, respectively); and (b): radiation pressure does not disrupt the infalling blob (Morfill *et al.*, 1984). In Case (b) the function “(momentum transferred from the polar cap)/(gravitational force acting on the blob) $\equiv 1$ is plotted as a function of the height z above the neutron star surface. Adapted from Morfill *et al.*, 1984.

consistency of the model, too⁴.

The fate of the instability blobs has been analysed in great detail by Morfill *et al.* (1984) (thereafter MO84), even if they treated the problem of accretion from a disk. It is very interesting the coincidence that the blob parameters at the neutron star surface are the same in our model of wind-accretion and their model of disk accretion. In this respect some of MO84 analysis is therefore applicable to our model, too.

MO84 gave some other constraints to the blob physical parameters; in particular they derived a relation between r_b and ρ_b by imposing that the accretion column at the magnetic polar cap of the neutron star is optically thin. This requirement is necessary in order that radiation produced by a blob can escape freely without interact with other falling blobs. They obtained that, in order to have an optically thin accretion column, the relation (Morfill *et al.*, 1984)

$$\rho_b(r_p) r_b(r_p) > \frac{4\dot{M}_x}{\pi^2 r_{\text{cap}} v_b(r_p)} \quad (6.43)$$

has to be satisfied, where r_{cap} is the radius of the polar cap. We have substituted the values of blob density and radius at the plasmopause instead of the same quantities evaluated at the neutron star surface because, in our model, the instability blobs fall freely up to r_p and then are channeled by the magnetic field lines onto the polar caps, therefore the blob properties at the neutron star surface are determined by those at the plasmopause. The second constraint is derived by imposing that the radiation pressure produced by a blob does not disturb and/or disrupt the motion of a subsequent blob. In Fig. 6.5 both the constraints are shown, from which we can see that blobs with $\rho_b(r_p) r_b(r_p) \gtrsim 50$ can reach the neutron star surface and that radiation pressure is not able to

⁴The compression factor Γ , derived equalling the expression of τ_{RT} of Eq. 6.42 and that of Table 6.1 is equal to about 7 (Low State).

disrupt, on average, an infalling blob (this is valid even if the blobs are “peeled off” by the radiation pressure (MO84)).

As the last step in our phenomenological model we need to determine a numerical value for α or β (because the two quantities are related as shown in Fig. 6.3).

In analogy with the theory which describe the flaring activity of our Sun as a shot noise process, we are inclined to associate the time scale α to the duration of a single shot. In this case we have an order of magnitude of this duration given by τ_{ff} (see Eq. 6.38 and Table 6.1), and therefore we will have

$$\alpha \approx \tau_{\text{ff}}^{-1} \approx 10^5 - 10^6 \text{ sec}^{-1} \quad (6.44)$$

where the range for α corresponds to the two luminosity states discussed in Table 6.1. Furthermore, from Fig. 6.3 we can obtain an estimate for β , which has to be

$$\beta \approx 0.5\alpha \approx 5 \cdot 10^4 - 5 \cdot 10^5 \text{ sec}^{-1} \quad (6.45)$$

in order to have the inflexion point in the observed power spectra in the frequency range 0.01–0.1 Hz. We are inclined to associate the oscillating part of the response function to a process of interaction of the radiation emitted with the strongly magnetized plasma surrounding the neutron star. A process which is surely important in the dynamics of the blobs is Compton cooling. Therefore let us assume as the physical process associated to the oscillating part the inverse Compton cooling of the infalling blobs. The time scale associated to this process is (Weymann, 1965)

$$\tau_c = \frac{3m_e c}{8\sigma_T u_r} \quad (6.46)$$

where σ_T is the Thomson scattering cross section and $u_r = \mathcal{L}_x / 4\pi r^2 c$ is the radiation energy density (see also Chapter 5). Inserting in Eq. 6.46 the X-ray luminosity of a blob, of the order of $\mathcal{L}_x / 100$, and its radius (from Table 6.1) we obtain the same order of magnitude shown in Eq. 6.45.

Of course, this is based on a phenomenological ground: the only observational evidence in favour of this hypothesis is the fact that the typical time scale of Compton cooling is of the order of $10^{-5} - 10^{-6}$ sec or less, *i.e.* of the same order of magnitude of β^{-1} . We cannot exclude other physical processes which might have time scales of the same order of magnitude of the Compton process: this is only an observation of the equality of two time scales. With this in mind we can describe the two parts of the response function from a phenomenological point of view as follows: the “exponential” part is connected with the duration of a single shot while the “oscillating” part is related with the interaction of the emitted X-rays with the surrounding plasma (one process should be Compton cooling of the blobs).

Bibliography

- Arons J. and Lea S.M. 1976a. Accretion onto magnetized neutron stars: Normal mode analysis of the interchange instability at the magnetopause. *Astrophysical Journal*, **210**, p.792.
- Arons J. and Lea S.M. 1976b. Accretion onto magnetized neutron stars: Structure and interchange instability of a model magnetosphere. *Astrophysical Journal*, **207**, p.914.
- Arons J. and Lea S.M. 1980. Accretion onto magnetized neutron stars: The fate of sinking filaments. *Astrophysical Journal*, **235**, p.1016.
- Burnard D.J., Lea S.M., and Arons J. 1983. Accretion onto magnetized neutron stars: X-ray pulsars with intermediate rotation rates. *Astrophysical Journal*, **266**, p.175.
- Chandrasekhar S. 1961. *Hydrodynamic and Hydromagnetic Stability*. Oxford University Press, Oxford.
- Consul P.C. 1989. *Generalized Poisson Distributions*. Marcel Dekker Inc., New York.

- Demmel V., Morfill G., and Atmanspacher H. 1990. A discrete-time model for inhomogeneous spherical accretion onto neutron stars. *Astrophysical Journal*, **354**, p.616.
- Frank J., King A.R., and Raine D.J. 1985. *Accretion Processes in Astrophysics*. Cambridge University Press, Cambridge.
- Hameury J.M., Bonazzola S., and Heyvaerts J. 1980. Stability of accretion column flows. *Astronomy & Astrophysics*, **90**, p.359.
- Hayakawa S. 1985. X-rays from accreting neutron stars. *Physics Reports*, **121**, p.318.
- Lamb F.K., Pines D., and Shaham J. 1978a. Period variations in pulsating X-ray sources. I. Accretion flow parameters and neutron star structure from timing observations. *Astrophysical Journal*, **224**, p.969.
- Lamb F.K., Pines D., and Shaham J. 1978b. Period variations in pulsating X-ray sources. II. Torque variations and stellar response. *Astrophysical Journal*, **225**, p.582.
- Morfill G.E., Trümper J., Bodenheimer P., and Tenorio-Tangle G. 1984. Nonstationary accretion onto neutron stars: some constraints and consequences. *Astronomy & Astrophysics*, **139**, p.7.
- Nagase F., Hayakawa S., Sato N., Masai K., and Inoue H. 1986. Circumstellar matter in the Vela X-1/HD 77581 system. *Publ. Astron. Soc. Japan*, **38**, p.547.
- Papoulis A. 1965. *Probability, Random Variables, and Stochastic Processes*. McGraw-Hill, New York.
- Sutherland P.G., Weisskopf M.C., and Kahn S.M. 1978. Short-term variability of Cygnus X-1. II. *Astrophysical Journal*, **219**, p.1029.
- Wang Y.M. and Robertson J.A. 1985. Late stages of the Rayleigh-Taylor instability: A numerical study in the context of accreting neutron stars. *Astrophysical Journal*, **299**, p.85.
- Weymann R. 1965. Diffusion approximation for a photon gas interacting with a plasma via the Compton effect. *Phys. Fluids*, **8**, p.2112.
- White N.E. and Carpenter G.F. 1978. The recurrent X-ray transient A0538-66. *Monthly Notices of R.a.S.*, **183**, p.11P.

7 Summary and Conclusions

The main goal of this Thesis was to try to clarify the physics which is hidden in the aperiodic component of the X-ray flux coming from X-ray binary pulsars. One of the results of the analysis performed on the data of the wind-fed X-ray binary pulsar GX 301-2 was the discovery of a correlation between the root mean square variability (rms) associated to the power frequency spectra and the pulse period derivative, and between the rms and the X-ray luminosity. From a physical ground we expected this type of correlation because rms is connected with the variability in the X-ray intensity which, in turn, is connected with the accretion rate and therefore with the pulse period derivative. In the case of pure Poissonian noise we expect a relation of the type $\text{rms} \propto 1/\sqrt{\langle I \rangle}$, where $\langle I \rangle$ is the mean X-ray intensity. The deviation from this relation can give a measure of the non Poissonian behaviour of the noise associated to the X-ray flux (see Fig. 4.20 for GX 301-2). What we observed is the fact that the relation between rms and $\langle I \rangle$ changed according to the spinning state of the source. Therefore the non Poissonian noise associated to the X-ray flux varies according to the sign of the angular momentum carried by the accreted matter. It should be quite interesting to search for a similar relation between rms and mean X-ray intensity in other X-ray pulsars and to verify whether this relation is universal or it is different from source to source. In the former case, *i.e.* in presence of an universal relation between rms and $\langle I \rangle$, we might assume that the relation is connected with the physics of plasma penetration into the magnetosphere of the neutron star, which is the same for the class of wind-fed binaries. In the case in which the correlation is not universal, but changes from source to source, we might assume that it is connected with some specific physical property of the binary system.

The observation of a change of slope in the power spectra of GX 301-2, and the most important property that the inflexion point is present in *all* the observations, in the same frequency interval, independently of the X-ray intensity and the spinning state of the source, led us to the development of a statistical model of power spectra, namely a shot noise process with a special response function, of the form

$$h(t) = B \cdot \underbrace{\cos \beta t}_{\text{Oscillating}} \cdot \underbrace{\exp[-\alpha t]}_{\text{Exponential}} u(t) \quad (7.1)$$

where $u(t)$ is the step function. Our response function is the product of an “exponential” part and an “oscillating” part, both of them depending on a free parameter. By imposing the position of the inflexion point in the frequency range $0.01 < f_o < 0.1$ we obtain a relation between α and β (it is quite interesting that the same property, *i.e.* the presence of a “knee” at $f \simeq 0.1$ Hz, has been observed in the power spectrum of the black hole candidate Cyg X-1 (Nolan *et al.*, 1981)). Then we were able to link the statistical description of power spectra with a physical scenario of inhomogeneous wind accretion. We derived, in the frame of the theory of plasma penetration developed in a series of papers by Arons and Lea (Arons and Lea, 1976b; Arons and Lea, 1976a; Arons and Lea, 1980; Burnard *et al.*, 1983), all the physical properties of the instability blobs, both

at the magnetospheric radius and at the neutron star surface. These properties were in agreement with the observations, and those at the neutron star surface were the same of the blob properties developed in the frame of disk-accretion (Morfill *et al.*, 1984). This coincidence led us to check a similar correlation between rms and pulse period derivative in the transient disk-fed X-ray binary pulsar EXO 2030+375 (Parmar *et al.*, 1989; Angelini *et al.*, 1989). This correlation seems to be present, although with a worse significance than that found for GX 301-2.

As the last step, we gave a possible physical meaning to the two free parameters present in the response function: the time scale connected with the “exponential” part of the response function is connected with the duration of a shot, *i.e.* with the physical properties of a lump. The time scale connected with the “oscillating” part of the response function is related to some physical process of interaction between the emitted X-ray radiation and the infalling matter. We found that the time scale of Compton cooling of the blobs has the right order of magnitude to satisfy the relation found between the two free parameters.

Of course our model is far from being complete. First of all we have assumed that the mass of an infalling blob remains constant during its voyage toward the neutron star surface. As it was shown by Arons and Lea (1980), this should not be the case, because of the disruption of the blob by Kelvin-Helmholtz instability. The main problem connected in the evaluation of this mass loss rate is concentrated in a parameter, which the authors call η_{KH} . The numerical value of η_{KH} is derived by analogy with the case of Kelvin-Helmholtz instability between two non magnetized fluids, and it is set equal to 0.1. It is important to emphasize that the non linear development of Kelvin-Helmholtz instability is not known, neither from experiments nor from numerical modelling. For all these problems we have not treated the effect of mass loss from the falling blobs, but this effect should have to be taken into account in a more sophisticated model.

Second, the time scales associated to the response function which we have obtained are not directly observable in the observed power spectra. What we are able to observe is the *effect* of these quantities in the power spectra, *i.e.* the presence of an inflexion point in the frequency range $0.01 < f_o < 0.1$ Hz, but not some feature associated to α or β . The freedom in the choice of α , due to the non unique inversion of a power spectrum, does not exclude that this time scale might be, for example, of the order of f_o . In this case, from Eq. 6.26, we will have a comparable β , and therefore α and β should be directly observable. Our choice of α was related to the physical meaning we gave to this parameter, namely the duration of a shot, and therefore the assumption $\alpha = \tau_{\text{ff}}$ (see Eq. 6.44). A different physical meaning, for example the association of α to τ_{dy} , should change our final result. Of course, the physical interpretation of this association and, more important, the physical meaning of the associated β , should not be easy to understand.

Our last remark is about the shape of our theoretical power spectra. In computing the power spectrum from our shot noise process we did not compute the effects due to the finite length of the runs, the sampling and integration of the data (this has been done by Sutherland *et al.* (1978) for a general shot noise process). This did not make possible a fitting procedure of our theoretical spectra with the observed ones, in order to extract the values of the free parameters of the response function. We have in plan to perform this analysis in the next future, in order to directly derive information on the free parameters. Given the fitting parameters, it will be possible to derive the power spectrum slope, which depends on the four parameters λ (the average number of shot per unit time), B (the amplitude of the shot), α and β . We have given a physical meaning to the parameters λ , α and β so only one parameter, B , was left.

Finally, a few words for our observational results. The pulse period measurements of 4U 1538-52 indicates that the source continues to spin-down in the period 1976-1988. This is not easy to understand at the light of the actual theories of wind accretion, which predict a general spin-up trend (Henrichs, 1983). This might be due to the fact that the optical companion has a dimension which is very close to its Roche lobe, therefore there should be the contemporary presence of Roche lobe overflow and accretion from the stellar wind. On the other hand, the pulse period history

of GX 301-2 is that of a typical wind-fed X-ray pulsars, showing an alternation of spin-up and spin-down states in a sort of “saw-tooth” behaviour. The pulse profiles of both sources show a double peak structure, with one peak brighter than the other, π separated in phase. We fitted the pulse shapes with the angular and energy dependence of the X-ray flux given by Meszaros and Nagel (1985) and extracted the geometry of the neutron stars, *i.e.* the angle between the magnetic field axis and the rotation axis, and the angle between the rotation axis and the line of sight. Our results from EXOSAT data confirmed previous estimates and were in agreement with a pencil beam emission pattern in both the sources. For the X-ray pulsar GX 301-2 we obtained a correlation between the secondary maximum height and the X-ray luminosity, in the sense that higher the height of the secondary maximum, lower the intensity of the source. We interpreted this effect as due to a change of the beaming emission pattern.

Bibliography

- Angelini L., Stella L., and Parmar A.N. 1989. The discovery of 0.2 Hz quasi-periodic oscillation in the X-ray flux of the transient 42 second pulsar EXO 2030+375. *Astrophysical Journal*, **346**, p.911.
- Arons J. and Lea S.M. 1976a. Accretion onto magnetized neutron stars: Normal mode analysis of the interchange instability at the magnetopause. *Astrophysical Journal*, **210**, p.792.
- Arons J. and Lea S.M. 1976b. Accretion onto magnetized neutron stars: Structure and interchange instability of a model magnetosphere. *Astrophysical Journal*, **207**, p.914.
- Arons J. and Lea S.M. 1980. Accretion onto magnetized neutron stars: The fate of sinking filaments. *Astrophysical Journal*, **235**, p.1016.
- Burnard D.J., Lea S.M., and Arons J. 1983. Accretion onto magnetized neutron stars: X-ray pulsars with intermediate rotation rates. *Astrophysical Journal*, **266**, p.175.
- Henrichs H.F. 1983. Spin-up and spin-down of accreting neutron stars. In *Accretion-Driven Stellar X-ray Sources*, Lewin W.H.G. and van den Heuvel E.P.J., editors. Cambridge University Press, Cambridge.
- Meszaros P. and Nagel W. 1985. X-ray pulsar models. II. Comptonized spectra and pulse shapes. *Astrophysical Journal*, **299**, p.138.
- Morfill G.E., Trümper J., Bodenheimer P., and Tenorio-Tangle G. 1984. Nonstationary accretion onto neutron stars: some constraints and consequences. *Astronomy & Astrophysics*, **139**, p.7.
- Nolan P.L., Gruber D.E., Matteson J.L., Peterson L.E., Rothschild R.E., Doty J.P., Levine A.M., Lewin W.H.G., and Primini F.A. 1981. Rapid variability of 10–140 keV X-rays from Cygnus X-1. *Astrophysical Journal*, **246**, p.494.
- Parmar A.N., White N.E., Stella L., Izzo C., and Ferri P. 1989. The transient 42 second X-ray pulsar EXO 2030+375. I. The discovery of the pulse period variations. *Astrophysical Journal*, **338**, p.359.
- Sutherland P.G., Weisskopf M.C., and Kahn S.M. 1978. Short-term variability of Cygnus X-1. II. *Astrophysical Journal*, **219**, p.1029.

Part III

Appendices

Appendix A

Time averaged background Subtracted Pulse Profiles as a Function of Energy of the ME EXOSAT Observations of GX 301–2

In this Appendix we will present the time averaged background subtracted pulse profiles of the ten ME EXOSAT observations of GX 301–2 analysed in this Thesis. The pulse profiles have not been normalized, therefore a direct confrontation is not immediate as it was in Chapter 3 and Chapter 4. We choose five energy bands, the range of which are the same for all the observations (see Table A.1)

Channel ID	PHA ME Channels	Energy (keV)
Ch1	4–12	0.94–3.14
Ch2	13–20	3.14–5.23
Ch3	21–30	5.23–8.02
Ch4	31–44	8.02–12.28
Ch5	4–37	0.94–10.09

Table A.1: Energy ranges for which pulse profiles of the EXOSAT observations of GX 301–2 were computed.

In Table A.2 the background level for the two “halves” is given for each observation, first for H1 and then for H2, together with the number of “swaps” (if any) and the “half” which was pointing the source. We computed the background level for the on source “half” taking the averaged count rate measured during slew manoeuvres. For observation 83/231 the detectors were switched off during slew manoeuvres so we have not a measure of the background level for the on source “half” H2.

Obs ID	Background (Counts/sec)	# Swaps	Half on source	Obs ID	Background (Counts/sec)	# Swaps	Half on source
83/231	H1: 17.73 ± 0.03	—	H2	84/111	H1: 16.79 ± 0.03 H2: 16.25 ± 0.05	—	H2
84/113	H1: 16.84 ± 0.04 H2: 13.29 ± 0.06	—	H2	84/115	H1: 16.70 ± 0.04 H2: 13.32 ± 0.08	—	H2
84/153	H1: 16.21 ± 0.05 H2: 12.75 ± 0.04	—	H2	84/159	H1: 16.29 ± 0.06 H2: 12.66 ± 0.06	—	H2
85/038	H1: 17.94 ± 0.03 H2: 13.69 ± 0.03	8	H1 & H2	85/047	H1: 18.66 ± 0.03 H2: 14.55 ± 0.03	3	H1 & H2
85/050	H1: 18.53 ± 0.04 H2: 14.49 ± 0.03	8	H1 & H2	85/070	H1: 17.08 ± 0.06 H2: 13.18 ± 0.06	3	H1 & H2

Table A.2: Background measurements for the ME EXOSAT observations of GX 301-2. A “swap” is a manoeuvre during which the on source “half” was changed.

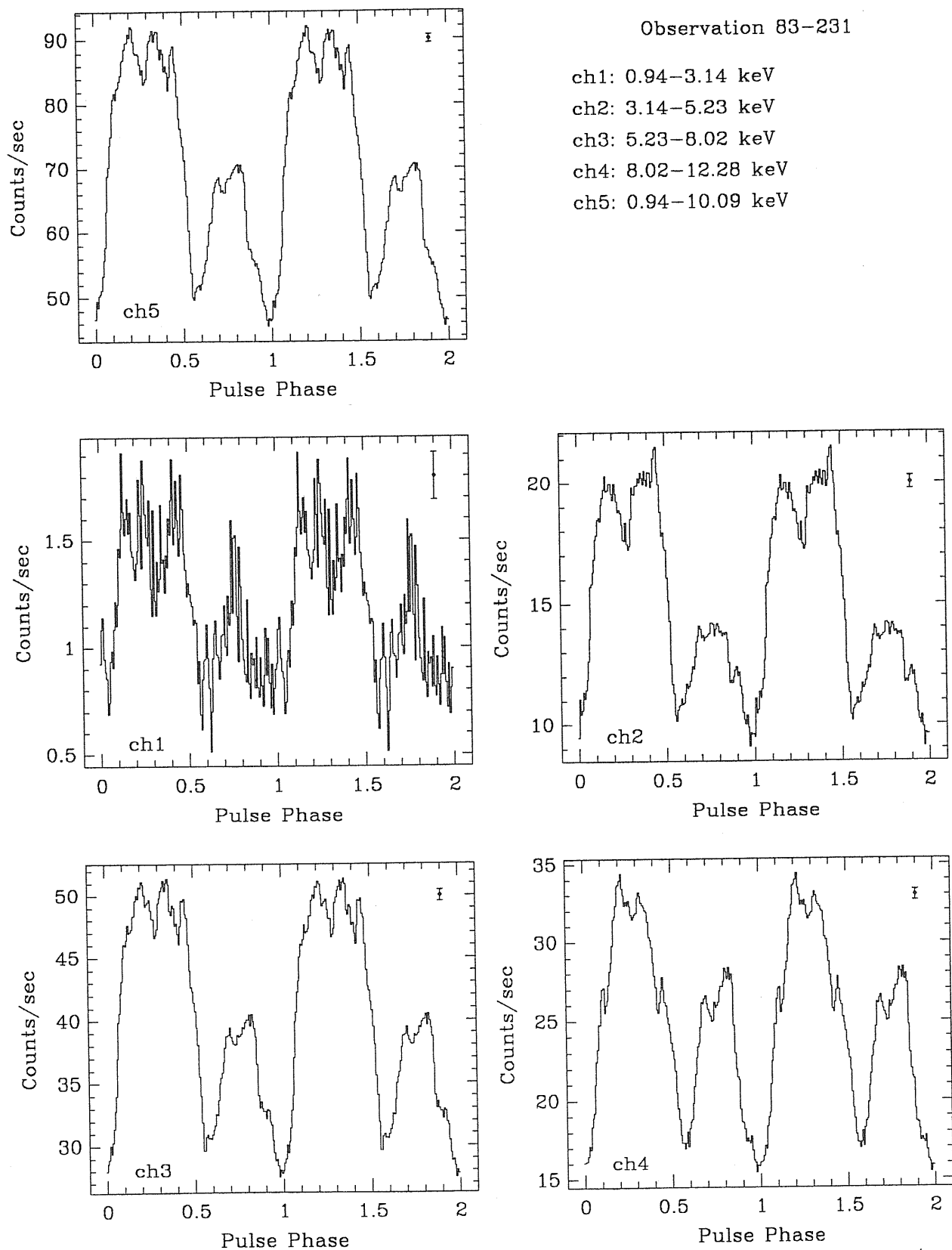


Figure A.1: Time averaged background subtracted pulse profiles as a function of energy for the 83/231 EXOSAT observation of GX 301-2.

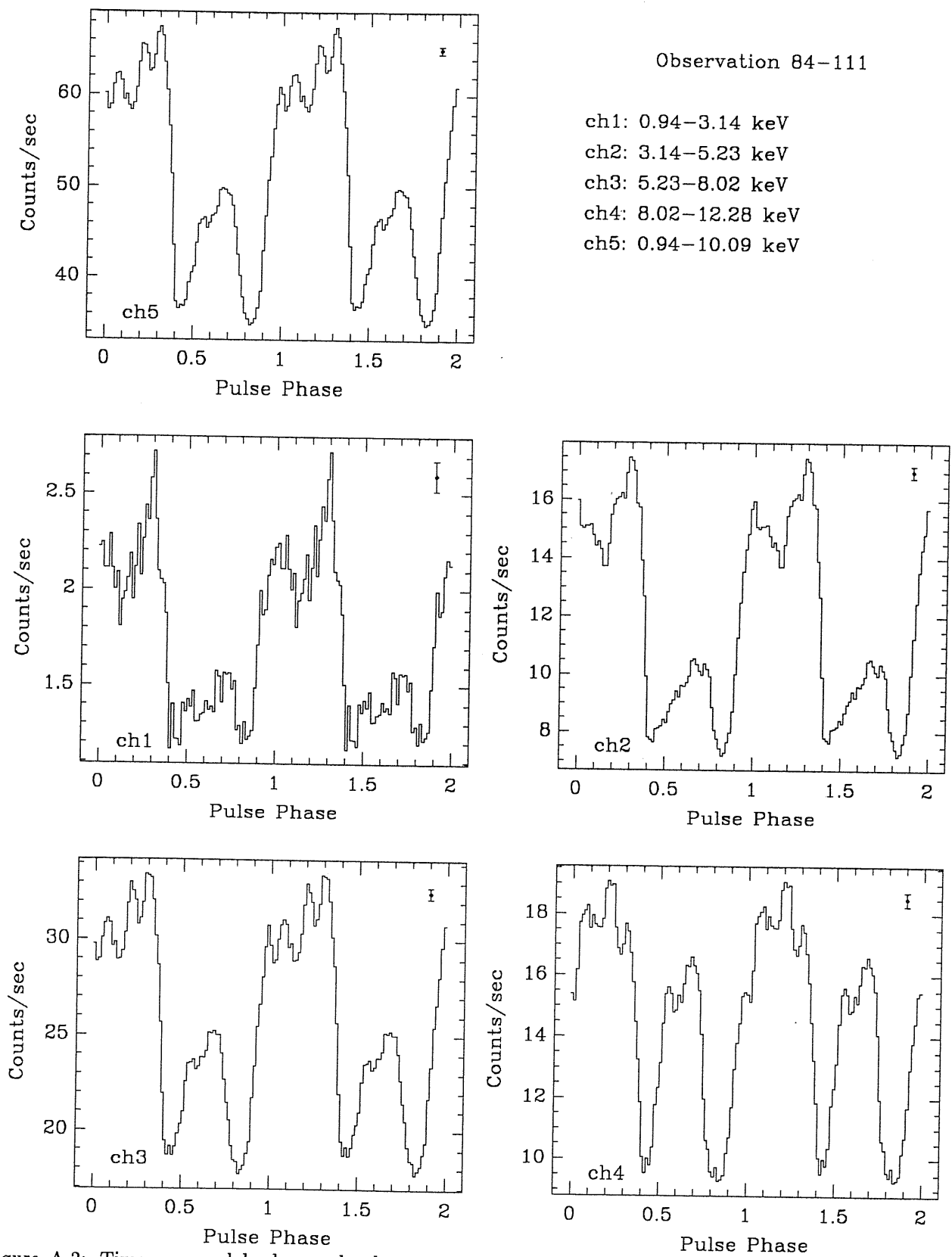


Figure A.2: Time averaged background subtracted pulse profiles as a function of energy for the 84/111 EXOSAT observation of GX 301-2.

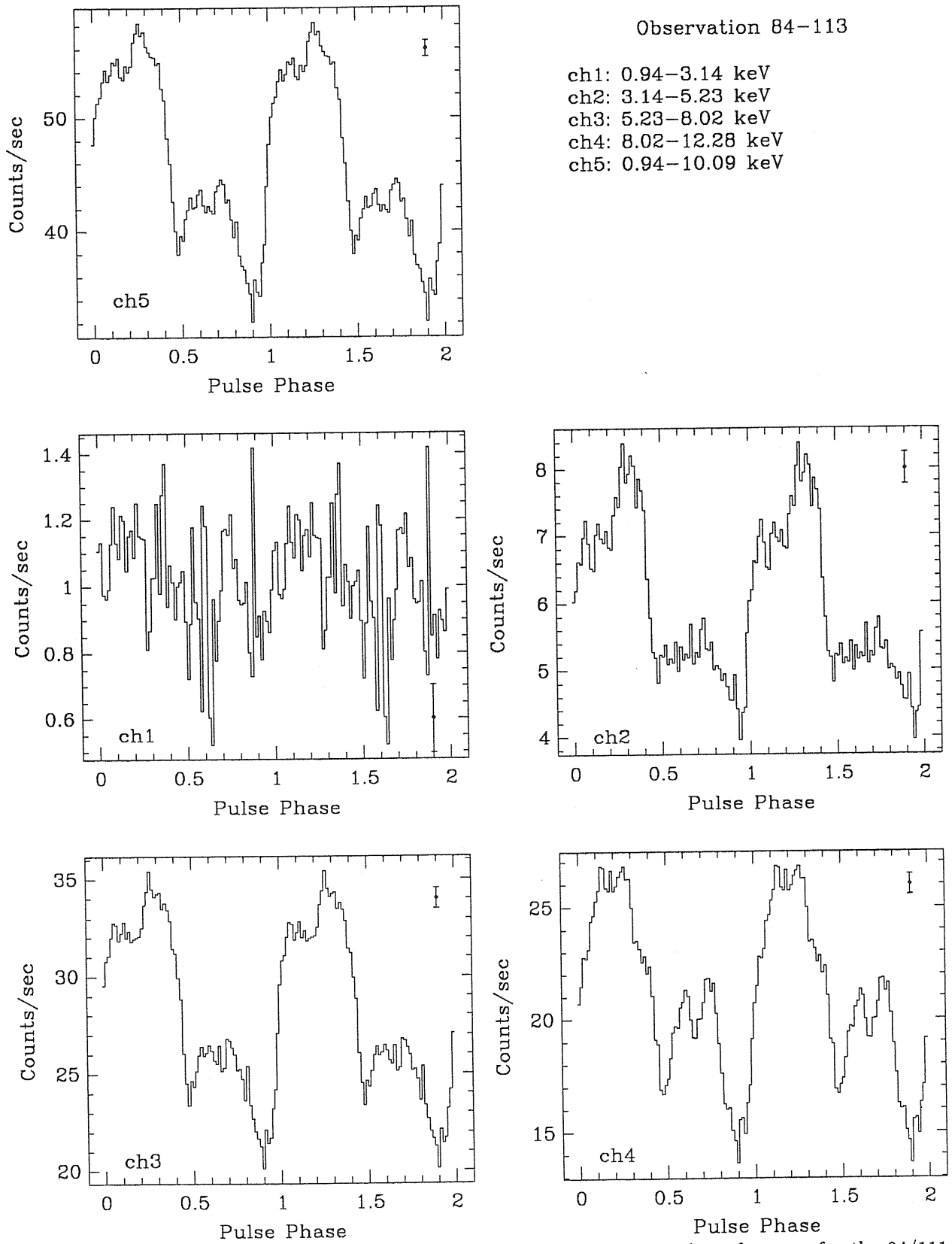


Figure A.3: Time averaged background subtracted pulse profiles as a function of energy for the 84/111 EXOSAT observation of GX 301-2.

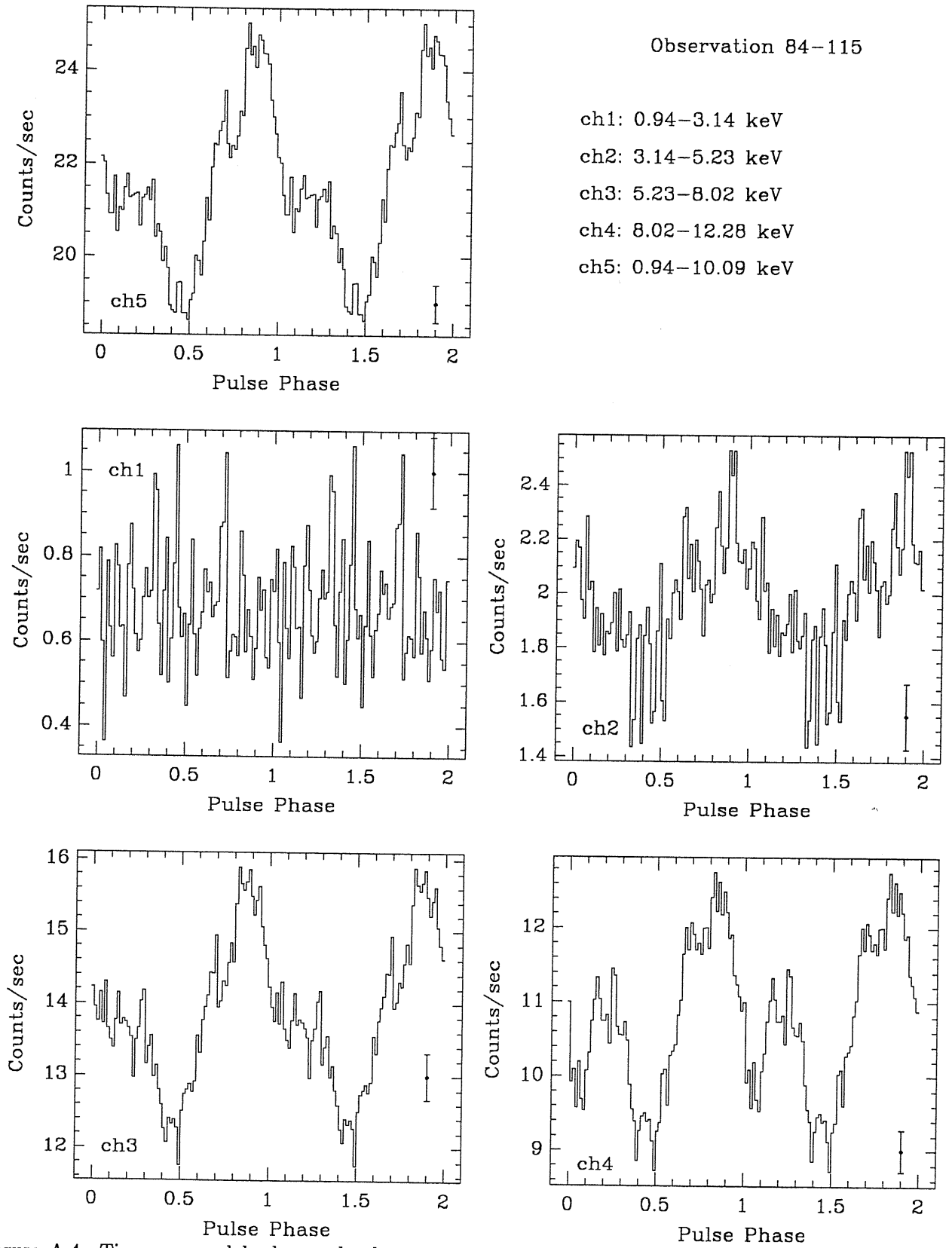


Figure A.4: Time averaged background subtracted pulse profiles as a function of energy for the 84/115 EXOSAT observation of GX 301-2.

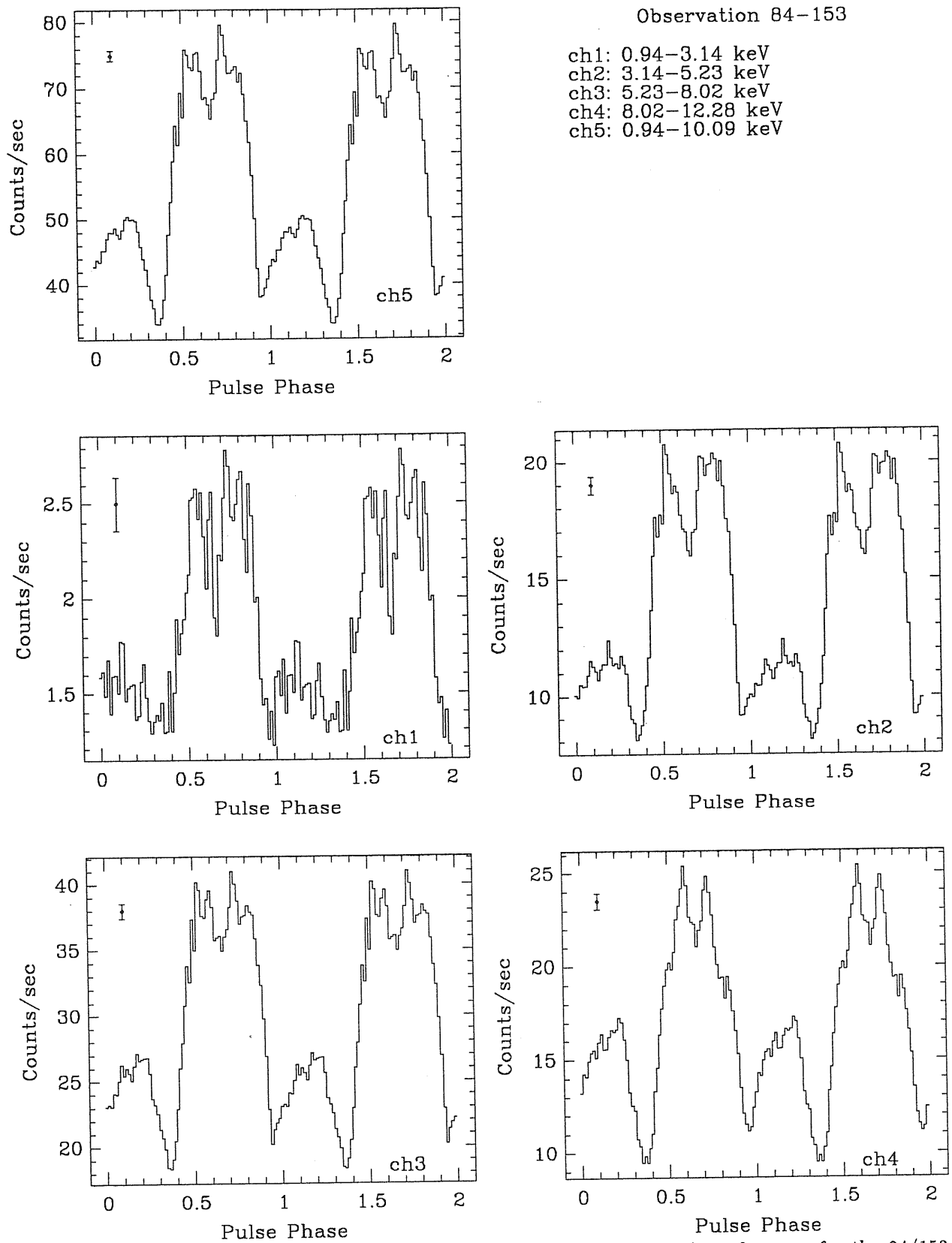


Figure A.5: Time averaged background subtracted pulse profiles as a function of energy for the 84/153 EXOSAT observation of GX 301-2.

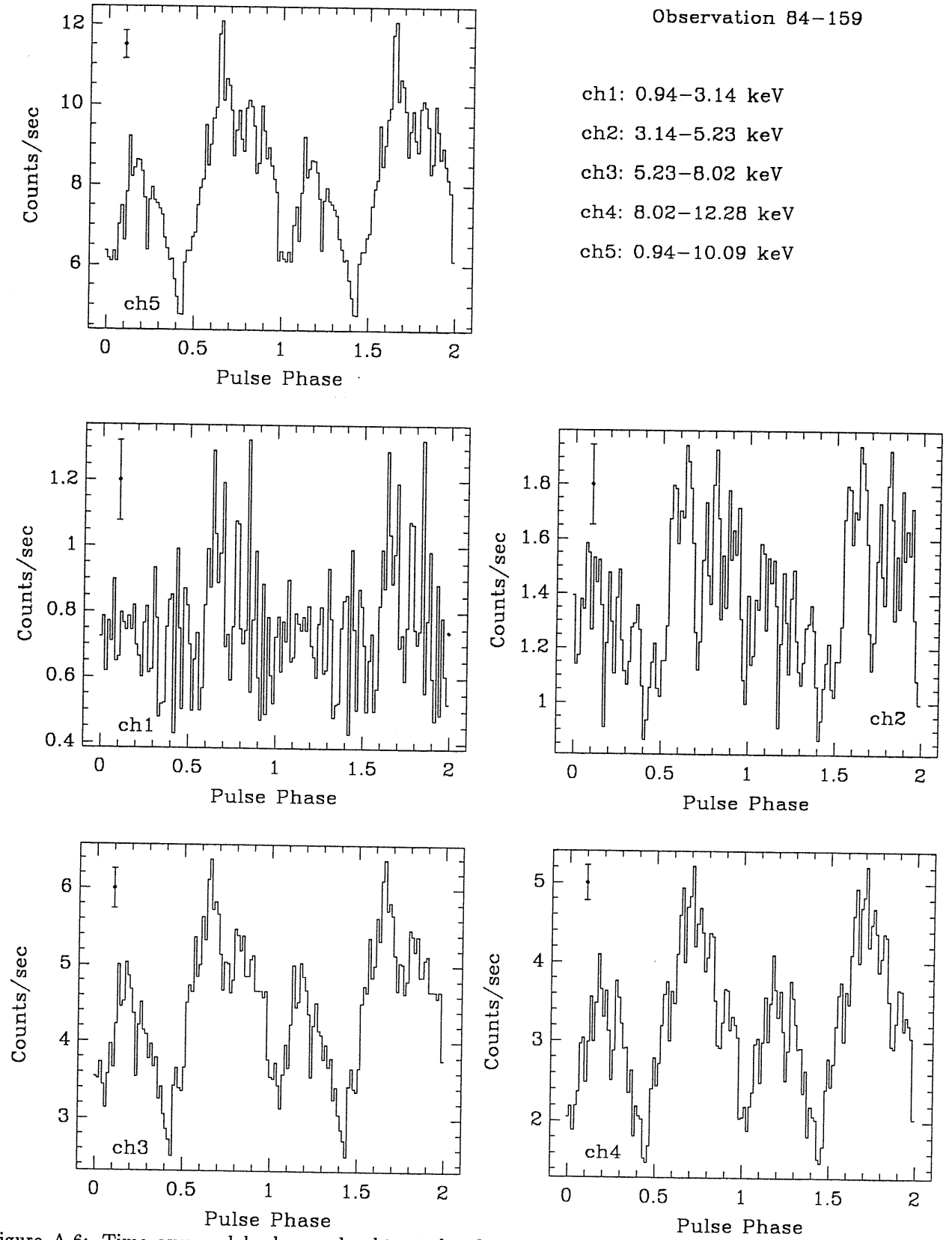
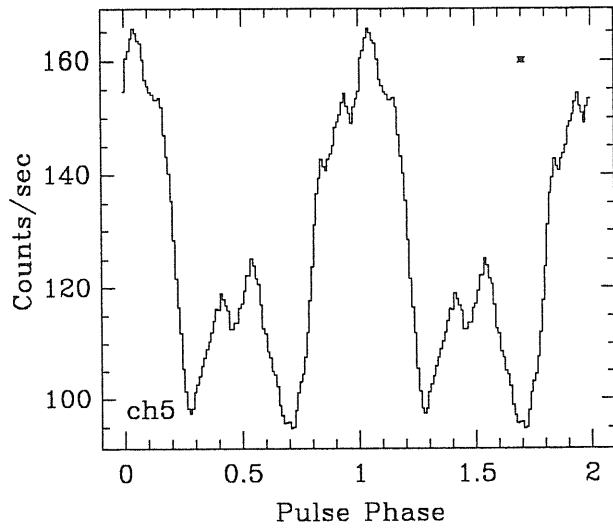


Figure A.6: Time averaged background subtracted pulse profiles as a function of energy for the 84/159 EXOSAT observation of GX 301-2.



Observation 85-038

ch1: 0.95-3.17 keV
 ch2: 3.17-5.28 keV
 ch3: 5.28-8.10 keV
 ch4: 8.10-12.42 keV
 ch5: 0.95-10.20 keV

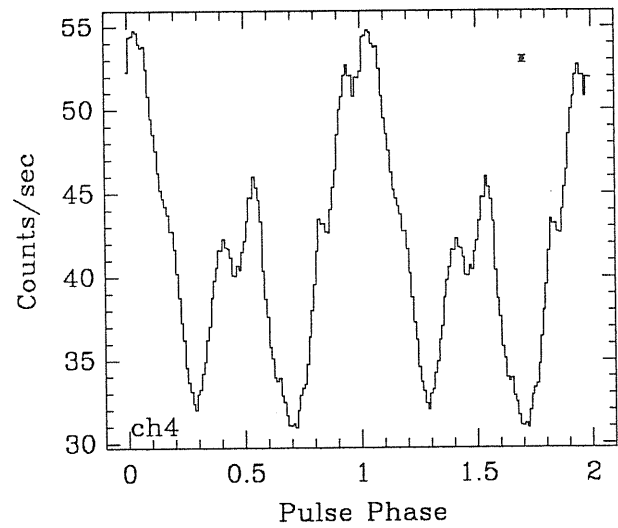
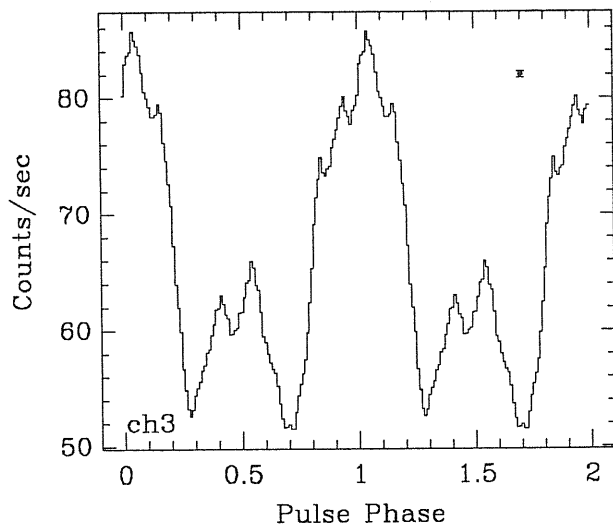
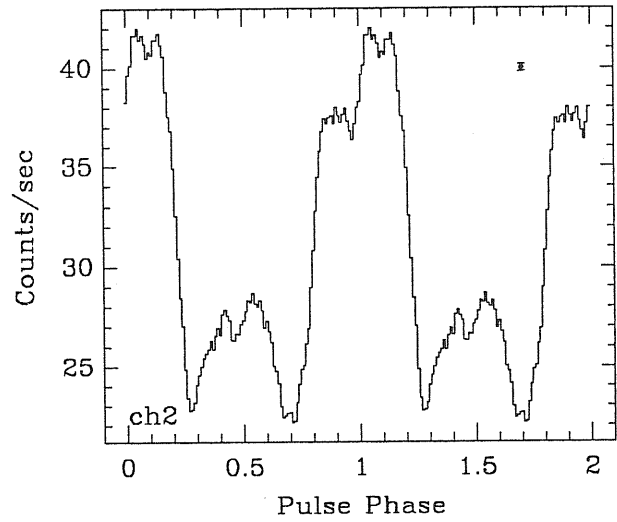
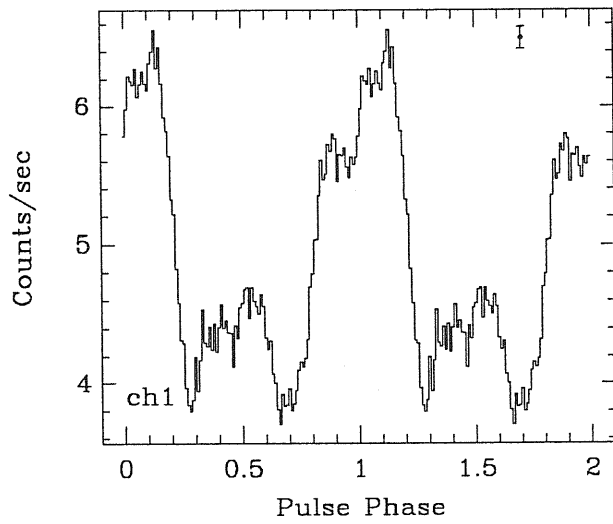


Figure A.7: Time averaged background subtracted pulse profiles as a function of energy for the 85/038 EXOSAT observation of GX 301-2.

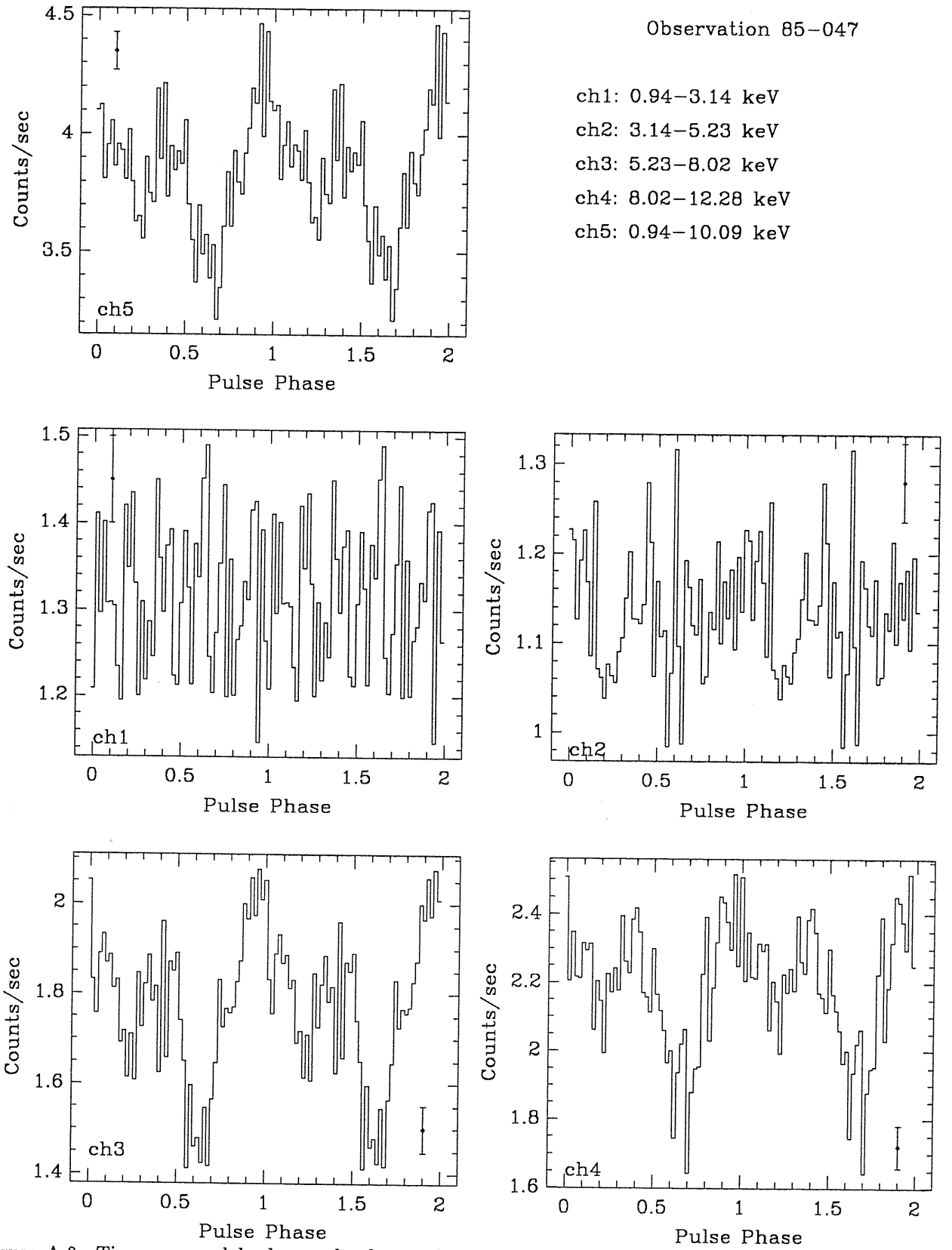


Figure A.8: Time averaged background subtracted pulse profiles as a function of energy for the 85/047 EXOSAT observation of GX 301-2.

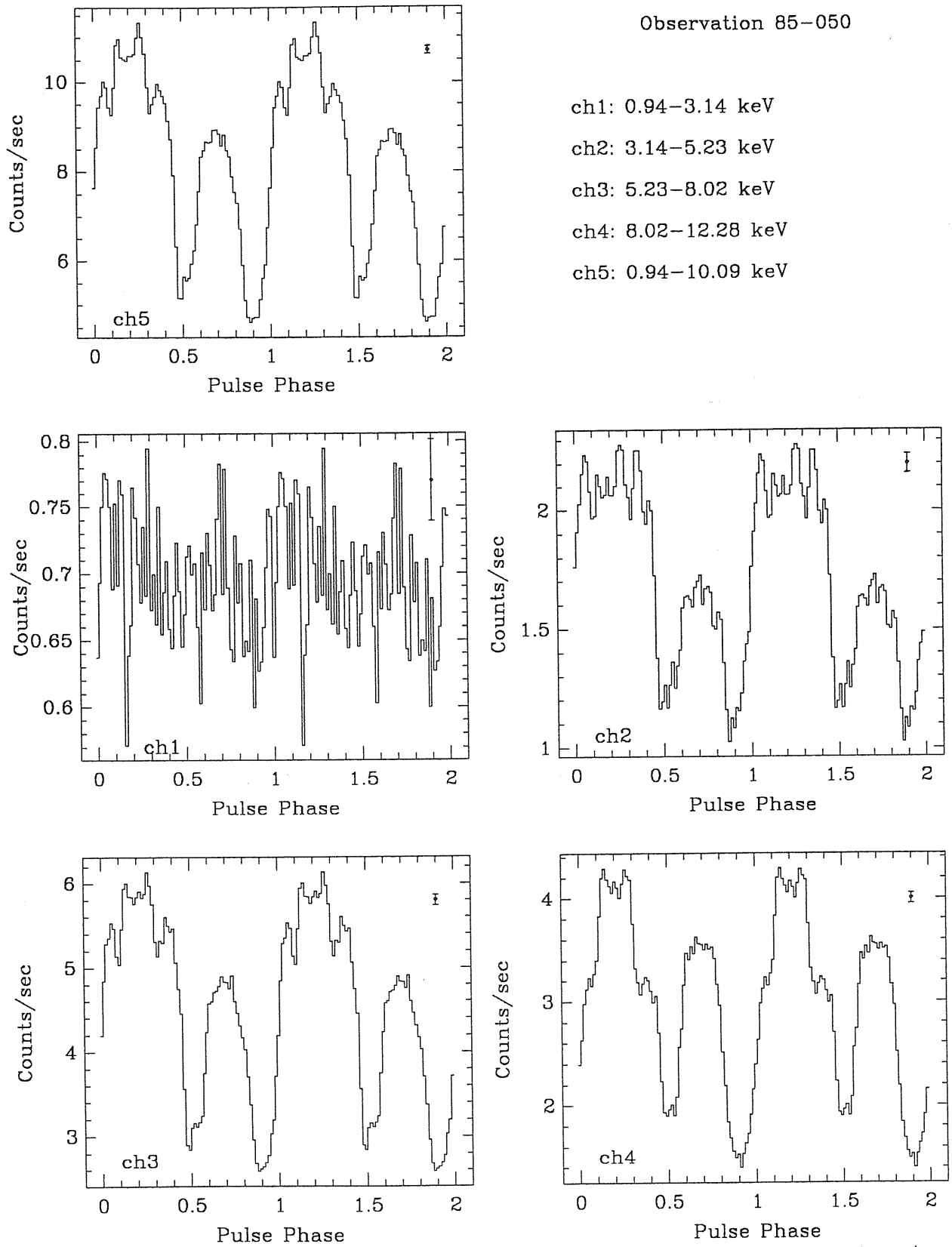


Figure A.9: Time averaged background subtracted pulse profiles as a function of energy for the 85/050 EXOSAT observation of GX 301-2.

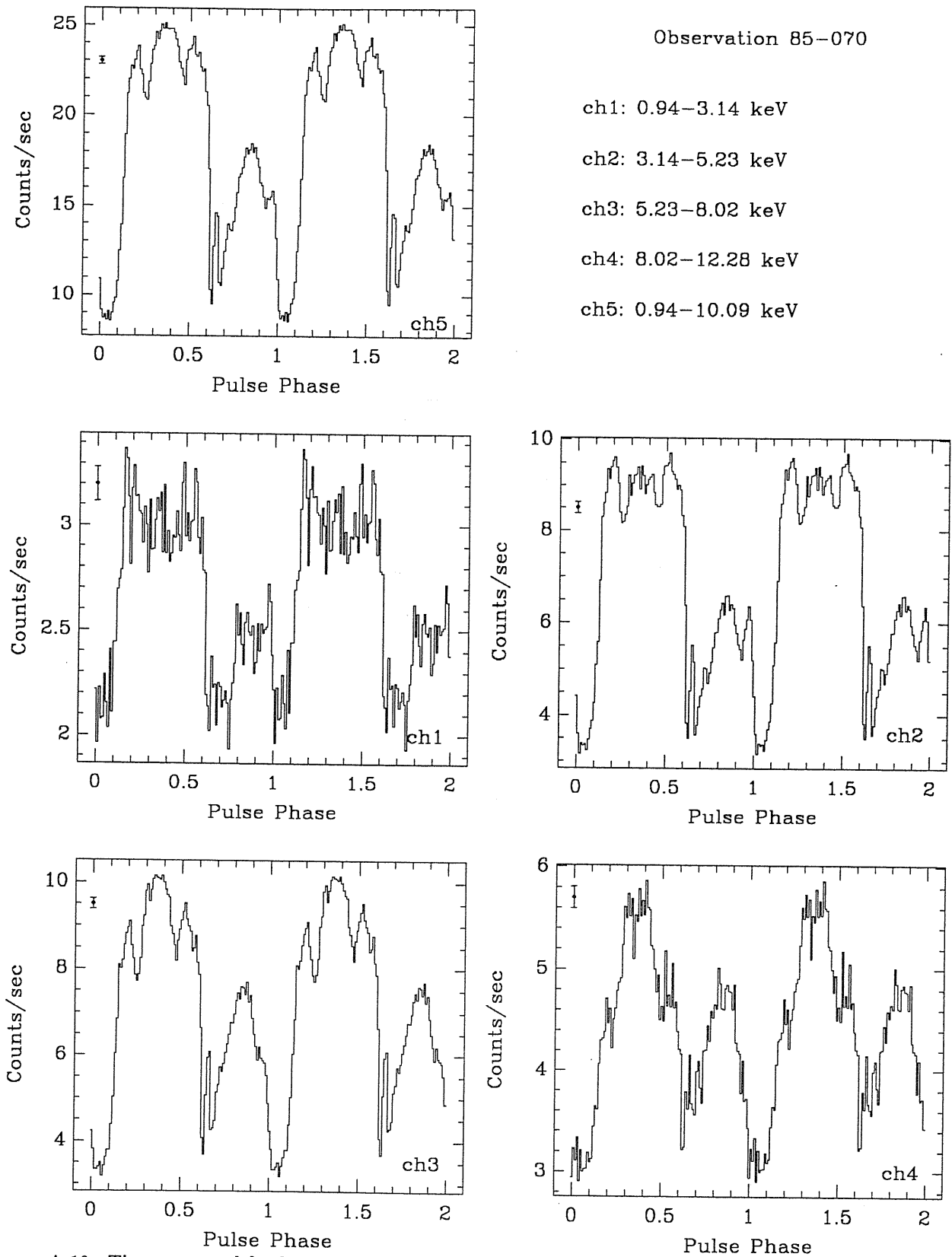


Figure A.10: Time averaged background subtracted pulse profiles as a function of energy for the 85/070 EXOSAT observation of GX 301-2.

Appendix B

Normalization of Power Spectrum Density Function

In this Appendix we will treat the problem of normalization of Power Spectrum Density function because our normalization is different from that generally adopted. In particular we will stress the differences between our treatment, based on Bendat and Piersol (1971) (BP) description, and that of Leahy *et al.* (1983) (LE), which has been discussed by Lewin *et al.* (1988).

The definition of Fourier transform of a function $x(t)$ is

$$X(f) = \int_{-\infty}^{+\infty} x(t) e^{-2\pi i f t} dt \quad (\text{B.1})$$

where $i = \sqrt{-1}$. This quantity will be, in general, complex. The *finite-range* Fourier transform is defined as

$$X(f, T) = \int_0^T x(t) e^{-2\pi i f t} dt. \quad (\text{B.2})$$

Assume now that the function $x(t)$ is not continuous but it is represented as series of N points equally spaced of a quantity h . Of course, each point of the series (which we will call time series) will be given by

$$x_n = x(nh) \quad n = 0, 1, 2, \dots, N-1. \quad (\text{B.3})$$

The discrete version of Eq. B.2 will be

$$X(f, T) = h \sum_{n=0}^{N-1} x_n \exp[-2\pi i f n h]. \quad (\text{B.4})$$

Selecting the discrete frequencies f_k according to

$$f_k = k f_0 = \frac{k}{T} = \frac{k}{Nh} \quad k = 0, 1, 2, \dots, N-1 \quad (\text{B.5})$$

then the discrete Fourier transform components evaluated in f_k are defined

$$X_k \equiv \frac{X(f_k, T)}{h} = \sum_{n=0}^{N-1} x_n \exp\left(-i \frac{2\pi k n}{N}\right) \quad k = 0, 1, 2, \dots, N-1 \quad (\text{B.6})$$

where the factor h has been included in the definition of X_k . Of course k really runs from 0 to $N/2$, because of the Nyquist frequency at this point. Furthermore, it is possible to start the summation from $n = 1$ because with the transformation $x_n \rightarrow x'_n = x_n - \bar{x}$, where \bar{x} is the mean, the term $X_0 = \sum_{n=0}^{N-1} x_n$ can be annulled. From here on we will assume that our time series has been mean subtracted, *i.e.* we will put $X_0 = 0$. Furthermore, we will define $N_p = \sum_{n=0}^{N-1} x_n$ (Lewin *et al.*, 1988) because of the meaning of total photons contained in the time series if we speak about light curves.

The X_k are computed numerically by means of Fast Fourier Transform algorithms, basically based on decomposing N in its factors and carrying out the Fourier transforms over the smaller number of terms. In every textbook the details of the procedure are well described (see *e.g.* BP; Press *et al.* (1986)), therefore we will not describe the algorithm.

Following BP the power spectrum estimate is defined as (BP pag. 327)

$$P_k|_{\text{BP}} \equiv \frac{2}{Nh} |X(f_k, T)|^2 = \frac{2h}{N} |X_k|^2. \quad (\text{B.7})$$

The total variance of the time series x_k becomes

$$\text{Var}(x_k) \equiv \sum_{k=0}^{N-1} (x_k - \bar{x})^2 \stackrel{x_k \rightarrow x'_k}{=} \sum_{k=0}^{N-1} x_k^2. \quad (\text{B.8})$$

By means of the Parseval theorem we have that

$$\sum_{k=0}^{N-1} x_k^2 = \frac{2}{N} \sum_{k=1}^{N/2} |X_k|^2 \quad (\text{B.9})$$

therefore substituting Eq. B.9 in Eq. B.8, by means of Eq. B.7 we obtain

$$\text{Var}|_{\text{BP}}(x_k) = \frac{1}{h} \sum_{k=1}^{N/2} P_k|_{\text{BP}}. \quad (\text{B.10})$$

On the other hand, LE defines the power spectrum estimate as

$$P_k|_{\text{LE}} \equiv \frac{2}{N_p} |X_k|^2. \quad (\text{B.11})$$

Repeating step by step the considerations made for Eq. B.7 we have that the total variance of the time series x_k in the LE normalization is

$$\text{Var}|_{\text{LE}}(x_k) = \frac{N_p}{N} \sum_{k=1}^{N/2} P_k|_{\text{LE}}. \quad (\text{B.12})$$

Dividing Eq. B.7 by Eq. B.11, the relation between the power spectrum estimates is

$$\frac{P_k|_{\text{BP}}}{P_k|_{\text{LE}}} = \frac{hN_p}{N} = c^2 h \quad (\text{B.13})$$

where c is the average count rate of the time series, defined as N_p/T .

What are the advantages of using a normalization instead of another? The common procedure of estimating power spectra of X-ray light curve is to divide the total observation in M data segments T long and to sum them to obtain the total power spectrum. In the case of the LE normalization, each data segment is weighted with its own N_p . This is very useful in the case of strongly variable

sources, as X-ray bursters, but for quite sources as those we have analyzed the problem was not present.

Counting statistics will modify the data, creating statistical fluctuations. Due to this effect, the power will have a non zero mean, also in absence of source variability, because of the presence of $P_{k,\text{fluct}}$. Normally we assume a Poissonian distribution for these fluctuations; in this case LE has demonstrated that, with his normalization, the mean value of the power is 2 and its variance 4. Furthermore, the power is distributed as a χ^2 random variable with two degrees of freedom. This is very useful for computing the probability that the power $P_{k,\text{fluct}}$ observed at a particular frequency exceeds a given threshold power P_{th} ; in fact this probability is

$$\text{Prob}(P_{k,\text{fluct}} > P_{\text{th}}) = Q(P_{\text{th},2}) \quad (\text{B.14})$$

where $Q(\chi^2_\nu)$ is the integral probability of the χ^2 distribution with ν degrees of freedom

$$Q(\chi^2_\nu) \equiv \frac{1}{2^{\nu/2}\Gamma(\nu/2)} \int_{\chi^2}^{\infty} t^{(\nu-2)/2} e^{-t/2} dt. \quad (\text{B.15})$$

In case of M segments of length T , the spectrum will be distributed as a χ^2_{2M} (of course N_p will be the total number of photons in each segment).

On the other hand, with the BP normalization the $P_{k,\text{fluct}}$ will have a mean and a variance different from 2 and 4, respectively.

Let us define the fractional root mean square variation (rms) in x_k as

$$\text{rms} \equiv \frac{1}{\bar{x}} \sqrt{\frac{\text{Var}(x_k)}{N}}. \quad (\text{B.16})$$

To obtain the expressions in the case of the two normalization, it is enough to substitute in Eq. B.16 the corresponding expressions for the variances (Eq. B.10 and Eq. B.12), obtaining

$$\text{rms}|_{\text{BP}} = \sqrt{\frac{N}{hN_p^2} \sum_{k=1}^{N/2} P_k|_{\text{BP}}} \quad (\text{B.17})$$

$$\text{rms}|_{\text{LE}} = \sqrt{\frac{1}{N_p} \sum_{k=1}^{N/2} P_k|_{\text{LE}}}. \quad (\text{B.18})$$

Of course, the value of the rms will not depend on the particular normalization. Indeed, by means of the definition of variance (Eq. B.8) we have

$$\frac{\text{rms}|_{\text{BP}}}{\text{rms}|_{\text{LE}}} = \sqrt{\frac{\text{Var}|_{\text{BP}}(x_k)}{\text{Var}|_{\text{LE}}(x_k)}} = \sqrt{\frac{\sum_{k=0}^{N-1} x_k^2}{\sum_{k=0}^{N-1} x_k^2}} = 1. \quad (\text{B.19})$$

From an operational point of view, in computing rms's it is necessary to take into account instrumental effects. For EXOSAT observations this essentially corresponds to correct the observed x_k for dead time effects (Tennant, 1987). This procedure is different for different ME OBC programs (see Chapter 2 for a brief description of the OBC programs on board the ME experiment). Following Belloni and Hasinger (1990), the rms, computed for HTR n data in the LE normalization, is given by the expression

$$\text{rms}_{\text{HTR}} = \frac{\sqrt{cP}}{c-b} \quad (\text{B.20})$$

where P is $\sum_{k=1}^{N/2} P_k|_{LB}$, c is the average count rate (in units of Counts/sec) and b is the background count rate, in the same units. On the other hand, for HERn observations, the rms has to be corrected for dead time effects, therefore

$$\text{rms}_{\text{HER}} = \frac{\sqrt{cP}}{e^{-C\tau_s} \left(\frac{c}{f(C)} - b \right)} \quad (\text{B.21})$$

where C is the qualified event rate (*i.e.* the total count rate incident on all detectors, in units of Counts/sec) and $\tau_s = 2.44 \cdot 10^{-4}$ sec is the sampling dead time. The dead time function $f(C)$ is defined as (Tennant, 1987)

$$f(C) \equiv \frac{1 - e^{-C\tau_s}}{C\tau_s}. \quad (\text{B.22})$$

Bibliography

- Belloni T. and Hasinger G. 1990. An atlas of aperiodic variability in HMXB. *Astronomy & Astrophysics*, **230**, p.103.
- Bendat J.S. and Piersol A.G. 1971. *Random Data: Analysis and Measurement Procedures*. Wiley Interscience, New York.
- Leahy D.A., Darbro W., Elsner R.F., Weisskopf M.C., Sutherland P.G., Kahn S., and Grindlay J.E. 1983. On searches for pulsed emission with application to four globular clusters X-ray sources: NGC 1851, 6441, 6624 and 6712. *Astrophysical Journal*, **266**, p.160.
- Lewin W.H.G., van Paradijs J., and van der Klis M. 1988. A review of quasi-periodic oscillations in low-mass X-ray binaries. *Space Science Review*, **46**, p.273.
- Press W.H., Flannery B.P., Teukolsky S.A., and Vetterling W.T. 1986. *Numerical Recipes. The Art of Scientific Computing*. Cambridge University Press, Cambridge.
- Tennant A.F. 1987. Power spectra, with application to EXOSAT data. *Monthly Notices of R.a.S.*, **226**, p.963.

List of Tables

2.1	EXOSAT orbital parameters	16
2.2	Technical characteristic of a Low Energy imaging telescope on board EXOSAT . . .	18
2.3	Technical characteristics of the Gas Scintillation Proportional Counter on board EXOSAT	18
2.4	Technical characteristics of the Medium Energy experiment on board EXOSAT . . .	20
3.1	Journal of the four ME EXOSAT observations of 4U 1538-52	23
3.2	Orbital parameters of 4U 1538-52	25
3.3	Pulse period history of 4U 1538-52	27
3.4	Fitting results on two ME EXOSAT PSDs of 4U 1538-52	33
3.5	Previous spectral measurements of 4U 1538-52	35
3.6	EXOSAT spectral measurements of 4U 1538-52	35
4.1	Journal of the ten ME EXOSAT observations of GX 301-2	46
4.2	Orbital parameters of GX 301-2	47
4.3	Orbital phases and mean intensities for the ten EXOSAT observations of GX 301-2	50
4.4	ME EXOSAT pulse period measurements of GX 301-2	54
4.5	Pulse period measurements of GX 301-2 obtained by other satellites than EXOSAT	54
4.6	Instantaneous pulse period change rates for the EXOSAT observations of GX 301-2	55
4.7	Summary of power spectra fits on the GX 301-2 EXOSAT observations	62
6.1	Blob physical properties for the X-ray binary pulsar GX 301-2	111
A.1	Energy ranges for which pulse profiles of the EXOSAT observations of GX 301-2 were computed	119
A.2	Background measurements for the ME EXOSAT observations of GX 301-2	120

List of Figures

1.1	Block diagram of the physical processes of production and emission of the X-ray flux in an X-ray binary pulsar.	7
1.2	Possible longitudinal geometries of the emission region above the polar cap of a neutron star	8
2.1	Exploded view of the EXOSAT observatory	16
2.2	Lunar and Earth occultation strips in the EXOSAT orbit	17
2.3	A schematic draft of a Low Energy imaging telescope on board EXOSAT	19
2.4	A schematic draft of the Gas Scintillator Proportional Counter on board EXOSAT	19
2.5	A schematic draft of the Medium Energy experiment on board EXOSAT	21
3.1	Portrait of the 4U 1538-52/QV Nor binary system with the four EXOSAT observations	24
3.2	Eclipse ingress of 4U 1538-52 in two EXOSAT observations	24
3.3	M_* - R_* relation for QV Nor	26
3.4	The 1-10 keV background subtracted light curve of 17 March and 10 August 1984 ME EXOSAT observations of 4U 1538-52	28
3.5	Pulse period history of 4U 1538-52	29
3.6	Time averaged background subtracted normalized pulse profile vs energy for the 84/077 EXOSAT observation of 4U 1538-52	30
3.7	Time averaged background subtracted normalized pulse profile vs energy for the 84/223 EXOSAT observation of 4U 1538-52	31
3.8	PSDs of the 84/077 and 84/220 observations of 4U 1538-52	32
3.9	Power Spectral Density function of the 84/223 observation of 4U 1538-52, with 16 msec time resolution	33
3.10	Hardness ratio for the 17 March 1984 ME EXOSAT observation of 4U 1538-52	35
3.11	Ratio between two energy spectra taken during the absorbing episode and outside it, for the 84/077 ME EXOSAT observation of 4U 1538-52	36
3.12	Hardness ratio as a function of the pulse phase for the 84/077 ME EXOSAT observation of 4U 1538-52	37
3.13	Ratio between energy spectra taken at different pulse phases, for the 84/077 ME EXOSAT observation of 4U 1538-52	39
3.14	Definition of the aspect angles β_m and β_o	41
4.1	Portrait of the GX 301-2/Wray 977 system with the ten EXOSAT observations	46
4.2	Picture of a possible explanation of the observed anticipation of the maximum in the X-ray emission from GX 301-2 with respect to the periastron passage	48

4.3	PSDs of the 83/231 and 85/070 background of GX 301-2	48
4.4	The 1–10 keV mean intensity vs orbital phase for the ten EXOSAT observations of GX 301-2	51
4.5	The 1–10 keV time averaged background subtracted light curve of the 85/038 observation of GX 301-2	52
4.6	The 1–10 keV time averaged background subtracted 700 sec rebinned light curve of the 85/038 GX 301-2 observation	53
4.7	χ^2 vs pulse period for the 85/038 EXOSAT observation of GX 301-2	53
4.8	Pulse period history of GX 301-2	56
4.9	“Saw-tooth” behaviour of the pulse period history of GX 301-2	56
4.10	Time averaged background subtracted normalized pulse profiles as a function of energy of the 85/038 ME EXOSAT observation of GX 301-2	58
4.11	Time averaged background subtracted normalized pulse profiles as a function of energy of the 85/070 ME EXOSAT observation of GX 301-2	59
4.12	Modulation index vs energy for the ten ME EXOSAT observations of GX 301-2 . .	60
4.13	PSDs of two ME EXOSAT observations of GX 301-2: 84/111 and 85/038	61
4.14	Fits to two power spectra of ME EXOSAT observations of GX 301-2	62
4.15	Pulse period derivative as a function of the X-ray intensity	63
4.16	Normalized secondary maximum heights as a function of the average X-ray intensity	65
4.17	Sketch of the emission geometry as a function of the pulse phase	66
4.18	Normalized secondary peak height as a function of energy of observation	68
4.19	Power spectrum of the 85/070 observation obtained by the HTR3 ME OBC program	69
4.20	Root-mean-square variability of power spectra as a function of mean intensity and modulation index	70
4.21	Root-mean-square variability of power spectra as a function of the accretion time scale	71
4.22	Root-mean-square variability of power spectra as a function of the accretion time scale for the X-ray pulsar EXO 2030+375	71
5.1	Geometry of capture in a wind-fed X-ray binary system	76
5.2	A close up of the accretion “tube” around a neutron star	80
5.3	The equilibrium shape of the magnetosphere	88
5.4	Schematic sketch of the regions around an accreting neutron star	90
5.5	Expression of the plasmopause radius as a function of the X-ray luminosity	93
5.6	Numerical simulations of Rayleigh–Taylor and Kelvin–Helmholtz instabilities at the magnetospheric boundary	96
6.1	Form of the power spectrum of an oscillating exponential shot noise, according to the K parameter	105
6.2	The α^2 – β^2 plane and the two different solutions for the power spectrum shape . . .	106
6.3	Allowed values of α and β for $f = f_o$	107
6.4	Picture of the physical scenario of noisy wind accretion	108
6.5	Constraints on the physical characteristics of instability blobs	112
A.1	Time averaged background subtracted pulse profiles vs energy for the 83/231 EXOSAT observation of GX 301-2	121
A.2	Time averaged background subtracted pulse profiles vs energy for the 84/111 EXOSAT observation of GX 301-2	122
A.3	Time averaged background subtracted pulse profiles vs energy for the 84/113 EXOSAT observation of GX 301-2	123

A.4	Time averaged background subtracted pulse profiles vs energy for the 84/115 EXO-SAT observation of GX 301-2	124
A.5	Time averaged background subtracted pulse profiles vs energy for the 84/153 EXO-SAT observation of GX 301-2	125
A.6	Time averaged background subtracted pulse profiles vs energy for the 84/159 EXO-SAT observation of GX 301-2	126
A.7	Time averaged background subtracted pulse profiles vs energy for the 85/038 EXO-SAT observation of GX 301-2	127
A.8	Time averaged background subtracted pulse profiles vs energy for the 85/047 EXO-SAT observation of GX 301-2	128
A.9	Time averaged background subtracted pulse profiles vs energy for the 85/050 EXO-SAT observation of GX 301-2	129
A.10	Time averaged background subtracted pulse profiles vs energy for the 85/070 EXO-SAT observation of GX 301-2	130

Subject Index

The underlined numbers denote the page where the corresponding entry is defined, all others indicate the place where it is used.

— Symbols —

4U 0115+63, 9
 4U 0352+30, 47
 4U 1538-52
 physical properties, 23ff
 4U 1626-67, 9
 4U 1907+09, 47

— A —

A0535+26, 2, 55, 65
 A0538-66, 101
 Absorption
 in energy spectra, 34
 Absorption velocity, 92
 Accretion column, 42, 112
 Accretion disk, 2, 5, 75, 83
 Accretion radius, 76
 in 4U 1538-52, 38
 in GX 301-2, 64
 Accretion rate, 76, 78
 Accretion wake, 65
 Alfvén
 Mach number, 85
 radius, 91
 surface, 91
 velocity, 85
 Angular momentum
 carried by stellar wind, 64, 79ff
 Aperiodic variability, 29
 Aspect angles, 41, 117
 in 4U 1538-52, 42
 in GX 301-2, 67

— B —

Be star, 47
 Black hole, 5
 Bremsstrahlung, 34
 Burster, 133

— C —

Campbell theorem, 103
 Chi square test, 50
 Compton cooling, 2, 91, 94, 109, 113
 Compton scattering, 86
 Contamination
 by galactic ridge emission, 34
 Corotation radius, 79
 in 4U 1538-52, 38
 in GX 301-2, 64
 Coulomb gauge, 88
 Coulomb logarithm, 87
 Crab unit, 20
 Curvature
 of the magnetic field, 89
 Cyclotron line, 8
 in 4U 0115+63, 9
 in 4U 1538-52, 9, 42
 in Her X-1, 9
 Cyg X-1, 2, 115

— D —

Dead time, 17, 133-134
 function, 134
 sampling, 134
 Doppler effect, 6, 45

— E —

- Eclipse angle, 25
- Eddington luminosity, 101
- Emission pattern
 - fan beam, 8, 41
 - pencil beam, 1, 8, 41–42, 117
- EXOSAT observatory, 15ff
 - Gas Scintillator Proportional Counter, 17
 - Low Energy experiment, 17
 - Medium Energy experiment, 1, 17, 20
 - OBC programs, 21
 - Pulse Height Analyzer, 20
 - OBC programs, 17, 69, 133
- EXO 2030+375, 2, 63–64, 70, 116

— F —

- Fast Fourier Transform, 29, 132
- Fastness parameter, 6, 94
- Fourier transform, 131ff

— G —

- Gaunt factor, 87
- GX 301–2
 - physical properties, 45ff

— H —

- Her X–1, 5, 9

— I —

- Instability
 - effects due to magnetic field, 95, 110
 - energy principle, 89
- Iron line, 8
 - in 4U 1538–52, 1, 34, 40

— K —

- Kelvin–Helmholtz instability, 6, 92ff, 94, 116
 - growth rate, 94
- Kopernik Mikolaj, 5

— L —

- Lagrangian point, 75
- Landau levels, 8
- Lighthouse effect, 6

— M —

- Mach number
 - acoustic, 85
 - Alfvén, 85
- Magnetopause, 86
- Magnetospheric radius, 6, 77, 101
 - in 4U 1538–52, 38
 - in GX 301–2, 64
- Magnetospheric shape, 88, 108
- Mass function, 25
- Modulation index, 38, 57, 69
- m_0 : dominant scale height, 108

— N —

- Normalization
 - of count rate, 29
- Nyquist frequency, 57

— P —

- P–Cygni profiles, 45
- Parseval theorem, 132
- Periastron, 47, 49, 65
- Plasmapause, 92
 - radius, 93
- Poisson distribution, 102, 133
- Poissonian noise, 115
- Power spectrum, 132
- Pulsed fraction, 38

— Q —

- Qualified event, 17
 - rate, 134
- QV Nor, 1, 25

— R —

- Random walk, 26, 40, 55, 63, 79
- Rankine–Hugoniot condition, 86, 110
- Rayleigh–Taylor instability, 6, 10, 89ff, 94
 - growth rate, 94, 110
- Reconnection
 - of magnetic field, 89
- rms, 1–2, 34, 40, 61, 69, 115, 133
 - normalization, 131ff
- Roche–lobe, 75, 116
 - overflow, 116
 - radius, 25, 47

— S —

Saw-tooth behaviour, 2, 55, 63, 65, 69, 117
Sco X-1, 5
Shot noise, 2, 11, 70, 101, 102, 115–116
 cosinusoidal exponential shot noise, 105
 exponential shot noise, 104
 oscillating exponential shot noise, 104
 power spectrum, 103
 response function, 2, 11, 70, 101, 115–116
Step function, 104, 115
Swap manoeuvre, 20, 49, 119

— T —

Thomson cross section, 87, 113
Thomson scattering, 42
Time scale
 bremsstrahlung, 87
 Compton cooling, 87, 113, 116
 cooling, 76
 dissipation, 85
 due to accretion, 38, 64, 70
 dynamical, 110
 in GX 301-2, 111
 exchange, 87
 free fall, 110, 113
 in GX 301-2, 111
 heating, 76
 Kelvin-Helmholtz instability, 95
 Rayleigh-Taylor instability, 95, 110
 in GX 301-2, 111
 saw-tooth, 2, 55
 in GX 301-2, 63
Topological dissipation, 84, 85

— V —

Vela X-1, 1, 9, 36, 40, 45, 55, 79, 101

— W —

White dwarf, 5
Wind accretion, 75ff
Wray 977, 45, 64–65

